

Dissertation zur Erlangung des Doktorgrades
der Fakultät für Chemie und Pharmazie
der Ludwig-Maximilians-Universität München

**Structural Investigations and Postsynthetic
Modifications in Covalent Organic
Frameworks**

Maria Silvia Lohse
aus
Dippoldiswalde, Deutschland

2018

Erklärung

Diese Dissertation wurde im Sinne von §7 der Promotionsordnung vom 28. November 2011 von Herrn Prof. Dr. Thomas Bein betreut.

Eidesstattliche Versicherung

Diese Arbeit wurde eigenständig und ohne unerlaubte Hilfe erarbeitet.

München, den 15. Januar 2018

.....

Maria Silvia Lohse

Dissertation eingereicht am: 16.11.2017

1. Gutachter: Professor Dr. Thomas Bein

2. Gutachter: Senior Lecturer Dr. Stefan Wuttke

Mündliche Prüfung am: 20.12.2017

Danksagung

Als Erstes möchte ich mich bei meinem Doktorvater Prof. Dr. Thomas Bein für die freundliche Aufnahme in seinen Arbeitskreis bedanken und für die Möglichkeit an diesem interessanten und herausfordernden Forschungsthema arbeiten zu können.

Besonderer Dank gilt Dr. Stefan Wuttke, der mich gerade in schwierigen Phasen immer wieder mit Optimismus und Tatendrang angespornt hat. Danke für die wunderbaren Kooperationen und die Erstellung des Zweitgutachtens.

Dr. Dana Medina und Julian Rotter danke ich für die gute Zusammenarbeit und die interessanten Kooperationen. Weiterhin danke ich meinen Kooperationspartnern Dirk De Vos, Rob Ameloot und Timothée Stassin für die exzellente Zusammenarbeit beim Milchsäureadsorptionsprojekt. Ich danke Johannes T. Margraf und Timothy Clark für die erfolgreiche Zusammenarbeit im Rahmen des Mixed Linker Projekts und besonders den Organikern Veronika Werner, Simon Herbert, John Markiewicz und Paul Knochel für die tatkräftige Versorgung unserer Projekte mit COF Linkern.

Ich danke dem Doktorandennetzwerk IDK-NBT für die schöne, wenn auch unerwartet kurze Zeit in einem internationalen Doktorandenkolloquium. Weiterhin danke ich meinen Praktikanten Sara, José, Guillaume, Lukas, Michelle und Bora.

Claudia Bellomo, Ksenia Fominykh und Erika Virmani danke ich für die entspannten und unterhaltsamen Tee- und Kaffeepausen. Weiterhin möchte ich meinen Kolleginnen aus dem ehemaligen "Ladies Office": Erika, Cindy, Dodo, Laura, Tina für die nette Büroatmosphäre danken. Ich danke der MOF/COF Subgroup und dem gesamten AK Bein für die freundliche Arbeitsatmosphäre.

Außerdem möchte ich mich bei Regina Huber und Corinna Heidt für die organisatorische Unterstützung sowie bei Tina Reuther für die zahlreichen Messungen und die Organisation der Labore bedanken. Dr. Steffen Schmidt und Dr. Markus Döblinger danke ich für die REM und TEM Messungen.

Meiner Mentorin Dr. Lydia Simon möchte ich für das sehr interessante und hilfreiche Coaching in meinem letzten Promotionsjahr danken.

Ein besonderer Dank soll hier auch an meine vorherigen Arbeitsstationen gehen, bei denen ich viel gelernt habe und die die Grundlage für meine Promotionstätigkeit gelegt

haben. Zunächst daher Dank an meiner Alma Mater, die TU Bergakademie Freiberg mit ihrer ansteckenden Begeisterung für Wissenschaft. Ich möchte weiterhin auch Prof. Signe Kjelstrup für die freundliche Aufnahme in ihren Arbeitskreis während meines Auslandssemesters danken. Ein ganz besonderer Dank geht an das legendäre Labor 217 in Freiberg, danke für die wundervoll verrückte Zeit.

Der größte Dank gilt meiner Familie. Durch ihre persönliche und finanzielle Unterstützung und die Tatsache, dass sie mein Interesse an der Wissenschaft von Anfang an gefördert haben, wurde diese Arbeit erst möglich gemacht. Ein besonderer Dank geht dabei an Max Lohse und Elsa Kloß, die den erfolgreichen Abschluss dieser Arbeit leider nicht mehr erleben konnten.

Ganz besonders muss ich mich bei meinem Mann Sebastian und meiner Tochter Nora bedanken. Die beiden haben mir immer zur Seite gestanden und mich in schwierigen Phasen immer wieder aufgeheitert. Insbesondere danke ich Sebastian für seine Hilfe und dafür, dass er mir immer den Rücken frei gehalten hat.

Abstract

The research on porous functional materials has seen a great increase in activities with the introduction of the first metal-organic frameworks (MOFs) in 1999. The construction of porous frameworks from secondary building units and organic linkers allows for the modular construction of porous crystalline frameworks. With the development of the purely organic covalent organic frameworks (COFs) in 2005, it is now possible to transfer this concept to the world of organic polymers and to synthesize organic porous and crystalline materials with a defined control over their composition and geometry.

In covalent organic frameworks, organic linkers are connected *via* reversible organic reactions. While the reversibility of their formation reaction allows for the arrangement of the building blocks in an ordered fashion, the symmetry and connectivity of the linkers predefines the symmetry of the lattice and the size and shape of the pores in this networks. Furthermore, by decorating the building blocks with certain functionalities, the chemical character of the pore walls in the COF can be defined.

A comprehensive overview over the structures realized in COFs to date alongside with a detailed discussion of synthesis strategies and applications of COFs is given in Chapter 1. Matrices are used to depict the linker combinations that have been reported for COF synthesis. The practical part of this work focuses on two main tasks in COF research: the control of the crystallinity of COFs and their postsynthetic modification to tune the properties of the frameworks. In addition, an application of postsynthetically modified COFs in liquid adsorption is presented.

In the first project of this thesis, the structural impact of functional side groups in COFs is investigated. For that, the benzodithiophene linker in BDT COF is functionalized with ethoxy side chains. With this linker, the COF BDT-OEt is synthesized as crystalline, highly porous framework. To investigate the structural changes upon incorporation of OEt functionalized linker, a series of COFs with increasing OEt content is prepared. A gradual, almost linear decrease of both the pore diameter and the crystallite domain size is found for an increased content of BDT-OEt. Furthermore, the composition of the resulting framework can be pre-determined by the ratio of the linkers used in the synthesis allowing for a fine-tuning of the structural properties of the mixed-linker COF. Theoretical

calculations applying Monte Carlo and DFT simulations reveal an increasing lateral offset of the COF layers upon incorporation of higher amounts of the OEt-functionalized linker.

In the second project, the impact of a self-assembled monolayer on the growth of COF-5 as thin film on substrates is investigated. The study reveals a formation of thin films on gold substrates that are non-functionalized as well as on mercaptohexadecane SAMs that are functionalized with CH₃, OH, and COOH, respectively. The films feature preferential orientation of the crystallites with the c-direction being aligned perpendicular to the substrate surface plane. For substrates functionalized with -OH or -COOH terminated SAMs, a remarkably high degree of orientation of the crystallites was found, indicating that the -OH and -COOH groups can act as modulating agent to promote the formation of highly ordered COF crystallites.

Postsynthetic modification is a versatile strategy to increase the available pool of functionalizations in solid materials. In COFs, this approach is to date limited to only a few reaction pathways. In order to broaden the spectrum of postsynthetic modification reactions in covalent organic frameworks, a reaction pathway for the incorporation of primary amines as functional groups in COFs is developed in the third project. First the nitro-functionalized chemically highly stable β -ketoenamine-linked COF TpBD(NO₂)₂ is synthesized. The nitro groups are then reduced to amines to yield the COF TpBD(NH₂)₂ while preserving the crystallinity and porosity of the framework. The accessibility of the established amino groups is demonstrated by a sequential modification, the aminolysis of acetic anhydride to create the amide COF TpBD(NHCOCH₃)₂.

Furthermore, the performance of the COFs is tested in the adsorption of lactic acid, a major precursor for biodegradable plastics. A strong impact of the COF functionalization on the adsorption performance was found, with the amino-functionalization leading to a distinct increase in lactic acid adsorption compared to the pristine nitro-functionalized COF.

In the last project, postsynthetically introduced primary amines are utilized to amend the optical absorption of a COF by postsynthetic modification. The amino COF TpBD(NH₂)₂ is applied in azo coupling with *N,N*-dimethylaniline and diphenylamine, respectively. The degree of modification can be increased up to a quantitative conversion of the amino groups to azo groups. Diffuse reflectance UV-vis measurements reveal the impact of the azo dye functionalization on the visible absorption of the COF.

With diphenylamine as coupling agent and a conversion of 50% of the amino groups, a strong bathochromic shift of the UV-vis absorption can be observed, demonstrating the tunability of the optical absorption in COFs *via* postsynthetic modification.

Contents

Danksagung	i
Abstract	iii
1 Covalent Organic Frameworks: Structures, Synthesis and Applications	1
1.1 Introduction	2
1.2 Coupling Chemistry and Topologies	3
1.3 Linkage Types of COFs	8
1.3.1 Boroxines and Boronic Esters	8
1.3.2 Imines	18
1.3.3 Hydrazones and Azines	37
1.3.4 Ketoenamines	39
1.3.5 Other Linkages	42
1.4 Postsynthetic Modification	45
1.4.1 Postsynthetic Intercalation and Complexation in COFs	45
1.4.2 Covalent PSM	49
1.5 Synthetic Methods and Morphologies	54
1.5.1 Controlling the Crystallinity	54
1.5.2 Processing	62
1.5.3 Special Morphologies	67
1.6 Properties and Applications	85
1.6.1 Storage and Separation of Gases	85
1.6.2 Storage and Separation from Solution	92
1.6.3 Catalysis	96
1.6.4 Electrochemical Energy Storage and Electrical Devices	104
1.6.5 Optoelectronics	113
1.6.6 Sensing	119
1.6.7 Drug Delivery	121
1.7 Conclusion and Perspectives	122

2	Characterization Methods	147
2.1	X-ray Diffraction and Scattering	147
2.2	Vibrational Spectroscopy	149
2.2.1	Infrared Spectroscopy	149
2.2.2	Raman Spectroscopy	150
2.3	UV-vis Spectroscopy	151
2.4	Atomic Emission Spectroscopy	152
2.5	Nuclear Magnetic Resonance Spectroscopy	152
2.6	Electron Microscopy	154
2.7	Sorption	155
2.8	Contact Angle Measurement	159
2.9	Thermogravimetric Analysis	160
3	From Benzodithiophene to Diethoxy-benzodithiophene Covalent Organic Frameworks - Structural Investigations	163
3.1	Introduction	164
3.2	Results and Discussion	166
3.3	Conclusion	178
3.4	Experimental	178
3.4.1	Materials	178
3.4.2	Synthesis of 4,8-diethoxybenzo[1,2- <i>b</i> :4,5- <i>b'</i>]dithiophene (1)	178
3.4.3	Synthesis of 2,6-dibromo-4,8-diethoxybenzo[1,2- <i>b</i> :4,5- <i>b'</i>]-dithiophene (2)	179
3.4.4	Synthesis of 4,8-diethoxybenzo[1,2- <i>b</i> :4,5- <i>b'</i>]-dithiophene-2,6-diylboronic acid (3)	180
3.4.5	COF synthesis	180
3.4.6	Computational details	181
3.4.7	Characterization	181
4	Highly Oriented COF Thin Films Grown on SAM-modified Substrates	195
4.1	Introduction	196
4.2	Results and Discussion	197
4.3	Conclusion	202
4.4	Experimental	202
4.4.1	Methods and Characterization	202

4.4.2	Preparation of Gold Substrates	203
4.4.3	Growth of Self-Assembled Monolayers on Gold Substrates	203
4.4.4	Solvothermal COF-5 Film Growth	204
5	Sequential Pore Wall Modification in a Covalent Organic Framework for Application in Lactic Acid Adsorption	207
5.1	Introduction	208
5.2	Results and Discussion	210
5.3	Conclusion	217
5.4	Experimental	218
5.4.1	COF Synthesis of TpBD(NO ₂) ₂	218
5.4.2	Postsynthetic Modifications	219
5.4.3	Batch Adsorption	219
5.4.4	Characterization	220
5.5	Appendix	221
5.5.1	FT-IR spectra	221
5.5.2	UV-Vis spectra	222
5.5.3	COF synthesis attempt with 3,3'-diaminobenzidine as an alternative route to TpBD(NH ₂) ₂	223
6	Postsynthetic Azo Coupling in a Chemically Stable β-ketoenamine COF	229
6.1	Introduction	230
6.2	Results and Discussion	232
6.3	Conclusion	240
6.4	Experimental	240
6.4.1	Methods and Characterization	240
6.4.2	Synthesis of TpBD(DMA) ₂	241
6.4.3	Synthesis of TpBD(DPA) ₂	241
6.5	Appendix	243
6.5.1	Protonation Equilibria	243
6.5.2	Scanning Electron Microscopy Images	244
6.5.3	Pore Size Distribution of TpBD(NH ₂) ₂	245
7	Conclusion and Outlook	249

List of Figures

1.1	Widely applied condensation reactions for the formation of COFs.	4
1.2	Common linker geometries and the resulting topologies realized in 2D COFs.	6
1.3	Structure of a boronic ester COF with three different boronic acid linkers.	15
1.4	Scheme of linker combinations in mixed linker COFs reported by Huang et al.	17
1.5	Dual-pore and triple-pore COFs realized with mixed linear linkers and the ETTA building block	19
1.6	Schematic representation of the synthesis of the brick-wall COF	20
1.7	PXRD patterns and structure models of of brick-wall COF	21
1.8	Synthesis of HPB-COF and HBC-COF	22
1.9	Schematic of SIOC-COF-7	23
1.10	Schematic construction principle of double-stage COFs from linkers with different functional groups	24
1.11	Reaction scheme for the synthesis of COF-505	25
1.12	Hybrid MOF/COF structures with coordinative bonds and imine linkages .	26
1.13	Hybrid MOF/COF structure from titanium(IV)isopropoxide and benzene-1,4-dialdehyde	27
1.14	Schematic representation of the β -ketoenamine COF formation <i>via</i> enol-keto tautomerization.	39
1.15	Synthesis of BPy COFs and subsequent complexation of Rh and Pd	47
1.16	Synthesis of X%N ₃ -COF-5 and postsynthetic pore wall modification with alkynes	49
1.17	Postsynthetic modification of TpASH in three steps to establish a folic acid functionalization	52
1.18	Synthesis of Ph-An-COF and postsynthetic cycloaddition	53
1.19	Amorphous-to-crystalline conversion of the COF TpBD on Fe ₃ O ₄ nanoparticles	56
1.20	Lock-and-key motif of propeller-shaped building blocks enabling a defect-free layer growth	59

1.21 Schematic representation of the synthesis of azine-linked COFs with fluorinated linkers	61
1.22 Schematic representation of the mechanochemical synthesis of the COFs TpPa-1, TpPa-2, and TpBD using a mortar and pestle	64
1.23 Mechanochemical COF synthesis using the terracotta technique	65
1.24 SEM micrographs of BDT-COF films	67
1.25 Thin-film formation of DaTp-COF	69
1.26 The synthesis of SCOF-1 with $\text{CuSO}_4 \times 5\text{H}_2\text{O}$ as reaction equilibrium regulator	70
1.27 Concentration-induced structure evolution of a co-condensation reaction of ABBA and HHTP on HOPG at room temperature	71
1.28 Schematic diagram of the processes for fabricating metal/COF stack multilayer <i>via</i> alternating physical deposition of metal materials and solvothermal deposition of COF and for patterning thin films <i>via</i> photolithography and reactive ion etching	76
1.29 Patterned COF thin film on ITO substrate	77
1.30 Microfluidic synthesis of MF-COF-1	79
1.31 COF@PBI-BuI hybrid membrane fabrication	82
1.32 Synthesis and functionalization of H_2P -COFs and their carbon dioxide adsorption capacity	89
1.33 Uptake of iodine in SIOC-COF-7 hollow microspheres	91
1.34 Lactic acid adsorption isotherms of $\text{TpBD}(\text{NO}_2)_2$, $\text{TpBD}(\text{NH}_2)_2$, and $\text{TpBD}(\text{NHCOCH}_3)_2$	94
1.35 Synthesis of the $\text{Au}(0)\text{@TpPa-1}$ catalyst using the solution infiltration method for nitrophenol reduction reaction	98
1.36 The cascade reaction of benzaldehydedimethylacetals with malononitrile with various reactants	101
1.37 Scheme of the synthesis of N_x -COFs from N_x -aldehydes and hydrazine . . .	102
1.38 Hydrogen production with N_x -COFs as photocatalyst in the presence of triethanolamine as sacrificial electron donor	103
1.39 TPB-DMTP-COF with triazole and imidazole molecules in the COF channels	105
1.40 Incorporation of PEDOT within a DAAQ-TFP COF film	107
1.41 Charge storage performance and device integration of a PEDOT-modified DAAQ-TFP film	108

1.42 Schematic representation of the synthesis and the charge and discharge process of the Por-COF/S composite	111
1.43 MP-COFs with different metals	114
1.44 Carrier mobility and photoelectric properties of CS-COF	118
1.45 Fluorescent behavior of 3D-Py-COF	120
1.46 Cell uptake of 5-FU loaded COFs	122
2.1 Generation of X-rays: (a) Bremsstrahlung. (b) Characteristic radiation.	147
2.2 Schematic representation of Bragg diffraction at a periodical lattice.	148
2.3 Schematic representation of the GID geometry.	149
2.4 Basic modes of vibration for the H ₂ O molecule.	150
2.5 Energy-level diagram showing the energy transitions for Rayleigh and Raman scattering.	150
2.6 Electron transitions in molecules with π -, σ - and n -electrons	151
2.7 Evolution of the magnetization vector in an NMR experiment	153
2.8 Schematic setup of a transmission electron microscope and a scanning electron microscope	155
2.9 Classification of physisorption isotherms according to IUPAC	156
2.10 Illustration of the contact angle and the interfacial tensions	160
3.1 Schematic representation of the synthesis of BDT COF, BDT:BDT-OEt 1 : 1 COF, and BDT-OEt COF	165
3.2 XRD patterns of BDT-OEt COF	167
3.3 ¹ H-NMR spectra of the hydrolyzed COFs	168
3.4 FT-IR plots of BDT COF, BDT:BDT-OEt COFs and BDT-OEt COF.	169
3.5 PXRD patterns of BDT COF, BDT:BDT-OEt COFs, and BDT-OEt COF	169
3.6 Molecular structure of the ethoxy-substituted BDT unit and probability distribution of the dihedral angle sampled over 10 ns	170
3.7 Nitrogen sorption isotherms and pore size distributions of the COF powders	171
3.8 TEM micrographs of BDT COF, mixed BDT : BDT-OEt COFs and BDT-OEt COF	172
3.9 SEM micrographs of BDT COF, mixed BDT : BDT-OEt COFs and BDT-OEt COF	173
3.10 TGA traces of BDT COF, mixed BDT : BDT-OEt COFs and BDT-OEt COF	174

3.11	^{11}B ssNMR spectrum and ^{13}C ssNMR spectrum of BDT-OEt COF	176
3.12	Sulfur-sulfur radial distribution functions of the ethoxy substituted and pristine BDT-COF	177
3.13	Simulation of BDT-OEt COF unit cells calculated in an eclipsed arrange- ment in the $P6$ space group	185
3.14	Simulation of BDT-OEt COF unit cells calculated in an eclipsed arrange- ment in the $P1$ space group	185
3.15	XRD patterns of BDT-OEt COF in $P1$ space group	186
3.16	Simulation of BDT-OEt COF unit cells calculated in a staggered arrange- ment with $P6_3$ space group	186
3.17	XRD patterns of BDT-OEt COF: experimental, simulated AA eclipsed ar- rangement, and simulated AB staggered arrangement; comparison of simu- lated XRD patterns of BDT COF and BDT-OEt COF	187
4.1	Contact angle measurements of functionalized gold substrates	198
4.2	Detector scan XRD measurements and TEM image	199
4.3	2D-GID analysis for COF-5 grown on SAM-modified and non-modified sub- strates	200
4.4	Scanning electron microscopy images	201
5.1	Schematic representation of the synthesis of $\text{TpBD}(\text{NO}_2)_2$ and postsynthetic modification to $\text{TpBD}(\text{NH}_2)_2$ and $\text{TpBD}(\text{NHCOCH}_3)_2$	209
5.2	PXRD patterns, FT-IR spectra and nitrogen sorption isotherms	210
5.3	Differential pore size distribution plots and thermogravimetric traces	211
5.4	SEM images	212
5.5	TEM images	213
5.6	^{15}N and ^{13}C solid state NMR spectra	214
5.7	Lactic acid adsorption isotherms	216
5.8	PXRD patterns of the TpBD -COFs before and after batch adsorption of lactic acid	217
5.9	FT-IR spectra	221
5.10	UV-Vis spectra	222
5.11	Reaction scheme for a proposed direct synthesis of $\text{TpBD}(\text{NH}_2)_2$	223
5.12	PXRD pattern of the reaction product formed from 3,3'-diaminobenzidine and 1,3,5-triformylphloroglucinol.	224

6.1	Schematic representation of the azo coupling reaction	231
6.2	PXRD patterns of TpBD(NH ₂) ₂ , azo coupling products TpBD(DMA) ₂ and TpBD(DPA) ₂	232
6.3	Spectroscopic characterization	235
6.4	¹³ C solid state NMR spectra of TpBD(NH ₂) ₂ , TpBD(DMA) ₂ , and TpBD(DPA) ₂	236
6.5	Nitrogen sorption isotherms of TpBD(DMA) ₂ and TpBD(DPA) ₂	236
6.6	Transmission electron microscopy images of TpBD(DPA) ₂ 25% and TpBD(DPA) ₂ 100%.	238
6.7	UV-Vis spectra of TpBD(NH ₂) ₂ and TpBD(DMA) ₂ 25% to TpBD(DMA) ₂ 100%.	239
6.8	UV-Vis spectra of TpBD(NH ₂) ₂ and TpBD(DPA) ₂ 25% to TpBD(DPA) ₂ 100%.	239
6.9	Protonation equilibria of TpBD(DMA) ₂ and TpBD(DPA) ₂	243
6.10	Scanning electron microscopy images of TpBD(NH ₂) ₂ , TpBD(DMA) ₂ 50%, TpBD(DMA) ₂ 100%, TpBD(DPA) ₂ 50%, TpBD(DPA) ₂ 100%.	244
6.11	Differential pore size distribution plot of TpBD(NH ₂) ₂	245

List of Tables

1.1	Structural diversity in COFs.	7
1.2	Building blocks of boroxine-linked COFs	8
1.3	Linker molecule combinations of boronic acids with linear catechols.	9
1.4	COFs with boronic ester linkage from small boronic acids without heteroatoms in the backbone.	10
1.5	COFs with boronic ester linkage with heteroatoms in the phenyl rings of the boronic acid.	11
1.6	COFs with boronic ester linkage and advanced nitrogen-rich groups in the backbone of the boronic acid.	12
1.7	COFs with boronic ester linkage with trigonal and elongated linear boronic acids.	13
1.8	Imine-linked COFs with 1,3,5-triformylbenzene as aldehyde linker	18
1.9	Imine-linked COFs from tridental aldehydes and linear to tridental amines	18
1.10	Imine-linked COFs from tridental aldehydes and linear to tridental amines (continued)	28
1.11	Imine-linked COFs from linear aldehydes with more than one phenyl ring and trigonal amines	29
1.12	Imine-linked COFs from linear aldehydes with up to one phenyl ring and trigonal amines	30
1.13	Imine-linked COFs from linear aldehydes and tetradental amines	31
1.14	Imine-linked COFs from linear aldehydes and tetradental amines (continued)	32
1.15	Imine-linked COFs from tetra- and hexadental aldehydes and linear amines	33
1.16	Imine-linked COFs from tetradental aldehydes and tetradental amines . . .	34
1.17	Imine-linked COFs with hexadental amines	34
1.18	Mixed linkage COFs with imine bonds and boroxine or boronic ester bonds	35
1.19	Mixed linkage COFs with imine bonds and boroxine or boronic ester bonds (continued)	35
1.20	Mixed linkage COFs with imine bonds and boroxine or boronic ester bonds (continued)	36

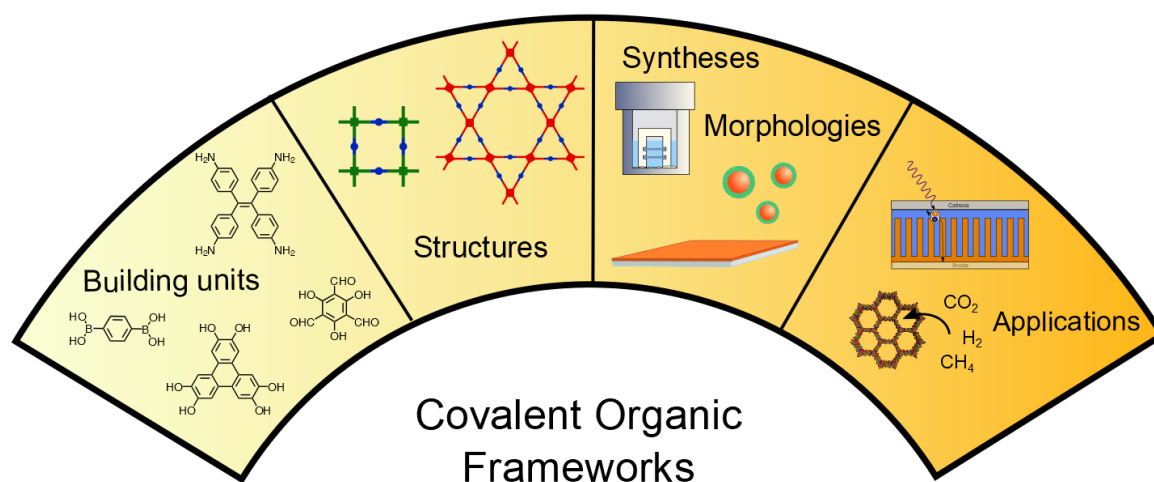
1.21	COFs with hydrazone linkage	37
1.22	Aldehyde linkers that were incorporated in azine-linked COFs	38
1.23	Mixed linkage COFs with imine and hydrazone bonds	38
1.24	Ketoenamine-linked COFs with TPG as linker	40
1.25	Ketoenamine-linked COFs with extended TPG linkers	41
1.26	Ketoenamine-linked COFs <i>via</i> Michael addition-elimination	41
1.27	COFs with imide linkage	42
1.28	COFs with imide linkage (continued)	42
1.29	Further reactions for COF formation and their structural representatives. .	44
1.30	Further reactions for COF formation and their structural representatives (continued).	45
3.1	Refined crystal data of BDT-OEt COF.	183
3.2	Fractional atomic coordinates of BDT-OEt COF.	184
5.1	ICP-OES elemental analysis determination of residual tin concentration in TpBD(NH ₂) ₂	212
5.2	Assignment of IR bands	221

Chapter 1

Covalent Organic Frameworks: Structures, Synthesis and Applications

This chapter is based on the manuscript of the article: “Covalent Organic Frameworks: Structures, Synthesis and Applications”

Maria S. Lohse and Thomas Bein, submitted to *Advanced Functional Materials*.



Abstract

Covalent organic frameworks (COFs) are crystalline porous polymers formed by a bottom-up approach from molecular building units having a pre-designed geometry that are connected through covalent bonds. They offer positional control over their building blocks in two and three dimensions. This control enables the synthesis of rigid porous structures with a high regularity and the ability to fine-tune the chemical and physical properties of the network. This Feature Article provides a comprehensive overview over the structures realized to date in the fast growing field of Covalent Organic Framework development; we discuss different synthesis strategies to meet diverse demands, such as high crystallinity, straightforward processability or the formation of thin films. Furthermore, we give insights into the growing fields of COF applications, including gas storage and separations, sensing, electrochemical energy storage and optoelectronics.

1.1 Introduction

Covalent Organic Frameworks (COFs) have attracted much interest in recent years due to the enormous potential design space offered by the atomically precise spatial assembly of molecular organic building blocks. COFs are crystalline, porous networks built from organic linkers *via* reversible covalent bond formation.¹⁻⁴ The size, symmetry and connectivity of the linkers predefine the geometry of the resulting framework. Thus, unlike typical linear polymers, COFs offer positional control over their building blocks in two and three dimensions. This control enables the synthesis of structures with high regularity and allows for fine-tuning the chemical and physical properties of the network. The defined nanoscale channels and spaces that are formed by the COF scaffolds represent an ideal environment for molecular storage, release and separation tasks, while the large and defined interface is beneficial for catalysis and sensing applications. Moreover, the regularity and connectivity of the organic units make COFs interesting candidates for applications that depend on charge carrier transport, including optoelectronics and electrochemical energy storage.

With their organic and crystalline character, COFs complement 'classical' inorganic porous crystalline materials such as zeolites,⁵⁻⁷ and hybrid-inorganic-organic metal organic frameworks (MOFs)⁸⁻¹⁰ on the one hand, and porous organic materials without long-range order like porous aromatic frameworks¹¹ and polymers with intrinsic microporosity^{12,13} on the other hand. The enormous possible design space available with COF structures is

reflected in the significant number of structures that have been realized for this structural class to date, although this research field is only twelve years young.

In this feature article, we aim to give a concise overview over the building blocks utilized in crystalline COF structures to date. First, we introduce the prerequisites and the coupling reactions for COF formation, alongside with matrices that provide an overview over the structures that have been realized for this materials class to date. In addition to assembling diverse molecular linkers in coupling reactions to generate the frameworks, additional functionality can be incorporated into COFs through postsynthetic modification. This method will be described in a subsequent section. Furthermore, we will introduce and discuss the different synthesis techniques and morphologies realized in COF synthesis. Thereby, a main focus will be on insights regarding the prerequisites for the formation of a crystalline COF rather than an amorphous structure. The last part of the article will address the multitude of properties of COFs and applications that have been realized so far, providing inspiration for the further development and utilization of these intriguing structures.

1.2 Coupling Chemistry and Topologies

Covalent organic frameworks are built from organic linkers *via* slightly reversible condensation reactions. While the covalent bonds established in the frameworks enable a high thermal stability, the reversible nature of the relevant coupling reactions permits the formation of a crystalline structure rather than an amorphous polymer, as it allows for error correction and rearrangement of the network by cleavage and re-formation of connections within the lattice.

The very first COFs were made by the co-condensation of boronic acids with catechols to form five-membered boronic ester rings as linkage between the building blocks, and by self-condensation of boronic esters to boroxines.¹⁴

Since then, a variety of different reactions have successfully been applied in the formation of COFs to date, see Figure 1.1 for the most commonly used reactions and Tables 1.29 and 1.30 in Section 1.3.5 for additional synthesis pathways that have been applied for only few structures.

As boroxines and boronic esters are rather sensitive towards hydrolysis, an important goal was the development of more stable coupling motifs, which was realized with the introduction of the imine linkage formed by the condensation between aldehydes and

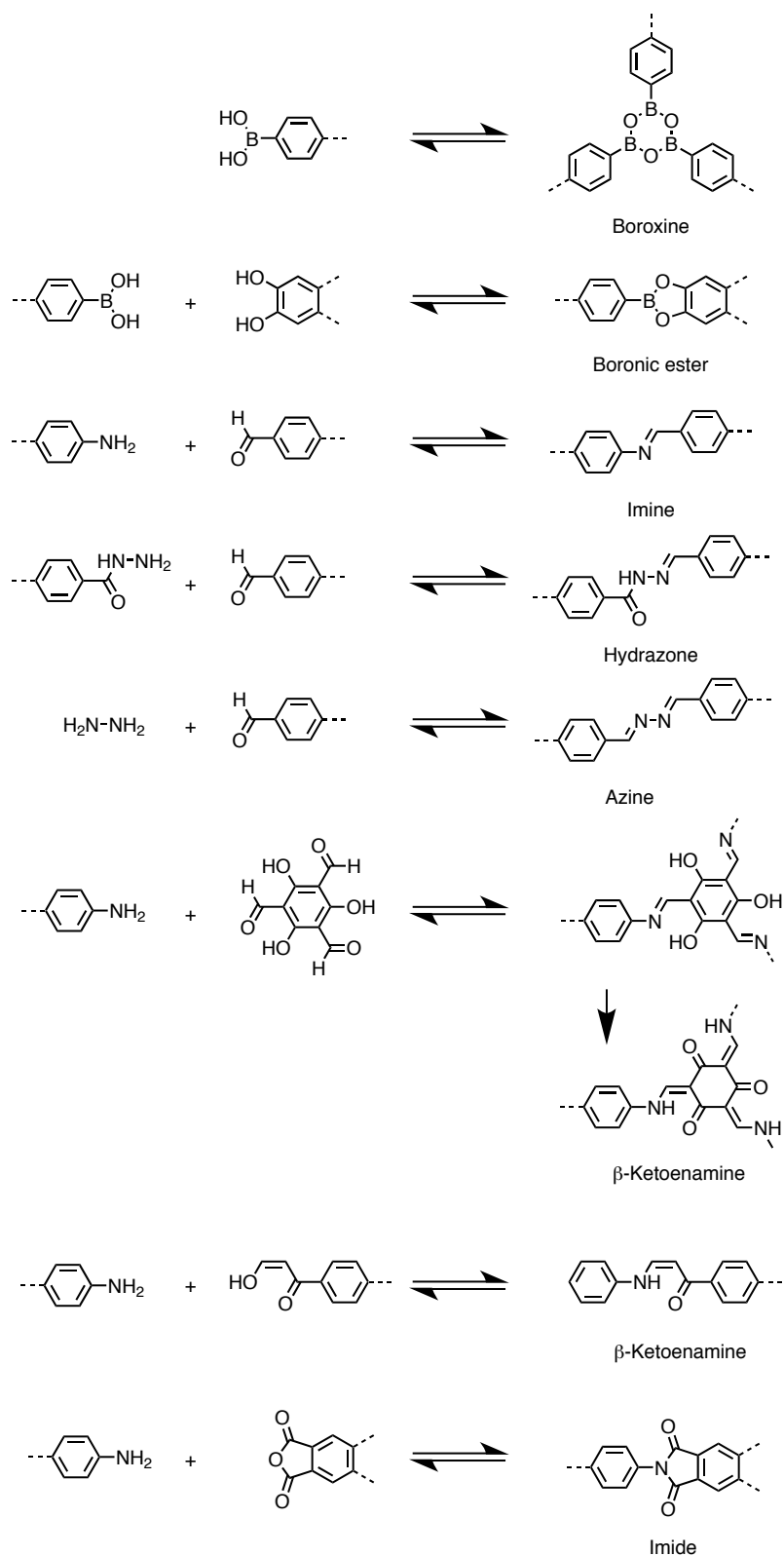


Figure 1.1: Widely applied condensation reactions for the formation of COFs.

primary amines, as well as with hydrazones, azines and imides, which will be discussed in detail in the next section.

A further improved chemical stability was found for β -ketoenamines that are formed from primary amines and 1,3,5-triformylphloroglucinol (TPG) and undergo a second and irreversible enol-keto-tautomerization to create networks that are stable against acids and bases.

In a COF lattice, the geometry of the framework is predetermined by the geometry and connectivity of the linkers. For example, trigonal planar linkers can co-condense to form sheets with hexagonal pores, while tetragonal linkers co-condensed with linear building blocks form tetragonal pores. These sheets then form stacks to generate a framework with 1D-channels. COFs made from stacked two-dimensional layers are commonly named 2D COFs, whereas 3D COFs are created from building blocks with connectivity in three dimensions, thus building up a 3D net.

An overview over common 2D geometries realized in COFs is given in Figure 1.2. To illustrate these construction principles, a few representative COF networks (2D and 3D COFs) are displayed in Table 1.1.

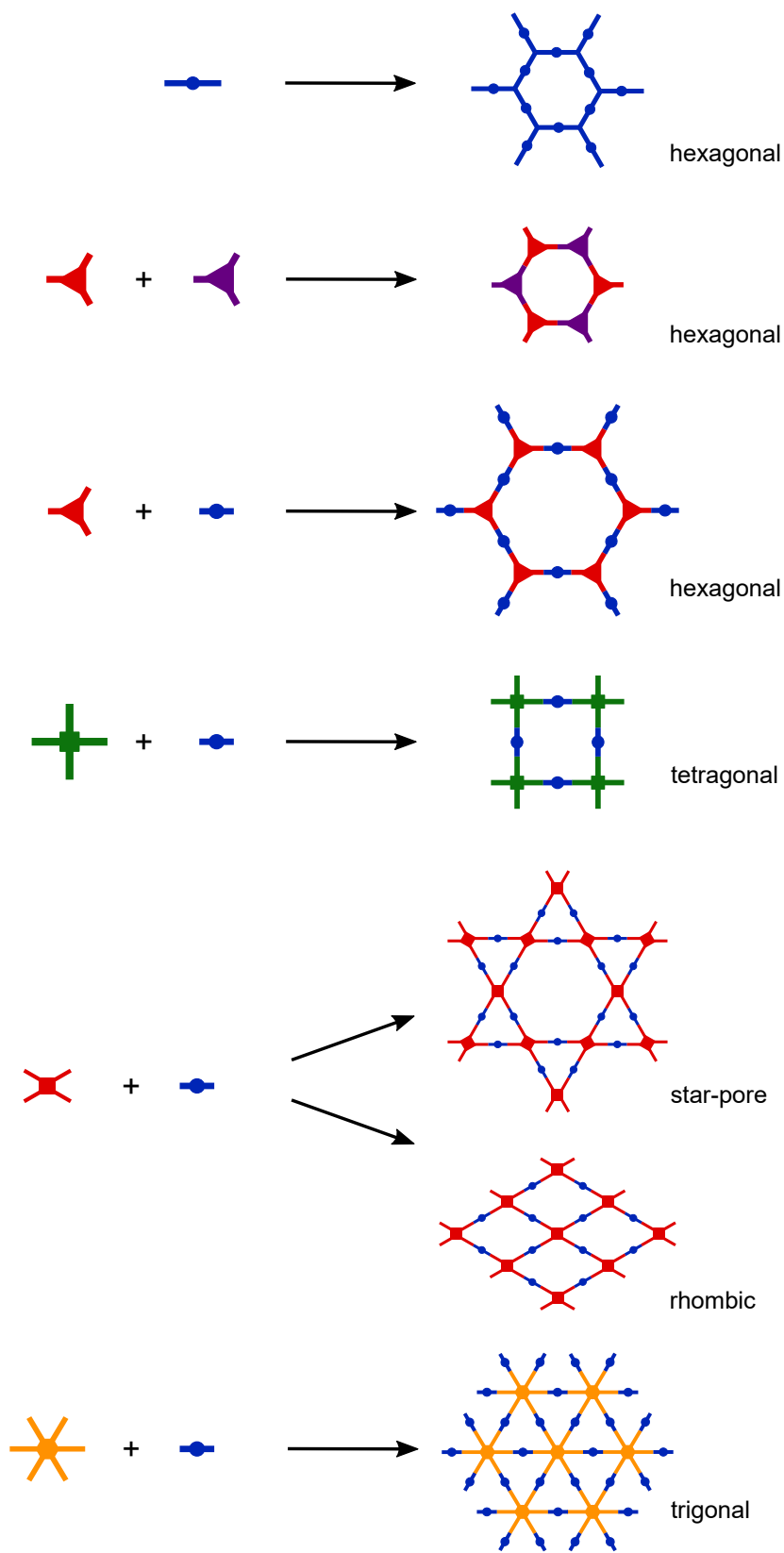
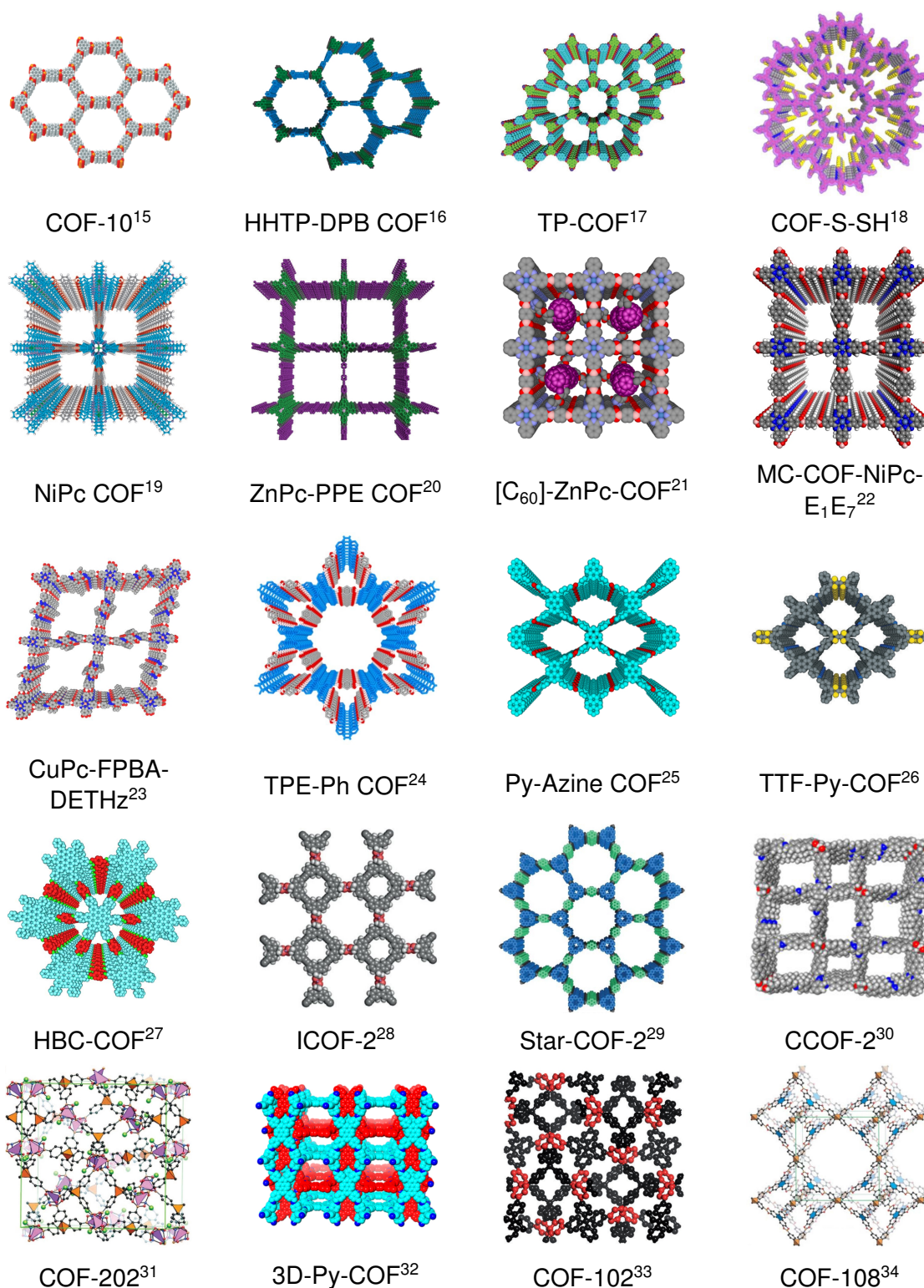


Figure 1.2: Common linker geometries and the resulting topologies realized in 2D COFs.

Table 1.1: Structural diversity in COFs.



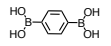
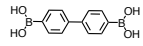
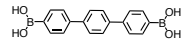
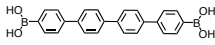
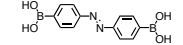
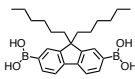
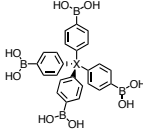
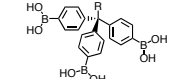
First line: COF-10, adapted with permission from ref. 15, copyright 2007 American Chemical Society. HHTP-DPB-COF, adapted with permission from ref. 16, copyright 2011 American Chemical Society. TP-COF, adapted with permission from ref. 17, copyright 2008 John Wiley and Sons. COF-S-SH adapted with permission from ref. 18, copyright 2017 American Chemical Society. Second line: NiPc COF adapted with permission from ref. 19, copyright 2010 John Wiley and Sons. ZnPc-PPE COF, adapted with permission from ref. 20, copyright 2012 John Wiley and Sons. [C₆₀]-ZnPc-COF, adapted with permission from ref. 21, copyright 2014 American Chemical Society. MC-COF-NiPc-E₁E₇, adapted from ref. 22, CC-BY 4.0 licence (<https://creativecommons.org/licenses/by/4.0/>). Third line: CuPc-FPBA-DETHz, adapted from ref. 23, CC-BY 4.0 licence (<https://creativecommons.org/licenses/by/4.0/>). TPE-Ph COF, adapted with permission from ref. 24, copyright 2016 American Chemical Society. Py-Azine COF, adapted with permission from ref. 25, copyright 2013 American Chemical Society. TTF-Py-COF, adapted with permission from ref. 26, copyright 2014 John Wiley and Sons. Fourth line: HBC-COF, adapted from ref. 27, CC-BY 4.0 licence (<https://creativecommons.org/licenses/by/4.0/>). ICOF-2 adapted with permission from ref. 28, copyright 2015 John Wiley and Sons. Star-COF-2, reproduced in part from ref. 29 with permission of The Royal Society of Chemistry. CCOF-2, adapted with permission from ref. 30, copyright 2016 American Chemical Society. Fifth line: COF-202, adapted with permission from ref. 31, copyright 2008 American Chemical Society. 3D-Py-COF, adapted with permission from ref. 32, copyright 2016 American Chemical Society. COF-102, adapted with permission from ref. 33, copyright 2012 John Wiley and Sons. COF-108 from ref. 34, reprinted with permission from AAAS.

1.3 Linkage Types of COFs

1.3.1 Boroxines and Boronic Esters

The self-condensation of boronic acids to boroxine rings and the co-condensation of boronic acids and catechols to boronic esters were the first reactions reported for the synthesis of COFs.

Table 1.2: Building blocks of boroxine-linked COFs

 COF-1 ^{14,35-53} SCOF-1 ⁵⁴ SCOF-2 ⁵⁵	 SCOF-2 ^{35,52} SCOF-1 ⁵⁵	 t.b.n. ³⁵
 t.b.n. ³⁵	 PPy-COF ^{35,56} Pyrene-COF ⁵⁷	 surface COF ABBA ⁵⁸
 SCOF-3 ⁵⁵	 X=C COF-102 ^{34,53,59-61} X=Si COF-103 ³⁴	 R= Toly COF-102-toly ⁶¹ R= allyl COF-102-allyl ^{33,62} R = -(CH ₂) ₁₁ -CH ₃ COF-102-C ₁₂ ³³ (all mixed with the tetraboronic acid)

t.b.n: structure to be named.

A full list of boroxine-linked COFs is given in Table 1.2. The slight reversibility of these reactions enabled the formation of crystalline, porous frameworks. The self-condensation of 1,4-benzenediboronic acid (BDDBA) to form a boroxine network yielded COF-1 with a pore diameter of 1.5 nm.

While the (approximately) eclipsed AA stacking motif is the most common packing modality in 2D COFs, this framework stacks in a staggered fashion, that is, in AB conformation. Upon removal of solvent guest molecules, these layers shift towards an AA stacking mode.¹⁴

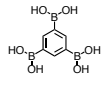
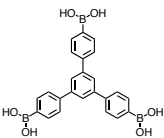
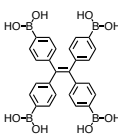
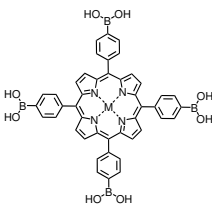
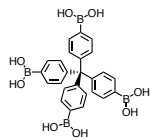
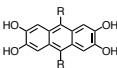
A variety of boroxine COFs could be accessed *via* on-surface condensation of the corresponding boronic acid precursors. For example, on graphite substrates linear diboronic acids with one to four phenyl rings and pyrene-2,7-diboronic acid were condensed to form regular surface COFs.³⁵

In the co-condensation of 2,3,6,7,10,11-hexahydroxytriphenylene (HHTP) and 1,4-benzenediboronic acid (BDDBA), the hexagonal framework COF-5 was formed whose layers

stack in an eclipsed AA fashion to yield a material with hexagonal 1D channels of 2.7 nm in diameter. COF-5 has been widely used as a model system and was synthesized using various methods that will be discussed in detail later in this article.

The elongation of the diboronic acid unit in COF-5 from BDBA to 4,4'-biphenyldiboronic acid leads to COF-10 with a pore diameter of 3.2 nm, while the combination of HHTP with the trigonal boronic acids 1,3,5-benzene triboronic acid and with 1,3,5-benzene tris(4-phenylboronic acid) forms COF-6 (pore diameter 0.86 nm) and COF-8 (pore diameter 1.64 nm), respectively.¹⁵

Table 1.3: Linker molecule combinations of boronic acids with linear catechols.

					
	R=H COF-18 Å ⁶³⁻⁶⁵ R=CH ₃ COF-16 Å ^{64,65} R=CH ₂ CH ₃ COF-14 Å ^{64,65} R=CH ₂ CH ₂ CH ₃ COF-11 Å ^{64,65}		TPE-Ph COF ²⁴	R=H, M=H ₂ H ₂ -COF ⁶⁶ R=H, M=Zn ZnP-COF ^{66,67} R=H, M=Cu CuP-COF ⁶⁶	MCOF-16 ⁸
	R=H Ph-An-COF ⁶⁹	R=CH ₃ BTP-COF ⁷⁰		M=H ₂ , R=H COF-66 ⁷¹	

The reverse building principle for boronate-coupled COFs uses tridentate boronic acids and linear catechols (Table 1.3). Its first representative, COF-18 Å, was prepared by the group of Lavigne by condensing 1,2,4,5-tetrahydroxybenzene with benzene-1,3,5-triboronic acid.⁶³

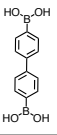
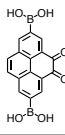
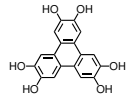
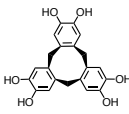
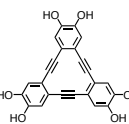
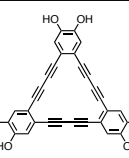
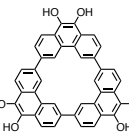
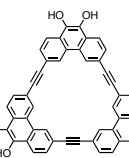
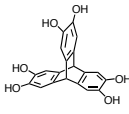
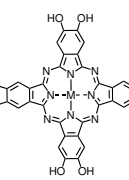
The resulting COF is microporous with a pore diameter of 18 Å, which was eponymous for the COF. In a similar way, by using 2,6-disubstituted 1,2,4,5-tetrahydroxybenzene units with methyl, ethyl, and propyl functionalization, COFs were synthesized with pore diameters of 16 Å, 14 Å, and 11 Å, respectively.⁶⁴ This alkylation also increased the degradation stability of these COFs in water.⁶⁵

In contrast, a remarkably large pore system was realized by our group by co-condensing 2,3,6,7-tetrahydroxy-9,10-dimethyl-anthracene with 1,3,5-benzenetris(4-phenylboronic acid), thereby reaching a pore diameter of 4.0 nm.⁷⁰

The unsubstituted 2,3,6,7-tetrahydroxyanthracene was co-condensed with the aforementioned benzene-1,3,5-triboronic acid. The anthracene units underwent a [4p+4p] cy-

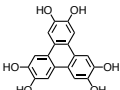
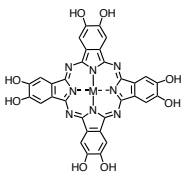
10 1. Covalent Organic Frameworks: Structures, Synthesis and Applications

Table 1.4: COFs with boronic ester linkage from small boronic acids without heteroatoms in the backbone.

					
	COF-5 ^{14,39,44,48,57,72-84} COF-5 (a.p.c.) ⁸⁵ SCOF-2 ⁵⁴ mixed-linker COFs (see Figure 1.4) ²²	X%N ₃ -COF-5 (mixed with BDBA) ⁸⁶	COF-10 ^{15,48,76,81,83,87-89} COF-10 (a.p.c.) ⁸⁵	TP- COF ^{17,74,76,81,83,90}	Dione- COF ⁹⁰
	CTC-COF ⁹¹		CTC-COF-2 ⁹²	CTC-COF-3 ⁹²	
	DBA-COF ¹⁹³ AEM-COF-1 ⁹⁴			Py-DBA-COF ¹⁹⁵	
	DBA-COF ²⁹³			Py-DBA-COF 2 and Py-MV-DBA-COF (mixed with the smaller linker in the row above) ⁹⁵	
	Star-COF-1 ²⁹		Star-COF-3 ²⁹	Star-COF-2 ²⁹	
	AEM-COF-2 ⁹⁴				
	TDCOF-5 ⁹⁶				
	M=H ₂ Pc-PBBA COF (a.p.c.) ⁹⁷ M=Co CoPc-COF ⁹⁸ M=Cu CuPc-COF ⁹⁸ M=Ni NiPc-PBBA COF ⁷⁴ NiPc-PBBA COF (a.p.c.) ⁸⁵ NiPc COF ¹⁹ mixed-linker COFs (see Figure 1.4) ²² M=Zn ZnPc-COF ⁹⁸ ZnPc-PBBA COF ⁹⁹ ZnPc-BBA COF ⁸²	M=Ni X%N ₃ -NiPc- COF (mixed with BDBA) ⁸⁶ M=Zn X%N ₃ -ZnPc- COF (mixed with BDBA) ²¹	M=Co CoPc-BPDA COF ¹⁰⁰	M=Zn ZnPc-Py COF ²⁰	

a.p.c.: the catechol linker was applied in the synthesis as acetonide protected catechol; BDBA: benzene-1,4-diboronic acid.

Table 1.5: COFs with boronic ester linkage with heteroatoms in the phenyl rings of the boronic acid.

						
	2D D-A COF ¹⁰²	T-COF-1 ¹⁰³ T-COF 2 (with additional boroxine formation) ¹⁰³	T-COF 3 ¹⁰³	TT-COF ^{104,105} T-COF 4 ¹⁰³	X=S BDT-COF ^{57,106-108} 1-S ¹⁰⁹ X=Se 1-Se ¹⁰⁹ X=Te 1-Te ¹⁰⁹	BDT- OEt COF (also mixed with BDT) ¹⁰⁷
	M=Ni 2D-NiPc- BTDA COF ¹¹⁰					

a.p.c.: the catechol linker was applied in the synthesis as acetonide protected catechol; BDBA: benzene-1,4-diboronic acid; BDT: (4,8-diethoxybenzo[1,2-b:4,5-b']dithiophene-2,6-diyl)diboronic acid.

claddition upon irradiation at 360 nm, thereby establishing connections between two adjacent COF layers. The cycloaddition was reversible and repeatable for several cycles.⁶⁹

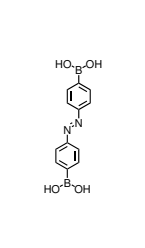
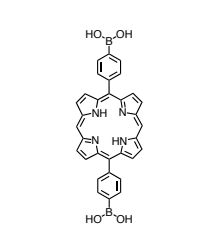
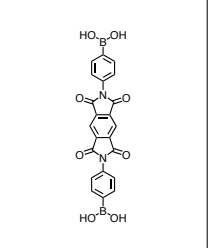
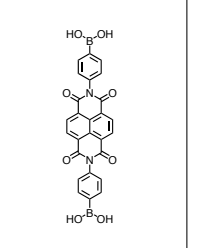
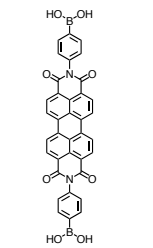
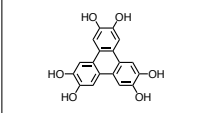
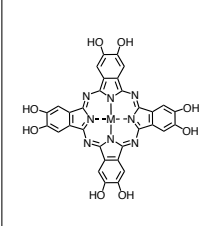
Zhang and Zhu built a COF from an azo-group-containing diboronic acid and HHTP. Under illumination (365 nm) 17% of the azo groups were isomerized from the trans to the cis state while the COF structure was preserved.¹⁰¹

Thiophene is a widely used building block of polymers in organic photovoltaics. It is, therefore, an interesting functionality for COF structures. For a detailed list of boronic ester COFs with the heteroatoms S, Se, and Te see Table 1.5. Our group synthesized a COF from thieno[3,2-*b*]thiophene-2,5-diyl diboronic acid and demonstrated charge transfer to fullerene molecules in the COF pores.¹⁰⁴

Dincă and coworkers prepared a structural series of COFs using HHTP and different thiophene-based diboronic acid units, namely 2,5-thiophenediboronic acid, bithiophene-2,5'-diboronic acid, and thieno[3,2-*b*]thiophene-2,5-diyl diboronic acid. Interestingly, with 2,5-thiophenediboronic acid, the expected hexagonal structure where HHTP forms the nodes and the diboronic acid the edges of the network was only formed when the reaction was performed under strict exclusion of water and a 3:2 ratio of diboronic acid to HHTP. If these conditions were not fulfilled, a second phase was formed, where the 2,5-thiophenediboronic acids formed boroxine rings which then co-condensed with HHTP. No second phase was formed with the other thiophenes.¹⁰³ The growth of oriented films of the thieno[3,2-*b*]thiophene-2,5'-diyl diboronic acid containing COF has been reported.¹⁰⁵

12 1. Covalent Organic Frameworks: Structures, Synthesis and Applications

Table 1.6: COFs with boronic ester linkage and advanced nitrogen-rich groups in the backbone of the boronic acid.

					
	Azo-COF ¹⁰¹ 2D-surface COF _{AH} ¹¹¹	TP-Por COF ¹¹²	D _{TP} -A _{PyrDI} -COF ⁸⁸	D _{TP} -A _{NDI} - COF ^{88,113}	
		M=Co CoPc- PorDBA COF ¹¹⁴	M=Ni D _{NiPc} -A _{PyrDI} - COF ¹¹⁵ M=Cu D _{CuPc} -A _{PyrDI} - COF ¹¹⁵	M=Ni D _{NiPc} -A _{NDI} - COF ¹¹⁵ M=Zn ZnPc-NDI COF ²⁰ D _{ZnPc} -A _{NDI} - COF ¹¹⁶ M=Cu D _{CuPc} -A _{NDI} - COF ¹¹⁵	M=Zn D _{ZnPc} -A _{PDI} - COF ¹¹⁵ M=Cu D _{CuPc} -A _{PDI} - COF ¹¹⁵

a.p.c.: the catechol linker was applied in the synthesis as acetone protected catechol; BDBA: benzene-1,4-diboronic acid; BDT: (4,8-diethoxybenzo[1,2-*b*:4,5-*b'*]dithiophene-2,6-diyl)diboronic acid.

We introduced a COF containing the benzodithiophene linker benzo[1,2-*b*:4,5-*b'*]dithiophene-2,6-diyl diboronic acid and demonstrated the formation of thin oriented films of this COF on different substrates. Furthermore, we showed electron transfer from the electron donating COF towards fullerene moieties in the COF pores.¹⁰⁶ We were also able to synthesize this COF in a room temperature vapor-assisted synthesis, which will be described in detail in Section 1.5.2.5,⁵⁷ and as a mixed-linker COF with a benzodithiophene unit bearing ethoxy side chains on the phenyl ring.¹⁰⁷

Duhović and Dincă extended the scope of heteroatoms in COF linkers by synthesizing the Se and Te equivalents of the benzodithiophene moiety. In the resulting COF structures, these analogs increase the charge carrier mobility, showing a better mobility for the greater chalcogen size.¹⁰⁹ By incorporating a thiadiazole unit in the diboronic acid linker, the group of Jiang was able to build an electron donor (thiadiazole) and electron acceptor (HHTP) framework.¹⁰²

By using the tetrahedral boronic acid tetrakis(4-dihydroxyborylphenyl)methane (TBPM) and its silicon derivative tetrakis(4-dihydroxyborylphenyl)silane (TBPS), Yaghi and coworkers formed COFs with a three-dimensionally linked network, either by self-condensation of the boronic acid (COF-102 and -103) or by co-condensation with HHTP (COF-105 and -108). The frameworks possess very high surface areas, reaching 4210 m² g⁻¹

for COF-103.¹⁵ Co-condensation of TBPM and 1,2,4,5-tetrahydroxybenzene resulted in a microporous COF with uniform pores of 0.64 nm in diameter.⁶⁸

Bunck and Dichtel applied a mixed linker strategy to incorporate truncated trigonal linkers with a dodecyl chain or an allyl group in the COF-102 network. The framework tolerated truncated linker content of 23% and 37% for allyl and dodecyl functionalization, respectively.³³

In a different truncation approach, a monoboronic acid was used to partially saturate boronic acid groups of TBPM in the synthesis of COF-102. Up to 36 mol% of *p*-tolylboronic acid were incorporated into the framework while a crystalline and porous structure was still formed. This strategy was also applicable with 4-nonylphenylboronic acid, 4-vinylphenylboronic acid and 4-formylphenylboronic acid.⁶¹

Table 1.7: COFs with boronic ester linkage with trigonal and elongated linear boronic acids.

	T-COF-OH ⁸⁴	HHTP-DPB COF ^{16,76,83} DPB-COF ⁸¹		COF-6 ¹⁵	COF-8 ^{15,117}	X=C COF-105 ³⁴ X=Si COF-108 ³⁴
						X=C DBA-3D- COF 1 ¹¹⁸
		M=Zn ZnPc- DPB COF ²⁰	M=Zn ZnPc- PPE COF ²⁰			

El-Kaderi et al. created a COF structure with a triptycene catechol linker where the planes of the phenyl rings are aligned in parallel to the pore channels, making the COF pores very small and the boron sites accessible for guest molecules. The investigated TDCOF-5 that was obtained from 1,4-benzene diboronic acid and hexahydroxytriptycene featuring accessible boron sites and thereby enhancing the gas sorption performance.⁹⁶ Playing on the theme of non-planar building blocks, an undulated layered structure was obtained by incorporating the bowl-shaped triangular linker hexahydroxy cyclotri-catechy-

lene into a COF lattice. The COF layers were found to have an AA stacking motif with the cyclotricatechylene units forming columnar stacks.⁹¹

Jiang and coworkers introduced 9,10-hydroxyphenanthrene cyclotrimer, a C_3 -symmetric macrocycle with catechol functional groups as a building block for boronic ester COFs. By condensing this molecule with BDBA, pyrene-2,7-diboronic acid and biphenyldiboronic acid, star-shaped COFs were formed that feature both micropores from the macrocyclic building block and mesopores that are established by the hexagonal arrangement of the linkers.²⁹

This concept was later expanded by the group of Zhang who elongated the edges of the phenanthrene cyclotrimer building block and the well-known HHTP with one ethynyl group each to form dehydrobenzoannulenes,⁹⁴ and by the group of McGrier who introduced the HHTP derivate elongated by two ethynyl groups⁹³ as well as a 3D COF with the smaller HHTP derivate,¹¹⁸ see Table 1.4. All of these macrocycle-based COFs possess high surface areas. However, the small pores present in the macrocycles could not be confirmed from the pore size distributions calculated from the nitrogen sorption isotherms in any of the presented COFs, indicating poor accessibility of these pores, probably due to an offset in the stacking arrangement of these COFs.

Dual-pore systems with accessible trigonal pores were later realized with another strategy using the boronic acid analog of the 1,1,2,2-tetraphenylethylene core as a linker, which was first used as the amine component in an imine COF (the amine-linker is abbreviated ETTA). Hence, Jiang and coworkers co-condensed the boronic acid functionalized ETTA building block (ethene-1,1,2,2-tetrayltetrakis(benzene-1,4-diyl)tetraboronic acid) with the aforementioned linear catechol 1,2,4,5-tetrahydroxybenzene (THB) to yield TPE-Ph COF with pores of 1.3 and 2.6 nm, respectively.²⁴

A widely used linker core for COFs is phthalocyanine, either in its H-form or complexed with a metal. This molecule is a good electron donor, making it an attractive building block for optoelectronic applications of COFs, and it offers excellent stacking ability. A potential drawback is the poor solubility.

The most commonly used COF architecture uses phthalocyanine catechols; the first corresponding COF was introduced by Spitler and Dichtel. They utilized a phthalocyanine in which the catechol groups were protected by acetonide groups, thereby increasing the chemical stability and solubility of the starting material. By co-condensing this linker with BDBA in the presence of the Lewis acid $\text{BF}_3 \times \text{OEt}_2$, which served as *in situ* deprotecting agent, a crystalline COF with an eclipsed stacking arrangement was formed.⁹⁷

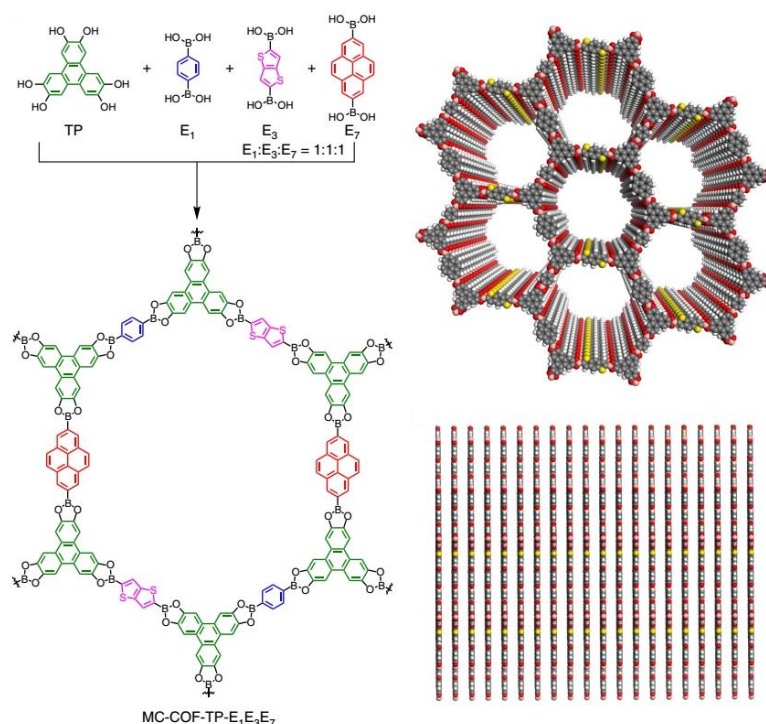


Figure 1.3: Structure of a boronic ester COF with three different boronic acid linkers. Adapted from ref. 22, CC-BY 4.0 licence (<https://creativecommons.org/licenses/by/4.0/>).

On the other hand, phthalocyanines were used in the form of boronic acids and were combined with linear catechols, mainly 1,2,4,5-tetrahydroxybenzene,^{66,67} but also with longer building blocks.⁷¹ Phthalocyanine building blocks have also been utilized for the synthesis of COFs as thin films on graphene.^{74,99} In this context, not only BDBA but also significantly elongated linkers were used to reach a maximum diameter of the resulting tetragonal pores of 4.4 nm with phenylbis(phenylethynyl) units acting as a boronic acid linker,²⁰ see Table 1.7.

Connecting the electron-donating phthalocyanines with pyromellitic diimide, naphthalene diimide, and perylene diimide as electron acceptors (Table 1.6), Jiang et al. created COF donor-acceptor superheterojunctions.^{115,116} The structurally related porphyrin core was used in the form of a linear diboronic acid as a COF linker and co-condensed with phthalocyanine catechols to form a porphyrin-phthalocyanine COF featuring a combination of two good electron donors.¹¹⁴

Utilizing the same linear porphyrin linker as electron donor in conjunction with HHTP as electron acceptor, we created a COF that represents an integrated D-A heterojunction.¹¹² This and several more phthalocyanine and porphyrin-based COF struc-

tures have been investigated as optoelectronic materials. They will be discussed in detail in Section 1.6.5.

A great expansion of the possible COF structures is realized when COFs with mixtures of different linkers are synthesized. Huang et al. reported a broad series of boronic ester COF structures with up to three different boronic acid linkers in the same structure (Figure 1.3). Most of the building blocks applied in these frameworks are mentioned in the tables of this section, but the authors additionally introduced naphthalene-2,6-diylboronic acid and (buta-1,3-diyne-1,4-diylbis(1,4-phenylene))diboronic acid as COF linkers (Figure 1.4).²²

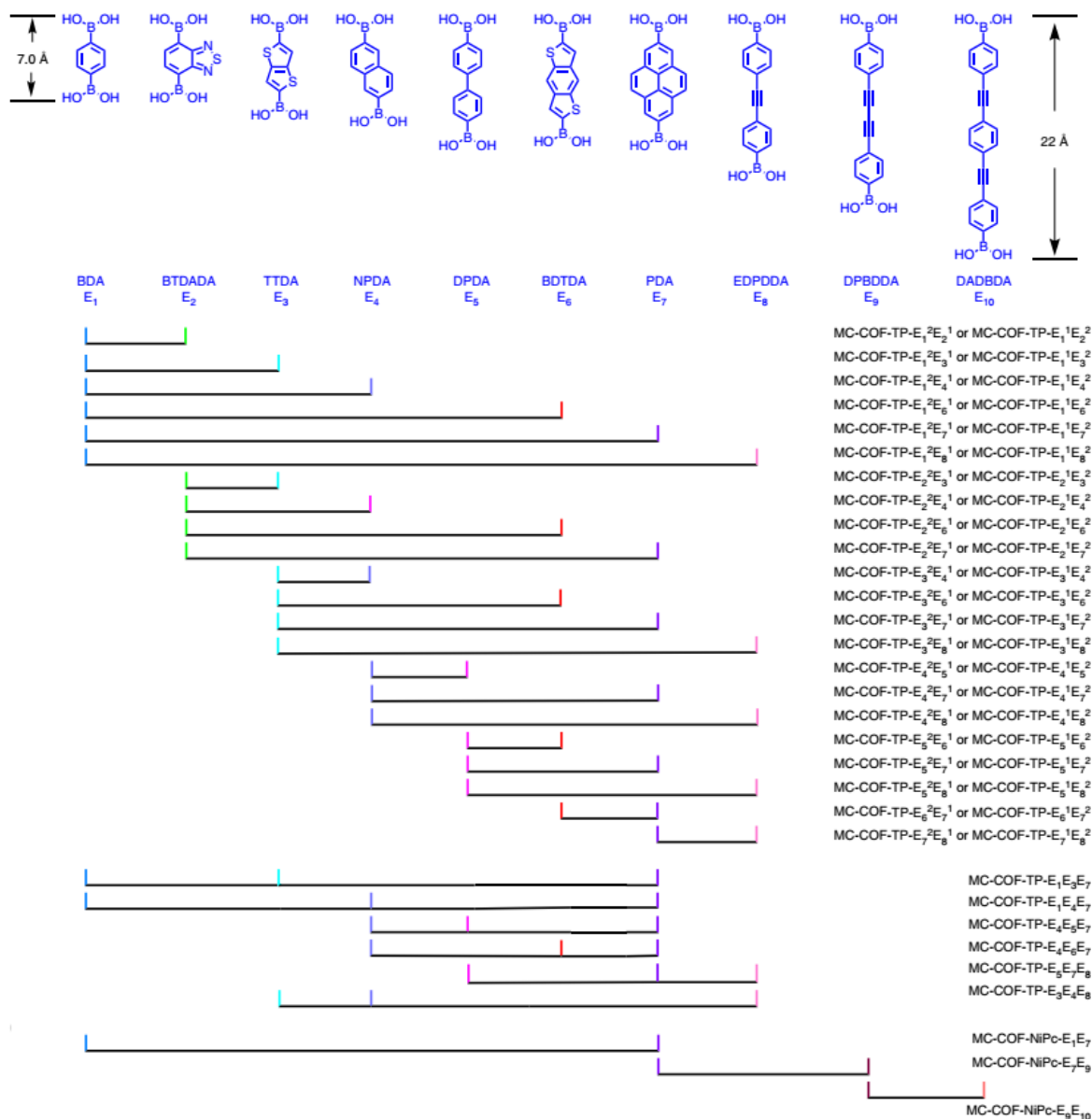


Figure 1.4: Scheme of linker combinations in mixed linker COFs reported by Huang et al. Adapted from ref. 22, CC-BY 4.0 licence (<https://creativecommons.org/licenses/by/4.0/>).

1.3.2 Imines

The condensation of aldehydes and amines yields imine bonds. By reacting an aromatic amine with an aromatic aldehyde, a conjugation of the π -systems of both linkers can be achieved, enabling conjugation over whole 2D COF layers. The first imine COF was introduced by Yaghi and coworkers in 2009. They reported a 3D COF made from tetrakis(4-anilyl)methane and terephthalaldehyde (TA), which crystallizes in a tetragonal framework with 5-fold interpenetration,¹¹⁹ see Table 1.14.

Table 1.8: Imine-linked COFs with 1,3,5-triformylbenzene as aldehyde linker

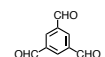
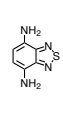
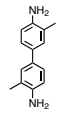
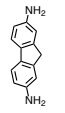
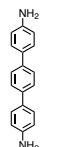
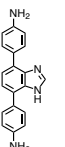
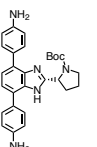
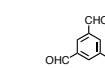
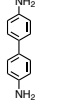
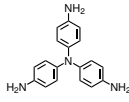
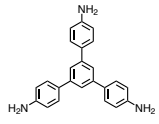
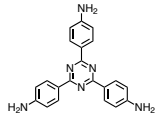
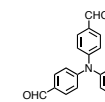
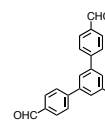
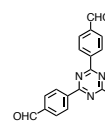
								
	TH-COF-1 ¹²⁰	surface COF ₁₊₄ ¹²¹	FL-COF-1 ¹²²	surface COF ₁₊₅ ¹²¹	LZU-70 ¹²³	LZU-72 ¹²³	PPN-30 ¹²⁴	BF-COF-1 ¹²⁵

Table 1.9: Imine-linked COFs from tridental aldehydes and linear to tridental amines

					
	COF-LZU ₁ ^{120,126-133} SCOF-LZU-1 ¹³⁴ surface COF ₁₊₂ ¹²¹ 2D surface COF _{BTA-PDA} ^{135,136}	surface COF ₁₊₃ ¹²¹ COF-1 ¹³⁷ PI-2-COF ¹³⁸ N2-COF ¹³⁹	N-COF ¹⁴⁰	RT-COF-1 ¹⁴¹⁻¹⁴³ MF-COF-1 ¹⁴³ sRT-COF-1 ¹⁴⁴ P-COF ¹⁴⁰	Nitrogen-rich COF ¹⁴⁵ PI-3-COF ¹³⁸ N3-COF ¹³⁹ T-COF ¹⁴⁰
	IISERP-COF ₂ ^{146,147}		TFPA-TAPA-COF ¹⁴⁸	TFPA-TAPB-COF ¹⁴⁸	
	NUS-15 ¹²⁷	sCOF-IC ₂ ¹⁴⁹		TFPB-TAPB-COF ¹⁴⁸	
	NUS-14 ¹²⁷				TTI-COF ¹⁵⁰

A 3D imine COF with larger pores was achieved by co-condensing (3,3'-bipyridine)-6,6'-dicarbaldehyde and tetrakis(4-anilyl)methane. It features pore flexibility that allows for expansion and contraction of the pores upon guest adsorption and removal, respectively. This resulted in a higher CO₂ sorption capacity of the COF at higher relative humidity,

as water vapor induced the transformation to the expanded form of the network, thereby acting as gate opener.¹⁵¹ Furthermore, tetra(amino)adamantane was used as an amine linker in combination with 1,3,5-triformylbenzene (TFB) or triformylphloroglucinol (in which case a ketoenamine COF is obtained) to create microporous 3D COF structures with small pore diameters of around 8 Å.¹²⁵

The first imine-based 2D COF was reported by Wang et al., who performed the condensation of 1,3,5-triformylbenzene (TFB) and 1,4-phenylenediamine (PDA), thus creating a layered COF with hexagonal channels, similar to the established boronic ester COFs,¹²⁶ (Table 1.9).

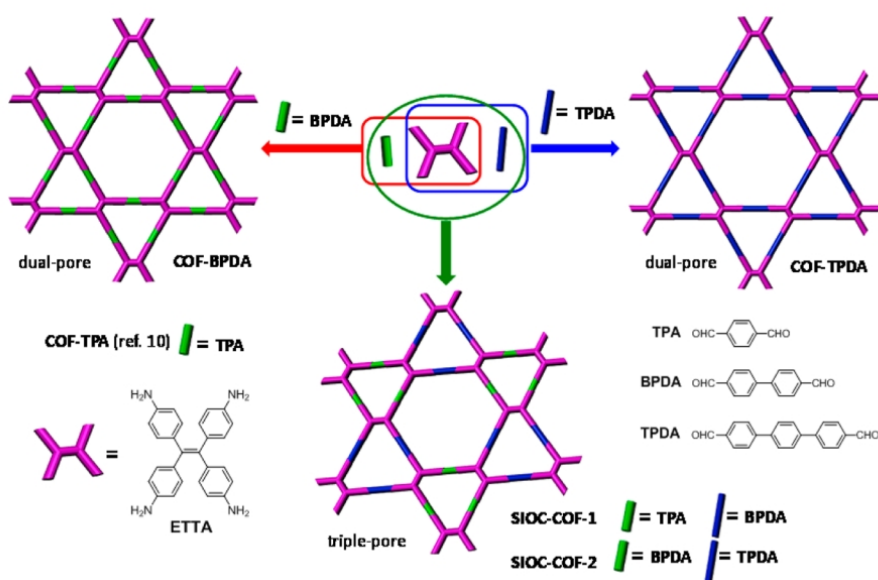


Figure 1.5: Dual-pore and triple-pore COFs realized with mixed linear linkers and the ETTA building block. Reprinted with permission from ref. 159. Copyright 2016 American Chemical Society.

However, imine COFs differ significantly from boronic ester COFs with respect to their higher stability against moisture. Although this stability also depends on the incorporated linkers, it has, together with the large library of available aldehyde and amine linkers and the possibility to construct conjugated π -systems throughout the whole COF sheets, made imine bonds very popular linkage motifs in COFs. To date, imine-formation is clearly the most common synthesis strategy to build COFs. Tables 1.8 to 1.17 provide a comprehensive overview over these structures, sorted by the connectivity of their linkers.

As for boronic ester COFs, phthalocyanines have also been widely used as linkers in imine linked COFs, both with amine or aldehyde functional groups. When they are

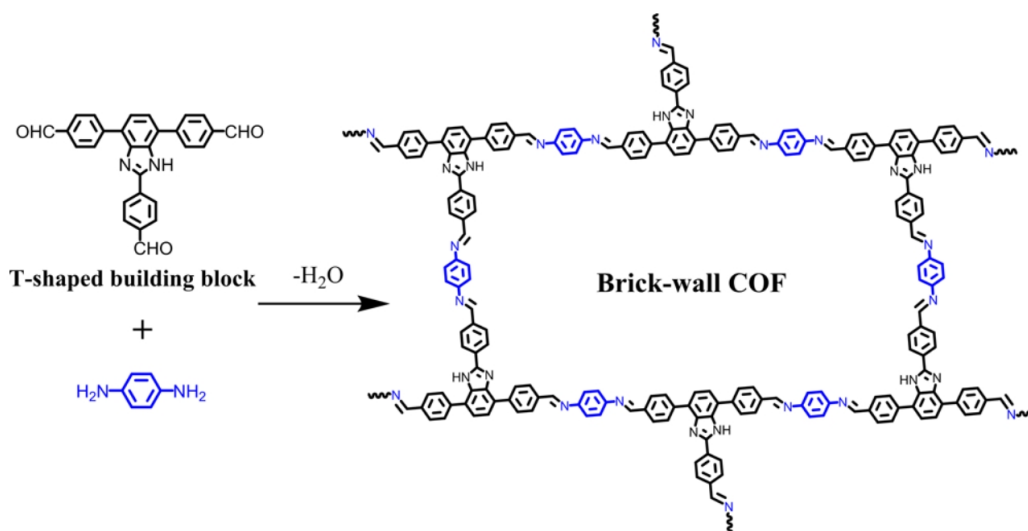


Figure 1.6: Schematic representation of the synthesis of the brick-wall COF. Reprinted with permission from ref. 158. Copyright 2016 American Chemical Society.

combined with linear linkers, tetragonal pores are formed upon stacking of 2D-sheets. The electron donating phthalocyanine units have also been used to create COFs that were investigated with respect to their optical and electrical properties (see Section 1.6.5 for a detailed discussion).

A large variety of topologies has been realized in imine COFs. Rhombic pores are formed when 1,3,6,8-tetrakis(*p*-formylphenyl)pyrene is used as a linker. El-Kaderi and coworkers introduced this building block that favors π -stacking and thereby forms highly crystalline COFs.¹⁶⁰ It was later incorporated in many other frameworks, both as amine and aldehyde.^{26,161–164} The pyrene aldehyde linker was also incorporated in 3D-Py-COF, which crystallizes in a two-fold interpenetrated structure.³²

Zhao and coworkers introduced the linker 4,4',4'',4'''-(ethene-1,1,2,2-tetrayl)tetraaniline (ETTA) that forms, together with terephthalaldehyde, a star-shaped dual pore system with hexagonal mesopores of 26.9 Å in diameter and triangular microporous pores of 7.1 Å nm in diameter.¹⁶⁵ This is in contrast to the aforementioned COFs built from pyrene aldehyde units, which have a symmetry similar to that of the ETTA building block.

Zhao et al. showed that linear linkers of different lengths can be mixed in these star shaped COFs and that it is thereby possible to prepare frameworks with pores of three different sizes (Figure 1.5), namely one hexagonal pore and two different triangular pores.¹⁵⁹

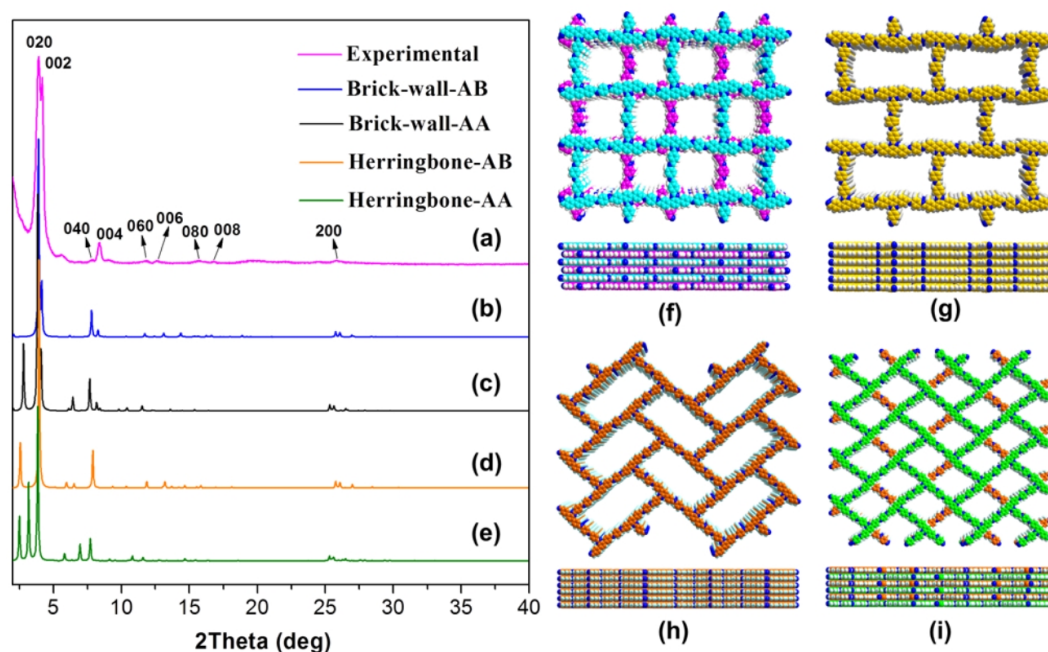


Figure 1.7: Experimental PXRD patterns of brick-wall COF (a); Simulated PXRD patterns of brick-wall COF: AB packing (b) and AA packing (c) structures; Simulated PXRD patterns of herringbone COF: AB packing (d) and AA packing (e) structures; Space-filling models of brick-wall COF: AB packing (f) and AA packing (g) structures; Space-filling models of herringbone COF: AA packing (h) and AB packing (i) structures. Reprinted with permission from ref. 158. Copyright 2016 American Chemical Society.

Further star shaped COFs were realized by combining the tetradental linker[1,1'-biphenyl]-3,3',5,5'-tetracarbaldehyde with linear amine linkers (1,4-phenylenediamine in COF-BTA-DAB and benzidine in COF-BTA-BZ).¹⁶⁶ Pang et al found that when exchanging the linear aldehyde linker, that was co-condensed with the ETTA building block, with one that featured bulky side groups, such as $-\text{CH}_2\text{CH}_3$ or $-(\text{CH}_2)_3\text{CH}_3$, the star-shaped pore geometry was not realized anymore. Instead, the framework formed one type of pores with rhombic shape.¹⁶⁷

A new COF topology was introduced by Cai et al. They utilized a T-shaped aldehyde linker in combination with the linear amine PDA (Figure 1.6). With these building blocks, rectangular pores are formed with two different possible arrangements: a brick wall or a herringbone arrangement. Comparison of calculated structures with the experimental XRD data revealed the formation of a brick wall framework with an AB packing of the COF layers (Figure 1.7).¹⁵⁸

Jiang and coworkers established another geometry of COF structures by introducing C_6 -symmetric linkers that are connected by the linear linker TA. Thereby, accessible tri-

angular pores are formed with a diameter in the micropore range. Specifically, using hexaphenylbenzene and hexabenzocoronene, triangular pores with a size of 12 Å and 18 Å are formed, respectively (Figure 1.8). The dense packing of the resulting π -stacked arrays may also be beneficial in optoelectronics.²⁷

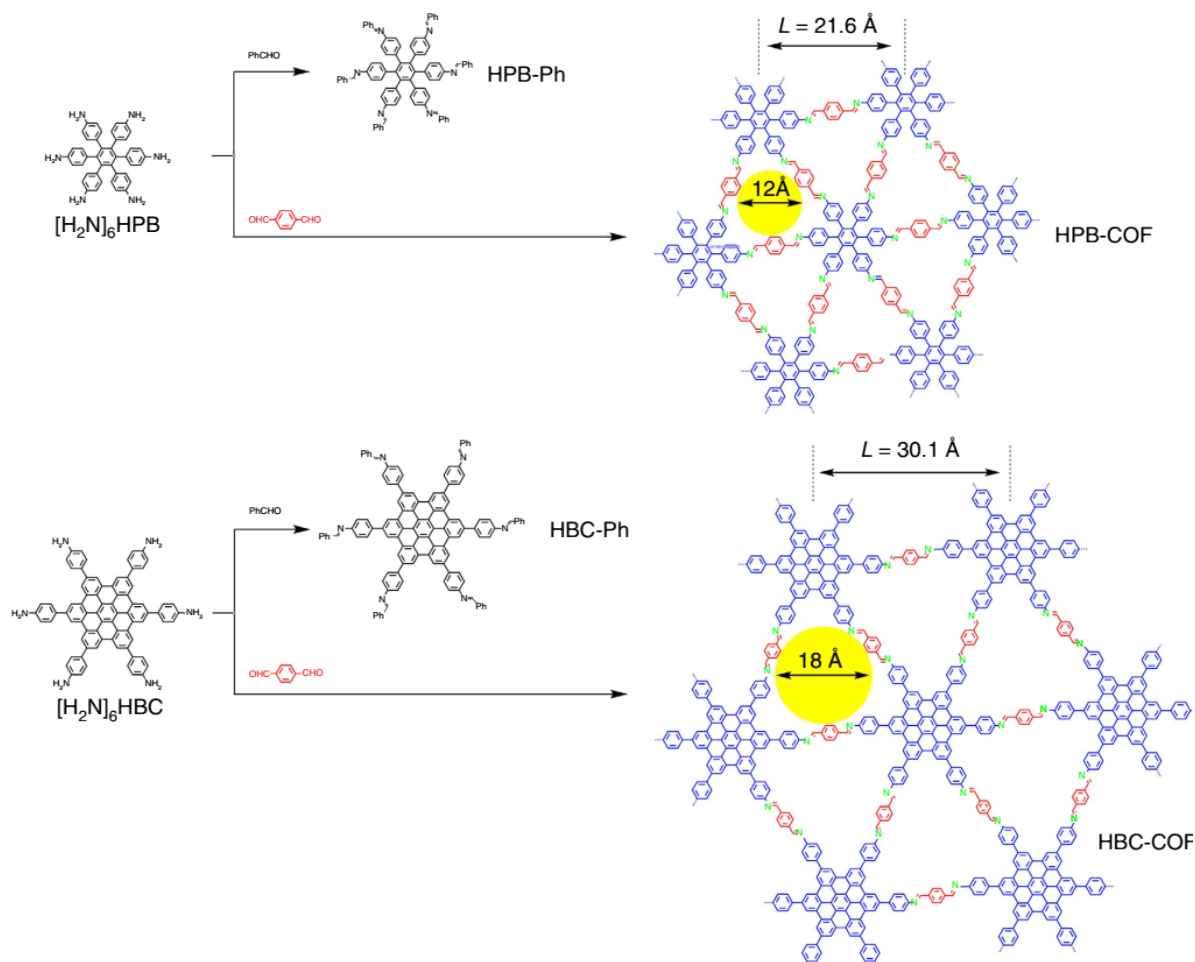


Figure 1.8: Synthesis of HPB-COF and HBC-COF. Adapted from ref. 27, CC-BY 4.0 licence (<https://creativecommons.org/licenses/by/4.0/>).

The group of Zhao later reported a COF coupling terephthalaldehyde with a hexaaza-triphenylene unit as amine linker, thereby forming triangular pores with two pore sizes of 11.3 Å and 15.2 Å, respectively.¹⁶⁸

Another dual pore system was realized by combining the hexaaldehyde linker 4',4''',4''''-nitrilotris([1,1'-biphenyl]-3,5-dicarbaldehyde) with the linear amines PDA and benzidine, respectively. Thereby two hexagonal pore systems are created. Interestingly, these COFs were found to stack in a staggered conformation, in contrast to most other 2D COFs.¹⁶⁹

Yin et al. introduced the hexadental linker 4,4''-bis(4-formylphenyl)amino-[1,1':4',1''-terphenyl]2'-5'-dicarbaldehyde. Co-condensation of this building block with PDA yielded the dual-pore SIOC-COF-7 with a large hexagonal and smaller parallelogram type pores (Figure 1.9).¹⁷⁰

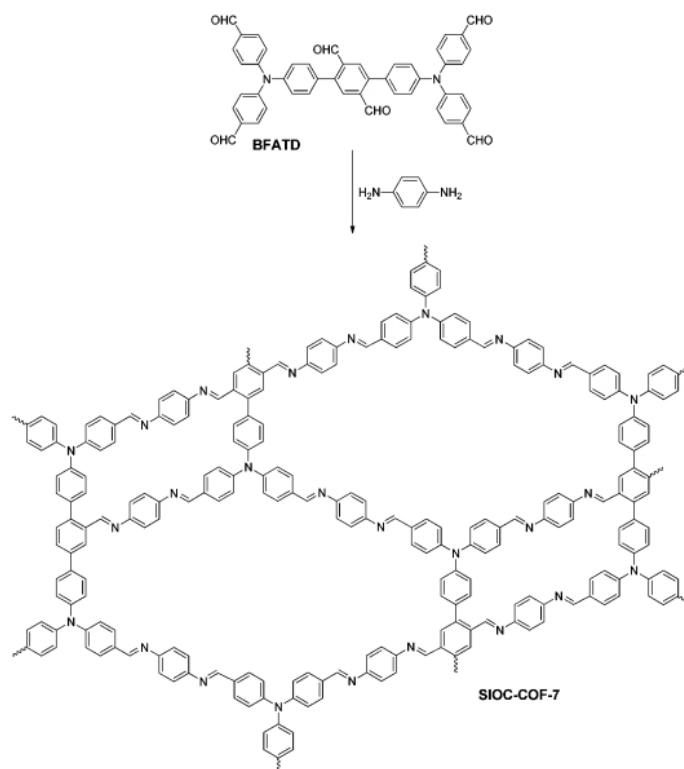


Figure 1.9: Schematic of SIOC-COF-7. Reproduced from ref. 170 with permission of The Royal Society of Chemistry.

Three pores in a COF structure were realized by Qian et al. by truncating a hexadental aldehyde linker to yield the building block (1,1':3',1''-terphenyl)-3,3'',5,5''-tetracarbaldehyde in which two of the four aldehyde groups are aligned in parallel. Co-condensing this aldehyde with PDA or benzidine leads to a COF with three different pores, where the very narrow pores between the parallel aldehydes were too small for nitrogen sorption analysis.¹⁷¹

A highly interesting concept for the design of COF structures was introduced by Zeng and coworkers.¹⁷² They used double stage connectors that feature functional groups of different types, e.g. an aldehyde group and a boronic acid. These building blocks can then interconnect linkers of different types, like amines and catechols (Figure 1.10). With this method, the number of possible COF structures is dramatically increased. Chen et

al. used this method to synthesize a variety of structures with different geometries and pore sizes.²³

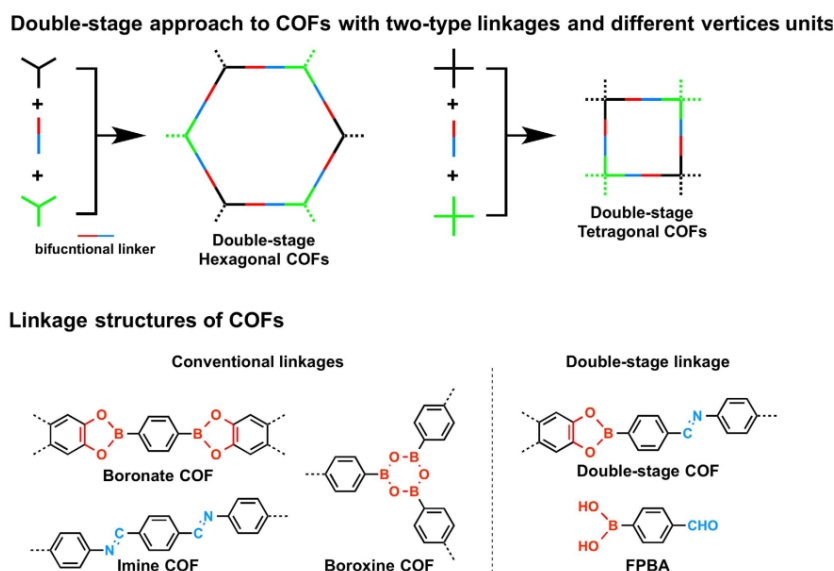


Figure 1.10: Schematic construction principle of double-stage COFs from linkers with different functional groups. Adapted from ref. 23, CC-BY 4.0 licence (<https://creativecommons.org/licenses/by/4.0/>)

With this synthesis method, three different strategies are possible. First, the double-stage linkage can connect to nodes that feature different linkages, as in the NTU-COF-2 or the HHTP-FPBA-TATTA COF. Second, if one functional site of the linker can undergo self-condensation, such as boronic acids forming boroxine rings, it can form nodes of the framework. These can then co-condense with the other linker, like in NTU-COF-1¹⁷² or TATTA-FPBA COF.²³

Third, the asymmetric linker can bind to all connectors of one linker type, thereby protecting it with the other connector type and thus resembling a linker of another linkage type. An example for this is CuPc-FPBA-TMBDA COF.²³ The concept of two different linkages in one COF has also been applied 3D COF synthesis¹⁷³ and for surface COF formation.¹⁷⁴

An intriguing COF geometry was created by Yaghi et al. using the copper complex of Cu(I)-bis[4,4'-(1,10-phenanthroline-2,9-diyl)dibenzaldehyde]tetrafluoroborate as aldehyde linker. The aldehyde groups of the (1,10-phenanthroline-2,9-diyl)dibenzaldehyde units are arranged in a nearly tetragonal way in the complex and were connected with benzidine as

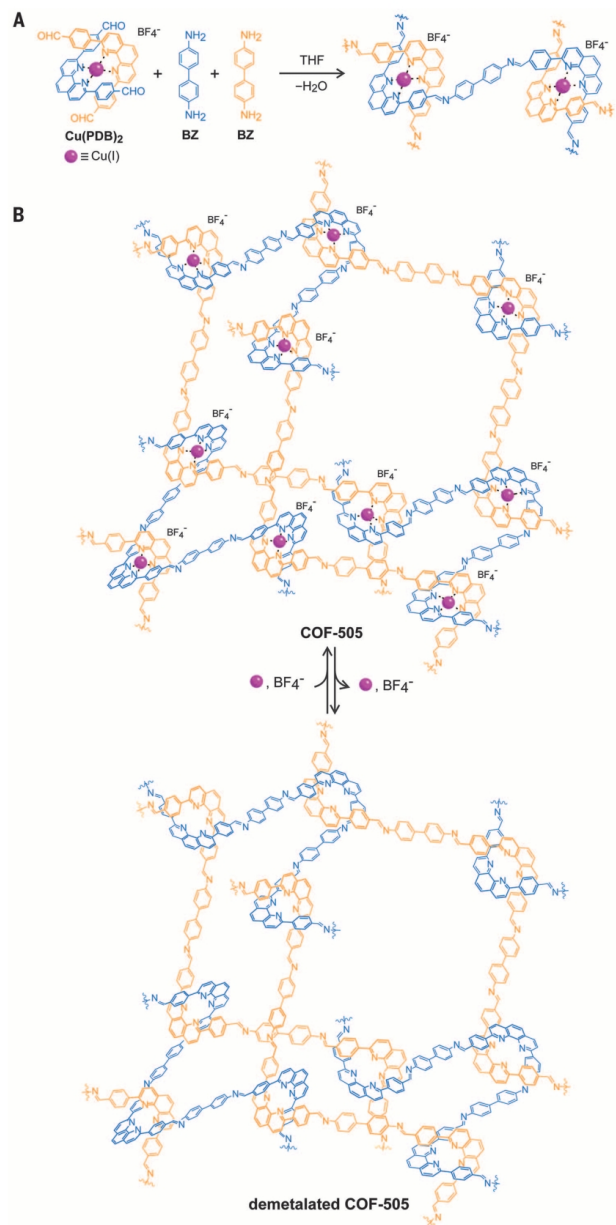


Figure 1.11: Reaction scheme for the synthesis of COF-505. COF-505 was constructed from organic threads using copper(I) as a template (A) to make an extended weaving structure (B), which can be subsequently demetalated and remetallated. From ref. 175. Reprinted with permission from AAAS.

amine linker. After formation of the COF, the copper was removed along with the BF_4^- , leaving a porous crystalline network of interwoven imine chains (Figure 1.11).¹⁷⁵

In a related strategy, Matzger and coworkers combined the construction principles of MOFs and COFs in one framework. Here, triangular carboxylic acids for the formation of a MOF feature an amino functional group. Upon reaction with $\text{Zn}(\text{NO}_3)_2 \times 6 \text{H}_2\text{O}$ and dialdehydes, frameworks with both covalent imine bonds and coordinative linkages are formed (Figure 1.12).¹⁷⁶

Another fusion of MOF and COF chemistry was demonstrated by Yaghi and coworkers by the *in situ* formation of amine-functionalized hexameric Ti(IV) clusters that are interconnected with terephthalaldehyde *via* imine bonds. In contrast to most pure COF materials, the layers are stacked in a staggered structure (Figure 1.13).¹⁷⁷

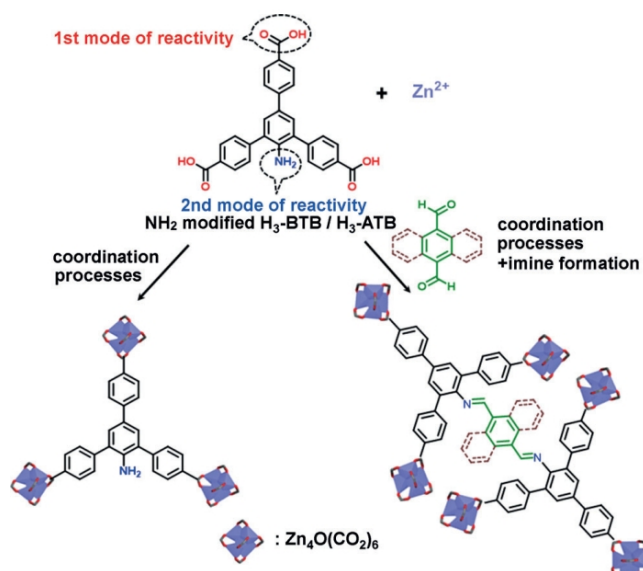


Figure 1.12: Hybrid MOF/COF structures with coordinative bonds and imine linkages. Reproduced with permission from ref. 176. Copyright 2015 John Wiley and Sons.

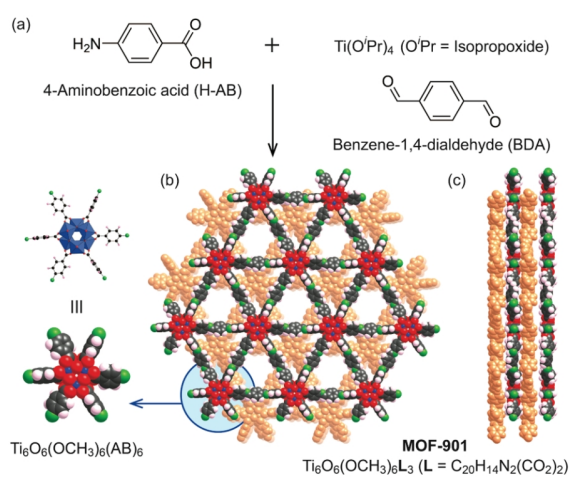


Figure 1.13: Hybrid MOF/COF structure from titanium(IV)isopropoxide and benzene-1,4-dialdehyde (a). The crystal structure of MOF-901 is projected along the *c*-axis (b) and *a*-axis (c). The discrete hexameric cluster, now incorporated into an extended, crystalline structure, is presented in the inset of (b). Atom colors: Ti, blue; C, black; O, red; N, green; H, pink; and second layer, orange. Capping methoxide moieties are removed for clarity. Reprinted with permission from ref. 177. Copyright 2016 American Chemical Society.

Table 1.10: Imine-linked COFs from tridental aldehydes and linear to tridental amines (continued)

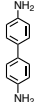
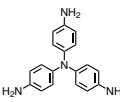
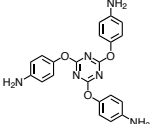
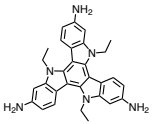
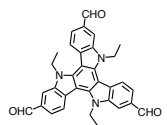
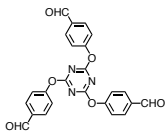
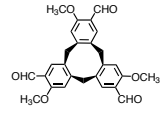
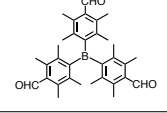
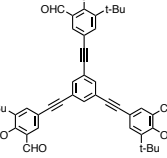
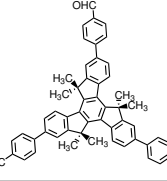
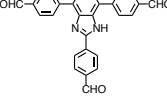
						
		TAT-COF-1 ¹⁵²				TAT-COF-2 ¹⁵²
		COF-SDU1 ¹⁵³			TPT-COF-1 ¹⁵⁴	
		CTV-COF-1 ¹⁵⁵	CTV-COF-2 ¹⁵⁵			
				BTMA-TAPA-COF ¹⁴⁸		
		Salen-COF ¹⁵⁶				
		SIOC-COF-8 ¹⁵⁷	SIOC-COF-9 ¹⁵⁷			
		brick-wall COF ¹⁵⁸				

Table 1.11: Imine-linked COFs from linear aldehydes with more than one phenyl ring and trigonal amines

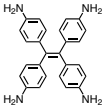
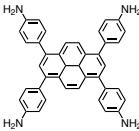
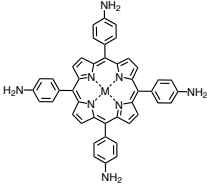
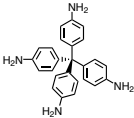
				NF-COF ^{178,179}
	3PA-TT COF ¹⁸⁰		3PB-TT COF ¹⁸⁰	
	3PA-2P COF ¹⁸⁰	aCTVCOF ²¹⁸¹	sCOF-IC2 ¹⁴⁹ TAPB-BPDA COF ¹⁸²	
	polyTB ¹⁸³			
			TAPB-TIDA COF ¹⁸²	
			COF LZU-20 ¹⁸⁴	
			PC-COF ¹⁸⁵	

Table 1.12: Imine-linked COFs from linear aldehydes with up to one phenyl ring and trigonal amines

		sCOF _{C+D} ¹⁸⁶		
	aCTV-COF-1 ¹⁸¹	SCOF-IC1 ¹³⁴ TAPB-PDA COF ^{182,187,188} TPB-TP-COF ^{189,190}	IISERP-COF4 ¹⁴⁷	TPT-COF-2 ¹⁵⁴
	aCTV-COF-4 ¹⁸¹	DhaTab ¹⁹¹ 2,5-DhaTab ¹⁹² SCOF-2 ¹⁹³	COF _{TTA-DHTA} ¹⁹⁴	
	aCTV-COF-3 ¹⁸¹	TPB-DMTP-COF ^{190,195} TAPB-DMTP-COF ¹⁹⁶		
		TAPB-BMTTPA-COF ¹⁹⁷		
		2,3-DhaTab ¹⁹⁸ SCOF-1 ¹⁹³	2,3-DhaTta ¹⁹⁸	
			TDFP-1 ¹⁹⁹	
		COF-V ¹⁸		
		TAPB-BPTA-COF ²⁰⁰ [HC≡C] _x -TPB-DMTP-COF (mixed with DMTP) ¹⁹⁰ COF-x (mixed with DMTP) ²⁰¹		

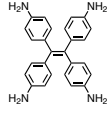
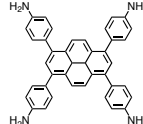
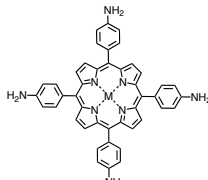
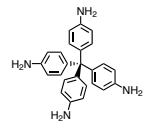
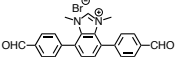
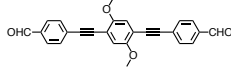
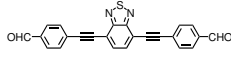
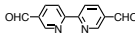
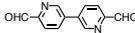
DMTP: 2,5-dimethoxyterephthalaldehyde.

Table 1.13: Imine-linked COFs from linear aldehydes and tetradental amines

				
	4PE-1P COF ^{165,180,189} (mixed with biphenyl as SIOC-COF-1) ¹⁵⁹	Py-1P COF ²⁰²	M=H ₂ COF-366 ^{71,203} H ₂ P-Ph COF ²⁰⁴ TAPP 2D-COF ²⁰⁵ M=Zn Zn-TAPP 2D-COF ²⁰⁵ M=Cu CuP-Ph COF ^{204,206} M=Ni NiP-Ph COF ²⁰⁴ M=Fe FeTAPP-TPA (mixed with metal-free phthalocyanine COF H ₂ TAPP-TPA) ²⁰⁷ M=Co COF-366-Co ²⁰⁸ Co-COF ²⁰⁹	COF-300 ^{119,210,211}
	COF-DHTA ¹⁶⁷	Py-DPh COF ¹⁶¹	M=H ₂ DhaTph ^{128,212} 2,5-DhaTph ¹⁹² H ₂ P-DPh COF ²⁰⁴ H ₂ P-DPhx COF(mixed with TA) ²⁰⁴ [HO]X%-H ₂ P-COF (mixed with TA) ²¹³ M=Cu CuP-DPh COF ²⁰⁴ CuP-DPhx COF(mixed with TA) ²⁰⁴ M=Ni NiP-DPh COF ²⁰⁴ NiP-DPhx COF (mixed with TA) ²⁰⁴	COF-301 ²¹⁴
			M=H ₂ DmaTph ²¹² sCOF-IC4 ²¹⁵	
	R=CH ₂ CH ₃ : COF-DETA ¹⁶⁷ R=(CH ₂) ₃ CH ₃ : COF-DBTA ¹⁶⁷			
		Py-2,3-DPh COF ¹⁶¹	M=H ₂ 2,3-DhaTph ^{192,216,217} M=Cu CuP-2,3-DHph COF ¹⁶³ M=Ni NiP-2,3-DHph COF ¹⁶³ M=Zn ZnP-2,3-DHph COF ¹⁶³ M=Fe Fe-DhaTph-COF ²¹⁸	
			M=H ₂ 2,3-DmaTph ^{216,217}	

TA: terephthalaldehyde.

Table 1.14: Imine-linked COFs from linear aldehydes and tetradental amines (continued)

				
			<p>M=H₂ [HC≡C]X-H₂P-COF (mixed with dihydroxy funct. linker)^{219,220}</p> <p>M=Ni [HC≡C]X-NiP-COF (mixed with methoxy-funct. linker)²²¹</p>	
		Py-1P _F COF (mixed with TA) ²⁰²	<p>M=Cu CuP-TFPh COF (also mixed with TA as CuP-TFPhx COF)²⁰⁶</p>	
			<p>M=Cu CuP-DHNAPh COF¹⁶³</p>	
	4PE-TT COF ¹⁸⁰			
	4PE-2P COF ¹⁸⁰ COF-BPDA ¹⁵⁹ (also mixed with TA as SIOC-COF-1)	Py-2P COF ²⁰²	<p>M=H₂ H₂P-Bph-COF²²²</p> <p>M=Co, Cu COF-367-M²⁰⁸</p>	COF-320 ^{151,223-225}
	4PE-3P COF ¹⁸⁰ COF-TPDA ¹⁵⁹ (also mixed with [1,1'-biphenyl]-4,4'- dicarbaldehyde as SIOC-COF-2)	PyTTA-TPhA-COF ²²⁶		
		PyTTA-BFBIm- iCOF ²²⁶		
		Py-2PE COF ²⁰²		
		Py-3PE COF ²⁰²		
		Py-3PE _{BTD} COF ²⁰²		
		Py-2,2'-BPyPh COF ¹⁶¹ BPy COF ²²⁷ (also mixed with 4,4'-biphenyl dialdehyde)	<p>M=Cu CuP-BPyPh COF¹⁶³</p>	
		Py-3,3'-BPyPh COF ¹⁶¹	<p>M=H₂ sCOF-IC5²¹⁵</p>	LZU-301 ¹⁵¹

TA: terephthalaldehyde.

Table 1.15: Imine-linked COFs from tetra- and hexadental aldehydes and linear amines

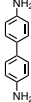
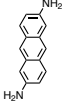
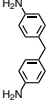
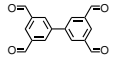
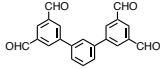
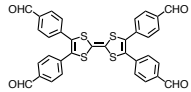
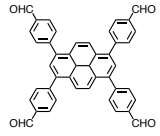
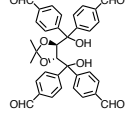
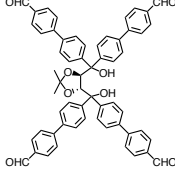
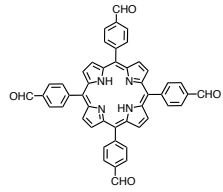
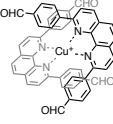
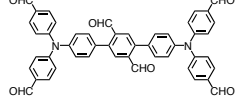
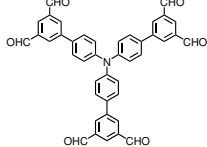
				
	COF-BTA-DAB ¹⁶⁶	COF-BTA-BZ ¹⁶⁶		
	TP-COF-DAB ¹⁷¹	TP-COF-BZ ¹⁷¹		
	TTF-Ph-COF ²⁶ TTF-COF ^{228,229} 4ATTF sCOF ²³⁰ 4ATTF-PPDA sCOF ^{230,231}	4ATTF-BPDA sCOF ²³⁰		
	ILCOF-1 ¹⁶⁰ COF _{TfPy-PPDA} ²³²	TF-BD COF ²²⁷	Py-An COF ¹⁶²	
				CCOF-1 ³⁰
				CCOF-2 ³⁰
	Por-COF ²³³			
		COF-505 ¹⁷⁵		
	SIOC-COF-7 ¹⁷⁰			
	SIOC-COF-3 ¹⁶⁹	SIOC-COF-4 ¹⁶⁹		

Table 1.16: Imine-linked COFs from tetradental aldehydes and tetradental amines

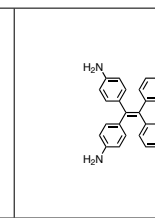
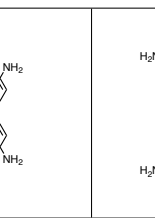
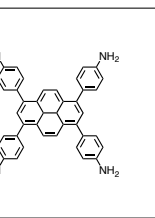
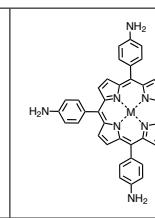
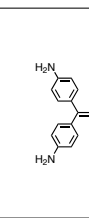
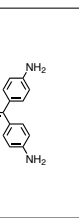
				
	SIOC-COF-5 ²³⁴			
	SIOC-COF-6 ²³⁴			
		TTF-Py-COF ²⁶		
			M=Cu, Ni, Zn MP-PyTTPh COF ¹⁶³	3D-Py-COF ³²

Table 1.17: Imine-linked COFs with hexadental amines

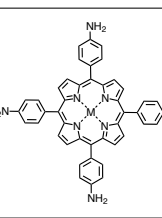
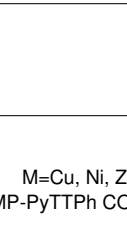
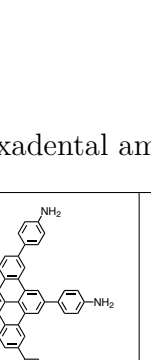
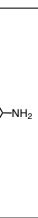
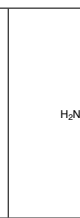
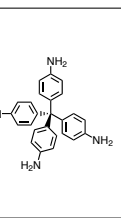
			
	HPB-COF ²⁷	HBC-COF ²⁷	HAT-COF ¹⁶⁸
			HAT-NTBA-COF ²³⁵
			HAT-NTBCA-COF ²³⁵

Table 1.18: Mixed linkage COFs with imine bonds and boroxine or boronic ester bonds

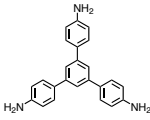
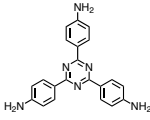
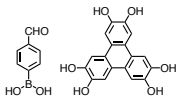
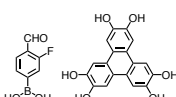
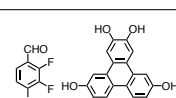
			
	NTU-COF-1 ¹⁷² sCOFA ¹⁷⁴	TATTA-FPBA COF ²³	DL-COF-1 ¹⁷³
	NTU-COF-2 ¹⁷²	HHTP-FPBA-TATTA COF ²³	
	sCOFB ¹⁷⁴		
		TATTA-FFPBA COF ²³	
			DL-COF-2 ¹⁷³
		HHTP-FFPBA-TATTA COF ²³	
		TATTA-DFFPBA COF ²³	
		HHTP-DFFPBA-TATTA COF ²³	

Table 1.19: Mixed linkage COFs with imine bonds and boroxine or boronic ester bonds (continued)

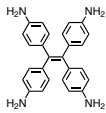
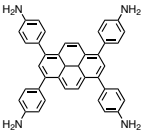
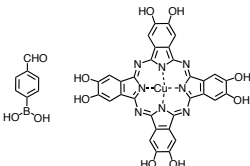
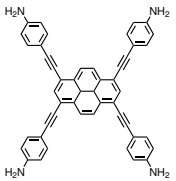
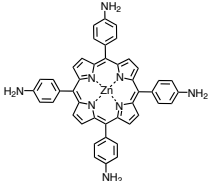
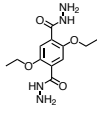
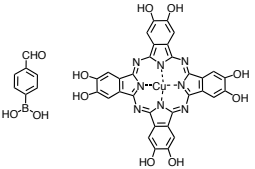
			
	CuPc-FPBA-TMBDA COF ²³	CuPc-FPBA-ETTA COF ²³	CuPc-FPBA-PyTTA COF ²³

Table 1.20: Mixed linkage COFs with imine bonds and boroxine or boronic ester bonds (continued)

			
	CuPc-FPBA-TABPy COF ²³	CuPc-FPBA-ZnP COF ²³	CuPc-FPBA-DETHz COF ²³

1.3.3 Hydrazones and Azines

Hydrazides reversibly co-condense with aldehydes to form hydrazones, thus enabling the use of this linkage for COF synthesis. This reaction type was first applied for COF formation by the group of Yaghi in 2011 in the synthesis of COF-42 from 2,5-diethoxyterephthalohydrazide and TFB, and of COF-43 from 2,5-diethoxyterephthalohydrazide and the elongated aldehyde linker TFPB.²³⁶

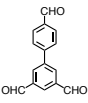
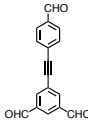
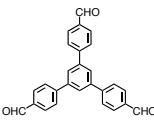
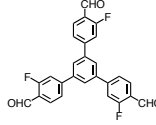
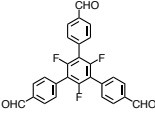
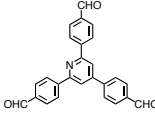
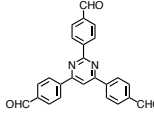
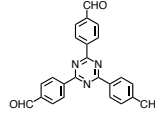
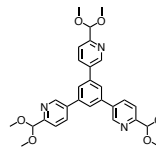
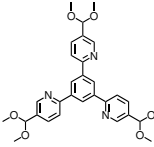
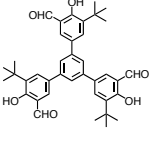
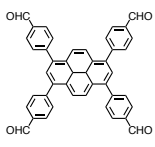
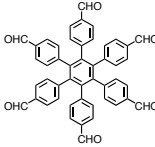
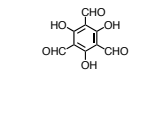
Table 1.21: COFs with hydrazone linkage

							tbh. ²³⁷
	tbh. ²³⁸	TFB-COF ²³⁹	COF-42 ²³⁶	COF-LZU8 ²⁴⁰		Tb-DANT-COF ²⁴¹	
			COF-43 ^{236,242}		TfpBDH ²⁴³		
			TFPT-COF ²⁴⁴				
			LZU-21 ¹⁸⁴				
	TpTh ^{128,245}	COF-JLU4 ²⁴⁶	NUS-3 ²⁴⁷		TpBDH ²⁴³	Tp-DANT-COF ²⁴¹	

Hydrazone COFs represent a small family of structures (see Table 1.21) that have been mainly applied in sensing^{240,243} and catalysis.^{239,244} When hydrazine is used as nitrogen-containing coupling partner for aldehydes, an azine linkage is established, as first reported by Dalapati et al. in the synthesis of Py-Azine COF from hydrazine and 1,3,5,8-tetrakis(4-formylphenyl)pyrene. This COF features rhombic pores of around 2 nm in diameter. The azine units in the COF walls were found to serve as docking sites for guest molecules, enabling an application of this COF in sensing.²⁵

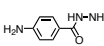
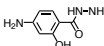
With the azine linkage, a variety of pore geometries besides the classical hexagonal type has been realized. Combining hexaphenylbenzene aldehyde, which had already been

Table 1.22: Aldehyde linkers that were incorporated in azine-linked COFs

 ACOF-1 ^{250,251} AB-COF ²⁵²	 HP-COF-1 ²⁴⁹	 HP-COF-2 ²⁴⁹	 N_0 -COF ²⁵³ sCOF _{A+B} ¹⁸⁶ TFPB-HZ ¹²⁷ NF-COF ²⁵⁴	 TF-COF 1 ²⁵⁴ (also mixed with TFPB as TF _X -COF) ²⁵⁵
 TF-COF 2 ²⁵⁴	 N_1 -COF ²⁵³	 N_2 -COF ²⁵³	 N_3 -COF ^{127,253}	 LZU-22 ¹⁸⁴
 PTP-COF ²⁵⁶	 COF-JLU3 ²⁵⁷	 Py-Azine COF ²⁵	 HEX-COF 1 ²⁴⁸	 COF-JLU2 ²⁵⁸ ATFG-COF ²⁵² NUS-2 ²⁴⁷

TFPB: 1,3,5-tris(4-formylphenyl)benzene.

Table 1.23: Mixed linkage COFs with imine and hydrazone bonds

	 TpAPH ²⁵⁹	 TpASH ²⁵⁹
---	---	---

used in imine COF synthesis (see Section 1.3.2), with hydrazine, triangular pores of only 1 nm were achieved.²⁴⁸ Incorporation of tritopic linkers with a linker elongation at only one of the three binding sites led to a heterogeneous dual pore structure in HP-COF-1 and HP-COF-2 (see Table 1.22 for a full list of building blocks in azine-linked COFs).²⁴⁹

COFs with a mixed ketoenamine and hydrazone linkage were developed by Mitra et al. using 1,3,5-triformylphloroglucinol (TPG) as aldehyde and the building blocks 4-aminobenzohydrazide and 4-amino-2-hydroxybenzohydrazide as the amine and hydrazine functionalized building blocks,²⁵⁹ see Table 1.23. Hydrazone and azine linkages were also accessible from the dimethyl acetals of the aldehyde linker *via* an *in situ* deprotection and condensation reaction.¹⁸⁴ The enol-keto tautomerization that was first applied in imine networks (see next section) can also be applied to hydrazone and azine systems when the aldehyde linker is replaced by TPG.^{128,241,243,245,247,252,258}

1.3.4 Ketoenamines

Stability enhancement is an important issue in COFs when it comes to applications. A strategy to obtain COFs that are not only stable in acids but also in strong bases was reported by Banerjee et al. in 2012. They used TPG as aldehyde linker for their COF synthesis. This building block features hydroxyl groups adjacent to the formyl groups. Upon COF formation, first an imine COF is formed which can then undergo an irreversible enol-keto tautomerization to form a ketoenamine linkage, see Figure 1.14. The thus formed ketoenamine COFs (see Tables 1.24 and 1.25 for the linker overview) feature high chemical stability, including against strong bases.

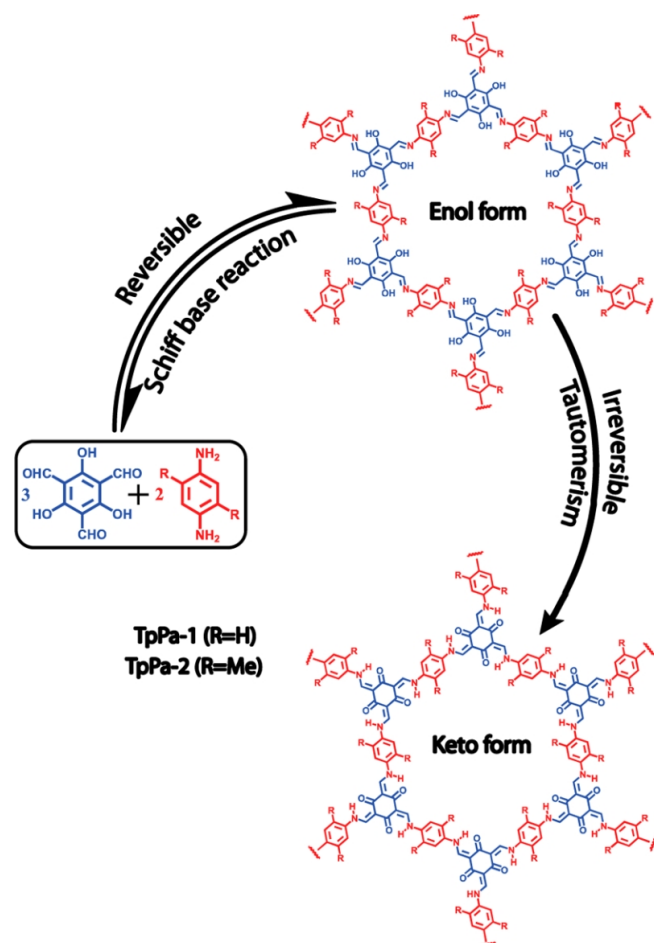


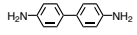
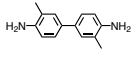
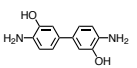
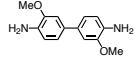
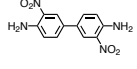
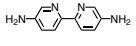
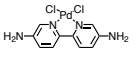
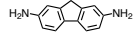
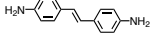
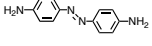
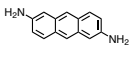
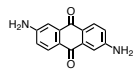
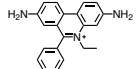
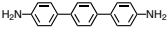
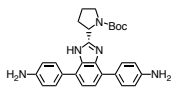
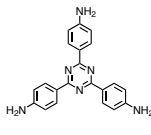
Figure 1.14: Schematic representation of the β -ketoenamine COF formation *via* enol-keto tautomerization. Adapted with permission from ref. 260. Copyright 2012 American Chemical Society.

In many cases, they were also found to be somewhat less crystalline than their imine counterparts, probably due to the introduction of an irreversible step in the COF for-

40 1. Covalent Organic Frameworks: Structures, Synthesis and Applications

mation that hinders error correction in the COF lattice.²⁶⁰ The authors also reported a structural series with many different amines incorporated into β -ketoenamine COFs. These COFs could be delaminated mechanochemically simply by grinding in a mortar, forming nanosheets that are a few COF layers thick.²⁶¹

Table 1.24: Ketoenamine-linked COFs with TPG as linker

 TpPa-1 ^{182,127,128,192,260–273} DAB-TFP COF ^{274–276}	 TpPa-2 ^{192,260–262,266,267,277–279}	 TpPa-(OH) ₂ ²⁶⁸ DABH-TFP COF ²⁰⁰	 TpPa-(OMe) ₂ ²⁶⁸
 TpPa-NO ₂ ^{192,261,267}	 TFP-DABA ²⁸⁰ TpPa-SO ₃ H ²⁸¹ NUS-9 ²⁸²	 NUS-10 ²⁸²	 TpPa-F ₄ ^{192,261}
 TpPa-Py (also mixed with 2,5-diaminobenzenesulfonic acid as TpPa-(SO ₃ H-Py)) ²⁸¹ TaPa-Py COF ²⁷⁶	 TpBD ^{192,261,262,266–268,270,283–286}	 TpBD-Me ₂ ^{192,261,267,283,287}	 TpBD-(OH) ₂ ²⁶⁸
 TpBD- (OMe) ₂ ^{192,261,267,268,283}	 TpBD-(NO ₂) ₂ ^{192,261,267,288}	 TpBpy ^{266,267,289–291}	 Pd@TpBpy ²⁹²
 TpFn ²⁶⁶	 Tp-Stb ²⁹³	 Tp-Azo ^{192,267,283,293,294} Azo-COF ²⁹⁵	 DaTp ²⁹⁶
 DAAQ-TFP COF ^{200,274,297,298} TpAQ ²⁸³ DAAQ ²⁶⁶ TpAnq ²⁶⁷	 EB-COF ²⁹⁹	 TpTD ²⁸³ TpTph ²⁶⁷	 LZU-76 ¹²³
 TRIPTA ³⁰⁰ TpTta ²⁶⁷ TS-COF-2 ³⁰¹	 BF-COF-2 ¹²⁵		

Interestingly, mechanical force was also a way to synthesize ketoenamine COFs by simply grinding TPG in a mortar together with the respective linker.²⁶² Networks with low crystallinity were obtained. We note that these frameworks showed very small surface areas below $70 \text{ m}^2 \text{ g}^{-1}$, while the solvothermal synthesis pathway yielded surface areas of more than $300 \text{ m}^2 \text{ g}^{-1}$.

Table 1.25: Ketoenamine-linked COFs with extended TPG linkers

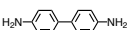
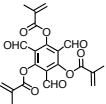
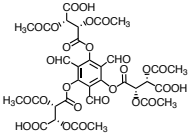
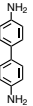
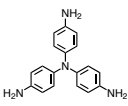
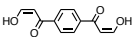
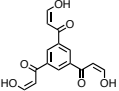
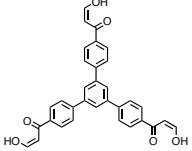
			
	TpPa-MA ³⁰²		
	CTPa-1 ³⁰³	CTPa-2 ³⁰³	CTpBD ³⁰³

Table 1.26: Ketoenamine-linked COFs *via* Michael addition-elimination

			
			2TPA ³⁰⁴
	3PD ³⁰⁴	3BD ³⁰⁴	
	3'PD ³⁰⁴		

The excellent chemical stability of ketoenamine COFs has been exploited for several different applications, including reversible redox processes in an acidic electrolyte for energy storage.^{274,297} Moreover, β -ketoenamine COFs have been used as proton conducting electrolyte.^{281,289,293,299}

We recently demonstrated the reduction of NO₂ groups to NH₂ groups in a β -ketoenamine COF under acidic conditions. The NH₂-functionalized β -ketoenamine COF was afterwards applied for lactic acid adsorption.²⁸⁸ Yan et al. synthesized a β -ketoenamine COF with a 3D lattice using the tetragonal amine 1,3,5,7-tetraaminoadamantane.¹²⁵

Recently, modified versions of the TPG linker have been introduced. Liu et al. reacted TPG with methacrylic anhydride and used the resulting methacrylate-functionalized building block to synthesize a TpPa-1 analogous COF that was used in high-performance liquid chromatography.³⁰² Qian et al. prepared a chiral TPG linker by modifying it with chi-

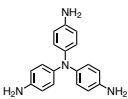
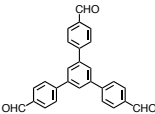
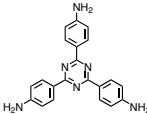
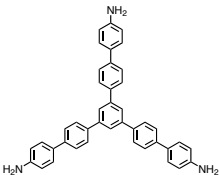
ral (+)-diacetyl-L-tartaric anhydride. The synthesized chiral COFs analogous to TpPa-1, TpPa-2 and TpBD were applied in chiral separation tasks.³⁰³

Another interpretation of the ketoenamine linkage motif was introduced by Rao et al., who utilized a Michael addition-elimination pathway to condense amines with β -ketoenols to form β -ketoenamines which feature an additional stabilization from intramolecular hydrogen bonding, see Table 1.26. Thereby, the direct one-step formation of the ketoenamine linkage motif is possible.³⁰⁴

1.3.5 Other Linkages

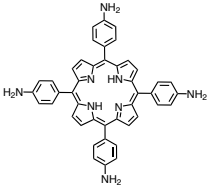
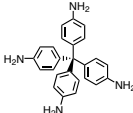
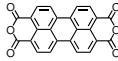
Besides the mainly used COF coupling chemistries described in the sections above, a number of additional linkages for COFs have been developed, see Tables 1.29 and 1.30. Already in 2008, the group of Yaghi constructed a 3D COF from the tetrahedral boronic acid tetrakis(4-dihydroxyboryl-phenyl)methane and *tert*-butylsilane triol, $t\text{BuSi}(\text{OH})_3$ that form borosilicate bonds.³¹

Table 1.27: COFs with imide linkage

				
	PI-COF-1 ³⁰⁵ PI-COF-mX (mixed with xDMMA) ³⁰⁶	PI-COF-2 ³⁰⁵	TS-COF-1 ³⁰¹	PI-COF-3 ³⁰⁵

DMMA: 4-[(dimethylamino)methyl]aniline.

Table 1.28: COFs with imide linkage (continued)

			
		PI-COF-5 ³⁰⁷	PI-COF-4 ³⁰⁷
	PI-COF ³⁰⁸		

In an ionothermal synthesis approach, Kuhn et al. applied the trimerization reaction of nitriles to synthesize the crystalline triazine framework CTF-1 from

1,4-dicyanobenzene.³⁰⁹ Later, additional crystalline structures were developed using 2,6-naphthalenedicarbonitrile, [1,1'-biphenyl]-4,4'-dicarbonitrile, and 5'-(4-cyanophenyl)-[1,1':3',1''-terphenyl]-4,4''-dicarbonitrile, respectively.^{310,311} Most triazine frameworks reported so far are amorphous, but this material class has been shown to be very stable and widely applicable in catalysis.³¹²

Furthermore, CTF-1 has been successfully applied in polysulfide sorption for Li-S batteries⁴⁵ and as membrane material for gas separation.³¹³ For a detailed review of covalent organic triazines we refer to Puthiaraj et al.³¹² The triazine-rich, but amine-linked TriCF was formed from melamine and cyanuric chloride³¹⁴ and the thermal decomposition of 1,3,5-(*p*-aminophenyl)benzene-borane yielded a crystalline, porous framework with a borazine linkage.³¹⁵

Squaric acid served as building block to form a squaraine-linked COF in a reaction with aromatic amines.³¹⁶ In further studies, 2,5-diamino-1,4-benzenediol dihydrochloride was co-condensed with trigonal aldehydes in the presence of cyanide as catalyst to give benzobisoxazole-linked COFs,³¹⁷ and Nandi et al. reported a COF synthesis based on benzimidazole linkage from the building blocks 3,3'-diaminobenzidine and TPG.³¹⁸

Yan et al. introduced isoquinoline as catalyst in the reaction of pyromellitic dianhydride with triangular amines to yield crystalline imide linked networks,³⁰⁵ see Tables 1.27 and 1.28 for a full list of imide-linked COFs. This concept was later transferred to tetrahedral amines for the formation of 3D imide COFs³⁰⁷ and for a hexagonal 2D COF intended for separation tasks,³⁰¹ as well as for a tetragonal 2D COF with perylene dianhydride units.³⁰⁸ In a microwave-assisted synthesis, the truncated PI COF was synthesized from the building blocks tris(4-aminophenyl)amine, pyromellitic dianhydride and 4-[(dimethylamino)methyl]aniline.³⁰⁶

Spiroborate-linked COFs were obtained from diol functionalized macrocycles and trimethyl-borate, see Table 1.30. The Li⁺-functionalized COFs showed high gas storage capacities and feature ionic centers in their backbone that enabled for Li-ion transport.²⁸

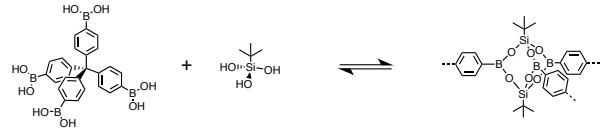
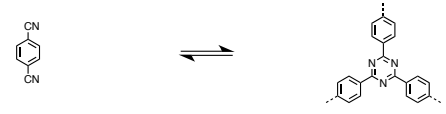
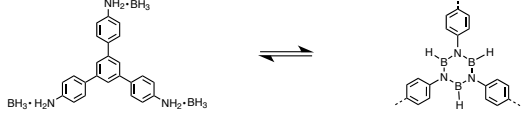
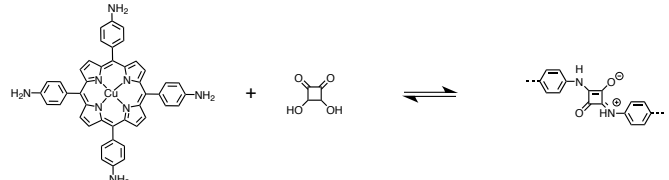
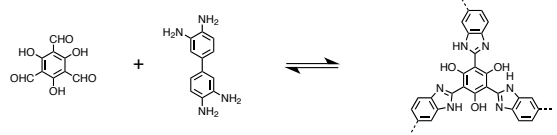
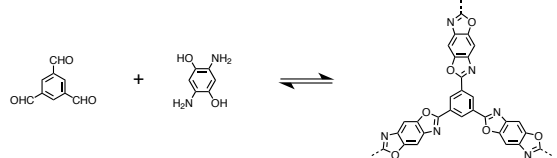
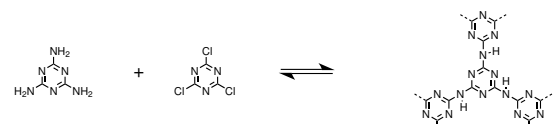
An unconventional COF synthesis pathway was reported by Nath et al. They used protected tetrakis(arylhydroxylamine)porphyrin that was deprotected upon treatment with tetrabutylammonium fluoride and transformed *in situ* to tetrakis(arylnitroso)porphyrin, which self-polymerized to build a porous crystalline COF with azodioxy linkage (Table 1.30).³¹⁹

A conjugated COF was reported by Guo et al. They formed phenazine linkages between triphenylene hexamine and tertbutylpyrene tetraone units. The resulting CS-COF

44 1. Covalent Organic Frameworks: Structures, Synthesis and Applications

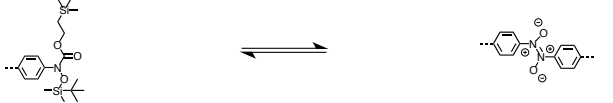
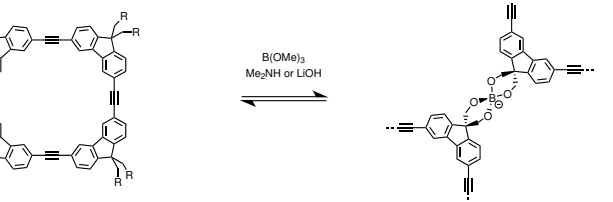
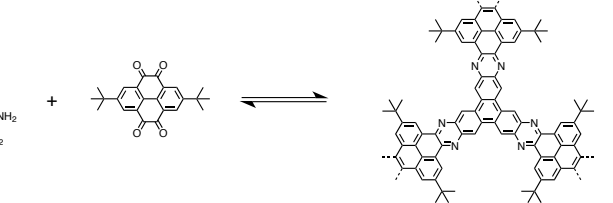
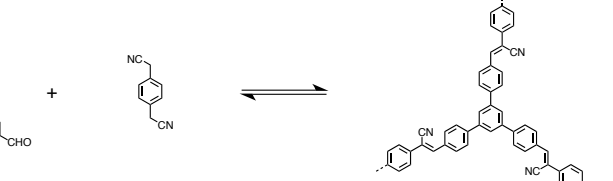
features extended π -delocalization³²⁰ Furthermore, the Knoevenagel condensation reaction was applied by Zhuang et al. to form the olefin-linked COF 2DPPV from 1,4-phenylene diacetonitrile and the trigonal aldehyde 1,3,5-tris(4-formylphenyl)benzene (TFPB).³²¹

Table 1.29: Further reactions for COF formation and their structural representatives.

Borosilicate		COF-202 ³¹
Triazine		with DCB: CTF-1 ^{45,82,309,313,322} with NDN: CTF-2 ³¹⁰ with BPCN: P2M ³¹¹ with CTCN: P4M ³¹¹
Borazine		BLP-2(H) ³¹⁵
Squaraine		CuP-SQ COF ³¹⁶
Benzimidazole		IISERP-COF ³¹⁸
Benzobisoxazole		with TFB: BBO-COF-1 ³¹⁷ with TFPB: BBO-COF-2 ³¹⁷
Amine		TriCF ³¹⁴

DCB: 1,4-dicyanobenzene; NDN: 2,6-naphthalenedinitrile; BPCN: 4,4'-biphenyldicarbonitrile, CTCN: 5'-(4-cyanophenyl)-[1,1':3',1''-terphenyl]-4,4''-dicarbonitrile; TFB: 1,3,5-triformylbenzene; TFPB: 1,3,5-tris(4-formylphenyl)benzene; t.b.n.: structure to be named.

Table 1.30: Further reactions for COF formation and their structural representatives (continued).

Azodioxy compound		from protected TAHAP: POR-COF ³¹⁹
Spiroborate		M=Li ⁺ : ICOF-1 ²⁸ M=[Me ₂ NH ₂] ⁺ : ICOF-2 ²⁸
Phenazine		CS-COF ³²⁰
Olefin		2DPPV ³²¹

TAHAP: tetrakis(arylhydroxylamine)porphyrin.

1.4 Postsynthetic Modification

COFs possess regular pores with a defined pore environment. Given a specific COF structure, this environment can be altered by using different linkers in the COF synthesis that are, for example, decorated with different functional groups or side chains, but the range of variations that can be used for the synthesis is limited. An alternative way to introduce large side groups or functional groups that would inhibit the COF formation consists of a modification step performed after the crystalline network is established. This approach also allows for the introduction of various pore modifications into one already established COF network.

1.4.1 Postsynthetic Intercalation and Complexation in COFs

In an early study, the postsynthetic introduction of pyridine moieties into the pores of the boronic ester COF-10 was shown to drastically improve the stability of the COF against hydrolysis.³²³ Kalidindi et al. investigated the sorption behavior of organometallic species

in COF-102. Ferrocene molecules were intercalated in an oriented way with the cyclopentadienyl units showing towards benzene rings of the COF, indicating a π - π -interaction, as determined by *ab initio* structure determination from powder diffraction applying a global optimization in the direct space method. The COF was stable upon loading with ferrocene and also retained its structure upon incorporation of cobaltocene or $[\text{Ru}(\text{cod})(\text{cot})]_2$.⁶⁰

The nitrogen in imine-linked COFs can serve as ligand for metal complexes. Thus, with a postsynthetic introduction of metal ions in COFs, the metal centers can be fixated at specific positions of the porous scaffold of the COF framework, leading to defined and separate reaction centers which could be favorable for applications in catalysis and sorption. The first example of a metal complex in a COF was reported by Ding et al. They synthesized the imine COF LZU-1 (from TFB and PDA), that was postsynthetically modified with $\text{Pd}(\text{OAc})_2$. Thereby, a shift of both, the binding energy of Pd and the ^{13}C NMR signal of the carbonyl group of the COF compared to the pristine materials indicated a coordination of the $\text{Pd}(\text{OAc})_2$ with two adjacent COF layers. 2D layered COF structures are favorable for this approach, as the coordination sites of adjacent layers have only a short distance that can be bridged by the complex.¹²⁶ The same postsynthetic pathway was later used in an otherwise metal-free imine COF with porphyrin nodes.²²² Likewise, molybdenum was immobilized in a hydrazone COF with TPG as aldehyde linker, by postsynthetically introducing $\text{MoO}_2(\text{acac})_2$. Infrared spectroscopy measurements indicated a location of the Mo moieties at the hydrazone linkages of the COF.²⁴⁵

Vicinal -OH groups in 2,3-dihydroxy terephthalaldehyde served as docking sites for vanadium that was introduced into the COF as $\text{VO}(\text{acac})_2$ and coordinated in the form of $\text{V}=\text{O}$ units.¹⁶¹ $\text{Co}(\text{OAc})_2$ was used to modify the bipyridyl units of the ketoenamine COF TpBpy (from TPG and 5,5'-diamino-2,2'-bipyridine) with Co^{2+} moieties. The framework retained its crystallinity even with a full saturation of the bipyridyl units with Co.²⁹⁰ The same COF was modified with $\text{Cu}(\text{OAc})_2$ to establish Cu species in the framework. In combination with a polymerized phosphonium salt this functionalized COF catalyzed the effective cycloaddition of epoxides and CO_2 .²⁹¹ The COF TpPa-2 (from TPG and 2,5-dimethyl-1,4-benzenediamine) was immersed in a solution of $\text{Ti}(\text{SO}_4)_2$ to yield Ti-ions coordinated to the COF, as was shown by XPS spectroscopy. The resulting material was utilized for phosphopeptide enrichment.²⁷⁹

The porphyrin units of DhaTph-COF (from 2,3-dihydroxybenzene-1,4-dicarbaldehyde and 5,10,15,20-tetrakis(4-aminophenyl)porphyrin) were postsynthetically modified with Fe(III) by immersing the COF in a solution of $\text{FeCl}_2 \times 4 \text{H}_2\text{O}$.²¹⁸ Similarly, $\text{Ni}(\text{COD})_2$ was

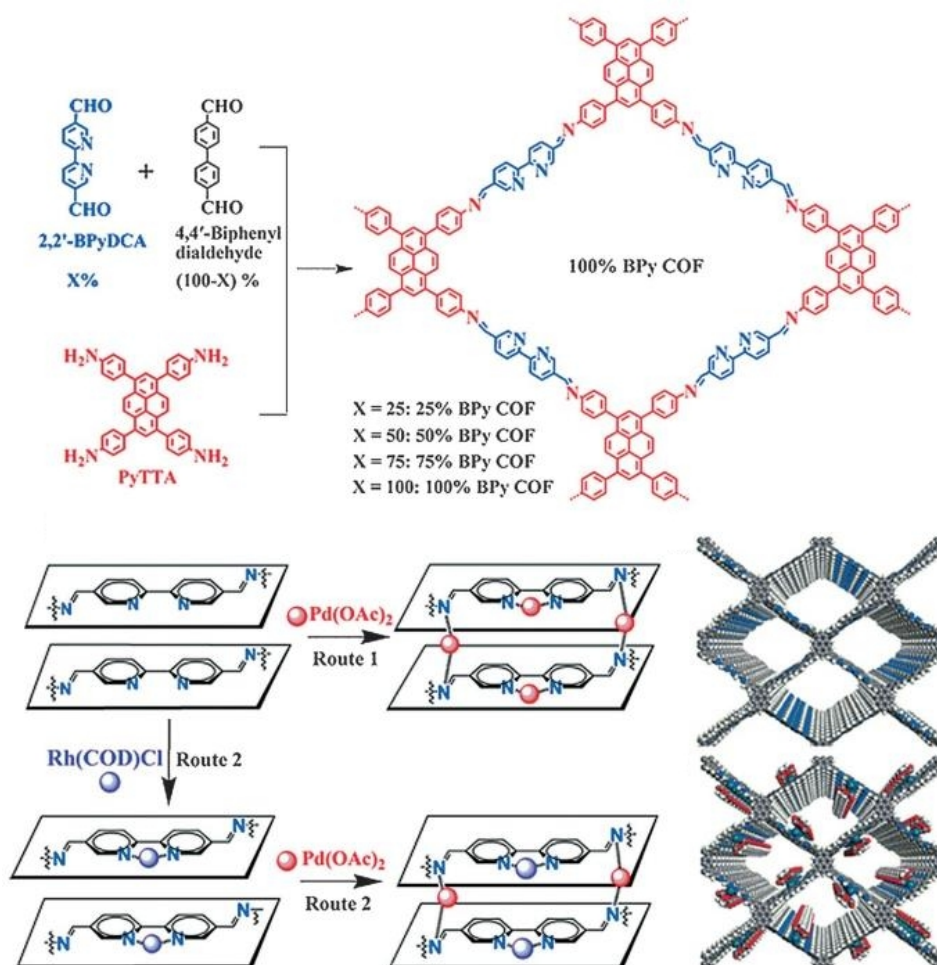


Figure 1.15: Synthesis of BPy COFs and subsequent complexation of Rh and Pd. Adapted from ref. 227. Copyright 2016 John Wiley and Sons.

used to complex Ni-ions to the dehydrobenzoannulene units of a boronic ester 3D COF with only minimal loss of porosity.¹¹⁸

Gao and coworkers investigated the possibility to achieve a complexation of two different metals in a COF. For this purpose, they synthesized a COF from 2,2'-bipyridyl-5,5'-dialdehyde, 4,4'-biphenyl dialdehyde and 4,4',4'',4'''-(pyrene-1,3,6,8-tetrayl)tetraaniline, an amine with a pyrene core. In the resulting COF, two nitrogen docking sites are present: the bipyridine and the imine. The authors then used two metal complexes of different sizes to achieve a complexation of two metals (Figure 1.15). The relatively large moiety Rh(COD)Cl was found to be located only at the bipyridine units, as it is too large to occupy the interlayer positions between the imines. This was demonstrated by the reduction in pore size upon modification with Rh(COD)Cl and by the unsuccessful attempt to incorporate large amounts of Rh(COD)Cl in bipyridine-free counterparts of the COF. In a second step, these imine positions could be filled by Pd(OAc)₂, as was confirmed by XPS measurements, yielding a bimetallic Pd and Rh functionalization of the COF.²²⁷

Similarly, MnCl₂ was introduced to the bipyridine sites and Pd(OAc)₂ was again coordinated at the imine position of the same COF to obtain a COF that showed good catalytic performance in a Heck-epoxidation tandem reaction.¹⁶⁴

The complexation of Pd(OAc)₂ in the COF LZU-1 (made from 1,4-phenylenediamine and 1,3,5-triformylbenzene) was used to prepare a Pd rich scaffold that was subsequently pyrolysed with the formation of Pd nanoparticles in the organic matrix.¹³² Another series of precursors for graphitization was prepared by intercalation of Ni(II), Fe(III), and Co(II) ions in an imine COF made from 1,3,5-tris(4-aminophenyl)benzene and TFB. It was noted that the incorporation of Ni and Co moieties (achieved by immersing the pristine COF in solutions of the metal acetylacetonates) resulted in the loss of crystallinity, while it was strongly reduced with Fe(III).¹⁴² The salen moieties in the imine-linked Salen-COF (made from 1,3,5-tris[(5-tert-butyl-3-formyl-4-hydroxyphenyl)ethynyl]benzene and 1,2-ethylenediamine) were applied as ligands for various metal ions and complexated with Cu²⁺, Ni²⁺, Zn²⁺, Co²⁺, and Mn²⁺, respectively. With all tested metals, a quantitative functionalization was achieved while the crystallinity of the frameworks was preserved. The Salen-COF complexed with Co²⁺ was successfully applied as catalyst in the Henry reaction.¹⁵⁶

1.4.2 Covalent PSM

The first postsynthetic modification in COFs by covalent bond formation was reported in 2011 by Jiang and coworkers. They introduced different fractions of an azide functionalized BDBA into boronic ester frameworks made from BDBA and HHTP or BDBA and a Ni-phthalocyanine catechol, respectively. After lattice formation, the azide moieties could react with various alkynes *via* copper-catalyzed click reaction. Functionalities as large as pyrene units were incorporated into the framework. By tuning the percentage of the incorporated azide, the amount of postsynthetically introduced groups could also be controlled (Figure 1.16).⁸⁶ With this approach, a modification was even possible with a functionalized fullerene that could be bound to the pore walls of a boronic ester phthalocyanine COF by covalent binding.²¹

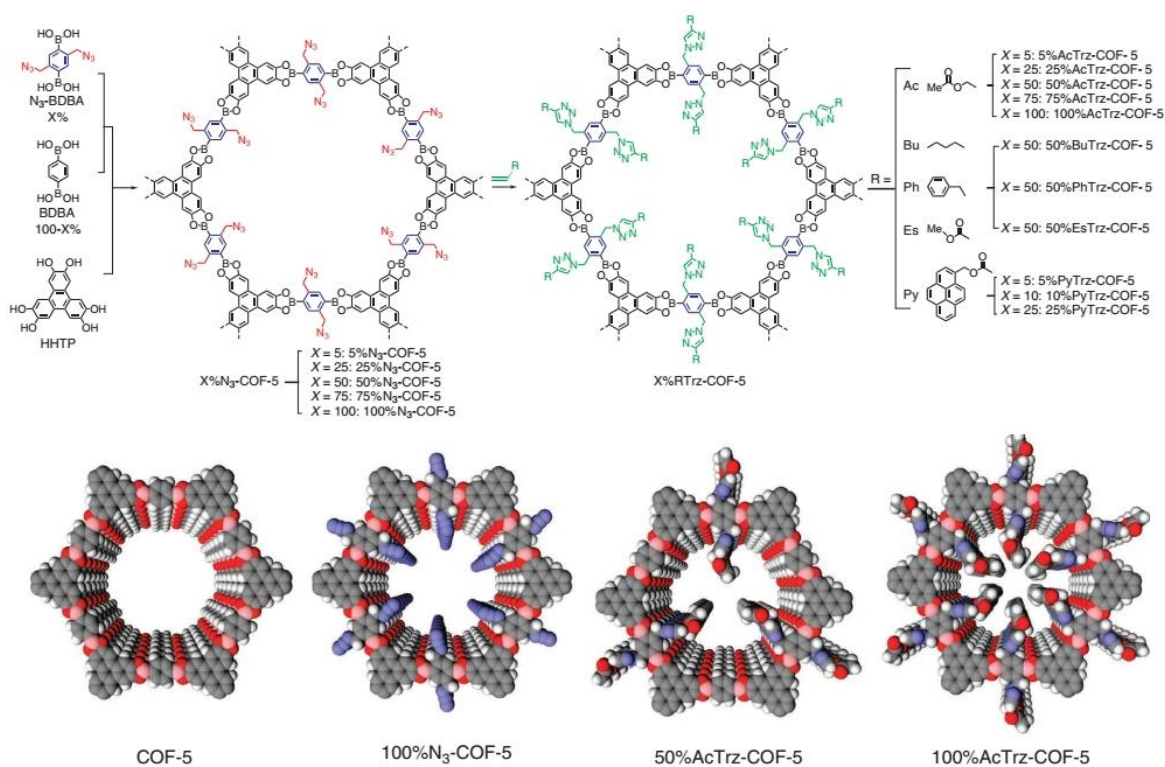


Figure 1.16: Synthesis of $X\%N_3$ -COF-5 and postsynthetic pore wall modification with alkynes. Adapted by permission from Macmillan Publishers Ltd: Nature Communications ref. 86, copyright 2011.

The reverse version of this click reaction starts with an alkyne-functionalized linker in the COF backbone that is later reacted with an azide. This click reaction has been used to tune the carbon dioxide storage capacity of COFs by postsynthetically introducing

functional groups including -COOH, -COOMe, -OH and -NH₂, with 50% NH₂ showing the highest capacity.²²⁰ In the same way, the postsynthetic incorporation of pyrrolidine azide was employed to design reaction centers for catalysis.^{190,219}

By using 4-azido-2,2,6,6-tetramethyl-1-piperidinyloxy, an azide of an organic radical, the tetragonal COF TEMPO-NiP-COF with Ni-porphyrine units and radical centers was formed that was later used for electrochemical energy storage.²²¹ The same radical was introduced into the TEMPO-COF (made from 1,3,5-tris(4-aminophenyl)benzene and 2,5-bis(2-propynyloxy)terephthalaldehyde), and the modified COF was also tested as energy storage material.²⁰⁰ A similar radical was introduced into an imine COF made from 1,3,5-tris(4-aminophenyl)benzene and substituted phenylenediamines by applying the same alkyne and azide click reaction.²⁰¹

A different strategy to establish covalent docking sites in a COF was shown by Bunck and Dichtel, who developed a truncation approach with a 3D boroxine COF. The tetragonal linker tetrakis(4-dihydroxyborylphenyl)methane was mixed with a truncated boronic acid node featuring an allyl group. This functional group could afterwards react with propanethiol in a thiol-ene reaction.⁶² The same reaction was applied in the imine-linked COF-V (from 1,3,5-tris(4-aminophenyl)benzene and 2,5-divinylterephthalaldehyde) that was modified with 1,2-ethanedithiol, benzene-1,4-dithiol and ethanethiol, respectively.¹⁸

In 2016, we demonstrated the first two-step postsynthetic modification in a COF. For this purpose, we started with the ketoenamine COF TpBD(NO₂)₂, made from 1,3,5-triformylphloroglucinol and 3,3'-dinitrobenzidine, bearing nitro groups. These were reduced to primary amines in a first step, leading to accessible amino-decorated pores. As amines are used as reactive starting materials for the COF synthesis, amino-pore-wall-functionalization in these COFs is only possible *via* postsynthetic modification. In a second step, the COF-bound amino groups could then be modified with acetyl chloride.²⁸⁸

Hydroxy groups present another type of functional group that can be used for postsynthetic modifications, as they are small and linker molecules with -OH groups are easily available. Furthermore, they can form covalent bonds with many functional groups, which is reflected by the number of reactions that have been published so far.

For example, succinic anhydride was reacted with hydroxyl-groups in a COF (made from 5,10,15,20-tetrakis(*p*-tetraphenylamino)porphyrin and a mixture of 2,5-dihydroxyterephthalaldehyde and terephthalaldehyde) in a ring opening reaction, establishing a carboxylic acid group functionalization that significantly improved the CO₂ storage capacity of the investigated COF.²¹³

The postsynthetic introduction of azobenzene and stilbene units *via* carbonyl chloride reaction into the same COF was shown to improve CO₂ uptake and CO₂/N₂ selectivity as well.³²⁴

Employing the formation of ether bonds, (2-bromoethyl)triethylammonium bromide was covalently bound to the walls of a COF made from 4,4',4'',4'''-(pyrene-1,3,6,8-tetrayl)tetraaniline and a mixture of 2,5-dihydroxyterephthalaldehyde and terephthalaldehyde, representing the first immobilization of an ionic liquid in COF pores.³²⁵

Mitra et al. used -OH groups as starting point for a three-step postsynthetic modification route in the mixed ketoenamine- and hydrazone-linked COF TpASH (see Table 1.23). First, the -OH groups were reacted with glycidol under epoxy ring opening to produce adjacent alkyl hydroxyl functionalities. In the second step, the latter served as anchoring points for 3-aminopropyltriethoxysilane (APTES), thus decorating the COF pores with primary aliphatic amino groups. The third step was the reaction of these amino groups with folic acid. As a result of these modification steps, exfoliation of the COF sheets occurred (Figure 1.17).²⁵⁹

Wang et al. synthesized another OH-functionalized COF by co-condensing 1,3,5-tris(4-formylphenyl)benzene with 2,5-diamino-1,4-dihydroxybenzene dihydrochloride. The -OH groups were later oxidized with O₂ and Et₃N, to yield the quinone form, and thus a COF that was inaccessible *via* direct condensation of the diaminoquinone with the aldehyde linker.²⁰⁰

Our group recently reported the synthesis of the boronic ester-linked T-COF-OH (from 2',5'-dihydroxy-[1,1':4',1'']terphenyl-4,4''-diboronic acid and HHTP), bearing -OH functional groups. These -OH groups were successfully postsynthetically modified with fluorescein isothiocyanate (a synthesis that also worked with free -OH groups in COF-5) and with n-octylisocyanate by immersing the COF into a solution of the respective reagent at room temperature for several days. In all cases, porosity and crystallinity were retained due to the mild reaction conditions.⁸⁴

Another interesting postsynthetic formation of covalent bonds in a COF was demonstrated by Jiang and coworkers in a boronic ester COF featuring anthracene units. By exposing this COF to irradiation at 360 nm, the anthracene units of adjacent COF layers underwent a [4p+4p] cycloaddition, thereby establishing connections between two adjacent COF layers (Figure 1.18). The cycloaddition was reversible and repeatable for several cycles.⁶⁹

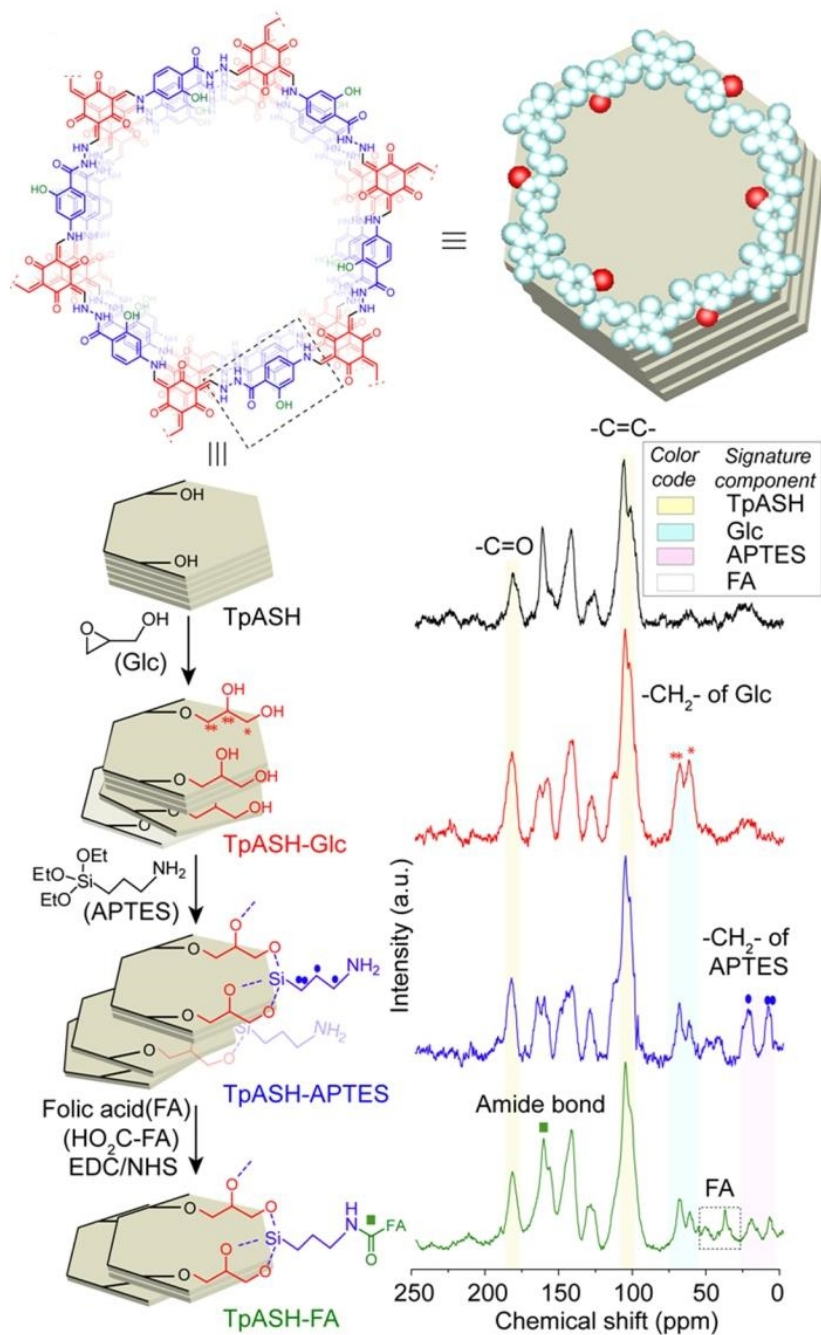


Figure 1.17: Postsynthetic modification of TpASH in three steps to establish a folic acid functionalization. Adapted with permission from ref. 259. Copyright 2017 American Chemical Society.

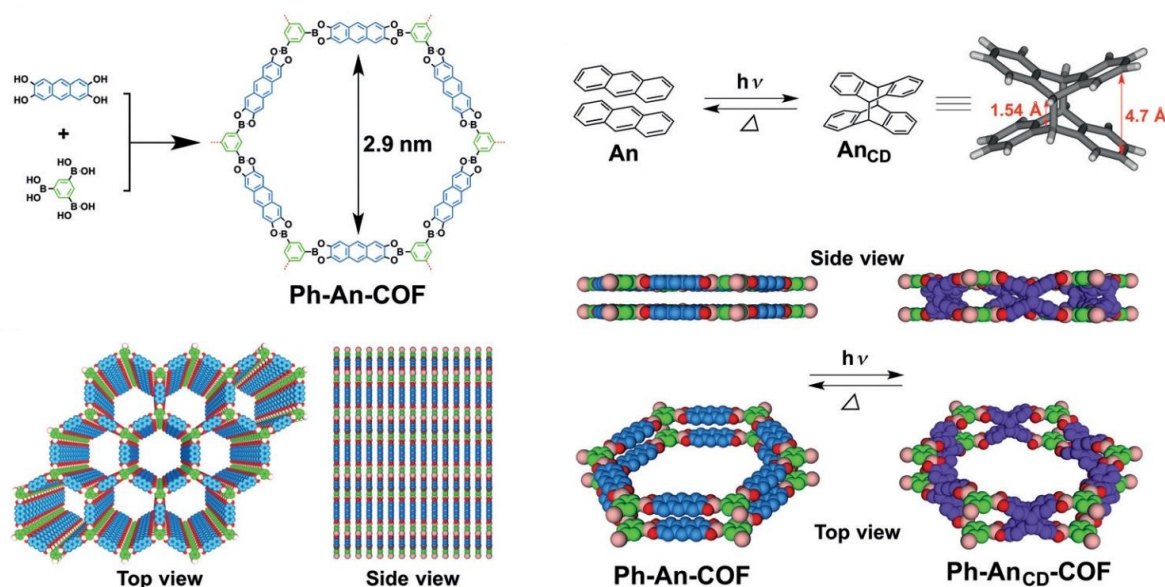


Figure 1.18: Synthesis of Ph-An-COF and postsynthetic [4p+4p] cycloaddition. Adapted with permission from ref. 69. Copyright 2015 John Wiley and Sons.

Another cycloaddition on an anthracene unit was performed in a β -ketoenamine COF (made from 1,3,5-triformylphloroglucinol and 2,6-diaminoanthracene) with a [4+2] cycloaddition with N-hexylmaleimide. The introduction of this bulky moiety resulted in delamination of the COF layers.²⁹⁶ Waller et al. reported the oxidation of the imine linkages of the 2D imine COFs TPB-TP-COF (made from tris(4-aminophenyl)benzene and terephthalaldehyde) and 4PE-1P-COF (from 1,1,2,2-tetrakis(4-aminophenyl)ethene and terephthalaldehyde) with sodium chlorite as oxidant and 2-methyl-2-butene as hypochlorous acid scavenger to establish RC(O)NHR amide linkages in the COFs. This conversion improved the stability of the frameworks in acidic and basic environments.¹⁸⁹

Guo et al. reported a postsynthetic modification starting from the ketoenamine COF TpBD-Me (from the linkers TPG and 3,3'-dimethylbiphenyl-4,4'-diamine) bearing methyl groups at the pore walls. These were postsynthetically brominated by applying N-bromosuccinimide and benzoylperoxide in a Wohl-Ziegler-reaction. In a second step, trimethylamine was introduced to establish quarternary ammonium units at the pore walls.²⁸⁷

Xu et al. synthesized COFs with imine and ketoenamine linkages (made from (*S*)-4,4'-(2-(pyrrolidin-2-yl)-1*H*-benzo[*d*]imidazole-4,7-diyl)dianiline with 1,3,5-triformylbenzene (COF LZU-72) or with 1,3,5-triformylphloroglucinol (COF LZU-76) featuring a Boc-protected pyrrolidine. The Boc group was postsynthetically cleaved by applying heat

or acidic conditions.¹²³ Summarizing, the substantial collection of postsynthetic modification strategies that have been published to date indicates the versatility of this approach towards expanding the structural and functional diversity of COFs.

1.5 Synthetic Methods and Morphologies

1.5.1 Controlling the Crystallinity

Crystallinity is a key property of covalent organic frameworks that distinguishes them from organic polymers. Thus, great efforts have been devoted to understanding the parameters that determine the degree of long-range order in COFs. However, this issue is not yet fully understood. One of the reasons is that the range of COF structures studied to date covers many different linkages and various building blocks with different solubility, geometry and linkage chemistry, all potentially leading to different polymerization/crystallization behaviour. An early and rather obvious concern was the reversibility of the COF formation reaction to enable the repair of defects in the structure, thus leading to a crystalline framework. Therefore, the first synthesis protocols for COFs used closed vials with limited water content in the reaction mixture. In the meantime other important parameters such as the solubility of the starting materials or factors related to the stacking ability of the COF layers have been identified in different COF structures. All of them represent pieces of the great puzzle offered by the crystallization of COFs.

While the first COF reactions were performed in sealed glass tubes at elevated temperature, Campbell et al. found that microwave reactions under ambient pressure represented another feasible method for COF synthesis and that the overpressure was not a prerequisite for COF crystallization.⁷³ The incorporation of truncated monomers has different effects on the crystallinity of COFs. In the 3D boroxine COF-102 made of (methanetetrayltetrakis(benzene-1,4-diyl))tetraboronic acid (see Section 1.3.1), truncated monomers representing defects in the COF network were incorporated to a large extent already at low initial concentrations.³³ In contrast, we found for COF-5 that was crystallized in the presence of a monoboronic acid nearly no incorporation of artificial defects up to an initial content of 10% truncated monomer was observed, but a more ordered structure with a distinctive higher BET surface area and increased domain size was obtained. This finding showed that the truncated monomer served as an efficient modulator for this particular COF synthesis.⁷⁹

Smith et al. also investigated the growth mechanism of the 2D boronic ester linked COF-5 and found that using the monofunctional 4-tert-butylcatechol did not lead to incorporation into the COF lattice, even when offering up to 12 equivalents in the reaction. Instead it served as competitor for HHTP and slowed down the COF formation while only having a small influence on the crystallite domain sizes. A more distinct effect was observed upon addition of H₂O, which increased the domain size noticeably. The authors also found the aggregation of formed COF crystallites to be irreversible, as the addition of monocatechol to the already fully crystallized COF did not result in a partial decomposition of the network, which would be expected under reversible dynamic conditions.⁷⁵ The initially homogeneous nucleation and growth of boronic ester COFs from fully dissolved monomers was found to be beneficial for the COFs' porosity, as no insoluble monomers could block the COF pores.⁷⁶

In imine-based COF systems, not only the water content but also the presence of the acid catalyzing the imine formation can be used to tune the synthesis conditions towards obtaining a crystalline product. In a mechanistic study, Smith et al. investigated the crystallinity of imine COFs depending on the concentration of acetic acid and water in the reaction mixture. For the synthesis of the COF TAPB-PDA from 1,3,5-tris(4-aminophenyl)benzene and terephthalaldehyde they found that the absence of acetic acid prevented the formation of a solid precipitate. The absence of water resulted in the fast precipitation of amorphous material. Only with a minimum concentration of > 3.3 M acetic acid and ≥ 1 M H₂O a crystalline framework was formed, demonstrating the great influence of these additives on a successful synthesis. Notably, once an amorphous polymer was formed, it could be transformed into a COF by being subjected to the optimal COF growth conditions in the absence of additional monomers.¹⁸⁷ A similar observation was made by Gao and coworkers, who demonstrated the decomposition of the imine-linked COF-I (from 4,4'-biphenyldiamine and TFB) under basic conditions and its subsequent rearrangement into a crystalline structure upon acidic treatment with acetic anhydride.¹³⁷

In addition to hydrolytic depolymerization, destruction of the COF structure can also occur by just delaminating the COF sheets, thereby destroying the long-range order in the z-stacking direction, while the molecular connectivity in the 2D sheets is retained. In this case, a rearrangement of the layers into a crystalline framework may be possible. This was demonstrated by Stegbauer et al., who obtained delaminated COF sheets after applying the hydrazone-linked TFPT-COF in photocatalysis or after simply sonicating the COF in water. Subsequently, the stacking of the layers was re-established by exposing the material

to the initial COF synthesis conditions (with the same solvent mixture and catalyst, but no fresh COF momomers). The reorganized TFPT-COF featured a BET surface area and crystallinity similar to the initial COF.²⁴⁴ A direct transformation of amorphous polymer to crystalline COF was achieved for the ketoenamine COF TpBD from TPG and benzidine. The polymer was first fabricated as a coating on Fe_3O_4 nanoparticles. Upon heating in a sealed pyrex tube with pyrrolidine as catalyst, the network rearranged to form crystalline porous COF, demonstrating the reversibility of the ketoenamine formation under these conditions (Figure 1.19).²⁸⁵

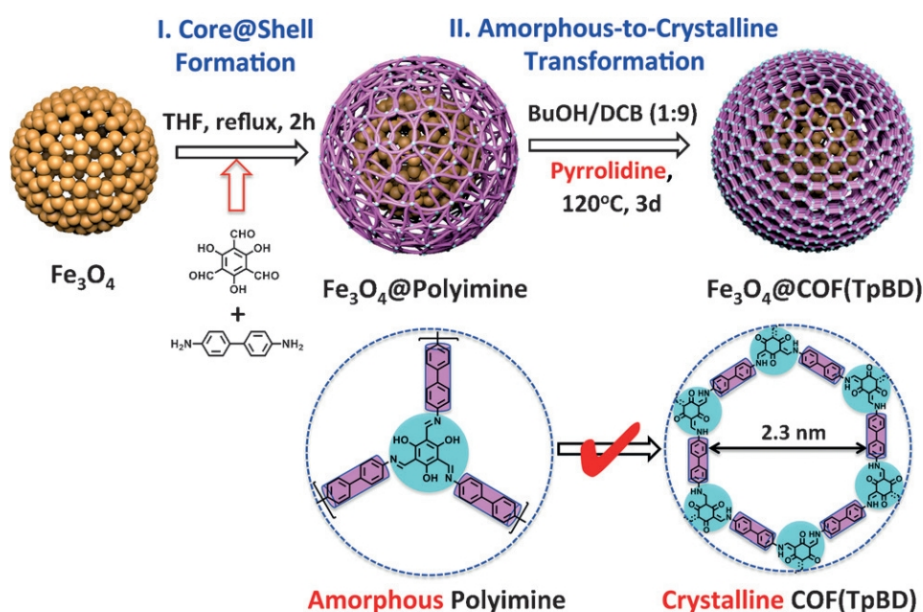


Figure 1.19: Amorphous-to-crystalline conversion of the COF TpBD on Fe_3O_4 nanoparticles. Reproduced with permission from ref. 285. Copyright 2016 John Wiley and Sons.

A well-known factor affecting the crystallinity of the product of a COF synthesis is the solvent or solvent mixture used. For example, this was shown in a study by Feng et al., where the crystallinity of the synthesized porphyrin boronic ester-linked COF showed great sensitivity towards the composition of the mesitylene : dioxane reaction mixture. The highest long-range order was achieved with a mesitylene : dioxane = 19 : 1 mixture, while mesitylene alone led to a poorly crystalline material and a dioxane content of 20% already resulted in an amorphous product.⁶⁷ It has to be noted that the impact of the exact composition of the solvent mixture is different for different systems and that this correlation has not been reported in detail for most COFs. Other factors include the catalyst system used for condensation reactions, as well as possible linker exchange. For example,

Matsumoto et al. reported the use of metal triflates rather than acetic acid as catalysts for the formation of imine COFs. They found that with these compounds, especially with $\text{Sc}(\text{OTf})_3$, highly crystalline COFs were formed already at room temperature and within reaction times of a few minutes. Notably, the accessible BET surface area was significantly higher than for the same COFs synthesized in solvothermal reactions.¹⁸²

Qiao et al. showed that the imine-linked COF TP-COF-BZ (from benzidine and [1,1':3',1''-terphenyl]-3,3'',5,5''-tetracarbaldehyde) can undergo linker exchange, with the benzidine units being exchanged with 1,4-phenylenediamine by suspending the COF in a solution of the latter at elevated temperatures. Within a few hours, a crystalline COF with the smaller amine linker was obtained.¹⁷¹

Besides these factors, the geometry and functionalization of the COF linkers themselves were shown to largely determine the crystallinity of the COF. In a simulation of boron-based COFs, Zhou et al. found that the exact AA stacking of the COF layers is not preferred, but that a slightly shifted stacking is energetically favorable.³²⁶

Heine et al. performed simulations of various shifted layer arrangements in boron-based COFs, namely serrated and inclined (in armchair and zigzag stacking), and found favorable Coulomb interactions between the layers in all shifted geometries. However, in many cases the rather small crystalline domain sizes of COFs in the range of tens of nanometers lead to line-broadening and limited detail in X-ray diffraction data, and it cannot be stated unambiguously which of the slightly different arrangements is realized in the COFs.³²⁷

In a recent study, we investigated the impact of side groups on the structure of the boronic ester-linked BDT-COF (from benzo[1,2-*b*:4,5-*b'*]dithiophene-2,6-diylidiboronic acid and HHTP). We introduced varying fractions of the ethoxy-functionalized BDT linker and observed the formation of a crystalline COF material for all fractions up to fully modified BDT-OEt-COF, while both the pore size and the crystallite domain size decreased with increasing BDT-OEt content.¹⁰⁷

The use of -OH functionalized aldehydes in imine COFs, where the -OH can form a hydrogen bond with the imine group, was not only shown to be beneficial for the stability of the COF framework but also resulted in a higher crystallinity of the frameworks compared to -OMe functionalized structures. The reason for this difference lies in the planarization of the COF structure with the formation of these hydrogen bond interactions, which have been observed in several structures.^{204,212}

The same effect was found for the azine-linked COF-JLU3 made from hydrazine and 1,3,5-tris(3'-tert-butyl-4'-hydroxy-5'-formylphenyl)benzene.²⁵⁷ Introducing methoxy

groups as substituents at the amine linker in imine COFs provided oxygen lone pairs that softened the interlayer repulsion in the COF stacks. This effect not only led to an increased crystallinity and very high surface areas, but also greatly improved the COFs' chemical stability.¹⁹⁰ In an early study, Tilford et al. demonstrated the decrease of crystallinity that results from the introduction of alkyl chains as substituents of 1,2,4,5-tetrahydroxybenzene in a boronic ester COF.⁶⁴

Following this trend, a decrease in crystallinity compared to non-functionalized linkers was observed for tetrafluoro functionalized biphenyl linkers in ketoenamine COFs made from 2,2',3,3',5,5',6,6'-octafluoro-[1,1'-biphenyl]-4,4'-diamine and TPG. The tetrafluoro-functionalized linkers exhibit a large twist angle and thus inhibit efficient stacking.²⁶¹

In contrast, if the diamine linker consists of only one ring, no rotary axis is present, and stacking is possible, resulting in a crystalline COF. In an imine COF made from a mixture of tetrafluoro-functionalized and unfunctionalized diamine linkers, the COF benefits from the favourable π -interactions between the two linker types and shows highest crystallinity and BET surface area for a content of 50% of the fluoro-substituted linker.²⁰⁶

Haase et al. observed a significantly reduced crystallinity of an azine COF with the trigonal building block 6,6',6''-(benzene-1,3,5-triyl)trinicotinaldehyde with one nitrogen in each of the peripheral phenyl rings, than for the COF with the isoelectric building block 4,4',4''-(1,3,5-triazine-2,4,6-triyl)tribenzaldehyde with three nitrogen atoms in the central phenyl ring, an effect that was attributed to the lower symmetry of the linker with peripheral functionalization.²⁵⁶

Our group recently demonstrated the benefits of propeller-like nodes in COF frameworks. The propeller-shaped tetradental amine linker ETTA (4,4',4'',4'''-(ethene-1,1,2,2-tetrayl)tetraaniline) stacks in a highly ordered fashion due to a lock-in mechanism of the four propeller-like phenyl rings. The resulting docking sites guide the attachment of successive building blocks during crystal growth, thus promoting long-range order in a group of structurally related COFs. A similar effect was also achieved with the tridentate linkers tris(4-aminophenyl)amine and tris(4-aminophenyl)benzene (Figure 1.20).¹⁸⁰

Similarly, with the building block 1,3,6,8-tetrakis(4-aminophenyl)pyrene, an ordered stacking of the COF sheets was reached. Both theoretical simulations and XRD data indicate an armchair conformation of the pyrene linker, which allows for a close packing of both the pyrene and the phenylenes, thus enabling the growth of very large COF domains as big as 0.5 μm .²⁰²

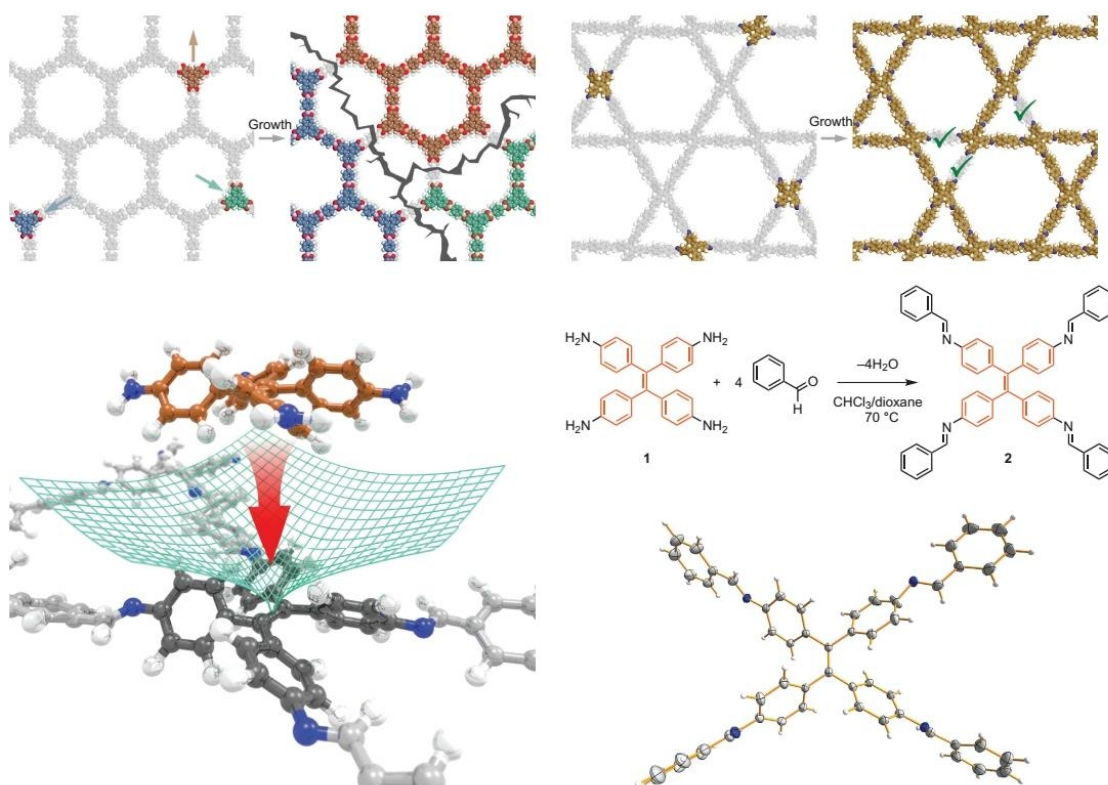


Figure 1.20: Lock-and-key motif of propeller-shaped building blocks enabling a defect-free layer growth. Adapted with permission from Macmillan Publishers Ltd: Nature Chemistry, ref. 180, copyright 2016.

Sun and Cheng propose a similar locking effect for the bowl-shaped aldehyde linker triformylcyclo-trianisylene (Table 1.10).¹⁵⁵ With the amine analog of the triformylcyclo-trianisylene, methoxy and hydroxyl side chains at the linear linker terephthalaldehyde drastically decreased the crystallinity in a COF structure built with these components compared to a COF with the unsubstituted dialdehyde linker.¹⁸¹

Increased flexibility was introduced into imine COF lattices by integrating the linker tri-(4-formacylphenoxy)-1,3,5-triazine.¹⁵³ The linker flexibility was also investigated with the amine form of this triazine core and was found to support the stacking of the triazine units, thus improving the crystallinity of the COFs.¹⁵⁴ Xu et al. applied the hexadental amine linker HAT-NH₂ (with a hexaazatriphenylene = HAT core) in combination with the tridentate aldehydes 4,4',4''-nitriлотribenzaldehyde and 4',4''',4''''-nitriлотris([1,10-biphenyl]-4-carbaldehyde) to form HAT-NTBA-COF and HAT-NTBCA-COF, respectively. In these frameworks, the imine bonds are present in two different orientations to achieve the for-

mation of a crystalline framework rather than the amorphous polymer that would result from one single orientation of the imine bonds.²³⁵

Dong and coworkers investigated the influence of the monomer planarity on the crystallinity of the COF in a series of nitrogen-rich COFs. They found that the planar triazine core linker 2,4,6-tris(4-aminophenyl)-1,3,5-triazine (TAPP) formed a highly crystalline COF upon co-condensation with 1,3,5-benzenetricarbaldehyde, while only poor crystallinity was observed with the non-planar building blocks 1,3,5-tris(4-aminophenyl)benzene or tris(4-aminophenyl)amine.¹⁴⁰ Salonen et al. utilized the strong dipole moment in pyrene-4,5-dione units to synthesize a highly crystalline boronic ester COF. The authors propose an antiparallel alignment of the dipolar pyrene-4,5-dione units in the COF as they have the most favorable interaction energy in this arrangement.⁹⁰

Incorporation of methyl groups in a truxene-based building block to form 3,8,11-tris(4-formylphenyl)-5,5,10,10,15,15-hexamethyltruxene did not hinder the formation of crystalline COFs in the co-condensation with PDA or benzidine, respectively. Instead, incorporation of the methyl groups changed the layer arrangement from the usual AA stacking to an inclined arrangement.¹⁵⁷

The building block 1,3,5-tris(4-formylphenyl)benzene was modified with fluorine atoms at the core or outer phenyl rings to synthesize azine COFs with the building blocks 1,3,5-trifluoro-2,4,6-tris(4-formylphenyl)benzene (TF-COF 2) and 1,3,5-tris(3-fluoro-4-formylphenyl)benzene (TF-COF 1). Integration of these modified building units into azine-linked COFs led to drastically increased BET surface areas (1820 and 2044 m² g⁻¹ for TF-COF-1 and TF-COF-2, respectively) compared to a COF with the non-functionalized linker (760 m² g⁻¹). The authors attribute this improvement to a polarization in the aromatic rings, caused by the fluorine substituents, that would enhance cofacial interactions, and to the increased reactivity of the azine groups in the fluorinated linkers (Figure 1.21).²⁵⁴ Also, when integrating the linker of TF-COF-1 in a mixture with non-fluorinated linker, the crystallinity and BET surface area of the resulting COFs increased for higher fraction of the fluorinated monomer with a distinct increase from the 75% fluorinated ($S_{\text{BET}} = 1064 \text{ m}^2 \text{ g}^{-1}$) to the 100% fluorinated COF ($S_{\text{BET}} = 1802 \text{ m}^2 \text{ g}^{-1}$). Quantum mechanical calculations of the stacking interactions in dimers of these linkers revealed that the fluorinated-fluorinated interaction is energetically favored in comparison to the stacking of a fluorinated with a non-fluorinated linker or of non-fluorinated linkers alone.²⁵⁵

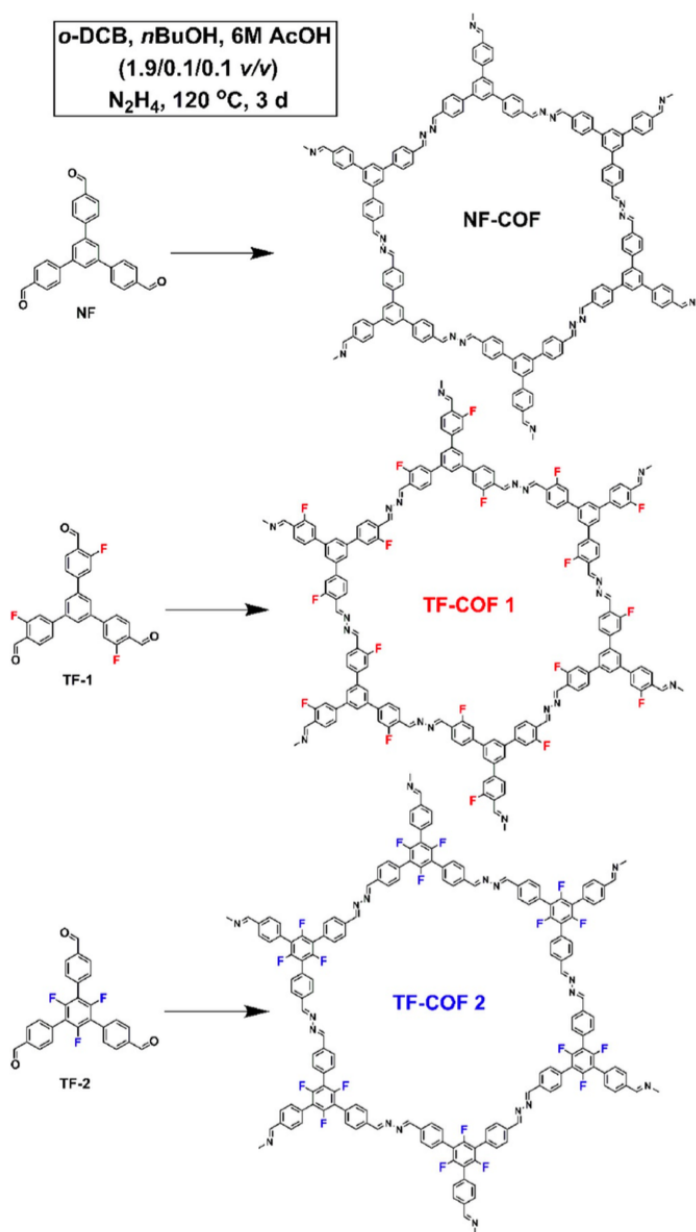


Figure 1.21: Schematic representation of the synthesis of azine-linked COFs with fluorinated linkers. Reproduced with permission from ref. 254. Copyright 2017 John Wiley and Sons.

1.5.2 Processing

1.5.2.1 Solvothermal Synthesis and Reactions under Ambient Pressure

The first syntheses of COFs were performed under solvothermal reaction conditions, and this method is to date still the most popular and most frequently applied synthesis method for COF formation. Thereby, the COF precursors are placed in a vial together with the desired solvent or solvent mixture and catalysts or modulators, if needed. The reaction vessel has to be a closed container, like a sealed pyrex tube, a steel autoclave with a Teflon liner or a glass bottle with a plastic cap. The reaction mixture in this vial can be heated above the boiling point of the solvent, allowing for an increased solubility of the precursors and improved kinetics. Although the solvothermal synthesis pathway in many cases leads to satisfactory results in terms of crystallinity and porosity of the products, it also has some drawbacks. The most important could be the difficult transferability to industrial applications, as scale up is challenging, and the slow reaction rates observed in many COF syntheses.

An early approach towards moving away from closed reaction vials was reported by Fischer and coworkers for the synthesis of COF-1. They introduced $\text{NH}_3\text{-H}_2\text{O}$ vapor to a clear solution of BDBA and obtained a COF-1-ammonia adduct. Upon heating, the NH_3 molecules were removed to yield the COF-1 as a guest-free framework. However, the crystallinity of the product was lower than for the solvothermal synthesis of COF-1.⁴¹

In recent years, protocols for the solution based synthesis of COFs under ambient pressure have been reported. Dichtel and coworkers used COF synthesis pathway from clear solution for the synthesis of a range of boronic ester COFs,^{75,76} and metal-triflate catalyzed room temperature syntheses of imine COFs that led to COFs with BET surface areas superior to the solvothermally synthesized frameworks,¹⁸² (see Section 1.5.1 for details).

Very recently, Peng et al. reported the room temperature batch synthesis of imine, enamine and azine linked COFs. For this, a mixture of the monomers was sonicated for homogenization and was then allowed to stand for 3 days. If linkers with a good π -stacking ability were used, the resulting COFs featured crystallinity and porosity equal to their solvothermal counterparts.

When building blocks with lower ability for π -stacking were used, namely hydrazine and 1,3,5-tris(4-formyl-phenyl)benzene, a COF was still formed but with a significantly lower BET surface area. Furthermore, a continuous flow synthesis of the COF LZU-1 (made from

1,4-phenylenediamine and 1,3,5-triformylbenzene) was demonstrated, yielding the COF in good quality,¹²⁷ a strategy that was also applied by Dichtel and coworkers to synthesize thin films (see Section 1.5.3.2).⁸¹ Furthermore, Lin et al. reported the formation of an imine COF shell around Fe₃O₄ nanoparticles in a room temperature synthesis in only 5 minutes.¹⁸⁸

1.5.2.2 Microwave-Assisted Synthesis

An early approach to overcome the relatively long reaction times of the solvothermal synthesis was the use of microwave irradiation for COF synthesis, reported by Campbell et al. in 2009. They demonstrated the synthesis of COF-5 in a microwave reaction in only 20 minutes. Subsequent purification by microwave extraction steps yielded a material with a BET surface area of more than 2000 m² g⁻¹, which is higher than the values reported for solvothermal synthesis. The same synthesis protocol was also successfully applied for the synthesis of COF-102.⁷³

Wei et al. observed similar effects for the β -ketoenamine COF TpPa-1, which showed better crystallinity and higher surface area and CO₂ capacity when synthesized under microwave irradiation within 60 min compared to a solvothermal synthesis, taking 60 min as well.²⁶⁹

In the synthesis of azine COFs with two pore sizes, derived from the introduction of desymmetrized aldehyde linkers 5-(4-formylphenyl)isophthalaldehyde and 5-[(4-formylphenyl)ethylene]isophthalaldehyde, microwave synthesis led to COF material with properties comparable to the solvothermally synthesized one.²⁴⁹ The microwave synthesis of TpPa-2 (a ketoenamine COF from TPG and 2,5-dimethyl-1,4-phenylenediamine) yielded porous COF particles with a narrow particle size distribution.²⁷⁸ Lee et al. applied microwave-assisted synthesis for the formation of the imide-linked PI-COF, made from the building blocks pyromellitic dianhydride and tris(4-aminophenyl)amine. By introducing the monofunctional molecule 4-[(dimethylamino)methyl]aniline in the synthesis, a truncation and functionalization of the network with dimethylamine groups was realized.³⁰⁶

1.5.2.3 Mechanochemical Synthesis

For some β -ketoenamine COFs, mechanical grinding of the COF linkers was found to yield the same COF structures as known from solvothermal reactions. In a very simple experimental setup, the two starting materials were ground with mortar and pestle. The

mechanochemically synthesized COFs were less crystalline compared to the solvothermally synthesized batches and had rather low BET surface areas of below $100 \text{ m}^2 \text{ g}^{-1}$.

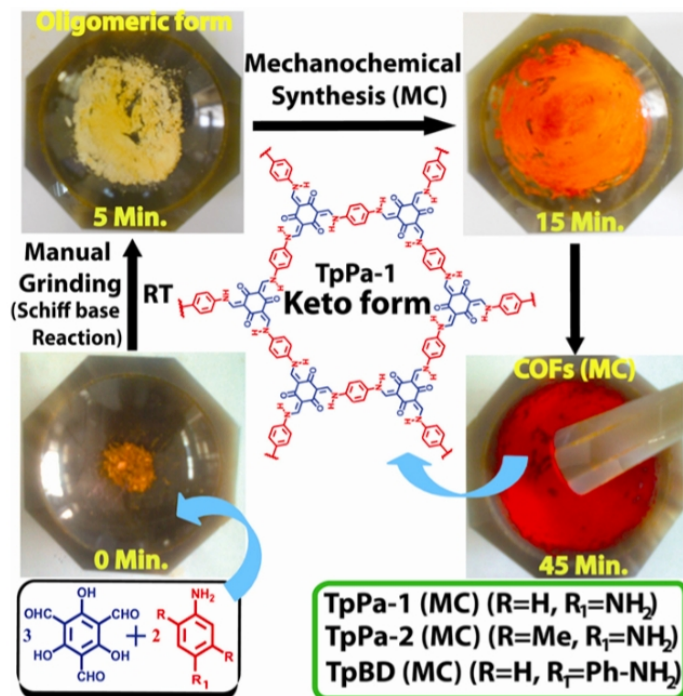


Figure 1.22: Schematic representation of the mechanochemical synthesis of the COFs TpPa-1, TpPa-2, and TpBD using a mortar and pestle. Reprinted with permission from ref. 262. Copyright 2013 American Chemical Society.

Nevertheless, their chemical stability was equivalent to the solvothermally synthesized batches. With this synthesis method, the COFs are formed as exfoliated thin sheets, which are also accessible *via* grinding solvothermally synthesized COF powder (Figure 1.22).²⁶²

A drastic increase in both, crystallinity and BET surface area was achieved by a liquid-assisted grinding method, where a catalytic amount of liquid was added to the COF precursors. This also increased the reaction rate. The method was successfully applied for the synthesis of β -ketoenamine, imine and hydrazine COFs.^{128,289}

By grinding the diamine linker together with *p*-toluenesulfonic acid and water and subsequent addition of TPG and heating to $170 \text{ }^\circ\text{C}$ for 1 min, the ketoenamine COFs were obtained in high quality and some with high surface areas. The reagent mixture had the consistence of dough and could be processed into various shapes without any additional binder, hence enabling the fabrication of COF sculptures *via* this ‘terracotta process’ (Figure 1.23).²⁶⁷

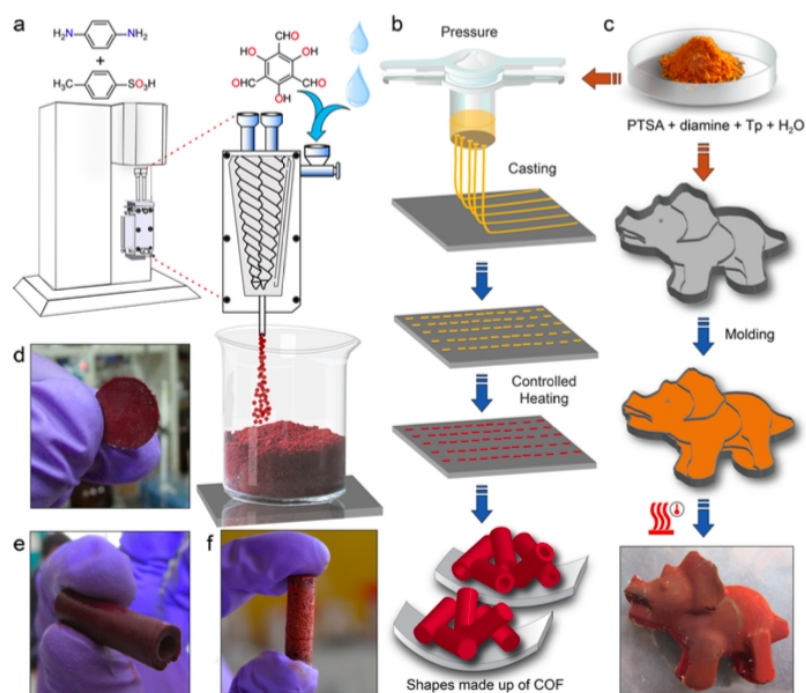


Figure 1.23: (a) Mechanochemical COF synthesis by extrusion. (b) Schematic representation of COF-bead fabrication using the terracotta technique. (c) Schematic representation of COF processing into sculpture *via* the organic terracotta process. (d-f) Digital photographs of COF membrane, hollow tube, and cylinder, respectively. Reproduced with permission from ref. 267. Copyright 2017 American Chemical Society.

Similarly, the synthesis was also performed from a solution of *p*-toluenesulfonic acid and water with various linear aromatic diamines with subsequent addition of TPG. These mixtures also formed doughs that were cast on glass and baked to yield self-standing membranes.²⁸³

On the other hand, when the sulfonic acid functionalized ketoenamine COFs NUS-9 and NUS-10 (made of 1,3,5-triformylphloroglucinol with 2,5-diaminobenzenesulfonic acid and 2,5-diaminobenzene-1,4-disulfonic acid, respectively) were synthesized mechanochemically, amorphous material was obtained and moderately crystalline materials with low surface areas were only achieved after recrystallization.²⁸²

Vazquez-Molina et al. found that pre-synthesized unoriented powder of 2D COFs can be aligned into anisotropic packing by applying mechanical stress, namely by pressing a pellet of the COF powder. XRD analysis revealed a preferred orientation of the COF layers perpendicular to the axis of the mechanical force.⁸²

1.5.2.4 Sonochemical Synthesis

Another alternative to solvothermal synthesis is the sonochemical approach. By the application of ultrasound, bubbles are formed in the solvent which grow and collapse in a process called cavitation, leading to very high local temperatures and pressures in the solution, thus accelerating the chemical reaction. Yang et al. investigated this synthesis method for the formation of COF-1 and COF-5. A short reaction time of only 0.5-2 h was achieved, resulting in a BET surface area of up to $2122 \text{ m}^2 \text{ g}^{-1}$; the reactions could be scaled up to a 0.5 L batch size.³⁹ With this mild synthesis method, COF-5 was also successfully deposited on carbon nanotubes and graphene.⁴⁴

1.5.2.5 Vapor-Assisted Conversion

A vapor-assisted conversion of COF precursors for the preparation of thin COF films has been developed by our group. In these syntheses, COF precursors such as (4,8-diethoxybenzo[1,2-*b*:4,5-*b'*]dithiophene-2,6-diyl)diboronic acid and 2,3,6,7,10,11-hexahydroxytriphenylene (HHTP) were dissolved in a solvent mixture of acetone and ethanol and dropcast on a substrate that was then placed into a desiccator together with a reservoir containing a 1 : 1 mixture of mesitylene and dioxane. After 72 h at room temperature, smooth, homogeneous COF films were obtained (Figure 1.24).

Thereby, a strong influence of the solvent in the reservoir on the crystallinity of the products could be observed. The film growth was demonstrated on various surfaces, with different COFs and with control over the film thickness by changing the amount of precursor in the droplet.⁵⁷

Jiang et al. reported the formation of COF nanofibers from 2,6-dihydroxynaphthalene-1,5-dicarbaldehyde and 2,4,6-tris(4-aminophenyl)pyridine in a vapor-assisted solid state transformation. Here, the two linkers were first mixed as solids and then this mixture was placed in a closed vessel next to a liquid reservoir containing a defined mixture of dioxane : mesitylene : 6 M AcOH = 5 : 5 : 1.

Exposure of the solid starting materials to the solvent vapor resulted in condensation to a COF structure with a fibrous morphology and moderate crystallinity and porosity. The authors found that the composition of the vapor has a strong influence on the crystallinity of the COF and that the acid in the vapour plays a key role in the formation of a crystalline product.¹⁷⁹

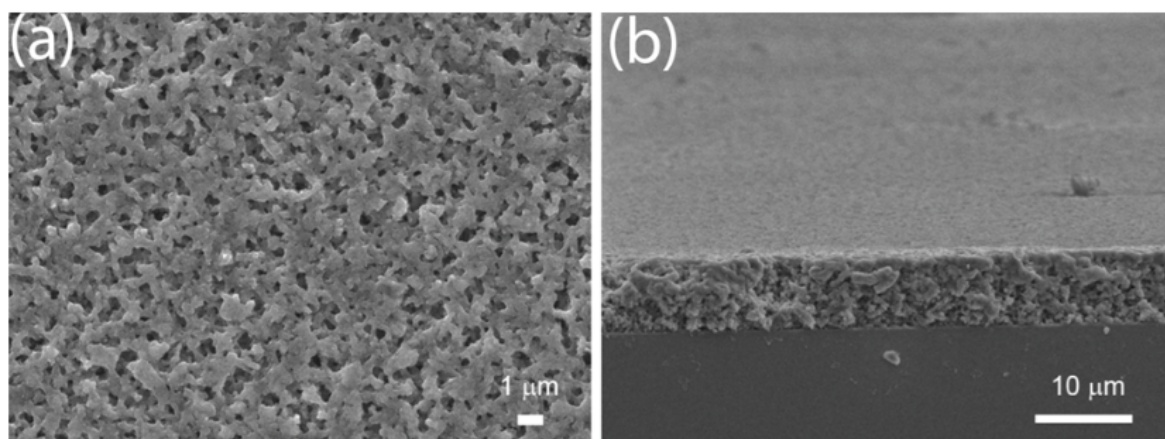


Figure 1.24: (a) Top view SEM micrograph of BDT-COF film synthesized by room temperature vapor-assisted conversion, representing the surface morphology. (b) Cross-section SEM micrograph. Reprinted with permission of the American Chemical Society from ref. 57.

1.5.3 Special Morphologies

1.5.3.1 Single Layered COFs

Single layered 2D COFs can be obtained by either exfoliating COF sheets from pre-synthesized 2D COF bulk material or by directly growing a single layer on a surface. The exfoliation of the COF can be achieved by sonication in a delaminating solvent^{51,117,242–244,304,308} or by mechanical grinding.^{200,261} These methods usually lead to COF sheets that are composed of several COF layers, but single layered material has recently been reported.²⁴⁷

The delamination of a β -ketoenamine COF containing anthracene units was achieved by postsynthetic cycloaddition of N-hexylmaleimide to the anthracene units, which resulted in perturbation of the stacking of the COF sheets and their delamination. Immersing these delaminated sheets in CH_2Cl_2 and transfer of this mixture to a water reservoir led to self-assembly of the COF layers at the air-water interface. Subsequently, they could be taken up as single or few layer sheets (Figure 1.25).²⁹⁶

A three-step postsynthetic modification pathway (reacting first the aromatic hydroxyl groups with glycidol to establish aliphatic hydroxyl groups which were then utilized as anchoring points for 3-aminopropyltriethoxysilane whose primary amine was in the third step reacted with folic acid) also resulted in the delamination of the COF sheets in the COF TpASH (from TPG and 4-amino-2-hydroxybenzohydrazide).²⁵⁹

The direct growth of COF structures as single layers (sCOFs) on substrates was achieved using the slightly reversible chemistry that had already been applied for COF powder synthesis, like the formation of boroxines and boronic esters and Schiff-base chemistry yielding imines.

However, in single layer growth, regularly ordered structures have also been obtained by applying reactions that would lead to amorphous material when used in bulk synthesis, like Ullmann coupling or esterification. A detailed review of single-layered structures formed by all these linkage modalities is given by Liu et al.³²⁸ Here, we will focus on the linkage motifs that were also successfully applied for COF powder synthesis.

COF-1 (also named SCOF-1) and COF-5 (also named SCOF-2) were grown on an Ag (111) substrate by sublimation of the linkers from two heated molybdenum crucible evaporators under ultrahigh vacuum. A nearly full surface coverage was reached for both COFs. COF-5 formed a very regular network while COF-1 showed many defects.⁵⁴ A different approach towards a COF-1 single layer was reported by Dienstmaier et al. and our group in 2011. The authors performed a pre-condensation of BDBA by heating it in the presence of water vapor to form COF-1 nanocrystals. Subsequently, these crystals were resuspended, drop-cast on highly oriented pyrolytic graphite (HOPG), and an annealing step at higher temperatures and with water vapor was applied. Thereby, large domains of a COF-1 monolayer with only a few defects were obtained. Direct annealing of BDBA on HOPG also led to a COF-1 monolayer with similar domain sizes and defect density.³⁸

A solvent-free vapor deposition route was reported by Spitzer et al. for the synthesis of surface COFs on HOPG from BDBA and 4,4'-biphenyldiboronic acid, respectively. With this technique, smoother and more ordered films were achieved, compared to a synthesis route where the monomers were dissolved in a solvent and brought to the HOPG surface by drop-casting.⁵² Similarly, boroxine COFs were grown by utilizing the thermal dehydration of $\text{CuSO}_4 \times 5 \text{H}_2\text{O}$ to achieve a continuous water vapor supply (Figure 1.26).⁵⁵

A further lattice expansion of these surface COFs was achieved by utilizing linear diboronic acids with up to four phenyl rings, and a pyrene diboronic acid was also successfully employed.³⁵ Yu et al. investigated the co-condensation of HHTP with 4,4'-biphenyldiboronic acid on HOPG. The structure formed on the surface was determined by the initially applied linker ratio. The highest surface coverage with COF-10 was found for the HHTP to boronic acid ratio of 1 : 4 while a ratio of 1 : 6 led to homopolymerization of the boronic acid to form a boroxine COF.⁸⁹

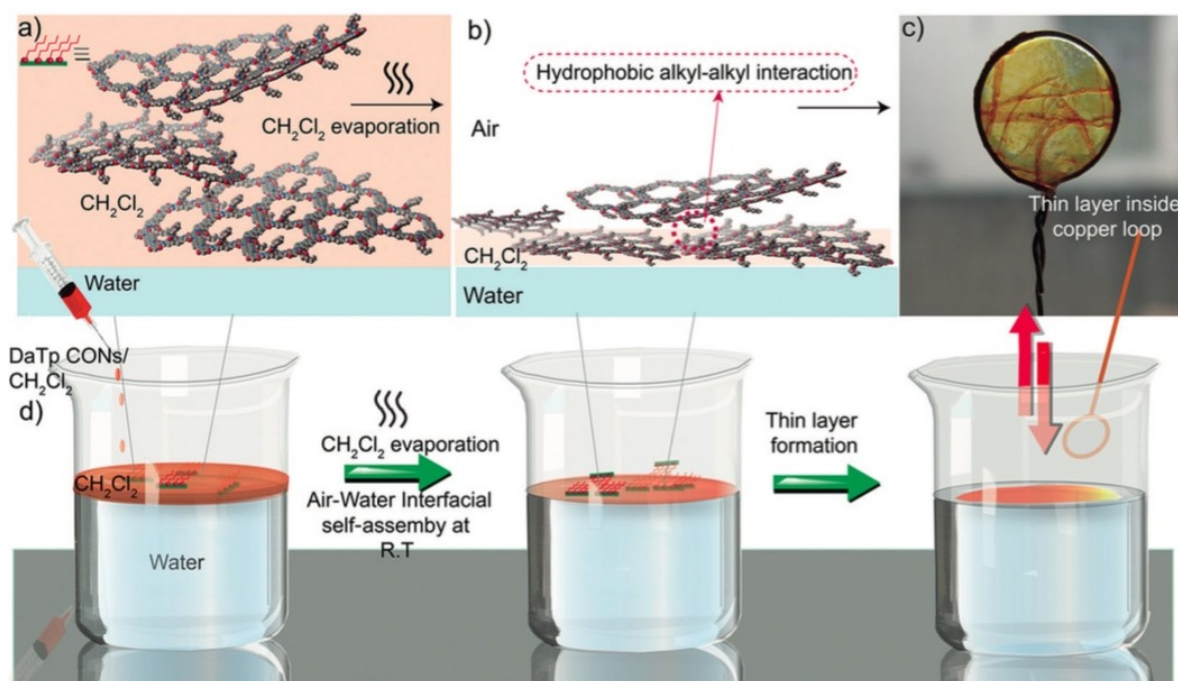


Figure 1.25: a) DaTp-CONs in DCM. b) LbL assembly after DCM evaporation. c) A thin layer inside a copper loop. d) Schematic representation of the thin-film formation at an air-water interface. Adapted with permission from ref. 296. Copyright 2016 John Wiley and Sons.

COF-1 on HOPG was applied by Cui et al. as a host for fullerene moieties by immersing the COF on HOPG in a solution of fullerene in heptanoic acid. A preferential adsorption of the fullerene on top of the COF layer, more specifically on top of the boroxine units rather than the phenyl rings, was observed.⁴² Later, Plas et al. prepared COF-1 on HOPG and added fullerene in 1-phenyloctane. They observed adsorption of the fullerene units in the pores of the COF layer, rather than at its nodes.⁴³ When they dissolved C₆₀ in trichlorobenzene, Cui et al. observed the selective adsorption of the trichlorobenzene molecules in the pores and adsorption of the fullerene at the top of the COF-1 layer.⁵⁰ This series of observations nicely illustrates the possibility to control the C₆₀ adsorption site on COF layers through the choice of the solvent.

On-surface self-condensation of the 4,4'-phenylazobenzoyl diboronic acid alone yields a boroxine COF layer with azo groups. The switching of these azo groups from the trans- to the cis-isomers upon irradiation with UV light led to cleavage of the boroxine bonds. Surprisingly, this process was shown to be reversible, as the initial hexagonal COF structure was recovered upon heating of the photoswitched COF layer.⁵⁸

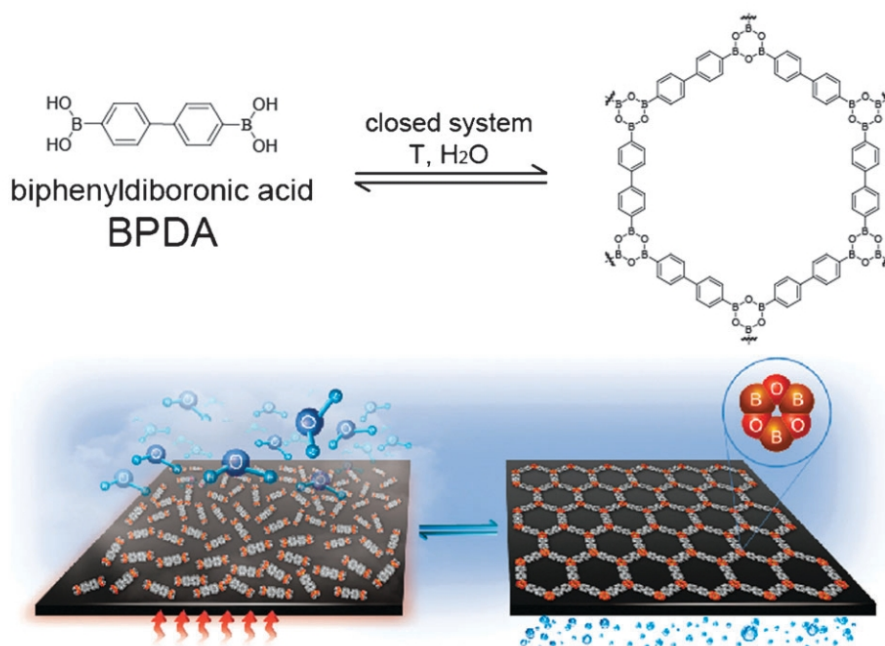


Figure 1.26: The synthesis of SCOOF-1 with $\text{CuSO}_4 \times 5 \text{H}_2\text{O}$ as reaction equilibrium regulator. Reproduced from ref. 55 with permission of The Royal Society of Chemistry.

Liu et al. investigated the growth of the azo-containing COF made from HHTP and 4,4'-phenylazobenzoyl diboronic acid at the octanoic acid/HOPG interface. They found that the monomer concentration of both building blocks is one of the main factors determining the resulting structure with a high concentration leading to multi-wall structures while at lower concentrations, the COF lattice is formed. Furthermore, a transformation from a single-wall COF to multiwall structures was observed after applying a voltage pulse, a process that was not reversible, indicating that the COF is not the thermodynamically most stable structure as single layer on HOPG (Figure 1.27).¹¹¹

Likewise, highly ordered imine structures were grown on HOPG using the condensation reaction of PDA with 1,3,5-triformylbenzene to form COF-LZU-1, and of TA with tris(4-aminophenyl)benzene, respectively. Thereby, the tridentate linker was dropcast on the HOPG substrate and the sample was placed in an autoclave. The linear linker was placed at the bottom of the autoclave and evaporated upon heating. $\text{CuSO}_4 \times 5 \text{H}_2\text{O}$ provided a limited amount of water vapor. The direct casting of both linkers on the substrate led to a much less ordered film.¹³⁴

The direct casting method was also applied to 1,3,5-triformylbenzene and various linear diamines with a length of up to three phenyl rings.¹²¹ Investigations of

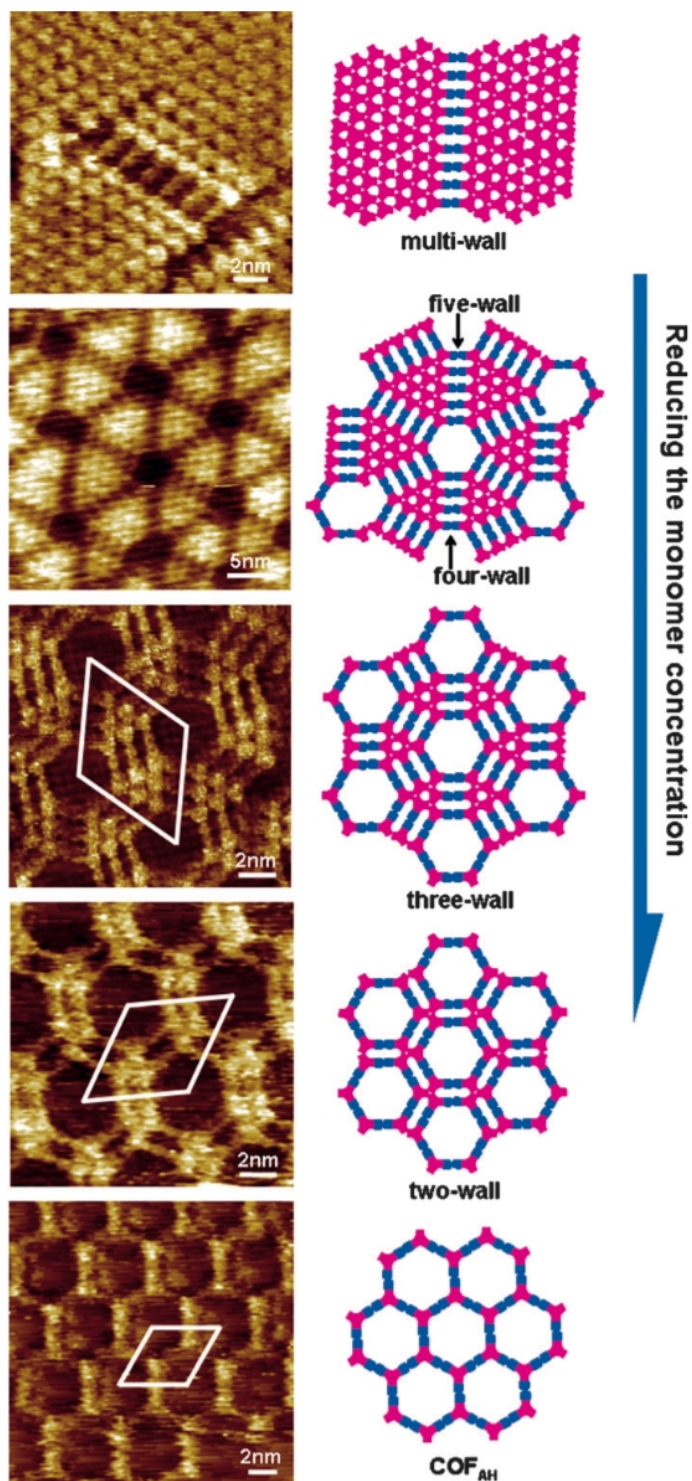


Figure 1.27: Concentration-induced structure evolution of a co-condensation reaction of ABBA and HHTP on HOPG at room temperature. Reproduced with permission from ref. 111. Copyright 2016 John Wiley and Sons.

the growth process of single layer COF LZU-1 on single layered graphene revealed a strong interaction between the substrate and the COF layer.¹³⁵ Moreover, COF layer growth on HOPG was performed by co-condensing 1,3,5-tris(4-aminophenyl)benzene with 2,3-dihydroxyterephthalaldehyde, 2,5-dihydroxyterephthalaldehyde, and the non-substituted aldehyde linker, respectively,¹⁹³ and for 1,3,5-tris(4-formylphenyl)benzene and benzidine.¹⁴⁹ Structures with higher defect concentrations were obtained for an azine COF layer from hydrazine and 1,3,5-tris(4-formylphenyl)benzene.¹⁸⁶

Imine COFs with porphyrins at the nodes were shown to form supramolecular assemblies with a perylene diimide derivative with the perylene guest being located in the tetragonal pores of the COF.²¹⁵ Imine-linked porphyrin COF layers were also grown on an iodine-modified Au(111) substrate with a mixture of Fe(III)-complexed and metal-free porphyrin used as nodes.²⁰⁷ Sun et al. investigated the host-guest interactions of COF-LZU-1 layers with coronene, copper phthalocyanine and fluorine substituted copper phthalocyanine. They found indications for a dynamic adsorption-desorption process of the guest molecules, and that the fluorine-substituted guest showed the strongest interaction with the COF host layer, due to hydrogen bonding interactions.¹³⁶

Condensation of tetrathiafulvalene tetraaldehyde and 1,4-phenylenediamine on HOPG resulted in the formation of (mainly double) layers of TTF-COF. This bilayer formation was attributed to the strong π - π interactions between the tetrathiafulvalene units.²³¹ Investigating the effect of a linker elongation in this COF, a reduced domain size and an increased number of trigonal pore structures was found for a COF layer built with the biphenyl amine benzidine serving as linear building block.²³⁰ The group of Blunt conducted structural investigations regarding the condensation of amino-functionalized porphyrin or Zn-porphyrins with TA, grown as single layered COF on a HOPG surface in the presence of water. They were able to show that the linkages in the formed 2D COF are not only made of imine bonds but that a large part of the bonds are non-conjugated hemiaminal linkages.²⁰⁵

Dual-linkage imine and boroxine COFs from amines and 4-formylphenylboronic acid or 3-formylphenylboronic acid were grown on HOPG as well. Notably, with the asymmetric linker 3-formylphenylboronic acid, clockwise and counterclockwise arrangements were formed that grew in phase-separated domains.¹⁷⁴

1.5.3.2 Thin Films

In an early study, Dichtel and coworkers were able to achieve the oriented growth of COF thin films on single-layer graphene, while the substrate was placed in the solvothermal reaction mixture. The grown COF crystallites were oriented perpendicular to the graphene layer. This synthesis was demonstrated for COF-5, TP-COF (from HHTP and pyrene-2,7-diboronic acid), and NiPcPBBA-COF (from 1,4-phenylenebis(boronic acid) and Ni octahydroxyphthalocyanine). In all cases, oriented smooth films were obtained that fully covered the substrates.⁷⁴ When transferring this method to a series of Zn-phthalocyanine COFs with boronic acid linkers of increasing lengths, they found that a solvent mixture of dioxane, MeOH, *N,N*-dimethylacetamide (DMA) and 1,2-dichlorobenzene (DCB) in 3 : 1 : 2 : 1 v/v ratio led to the formation of oriented crystalline films in all cases, while with the solvent mixture of only DMA/DCB crystalline, but unoriented films were formed.²⁰

A remarkably high degree of orientation of a COF film was reached with the complex solvent system described above and a diphenylbutadiyne boronic acid linker. Grazing incidence X-ray diffraction measurements indicated a mosaic spread below 0.2° and a correlation length in the stacking direction of 31 nm.²⁰ By changing the solvent system of the solvothermal COF synthesis towards a 1 : 3 MeOH : dioxane mixture, an oriented film of ZnPcPBBA was achieved. The film grew selectively on single-layered graphene but not on SiO₂, probably due to adsorption of the ZnPc units on the SLG prior to COF growth. This selectivity was used to grow COF islands on a substrate with an SLG pattern.⁹⁹

The formation of oriented films of BDT COF¹⁰⁶ made from HHTP and (4,8-diethoxybenzo[1,2-*b*:4,5-*b'*]dithiophene-2,6-diyl)diboronic acid, and TP-Por COF¹¹² made from HHTP and 5,15-bis(4-boronophenyl)porphyrin, was demonstrated by our group on ITO (indium doped tin oxide), nickel oxide (NiO), and MoOx, respectively. Applying a solvothermal reaction route with the substrates placed upside down in the reaction mixture, thin, well-oriented and porous films were obtained. GISAXS measurements confirmed the vertical alignment (relative to the substrate) of the 2D COF channels in these films. In an intriguing approach, Feldbluym et al. prepared unsupported smooth COF films at the solution/air interface.¹⁸³ For this purpose, the COF precursors, a benzene dithiophene carbaldehyde, and tris(4-aminophenyl)amine, were dissolved in *N,N*-dimethylformamide (DMF) and acetic acid was added. The obtained solution was transferred into a petri dish that was kept in a sealed container with H₂O-saturated atmosphere for 2-3 days; during

this time a film was grown on the liquid/gas phase interface. This film could be transferred to a substrate of choice. It was approx. 50 nm thick and rather rough and showed a slightly preferred orientation of the COF layers parallel to the liquid/air interface.

Thinner and smoother films were obtained when the initial synthesis mixture was first incubated at 100 °C for 24 h and the COF bulk material that was formed at that time was removed, and the film growth was repeated with the thus obtained supernatant. Bisbey et al. reported a continuous flow synthesis pathway for the synthesis of boronic ester COF thin films. With this method, crystalline oriented films were accessible with a higher film thickness than with the conventional solvothermal route. As the growth rates of the COF films under continuous flow conditions were found to be constant, an efficient control over the film thickness was possible.⁸¹

The growth of COFs as thin oriented films was shown to be highly advantageous for novel applications. For example, this was demonstrated by DeBlase et al. for the anthraquinone COF DAAQ-TFP made from 2,6-diaminoanthraquinone (DAAQ) and 1,3,5-triformylphloroglucinol (TFP) (we note that for the building block 1,3,5-triformylphloroglucinol, two different abbreviations, TPG and TFP are used in the literature). Initially, thick unoriented films of DAAQ-TFP COF powder immersed in a carbon black binder were prepared and investigated as a capacitive electrode material.²⁷⁴ The formation of oriented films of the same COF was later achieved by the slow addition of TFP in DMF to a solution of 2,6-diaminoanthraquinone (DAAQ) in DMF while an Au substrate was placed in the DAAQ solution. Films prepared with this method were 60-560 nm thick and oriented. Compared to unoriented films, the capacitance was significantly increased (see Section 1.6.4 for details).²⁹⁷

Solvothermally grown, oriented thin films of COF_{TFPy-PPDA} (from 1,3,6,8-tetrakis(*p*-formylphenyl)pyrene and 1,4-phenylenediamine) were applied as transport channel in an organic field-effect transistor.²³² Similarly, Chen et al. demonstrated a distinct increase of the photoresponse of oriented TT-COF films compared to randomly oriented material.¹⁰⁵

Smith et al. prepared COF-5 as a colloidal solution. By varying the concentration of the co-solvent CH₃CN, the particle size could be varied between 45 and 240 nm. From this, they were able to form films by simply evaporating solvent from the colloidal suspension. The films were free-standing, porous and >10 μm thick. Remarkably, grazing incidence X-ray diffraction revealed preferential orientation of the 2D COF layers perpendicular to the plane of the film, in contrast to the parallel orientation that is accessible *via* direct solvothermal growth.⁸³

Non-oriented COF films were prepared by the vapor-assisted conversion of COF precursors on a substrate. In this method, the COF precursors were dissolved in a solvent mixture and drop cast on a substrate that was placed in a desiccator together with a solvent reservoir. Smooth, homogeneous, but unoriented films of adjustable thickness were obtained; for details see also Section 1.5.2.5.⁵⁷ In an early study, Yang et al. prepared films of COF-1 and COF-5 on alumina discs applying the sonochemical synthesis method described in Section 1.5.2.4. A dense, homogeneous film was formed.³⁹ Selective growth of COF-366 (from tetrakis(*p*-aminophenyl)porphyrin and TA) on hexagonal boron nitride but not on silicon wafer was achieved *via* a solvothermal synthesis route.²⁰³

Wang et al. prepared COF-LZU-1 (from 1,3,5-triformylbenzene and 1,4-phenylenediamine) as a thin film on silicon by first modifying the substrate with an NH₂-terminated self-assembling monolayer. This substrate was then successively exposed to solutions of the linkers TFB and PDA, respectively. By repeating the linker exposure steps for up to four times, non-oriented rough films with a thickness of up to 25 ± 3 nm were obtained.¹²⁹ A related surface functionalization approach was used by Bao et al., who modified the surface of a glass or fused silica capillary column with polydopamine. Subsequently, they prepared a solution of both linkers for COF-5, BDBA and HHTP, and filled the polydopamine-modified glass capillary tube (featuring catechol groups) with this solution. Then the capillary was heated at 100 °C for 20 h and subsequently washed. By repeating the polydopamine and COF-5 deposition steps, an unoriented, rough film of COF-5 and polydopamine was formed on the capillary wall.⁷⁸

Niu et al. pre-synthesized the COF LZU-1 and prepared a suspension of this COF with a particle size over 300 nm. A capillary that was modified with glycidoxypropyltrimethoxysilane, featuring epoxy groups, was then filled with the COF suspension and heated at 70 °C for 4 h, leading to the formation of a rough film of COF-LZU1 attached to the capillary wall.¹³¹

Similarly, Qian et al. prepared a COF-modified fused silica capillary column first with 3-aminopropyltriethoxysilane and subsequently injected the pre-mixed COF linker solutions (1,3,5-triformylbenzene functionalized with chiral (+)-diacetyl-L-tartaric anhydride and 1,4-phenylenediamine, 2,5-dimethyl-1,4-phenylenediamine and benzidine) into the column, followed by heating at 90 °C for 4 h. These columns were then applied in chiral separation tasks.³⁰³ De la Peña Ruigómez et al. performed the room temperature synthesis of RT-COF-1 from solution using 1,3,5-tris(4-aminophenyl)benzene and 1,3,5-benzenetricarbaldehyde with *m*-cresol or DMSO as a solvent. Patterning the COF in the

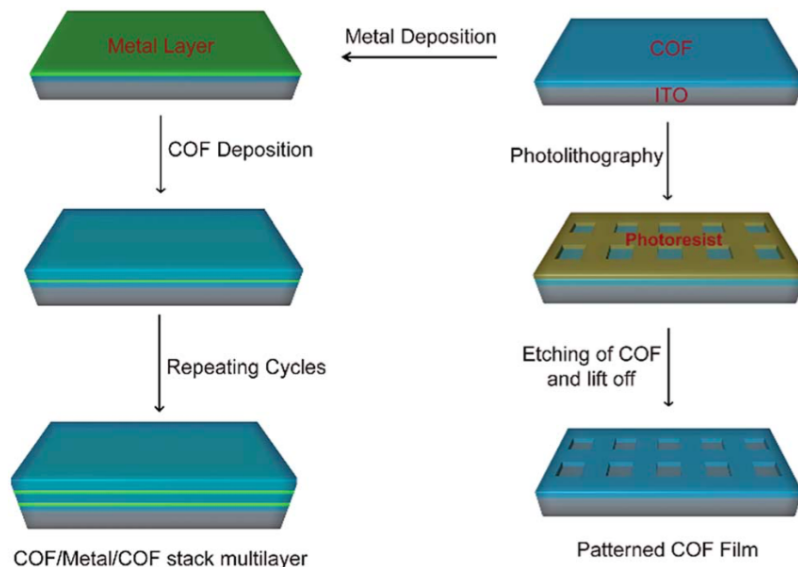


Figure 1.28: Schematic diagram of the processes for fabricating metal/COF stack multilayer *via* alternating physical deposition of metal materials and solvothermal deposition of COF (left) and for patterning thin films *via* photolithography and reactive ion etching (right). Reproduced from ref. 275 with permission of The Royal Society of Chemistry.

form of stripes was achieved using lithographically controlled wetting on an SiO_2 substrate, and as dots *via* ink-jet printing on SiO_2 and acetate paper, respectively. With both methods, rather rough, and with the inkjet method only partially covered COF coatings were achieved.¹⁴¹

Thin, oriented films of the ketoenamine COF TpPa-1 (also named DAB-TFP COF) from the linkers 1,3,5-triformylphloroglucinol and 1,4-phenylenediamine were prepared in a solvothermal synthesis route on ITO, FTO, silicon, and platinum by Lu and coworkers. Repeated deposition of Pt and COF layers was shown to be a suitable method for the preparation of Pt/COF multilayered structures. By coating a COF film on an ITO substrate with a photoresist and photolithographically patterning of this film followed by reactive ion etching of the COF layer, a COF film with square holes was obtained with a potential application for device fabrication (Figures 1.28 and 1.29).²⁷⁵

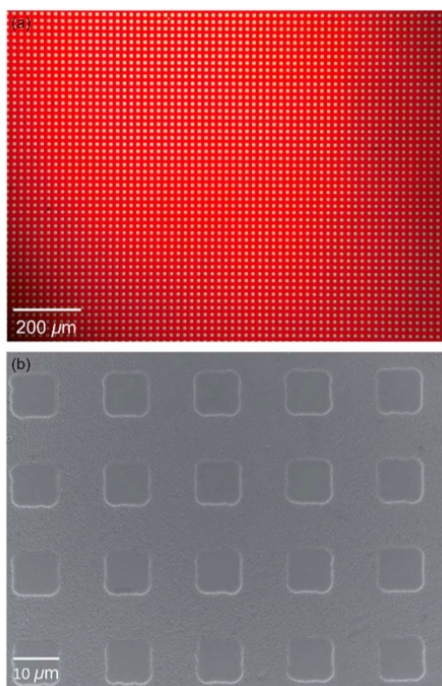


Figure 1.29: (a) Optical image and (b) SEM image of patterned COF thin film on ITO substrate. Reproduced from ref. 275 with permission of The Royal Society of Chemistry.

Wang et al. investigated the growth of thin films of COF-LZU1 on silicon substrates modified with (3-aminopropyl)triethoxysilane (APTES), octadecyltrichlorosilane (OTS), and on bare silicon with a native oxide layer of SiO₂. They found that below a certain monomer concentration, only amorphous material was grown as a film and that the crystallinity of the already deposited material increased over time in a direct conversion of amorphous material and non-oriented crystallites into a crystalline and oriented COF film.¹³³

1.5.3.3 Nanoparticles, Nanofibers and Hollow Structures

Generally, in most syntheses COFs precipitate as particle aggregates in the μm range, but for some systems, the formation of nanoparticles or the assembly of COF crystallites into fibrous or hollow spherical morphologies has been observed. Bai et al. reported the synthesis of COF nanoparticles prepared in a 3 d solvothermal synthesis from 1,3,5-triformylbenzene (TFB) and 2,4,6-tris(4-aminophenyl)-1,3,5-triazine (TAPP) (PI-3-COF) and 4,4-biphenyldiamine (PI-2-COF), respectively. Spherical COF particles with a size of ≈ 50 nm were obtained for PI-2-COF while PI-3-COF formed needles Both COFs were applied as hosts for drug delivery (see Section 1.6.7).¹³⁸

Smith et al. developed a synthesis method for colloidal boronic ester COFs (from the co-condensation of HHTP with 1,4-benzenediboronic acid, 4,4'-biphenylbis(boronic acid), 2,7-pyrenebis(boronic acid), and 4,4'-diphenylbutadiynebis(boronic acid)). They found that by using CH₃CN, a solvent that impedes the aggregation of the COF particles in the synthesis, nanoparticles are created that form a stable colloidal solution with the CH₃CN concentration determining the particle size. From these solutions, oriented films can be prepared⁸³ as described in Section 1.5.3.2. A COF made from the linkers 2,6-dihydroxynaphthalene-1,5-dicarbaldehyde (DHNDA) and TAPP was found to form nanofibers both in a solvothermal¹⁷⁸ and in a vapor-assisted solid state synthesis¹⁷⁹ (see also Section 1.5.2.5). In the solvothermal synthesis, a transformation of initially formed small COF particles into nanofibers was observed within the first 24 h of the reaction. Similar results were found for the vapor assisted synthesis reaction, but here the full conversion into the nanofibers took 48 h. The nanofibers were mostly branched with a diameter of 50-80 nm. In general, the nanofibers only had a low crystallinity, and low surface areas of 416 m² g⁻¹ and 280 m² g⁻¹ for the COF synthesized solvothermally and vapor-assisted, respectively.

A direct synthesis of COF nanofibers was achieved by microfluidic synthesis of MF-COF-1 made from TFB and 1,3,5-tris(4-amino-phenyl)benzene (Figure 1.30). The resulting COF consisted of fibers of ≈ 70 nm in diameter and the COF had a moderate surface area of 535 m² g⁻¹.¹⁴³

Hollow COF nanorods were prepared by the group of Banerjee, applying an indirect approach. They used ZnO nanorods as structural templates. The β -ketoenamine COF TpPa-1 (from 1,3,5-triformylphloroglucinol and 1,4-phenylenediamine) was grown in a solvothermal reaction on the surface of the ZnO rods, which were subsequently dissolved, yielding hollow COF nanorods that were approximately 200-300 nm in width and 750-1500 nm in length.²⁶⁵ The authors also found that the COF ThaTab, made of 2,5-dihydroxyterephthalaldehyde and 1,3,5-tris(4-aminophenyl)benzene, undergoes a ripening process after the initial crystallization to form large hollow spheres of 0.5 to 4 μ m in diameter.¹⁹¹

Additional COFs that grew as hollow spheres in conventional solvothermal routes include COF LZU-1,^{126,132} SIOC-COF-3 and SIOC-COF-4 (from the co-condensation of the hexaaldehyde linker 4',4''',4''''-nitriлотris([1,1'-biphenyl]-3,5-dicarbaldehyde) with PDA or benzidine),¹⁶⁹ and SIOC-COF-7 from 4,4''-bis(4-formylphenyl)amino-[1,1':4',1''-terphenyl]2'-5'-dicarbaldehyde and PDA.¹⁷⁰

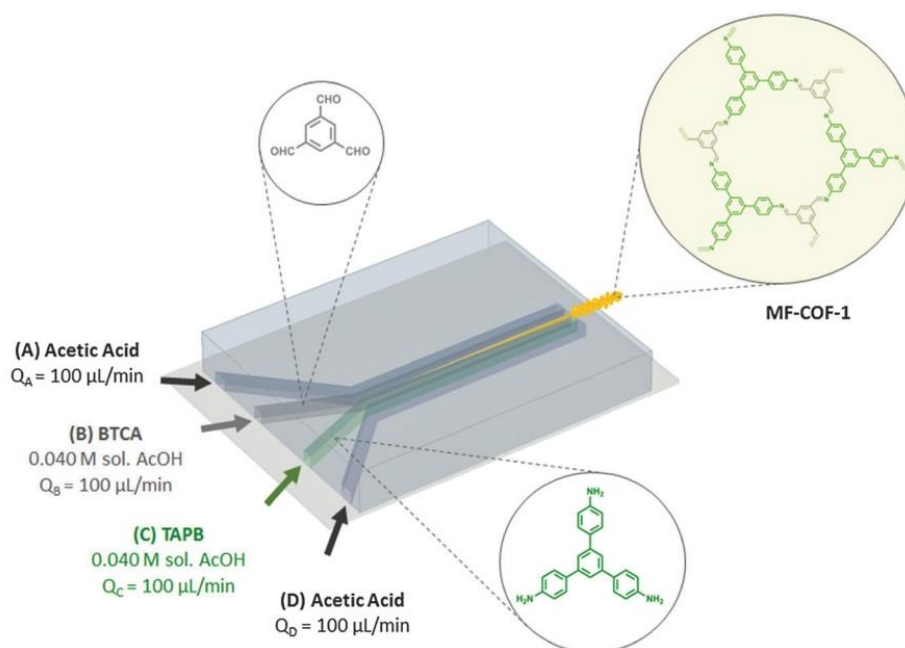


Figure 1.30: Microfluidic synthesis of MF-COF-1. Adapted from ref. 143 with permission of The Royal Society of Chemistry.

1.5.3.4 Composites

Nanoparticles in COFs. Covalent organic frameworks have been shown to serve as valuable components in composite materials. Hereby the COF has been used in various functions. One approach is the use of the porous COF structure as a scaffold for the encapsulation of a catalytically active material. This has been demonstrated for metal nanoparticles by Pachfule et al. They soaked the pores of the ketoenamine COF TpPa-1 (from 1,3,5-triformylphloroglucinol and 1,4-phenylenediamine) with a solution of $\text{HAuCl}_4 \times 3\text{H}_2\text{O}$. Upon addition of NaBH_4 , the Au(III) was reduced to yield Au(0) nanoparticles with an average diameter of 5 nm in the COF framework.²⁶³ Similarly, Pd(0) nanoparticles with an average diameter of 7 nm were created from Pd(OAc)_2 precursor in the pores of TpPa-1.²⁶⁴ Both composites were applied in catalytic reactions (see Section 1.6.3), but while the Au nanoparticle composite could be used repeatedly without changes in catalytic activity, the Pd particles underwent sintering already during the first catalytic cycles, which significantly decreased the catalytic conversion rate.

A similar strategy was applied with the ketoenamine COF TpPa-2, where 2,5-dimethyl-1,4-phenylenediamine is used as amine linker, to create CdS nanoparticles in the COF structure. For this purpose, a suspension of the COF in a solution of the precursor

$\text{Cd}(\text{OAc})_2$ in DMSO (as source for sulfur) was prepared. Upon heat treatment at 180 °C in an autoclave, CdS nanoparticles of 20-25 nm in diameter were generated in the COF sheet matrix, that were distributed in the COF sheet matrix. By varying the initial COF to $\text{Cd}(\text{OAc})_2$ ratio, composites with different COF to nanoparticle ratios were obtained, ranging from a 50 : 50 mixture to a 99% CdS material.²⁷⁷ For photocatalytic applications of these hybrid materials, see Section 1.6.3.

A composite of the COF TpBpy (made from 2,2'-bipyridine-5,5'-diamine (Bpy) and 1,3,5-triformylphloroglucinol (TPG)) with Pd nanoparticles was synthesized by using units of the Bpy linker that were pre-modified with PdCl_2 . The COF was formed upon co-condensation with TPG, and the Pd(II) was reduced *in situ* during COF synthesis to Pd(0) nanoparticles of 12 ± 4 nm in diameter in the COF matrix.²⁹² $\text{Co}_x\text{Ni}_y(\text{OH})_2$ nanoparticles were embedded in a nitrogen-rich COF made from tris(4-formylphenyl)amine and 1,4-phenylenediamine by suspending the COF in a solution of $\text{NiCl}_2 \times 6\text{H}_2\text{O}$ and/or $\text{CoCl}_2 \times 6\text{H}_2\text{O}$ at different ratios and subsequent reduction of the metal species with NaBH_4 . With this method, a variety of Ni : Co ratios was accessible with the metal species being mainly the M^{2+} species but indications for the presence of M^0 were also found. The composites were applied as electrocatalyst for the oxygen evolution reaction in water splitting.¹⁴⁶

The ketoenamine COF TpPa-1 decorated with magnetic Fe_3O_4 nanoparticles was created by adding TPG to NH_2 -surface functionalized Fe_3O_4 particles (to yield an aldehyde-terminated surface functionalization) and subsequent addition of TPG and PDA solution to these particles. This synthesis resulted in a branched morphology of the TpPa-1 COF with the Fe_3O_4 particles located at the tips of the COF agglomerates.²⁷² Gao et al. reported the immobilization of polymolybdic acid $\text{H}_3[\text{P}(\text{Mo}_3\text{O}_{10})_4]$ (PMA) in the 3D imine COF-300 (from terephthalaldehyde and tetrakis(4-anilyl)methane). For this purpose, the COF was stirred in a PMA solution for 24 h and washed subsequently. Mo contents of up to 16% were reached. The material was tested as catalyst for several olefin epoxidation reactions, but revealed a lower catalytic activity than bare PMA.²¹¹

Polymers and salts in COFs. In the pores of a COF film (on a gold substrate) made from DAAQ and TPG (DAAQ-TFP-COF), 3,4-ethylenedioxythiophene was electropolymerized *via* cyclic voltammetry. This polymer pore filling resulted in a significantly higher cycling stability and current response of the COF film in cyclic voltammetry.²⁹⁸ The ionic liquid 1-ethyl-3-methylimidazolium bis(trifluoromethylsulfonyl)imide was immobilized in the 3D COF-320 (from 4,4'-biphenyldicarboxaldehyde and tetrakis(4-anilyl)methane) by

mixing the two powders and subsequent heating to 90 °C. Embedded in the COF, the ionic liquid underwent no phase transition in the temperature range from -160 to 190 °C.²²⁵ The phosphonium salt ethyldiphenyl(4-vinylphenyl)phosphonium bromide was polymerized in the pores of TpBpy-COF (from TPG and 5,5'-diamino-2,2'-bipyridine) and the composite was subsequently treated with Cu(OAc) to establish Cu moieties at the bipyridyl units. The polymer was shown to have some flexibility in the COF pores, which was advantageous for the application of the composite in catalysis (cycloaddition of epoxides and CO₂).²⁹¹

COF-matrix composites. COF/polymer hybrid membranes have been prepared by casting a solution of COF and polymer mixture and subsequent evaporation of the solvent. Biswal et al. prepared COF-polybenzimidazole hybrid membranes with the COFs TpBD (from TPG and benzidine) and TpPa-1 (from TPG and 1,4-phenylenediamine), respectively (Figure 1.31). The membranes were chemically stable and showed a high gas permeability for H₂, CO₂, and CH₄. With these membranes, they achieved high hydrogen selectivities from gas mixtures, namely 82.7 for H₂/N₂ (with TpBD(40%)@PBI-BuI), up to 165.5 for H₂/CH₄ (with TpPa-1(40%)@PBI-BuI), and 3.9 H₂/CO₂ (with TpBD(40%)@PBI-BuI).²⁷⁰

The two COFs NUS-2 (from TPG and hydrazine) and NUS-3 (from TPG and 2,5-diethoxy-terephthalohydrazide) were first delaminated in a sonication step and subsequently mixed with the polymer Ultem, a poly(ether imide) or polybenzimidazole (PBI) to fabricate flexible membranes. Thereby, gas permeabilities were increased compared to the pristine polymers while the composites also featured improved gas selectivities. Specifically, for NUS-2@PBI membranes, a remarkably high H₂/CO₂ permselectivity of up to 31.4 under higher pressures (for 20 wt% NUS-2@PBI) could be achieved.²⁴⁷

In a different approach, CTF-1 (from 1,4-dicyanobenzene) was milled and sonicated to yield delaminated separate COF sheets in a stable suspension in water. This suspension was then mixed with a suspension of graphene oxide sheets in water and restacked by filtration, yielding COF-graphene oxide mixed membranes that showed very high H₂ permeabilities and H₂/CO₂ selectivities. For example, a membrane with an H₂ permeability of $1.7 \times 10^{-6} \text{ mol m}^2 \text{ Pa}^{-1} \text{ s}^{-1}$ featured an H₂/CO₂ selectivity of 17.4.³¹³

TpPa-2 COF (made from 2,5-dimethyl-1,4-phenylenediamine and TPG) containing mixed matrix membranes were prepared by mixing TpPa-2 with polysulfone, where a COF content of only 0.2 wt% significantly improved the performance of the membranes in removal of organic foulants from water, presumably due to the regular porous structure of the COF.²⁷⁸

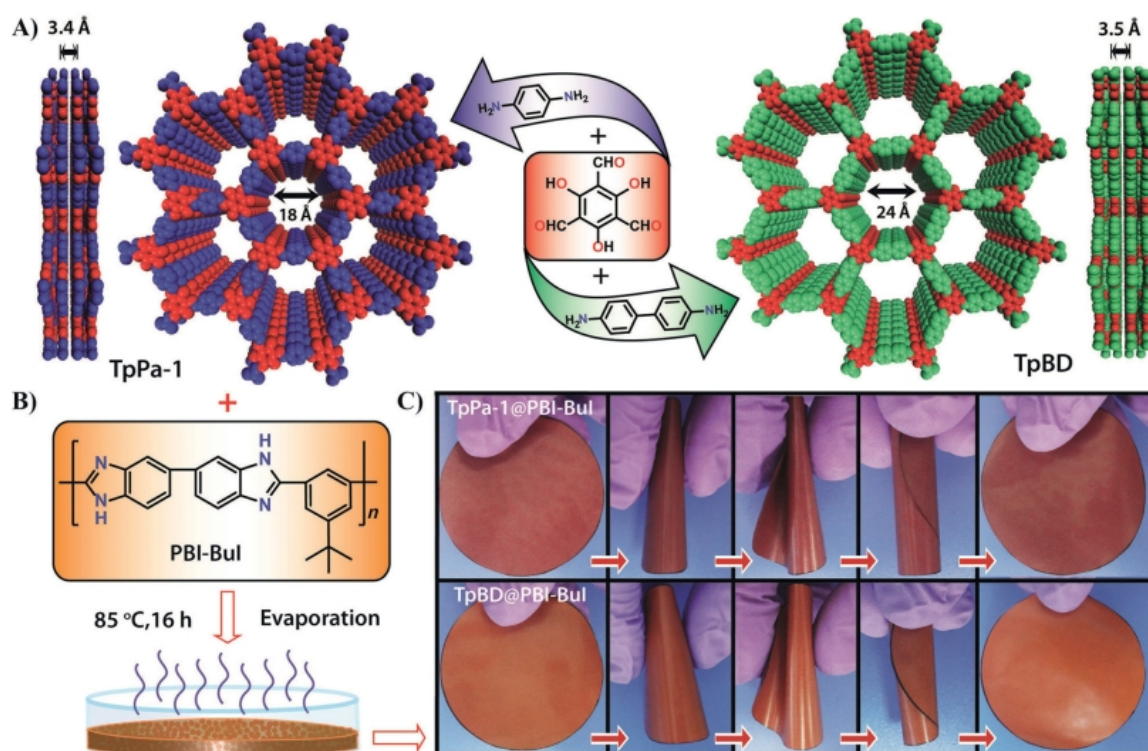


Figure 1.31: A) Schematic representations of the synthesis of COFs and their packing models indicating the pore aperture and stacking distances. B) Overview of the solution-casting method for COF@PBI-Bul hybrid membrane fabrication. C) Digital photographs showing the flexibility of TpPa-1 and TpBD(50)@PBI-Bul hybrid membranes. Reproduced with permission from ref. 270. Copyright 2016 John Wiley and Sons.

Another mixed matrix membrane was prepared from the azine linked COF ACOF-1 (from TFB and hydrazine) with the polymer Matrimid[®] and utilized for CO₂/CH₄ separation. The mixed COF and polymer membrane featured a higher CO₂ permeability than Matrimid alone.²⁵¹ Mixed matrix membranes were also prepared from sulfonic acid functionalized ketoenamine COFs COF NSU-9 (from TPG and 2,5-diaminobenzenesulfonic acid) and NUS-10 (from TPG and 2,5-diaminobenzene-1,4-disulfonic acid) blended with polyvinylidene fluoride for proton conduction (see Section 1.6.3 for details).²⁸²

A TpPa-1 COF blend with magnetic graphene (loaded with Fe) was used for the immobilization of trypsin. For that, glutaraldehyde was covalently attached to the COF which then featured aldehyde anchoring positions to covalently bind trypsin.²⁷¹ Methacrylate-functionalized TpPa-1 was pre-synthesized (by reacting TPG with methacrylic anhydride prior to COF synthesis) and then embedded in a polymethylmethacrylate matrix for chromatography, for details see Section 1.6.2)³⁰²

Several composites intended as membranes have been reported in which a COF was grown or attached as a coating on another functional material. For example, Lu et al. reported the modification of a porous α -Al₂O₃ substrate with the 3D imine COF-320, composed of tetrakis(4-anilyl)methane and 4,4'-biphenyldicarboxaldehyde. For this purpose, 3-aminopropyltriethoxysilane and 4,4'-biphenyldicarboxaldehyde were first used to establish an aldehyde functionalization at the Al₂O₃ substrate. The COF synthesis reaction was then performed under solvothermal conditions and created an ≈ 4 μ m thick COF film on the Al₂O₃ substrate. This material was applied in gas permeation experiments and showed moderate H₂ selectivities (2.5 for H₂/CH₄ and 3.5 for H₂/N₂).²²⁴

A different approach was pursued by Li et al. They first synthesized COF-1 in a conventional solvothermal synthesis and subsequently delaminated the COF sheets by sonication in dichloromethane. A macroporous α -Al₂O₃ substrate with a thin SiO₂-ZrO₂ layer was then coated with the COF sheets. With this method a very smooth and crack-free membrane was produced that featured a very high H₂ permeability of 1×10^{-6} mol m² Pa⁻¹ s⁻¹ but a low H₂/N₂ selectivity of up to 4.2.⁵¹

COF-MOF composite membranes were fabricated by Fu et al. by first growing solvothermally a COF-300 film (made from tetrakis(4-anilyl)methane and terephthalaldehyde) on a polyaniline membrane and subsequently, solvothermally growing a film of the MOF ZIF-8 or Zn₂(bdc)₂(dabco) from MOF synthesis mother liquors. These hybrid membranes showed excellent performance in gas separation. They featured H₂/CO₂ selectivities of 12.6 for a [COF-300]-[Zn₂(bdc)₂(dabco)] composite and 13.5 for a [COF-300]-[ZIF-8] composite.²¹⁰

Using a sonochemical synthesis, Yoo et al. coated carbon nanotubes and graphene flakes with COF-5. In CO₂ adsorption experiments, the COF-5 coated carbon nanotubes showed a higher CO₂ uptake of 1.42 wt% compared to bulk COF-5 (1.25 wt%). However, the CO₂ uptake was lowered in comparison to bare COF-5 when it was coated on graphene.⁷⁷ Recently the authors reported the use of COF coated carbon nanotubes for trapping polysulfide species in lithium-sulfur batteries. In their study, they grew COF-5 and COF-1 solvothermally on carbon nanotubes. In the lithium sulfur batteries, the COF-1 coated structures were placed between the sulfur cathode and a polyethylene separator membrane and allowed for the enhanced deposition/dissolution of Li₂S species, thereby improving the performance of Li-S cells.⁴⁴ For more details see Section 1.6.4.

Amino-functionalized multi-wall carbon nanotubes were coated with COF_{TTA-DHTA} (from 4,4',4''-(1,3,5-triazine-2,4,6-triyl)trianiline and 2,5-dihydroxyterephthalaldehyde) in

a solvothermal reaction. The resulting composite was investigated regarding its performance as capacitive electrode material, see Section 1.6.4.¹⁹⁴

The ketoenamine COF TpBD (from TPG and benzidine) was used as a shell for Fe_3O_4 nanoparticles. This material was tested for its photothermal conversion efficiency in water, for potential therapeutic applications. Upon irradiation with a 785 nm laser, the COF coated particles featured a high photothermal conversion efficiency of 21.5%.²⁸⁵ Fe_3O_4 particles with a shell of TpBD COF were also applied in water purification (see Section 1.6.2).²⁸⁶ and Fe_3O_4 particles with a shell of an imine-linked COF made from terephthalaldehyde and 1,3,5-tris(4-aminophenyl)benzene were applied in the enrichment of peptides (see Section 1.6.2).¹⁸⁸

Similarly, the ketoenamine COF TpPa-1 was solvothermally grown on Fe_3O_4 nanoparticles, which were then applied in glycopeptide enrichment.²⁷³ Au nanoparticles of 15 nm in diameter were coated with polyvinylpyrrolidone (PVP) to facilitate their encapsulation into COF particles and subsequently introduced in a solvothermal COF synthesis of 1,3,5-tris(4-aminophenyl)benzene and 2,5-dimethoxyterephthalaldehyde. With this strategy, spherical COF particles containing one or more Au nanoparticles were obtained. This synthesis pathway worked also well for PVP-modified 50 nm Au nanoparticles, Au nanorods and 3.8 nm Pt nanoparticles.¹⁹⁶ In another study, a nanofibrous imine-linked COF from 2,6-dihydroxynaphthalene-1,5-dicarbaldehyde and 2,4,6-tris(aminophenyl)pyridine was coated on graphene oxide.¹⁷⁹

Mullangi et al. utilized the highly hydrophobic character of two nitrogen-rich COFs (IISERP-COF 2 from PDA and tris(4-formylphenyl)amine and IISERP-COF 4 (from TA and TAPP) to prepare functional coatings. By coating the COFs on paper or cloth, highly hydrophobic, thus self-cleaning materials were obtained.¹⁴⁷ The crystalline triazine framework TriCF (from melamine and cyanuric chloride) was used as additive in poly- α -olefin (PAO)-10 oil. The resulting oil blend featured an improved tribological performance in steel-steel and steel-copper systems.³¹⁴

The numerous examples for the use of COFs serving as a component in composites discussed in this chapter illustrate the advantages provided by COFs in combination with other materials due to their regular, porous structure and their modular synthesis. This becomes particularly apparent in the fields of catalysis and membrane separations, especially those based on single 2D COF sheets obtained by sonication.

1.6 Properties and Applications

1.6.1 Storage and Separation of Gases

The gas storage and separation performance of COFs has been investigated for a broad range of structures. Detailed reviews of this field are given by Kalidindi et al.³²⁹ for H₂ and by Zeng et al.³³⁰ for CO₂. In the following, a selection of COFs with high storage capacities is presented and trends as well as important factors influencing the gas storage capacities are discussed. Hydrogen is an important alternative energy source for the ‘post-carbon’ future, especially for the replacement of conventional fuel in cars. For its application, efficient storage methods are needed that offer high H₂ storage capacity and are based on lightweight materials. Covalent organic frameworks with their regular porous structure and large surface areas were seen as promising candidates, and thus hydrogen storage was one of the first applications investigated with COFs.

Furukawa and Yaghi studied the gas sorption behavior of different 2D and 3D COFs with boroxine and boronic ester linkages. They found very high values for the adsorption of hydrogen at 77 K and 35 bar in the 3D structures COF-102 (72.4 mg g⁻¹) and COF-103 (70.5 mg g⁻¹), and substantially lower capacities for the 2D structures (14.8 mg g⁻¹ for COF-1, 35.8 mg g⁻¹ for COF-5, 22.6 mg g⁻¹ for COF-6, 35.0 mg g⁻¹ for COF-8, and 39.2 mg g⁻¹ for COF-10). Within the group of 2D COFs, the H₂ uptake did not linearly increase with the pore volume when the pore diameter exceeded the microporous range, an effect that was also found for methane storage, but not for CO₂. Thus, micropores were seen to be favorable for high hydrogen and methane storage capacity.³³¹

Two imine and boroxine dual linkage 3D COFs were synthesized by Li et al. from 1,3,5,7-tetraaminoadamantane with 4-formylphenylboronic acid (DL-COF-1) and 2-fluoro-4-formylphenylboronic acid (DL-COF-2), respectively. These COFs exhibited high gas sorption performance of 2.09 wt% of H₂ (at 77 K and 1 bar), 26.7 wt% of CO₂ (at 273 K and 1 bar), and 2.57 wt% of CH₄ (at 273 K and 1 bar) for DL-COF-1 and 1.73 wt% of H₂ (at 77 K and 1 bar), 21.8 wt% of CO₂ (at 273 K and 1 bar), and 2.10 wt% of CH₄ (at 273 K and 1 bar) for DL-COF-2.¹⁷³

The gas storage ability of COFs has also been addressed in several theoretical studies. Particular attention has been focused on the introduction of metal species into the COF for improved H₂ or CO₂ storage, using transition metals,³³² as well as Li, Na, K³³³ and Ca,^{334,335} with Li demonstrating to be a highly promising candidate.³³⁶⁻³³⁸ The so-called

spillover effect, in which the hydrogen molecule dissociates at the metal site followed by migration of hydrogen atoms to the substrate (the COF), which results in chemisorption of hydrogen, can substantially increase the hydrogen storage capacity of a porous material and has been investigated thoroughly in theoretical investigations.³³⁹⁻³⁴³

Detailed discussions of theoretical gas sorption studies in COFs can be found in Kaldindi et al., who reviewed the hydrogen storage prospects of COFs and their metal composites,³²⁹ and in the review by Zeng et al. about CO₂ capture in COFs, mentioned above.³³⁰

Doping of the azine COF AB-COF (made from hydrazine and 1,3,5-triformylbenzene) with Zn enhanced the CO₂ uptake at 273 K from 3.38 mmol g⁻¹ (28 wt%) to 4.68 mmol g⁻¹ (35 wt%), and with Li a value of 4.33 mmol g⁻¹ (35 wt%) was reached.²⁵²

A spiroborate COF obtained from diol-functionalized macrocycles and trimethylborate features negative ionic centers. When Li⁺ is introduced as the counterion in the COF, high gas storage capacities can be observed for H₂ (3.11 wt% H₂ at 77 K and 1 bar) and CH₄ (4.62 wt% CH₄ at 273 K and 1 bar).²⁸ In contrast, a 3D boronic acid COF with dehydrobenzoannulene units that can complex metals was modified with Ni to achieve a COF with a high BET surface area of 4763 m² g⁻¹, but without improvement of the capacity or selectivity for ethylene and ethane upon metalation.¹¹⁸

In a hydrothermal synthesis, ketoenamine COFs were synthesized that featured high CO₂ storage capacities at 273 K and 1 bar (TpBpy: 73 cm³ g⁻¹, DAAQ: 82 cm³ g⁻¹ and TpBD: 95 cm³ g⁻¹). The COF TpBpy also had a high H₂ storage capacity of 108 cm³ g⁻¹ at 77 K and 1 bar.²⁶⁶

Among the imine-based COFs, very high CO₂ capacities were found for the microporous β -ketoenamine COF TpPa-1, prepared from TPG and PDA in a microwave reaction (21.8 wt% at 273 K and 1 bar)²⁶⁹ and for COF-JLU2, also a microporous β -ketoenamine COF, built from TPG and hydrazine that was able to store up to 21.7 wt% CO₂ at 273 K and 1 bar.²⁵⁸ Furthermore, this latter COF features a high H₂ storage capacity of 1.6 wt% at 77K and 1 bar.²⁵⁸ The mixed boroxine and imine COF NTU-COF-2 from the building blocks HHTP, 4-formylphenylboronic acid and 1,3,5-tris(4-aminophenyl)benzene features a high H₂ uptake of 1.55 wt% at 77 K and 1 bar but only a moderate CO₂ capacity of 10.2 wt% at 273 K and 1.0 bar.¹⁷²

The “brick-wall” COF from PDA and 4,4',4''-(1*H*-benzo[*d*]imidazole-2,4,7-triyl)tribenzaldehyde reported by Cai et al. features a CO₂ capacity of 3.95 wt% at 273 K and of 40.43 wt% at 195 K, due to the nitrogen-rich COF backbone.¹⁵⁸ COFs

with ETTA as linker showed very high CO₂ (273 K, 1 bar) and H₂ (77 K, 1 bar) capacities of 19.8 wt% and 1.66 wt% for SIOC-COF-5 (from ETTA and [1,1'-biphenyl]-3,3',5,5'-tetracarbaldehyde) and 13.9 wt% and 1.79 wt% for SIOC-COF-6 (from ETTA and 4,4',4'',4'''([1,1'-biphenyl]-4,4'-diylbis(azanetriyl))tetrabenzaldehyde), respectively.²³⁴ Zhai et al. observed an increased CO₂ uptake with an increasing fraction of triarylamine units in a series of imine COFs, with the highest values for a COF made only from triarylamine core building blocks (TFPA-TAPA-COF from tris(4-formylphenyl)amine and tris(4-aminophenyl)amine, 5.2 and 10.5 wt% at 1 bar and 298 and 273 K, respectively).

For frameworks where only one of the two components featured a triarylamine core, lower CO₂ capacities were found (BTMA-TAPA-COF from tris(4-aminophenyl)amine and 4,4',4''-boranetriyltris(2,3,5,6-tetramethylbenzaldehyde); 4.5 and 8.4 wt% at 298 and 273 K; TFPA-TAPB-COF from tris(4-formylphenyl)amine and 1,3,5-tris(4-aminophenyl)benzene; 3.3 and 6.1 wt% at 1 bar and 298 and 273 K, respectively). The triarylamine-free COF TFPB-TAPB-COF (from 1,3,5-tris(4-aminophenyl)benzene and 1,3,5-tris(4-formylphenyl)benzene) showed the lowest capacities (1.2 wt% at 298 K and 2.0 wt% at 273 K).¹⁴⁸ Incorporation of the 4,7-diaminobenzo[1,2,5]thiadiazole unit into the structure of COF-LZU-1 (made with 1,3,5-triformylbenzene and 1,4-phenylenediamine) yielded the TH-COF-1 with a drastically increased CO₂ capacity at 1 bar of 12.8 wt% and 9.7 wt% at 273 and 298 K, respectively (COF-LZU-1: 4.7 wt% and 4.2 wt%).¹²⁰

Benzobisoxazole-linked COFs featured a high CO₂ uptake with 15.1 wt% at 273 K and 1.2 bar for the COF BBO-COF-1 from TFB and 2,5-diamino-1,4-benzenediol dihydrochloride. When the larger aldehyde linker 1,3,5-tris(4-formylphenyl)benzene was used, a higher BET surface area was reached, but the CO₂ capacity was only 112.3 mg g⁻¹, showing the benefit of a higher nitrogen density in the framework with a smaller aldehyde linker.³¹⁷ The ionic benzimidazolium units in the COF PyTTA-BFBI*m*-iCOF, synthesized from the building blocks 4,4',4'',4'''-(pyrene-1,3,6,8-tetrayl)tetraaniline and 5,6-bis(4-formylbenzyl)-1,3-dimethyl-benzimidazolium bromide, drastically increased the CO₂ capacity of this COF to reach 93 and 177 mg g⁻¹ at 1 bar and 298 and 273 K, respectively. In comparison, a COF lacking the ionic sites only reached capacities of 36 mg g⁻¹ at 298 K and 65 mg g⁻¹ at 273 K and 1 bar.²²⁶

Postsynthetic modification can influence the CO₂ capacity but the effect depends greatly on the respective functionalization. For example, Jiang and coworkers synthesized a COF from a phthalocyanine amine and terephthalaldehyde and a COF series in which the unfunctionalized aldehyde was mixed with 2,5-dihydroxyterephthalaldehyde. Upon post-

synthetic modification of the OH groups with succinic anhydride, the channel walls were decorated with COOH groups. This introduction of COOH functional groups increased the CO₂ capacity for all members of the series. Most drastically, while the CO₂ capacity was only 3.5 wt% at 298 K for the 100% OH functionalized COF ($S_{\text{BET}} = 1284 \text{ m}^2 \text{ g}^{-1}$), it increased up to 7.6 wt% at 298 K for a 100% COOH functionalized COF that has a BET surface area of only $364 \text{ m}^2 \text{ g}^{-1}$.²¹³

A high degree of pore functionalization can also reduce the CO₂ capacity if the decrease in porosity overrides the effect of enhanced interactions of the newly introduced groups with CO₂. Postsynthetic modification of the COF described above (from a phthalocyanine amine and terephthalaldehyde mixed with 2,5-dihydroxyterephthalaldehyde) with the acyl chloride 4-phenylazobenzoyl chloride led to a remarkable CO₂ storage capacity of 20.7 wt% at 273 K and 11.5 wt% at 298 K and 1 bar in a COF that featured 25% modification, while higher amounts of functionalization decreased again the capacity. Similarly, the CO₂/N₂ selectivity in this COF series was at maximum for 25% modification (78 and 111 at 1 bar and 273 and 298 K, respectively).³²⁴

The same trend was observed in a structural COF series, similar to the one described above, but with 2,5-bis(2-propynyloxy)terephthalaldehyde as a linker, which was later functionalized with azide compounds with different substituents. Functionalization with MeOAc, AcOH, EtOH, and EtNH₂ was performed and the maximum CO₂ capacity was found at 50% functionalization in all cases (Figure 1.32).²²⁰

This example also illustrates that the CO₂ capacity is typically increased for structures that allow for specific interactions and not only dependent on the BET surface area, because of the capability of nitrogen and oxygen to engage in strong dipole-quadrupole interactions with CO₂.

This structure-property trend was also validated for N2-COF (from TPB and benzidine) and N3-COF from TPB and 2,4,6-tris(4-aminophenyl)-1,3,5-triazine, whose gas sorption ability was investigated by Bai et al. While the N2-COF had a higher BET surface area than the N3-COF ($1496 \text{ m}^2 \text{ g}^{-1}$ vs. $1142 \text{ m}^2 \text{ g}^{-1}$, its CO₂ capacity was lower ($92 \text{ cm}^3 \text{ g}^{-1}$ compared to $101 \text{ cm}^3 \text{ g}^{-1}$ for the N3-COF).¹³⁹

An important property of porous materials closely related to the capacity for CO₂ is their selectivity in the adsorption of CO₂ from gas mixtures. This property plays a major role in Carbon Capture and Sequestration (CCS) that is done either as post-combustion CO₂ capture in power plants or *via* direct sequestration from the air. On the other hand, a high CO₂/H₂ selectivity enables the use as a pre-combustion absorbent for

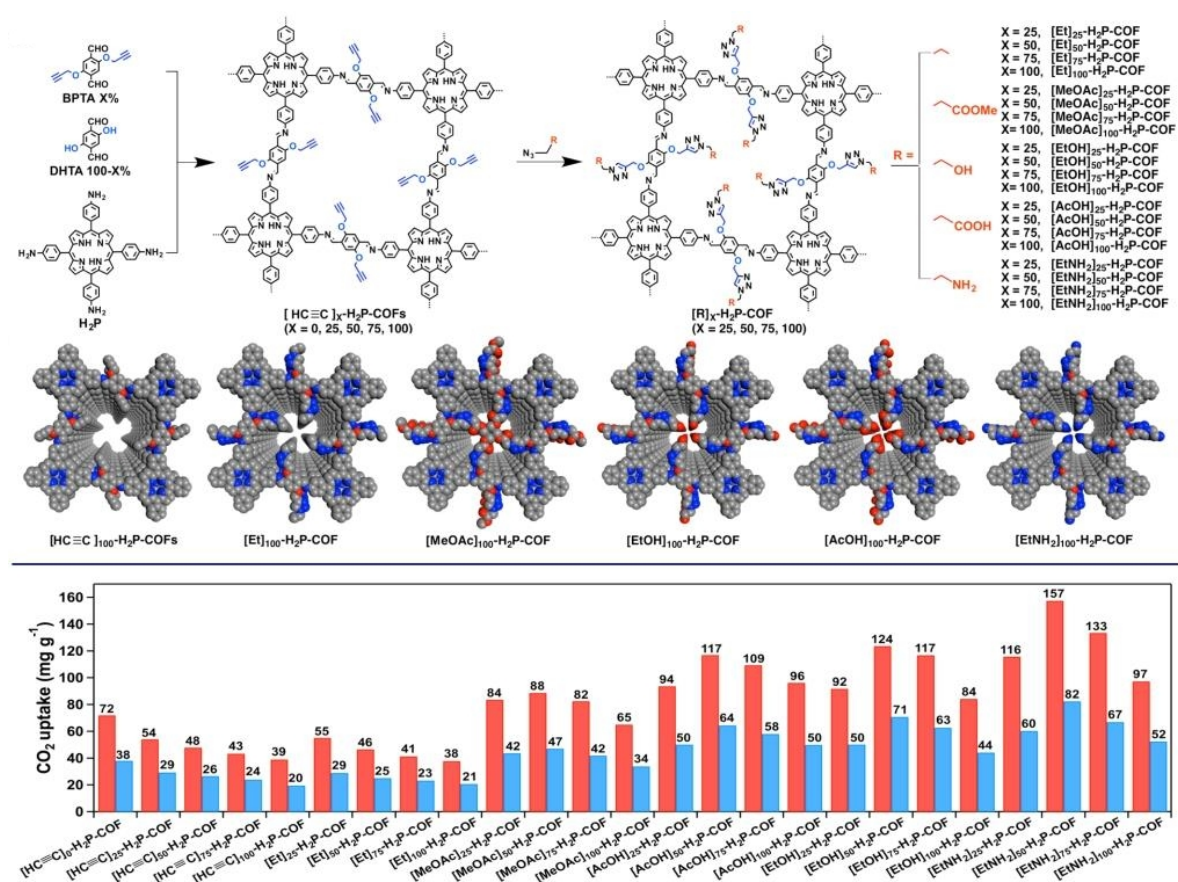


Figure 1.32: Synthesis and functionalization of H₂P-COFs, carbon dioxide adsorption capacity of the COFs at 273 (red) and 298 K (blue) and 1 bar, respectively. Adapted with permission from ref. 220. Copyright 2015 American Chemical Society.

CO₂. Moreover, pressure swing adsorption on porous solids is one of the main techniques in industrial methane enrichment for biogas production. Thereby, a high CO₂/CH₄ selectivity is desired.³⁴⁴ The above separation tasks have been studied for a range of COFs.

Incorporation of functional polar groups increases the CO₂ uptake in COFs, as described above, and similarly, it increases the CO₂ selectivity in CO₂/N₂ mixtures. Accordingly, enhanced selectivity was found for the aforementioned COF-JLU2, made from 1,3,5-triformylphloroglucinol and hydrazine hydrate (77, determined on the basis of initial slope calculations in the pressure range of 0 to 0.1 bar)²⁵⁸ and for the 100% COOH functionalization of [HO₂C]100%-H₂P-COF, made from phthalocyanine amine and terephthalaldehyde mixed with 2,5-dihydroxyterephthalaldehyde and subsequent modification with succinic anhydride (77 determined from ideal adsorbed solution theory (IAST) with CO₂/N₂ (15 : 85 v/v) at 298 K and 1 bar).²¹³ The CO₂/N₂ selectivity of the brick wall

COF (from PDA and 4,4',4''-(1*H*-benzo[*d*]imidazole-2,4,7-triyl)tribenzaldehyde was 68 at 273 K.¹⁵⁸

High methane uptake was measured (at 273 K and 1 bar) for ACOF-1 (an azine COF built from TFB and hydrazine), with 1.15 wt%,²⁵⁰ and Hex-COF-1 (from an hexaphenylbenzene aldehyde linker and hydrazine) with 2.3 wt%.²⁴⁸ The aforementioned framework COF-JLU2, built from TPG and hydrazine showed an even higher methane storage capacity of 3.8 wt% at 273 K and 1 bar.

Compared to the above nitrogen-containing COFs, the methane capacity in 2D boron-based COFs was lower (0.59 wt% for CoPc-BPDA COF, built from 4,4'-biphenylboronic acid and a copper phthalocyanine linker),¹⁰⁰ but comparable to ACOF-1 for TD-COF-5 (a boronic ester COF derived from 1,4-benzenediboronic acid and hexahydroxytriptycene) with 1.07 wt%. It was reasoned that due to the triptycene units in TD-COF-5, the boronic ester groups are not stacked in flat sheets but point to the pore surface which allows for better interactions with guest molecules.⁹⁶ COF TpAzo (from TPG and 4,4'-azodianiline) features an azo group in the linear linker. It has a relatively large BET surface area for a TPG-containing COF (1286 m² g⁻¹) and good gas storage and separation properties. It showed a high methane uptake of 1.12 wt% at 1 bar and 273 K, but also a high selectivity for CO₂/N₂ (127) and CO₂/CH₄ (39) at 273 K, demonstrating the effect of both high microporosity for gas sorption and azo groups for CO₂ separation tasks, respectively.²⁹⁴

The imide-linked PI COF (with the building blocks pyromelitic dianhydride and tris(4-aminophenyl)amine was tested as adsorbent for SO₂. It was able to store up to 41 wt% SO₂ at 298 K and 1 bar. Incorporation of the truncating monofunctional building block 4-[(dimethylamino)methyl]aniline resulted in a distinct decrease of BET surface area, but only a slightly reduced SO₂ sorption capacity, indicating a favorable interaction of the dimethylamino groups of the truncated sites with SO₂.³⁰⁶

The dual-pore COF SIOC-COF-7 (from 4,4''-bis(4-formylphenyl)amino)-[1,1':4',1''-terphenyl]2',5'-dicarbaldehyde and 1,4-phenylenediamine) was found to grow as hollow spheres in a conventional solvothermal synthesis route and tested for iodine vapor sorption. The COF particles were able to adsorb as much as 481 wt% of iodine at 348 K and 1 bar, with a large fraction of the capacity being attributed to the filling of the inner void of the hollow spheres (Figure 1.33). Similarly, when a solution of iodine in hexane was applied, the COF spheres adsorbed the iodine from the solution with a capacity of 127 wt%.¹⁷⁰

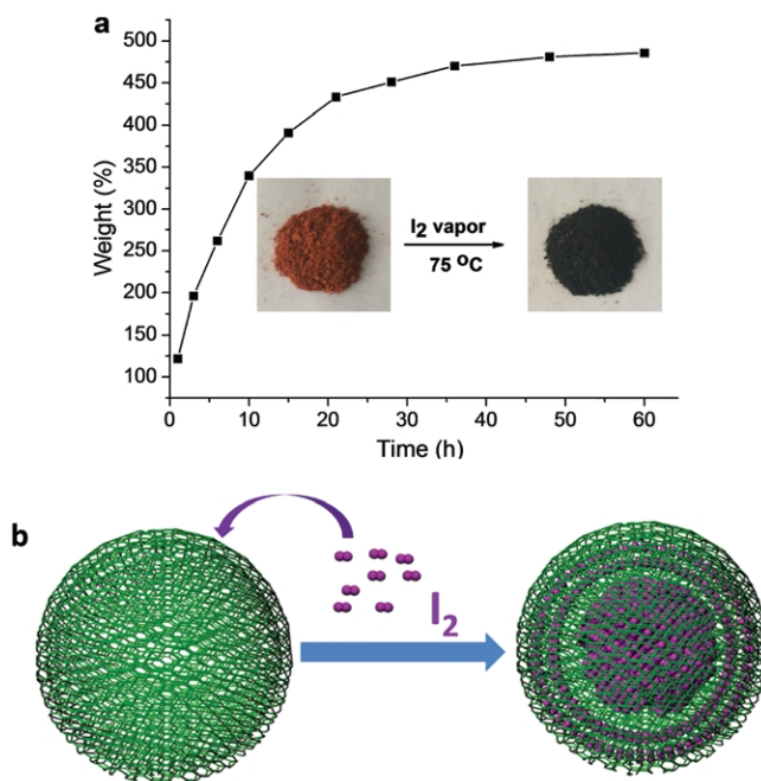


Figure 1.33: (a) Gravimetric uptake of iodine in SIOC-COF-7 hollow microspheres as a function of time at 75 °C. (b) Illustration of iodine capture in the spherical COF. Reproduced from ref. 170 with permission of The Royal Society of Chemistry.

A high separation selectivity for propane and C₂ hydrocarbons over CH₄ was found for the microporous 3D boronic ester COF made from tetrakis(4-dihydroxyborylphenyl)methane and 1,2,4,5-tetrahydroxybenzene.⁶⁸

The storage capacity and separation performance for CH₄ and C₂H₆ in a series of nitrogen-rich COFs derived from the co-condensation of TFB with the amines tris(4-aminophenyl)amine (N-COF), 1,3,5-tris(4-aminophenyl)benzene (P-COF), and TAPP (T-COF) was investigated.

T-COF showed the highest uptakes (at 298 K and 1 bar) (5.31 mmol g⁻¹ C₂H₆ and 0.78 mmol g⁻¹ CH₄) in agreement with its higher BET surface area of 1149 m² g⁻¹ (N-COF: 692 m² g⁻¹, CH₄ uptake 0.63 mmol g⁻¹, C₂H₆ uptake 3.09 mmol g⁻¹) (P-COF: 435 m² g⁻¹, CH₄ uptake 0.36 mmol g⁻¹, C₂H₆ uptake 2.64 mmol g⁻¹).

In contrast, the C₂H₆/CH₄ adsorption selectivity from an equimolar mixture of these two gases was found to be highest for N-COF with a selectivity of 18.8 (P-COF 12.1, T-COF 10.0).¹⁴⁰

A range of COFs was used as a component for the preparation of membranes that were afterwards applied in separation tasks. A detailed description of these membranes including their performance is given in Section 1.5.3.4.

Ketoenamine COFs prepared by the ‘terracotta process’ described in Section 1.5.2.3 were tested for applications in water sorption for dehumidification tasks. They featured high water capacities at 298 K and 1 bar of 52 wt% ($649 \text{ cm}^3 \text{ g}^{-1}$), 49 wt% ($608 \text{ cm}^3 \text{ g}^{-1}$), and 61 wt% ($756 \text{ cm}^3 \text{ g}^{-1}$) for TpPa-1, TpAzo, and TpBD, respectively. The highest uptake was achieved for the COF TpBpy from the building blocks TPG and a bipyridyl amine with 78 wt% ($974 \text{ cm}^3 \text{ g}^{-1}$).²⁶⁷ These values were higher than for solvothermally-synthesized ketoenamine COFs ($549 \text{ cm}^3 \text{ g}^{-1}$ for TpPa-1, $508 \text{ cm}^3 \text{ g}^{-1}$ for TpAzo, $181 \text{ cm}^3 \text{ g}^{-1}$ for TpBD).¹⁹² and the azine-linked AB-COF (41 wt%).²⁵²

The ketoenamine COF TpBD was prepared as coating in a gas chromatography capillary column in a room temperature synthesis. With this coating, separation of a range of small organic molecules including octane and nonane and α -pinene/ β -pinene was achieved with high resolution.²⁸⁴ Separation of enantiomers was achieved by using chiral ketoenamine COFs obtained from a TPG linker, modified with chiral (+)-diacetyl-L-tartaric anhydride and linear amines. The COFs were able to separate racemic mixtures of compounds like (\pm)limonene, (\pm)-1-phenyl-1-propanol or (\pm)-methyl lactate with large separation factors and high resolution.³⁰³

1.6.2 Storage and Separation from Solution

The large pore sizes of COFs make them suitable for the sorption and separation of larger molecules from solution, a field of application that has recently attracted increasing attention. Niu et al. applied the COF-LZU-1 (from PDA and TFB) in electrochromatography. They first modified a fused silica chromatography column with glycidoxypropytrimethoxysilane as anchoring moiety and subsequently prepared a layer of COF-LZU-1. The capillary was able to separate benzene and several alkylbenzenes with a high reproducibility. Separations of mixtures of polyaromatic hydrocarbons or aniline derivatives were also demonstrated.¹³¹

In a similar way, Bao et al. utilized COF-5 as the stationary phase in electrochromatography. They modified a fused silica chromatography column with polydopamine anchoring groups and a thin layer of COF-5 as the stationary phase. This column was successfully applied in electrochromatographic separation of methylbenzenes, naphtha-

lene, and 4-methylbiphenyl. For the latter two compounds, peak tailing was observed that indicated strong π - π -interactions of these analytes with the COF-5 stationary phase.⁷⁸

We recently reported the postsynthetic reduction of NO_2 groups to the primary amines in the COF TpBD(NO_2)₂, synthesized in the co-condensation of TPG and 3,3'-dinitrobenzidine. Subsequently, these NH_2 -groups were further modified with acetic anhydride to yield the corresponding amides. As ketoenamine COFs are very stable in acidic environments, they could be applied for the task of lactic acid adsorption from aqueous solution. Here, the amino-functionalized COF, TpBD(NH_2)₂ showed the highest lactic acid capacity and a high uptake of up to 6.6 wt% was achieved (Figure 1.34).²⁸⁸

The task of dye removal from solution was addressed with the imide-linked COF TS-COF-1 (from pyromellitic dianhydride and 1,3,5-tris(4-aminophenyl)triazine). It showed an exceptionally high capacity of 169 wt% for the adsorption of methylene blue dye. This was attributed to the combination of the high density of heteroatoms in the pore walls, the high BET surface area of $1484 \text{ m}^2 \text{ g}^{-1}$ and the large pore volume (pore diameter of 3.3 nm).³⁰¹

TpPa-2 COF/polysulfone mixed matrix membranes were applied for water purification and showed a retention of organic foulants of over 90%.²⁷⁸ The ketoenamine COFs TpBD (from benzidine and TPG) and TpTD (from terphenyl amine and TPG) were prepared as self-standing membranes (see section on mechanochemical synthesis). They showed high permeance for various solvents and were applied for the removal of dyes from water, the removal of drugs from various solvents, and the removal of bacteria from water, respectively.²⁸³

A TpPa-1 COF and Fe_3O_4 nanoparticles composite in which the magnetic particles are located at the tips of branched COF agglomerates showed good performance in the removal of polyaromatic hydrocarbons from aqueous solution, probably due to the low density of the branched composite structure.²⁷²

Fe_3O_4 nanoparticles with a shell of the ketoenamine COF TpBD (from TPG and benzidine) were applied in the removal of bisphenol A and bisphenol AF from aqueous solution. It was found that the composite features high capacities of 160.6 and 237.7 mg g^{-1} for bisphenol A and bisphenol AF, respectively. Fast desorption of the guest molecules in ethanol and reusability of the particles was also demonstrated.²⁸⁶

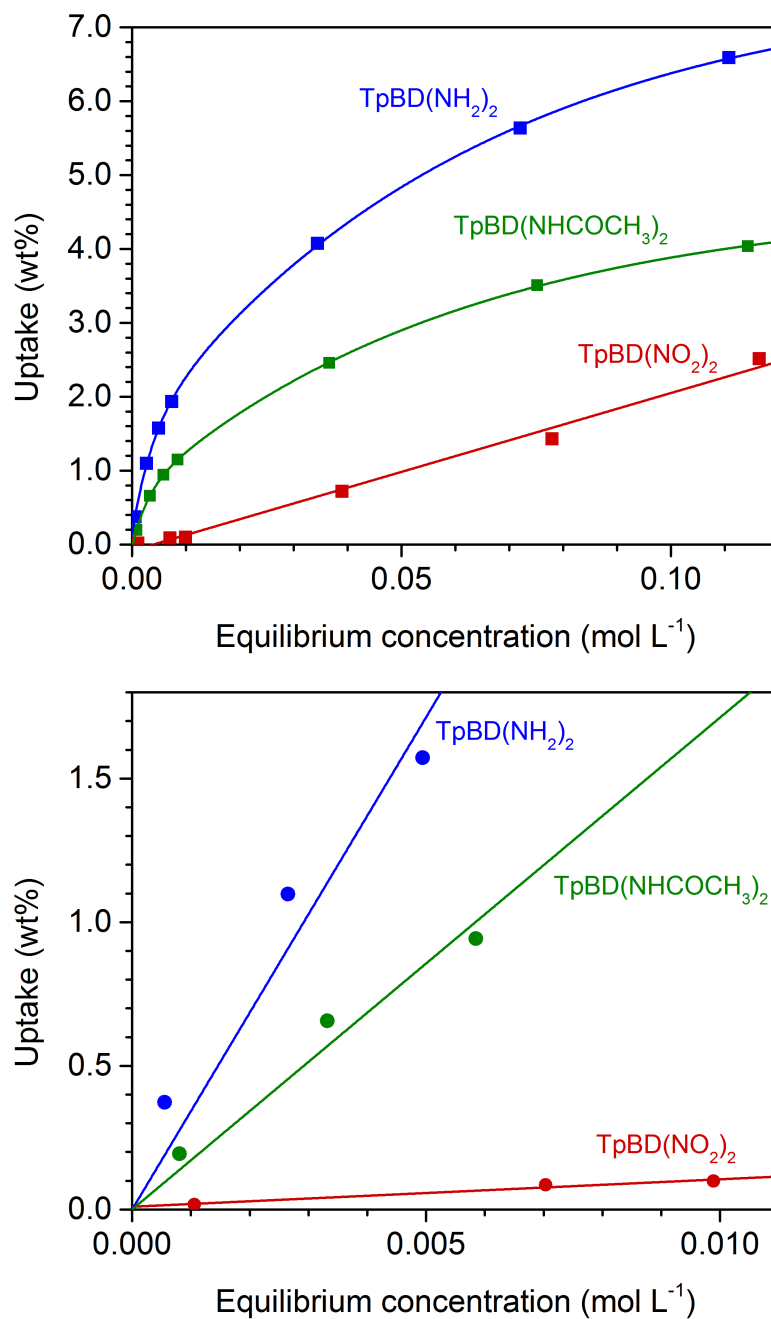


Figure 1.34: Lactic acid adsorption isotherms from aqueous solutions at natural pH (top) and detail of the low concentration range and linear fit (bottom) of the lactic acid adsorption isotherms of TpBD(NO₂)₂ (red), TpBD(NH₂)₂ (blue) and TpBD(NHCOCH₃)₂ (green). Reprinted with permission of the American Chemical Society from ref. 288.

The cationic COF PyTTA-BFIm-iCOF, (from 4,4',4'',4'''-(pyrene-1,3,6,8-tetrayl)tetraaniline and 5,6-bis(4-formylbenzyl)-1,3-dimethyl-benzimidazolium bromide) showed to be a highly efficient scaffold for the removal of methyl orange from an ethanol/water mixture with a capacity as high as 553 mg g⁻¹.²²⁶

Mercury species were efficiently removed from aqueous solution by an imine COF made from 1,3,5-tris(4-aminophenyl)benzene and a methylthio-functionalized 1,4-phenylenediamine. The capacity of the COF for Hg(II) was remarkably high with 734 mg g⁻¹, which corresponds to 76% accessible methyl sulfide groups. It also featured a high adsorption rate constant of 6.31 g mg⁻¹ min⁻¹ and was stable and usable at low pH conditions.¹⁹⁷

Similarly the sulfur groups in the imine COF-V (from 2,5-divinylterephthalaldehyde and 1,3,5-tris(4-aminophenyl)benzene), which was postsynthetically modified with 1,2-ethanedithiol *via* thiol-ene 'click' reaction with the vinyl groups of the COF, were applied for mercury removal. The Hg²⁺ uptake capacity of this COF was even higher with 1350 mg g⁻¹ (863 mg g⁻¹ for Hg⁰) and an initial adsorption rate for Hg²⁺ as high as 143 mg g⁻¹ min⁻¹. Selectivity investigations revealed a high affinity of the COF for Hg²⁺, Pb²⁺, and Cu²⁺ in the presence of Ca²⁺, Mg²⁺, Zn²⁺, and Na⁺. Modification with benzene-1,4-dithiol or ethanethiol resulted in COF structures with lower performance in Hg²⁺ removal, supposedly due to a less effective complexation of the mercury in these structures.¹⁸

Ti⁴⁺-modified TpPa-2 COF was utilized in phosphopeptide enrichment. Here, the Ti⁴⁺ ions were introduced into the COF by immersing the COF in a solution of Ti(SO₄)₂. TpPa-2-Ti⁴⁺ selectively adsorbed phosphopeptides in the presence of non-phosphopeptides.²⁷⁹ Lin et al. decorated Fe₃O₄ nanoparticles with a COF shell by co-condensing terephthalaldehyde and 1,3,5-tris(4-aminophenyl)benzene. These coated nanoparticles easily aggregated from a dispersion when a magnet was used. They were applied in peptide separation and showed the selective adsorption of peptides in the presence of proteins.¹⁸⁸

Similarly, Fe₃O₄@TpPa-1 was successfully used for the hydrophilic enrichment of N-glycopeptides from standard glycoproteins and human serum digests. This was attributed to the hydrophilic and nitrogen-rich character of the COF and the presence of amino groups.²⁷³ A methacrylate-functionalized TpPa-1 in a polymethylmethacrylate matrix was employed in high-performance liquid chromatography (HPLC) for the separation of small molecules with improved performance compared to a methacrylate only column. For molecules larger than the COF pores, no retention was observed, indicating a size exclusion effect in the separation.³⁰²

1.6.3 Catalysis

The regular pore channels in COFs assembled from molecular building blocks represent defined compartments that have attracted much attention for applications in heterogeneous catalysis. Thereby the COF walls have been used directly, or they have been utilized as coordination sites for metal species, thus establishing a well-defined environment for the metals and their efficient spatial distribution.

Metal-loaded COFs. Ding et al. were the first to incorporate metal moieties for catalysis in COFs. They coordinated Pd-species from Pd(OAc)₂ to the nitrogen atoms in the imine-linked COF-LZU1. The resulting Pd-loaded COF Pd@COF-LZU1 catalyzed the Suzuki-Miyaura coupling reaction of phenylboronic acid with several halides in high yields. The catalyst activity was retained in repeated cycles, however, the COFs crystallinity degraded in the first cycles.¹²⁶

Incorporating palladium acetate in COF-SDU1, built from tris(4-formacylphenoxy)-1,3,5-triazine and 1,4-phenylenediamine, a heterogeneous catalyst for the one-pot cross coupling of phenylsilane with 4-iodotoluene was obtained. It showed good yields also with derivatives of 4-iodotoluene, and good recyclability while the crystalline structure of the COF was maintained after 4 cycles.¹⁵³ Moreover, a Pd(OAc)₂ functionalized imine COF containing porphyrin units was utilized as a catalyst for Suzuki coupling.²²²

A catalyst formed by the combined complexation of Pd(OAc)₂ and MnCl₂ × 2 H₂O in Py-2,2'-BPyPh COF (from 4,4',4'',4'''-(pyrene-1,3,6,8-tetrayl) tetraaniline (PyTTA) and 2,2'-bipyridine-5,5'-dicarbaldehyde (2,2'-BPyDCA)) was shown to catalyze the combination of the Heck reaction between iodobenzene and styrene to form trans-stilbene and a subsequent epoxidation to trans-stilbene oxide.¹⁶⁴

Likewise, Pd(OAc)₂ and chloro(1,5-cyclooctadiene)rhodium(I) were used in an imine COF (from PyTTA and a mixture of 2,2'-BPyDCA and 4,4'-biphenyldialdehyde) for a two-step synthesis of the Rh(I) catalyzed addition of phenylboronic acid to benzaldehyde to yield diphenylmethanol, and its subsequent Pd(II) catalyzed oxidation to benzophenone.²²⁷ The epoxidation of olefins was performed with molybdenyl acetylacetonate (MoO₂(acac)₂) complexed in a hydrazone-linked COF made from 1,3,5-triformylphloroglucinol and 1,4-dicarbonyl-phenyl-dihydrazide.²⁴⁵

Salen-COF (made from 1,3,5-tris[(5-tert-butyl-3-formyl-4-hydroxyphenyl)ethynyl]-benzene and 1,2-ethylenediamine) was complexed with Co²⁺-ions and showed good catalytic activity for the Henry reaction, the C-C bond formation of a nitroalkane with an

aldehyde or ketone in the presence of a base.¹⁵⁶ Pachfule et al. created metal nanoparticles *in situ* in the pores of the β -ketoenamine COF TpPa-1, synthesized from 1,3,5-triformylphloroglucinol and 1,4-phenylenediamine.

The Pd nanoparticle/COF hybrid structure Pd(0)@TpPa-1 catalyzed the Sonogashira coupling, Heck reactions, and a one-pot sequential Heck-Sonogashira reaction. Furthermore, the authors found that the Pd(OAc)₂ loaded COF TpPa-1 served as an activating agent for the intramolecular oxidative coupling of diphenylamine to 9H-carbazole.²⁶⁴ Similarly, the Pd(0) nanoparticle loaded COF TpBpy (from TPG and 2,2'-bipyridine-5,5'-diamine) was found to catalyze the tandem synthesis of 2-substituted benzofuranes from terminal alkynes and 2-bromophenols in high yields.²⁹² The Au nanoparticles in the hybrid Au(0)@TpPa-1 structure showed high performance in the catalytic reduction of nitrophenol with NaBH₄ (Figure 1.35).²⁶³

The same reaction was investigated with Au nanoparticles embedded in spherical shells of an imine COF made from 1,3,5-tris(4-aminophenyl)benzene and 2,5-dimethoxyterephthalaldehyde. It was found that the size, shape, and loading of the Au nanoparticles were important factors determining the catalytic performance of the system and that composites with higher loadings and a better surface-to-volume ratio of the gold nanoparticles showed higher conversion efficiencies.¹⁹⁶

Furthermore, an imine COF constructed from Co-porphyrin amine and terephthalaldehyde was used for electrochemical CO₂ reduction in water. The conversion could be considerably enhanced by replacing the monophenyl linker with a biphenyl and by replacing 90-99% of the Co-ions with Cu.²⁰⁸

Co-ions were complexed by bipyridyl linkers in a ketoenamine COF and could be used more than 1000 times as electrocatalyst for the oxygen evolution reaction (OER) in the electrochemical water-splitting reaction, which ran with a turnover frequency of 0.23 s⁻¹ at an overpotential of 400 mV.²⁹⁰ In a related study, tris(4-formylphenyl)amine was co-condensed with PDA to obtain an N-rich COF that served as a scaffold for Co_xNi_y(OH)₂ nanoparticles. This composite material was used in electrocatalytic water splitting and showed a remarkably low overpotential for the OER of only 258 mV at 10 mA cm⁻² and a turnover frequency of 0.19 s⁻¹ at an overpotential of 408 mV.¹⁴⁶

Seo et al. coated HOPG with the Fe-DhaTph-COF (from 2,3-dihydroxybenzene-1,4-dicarbaldehyde and 5,10,15,20-tetrakis(4-aminophenyl)porphyrin pre- or postsynthetically modified with Fe(III)) *via* dip-coating or drop-casting. In the oxidation of the HOPG with H₂O₂ or H₂O₂/NaOCl, the Fe(III)-porphyrine units acted as catalyst to accelerate

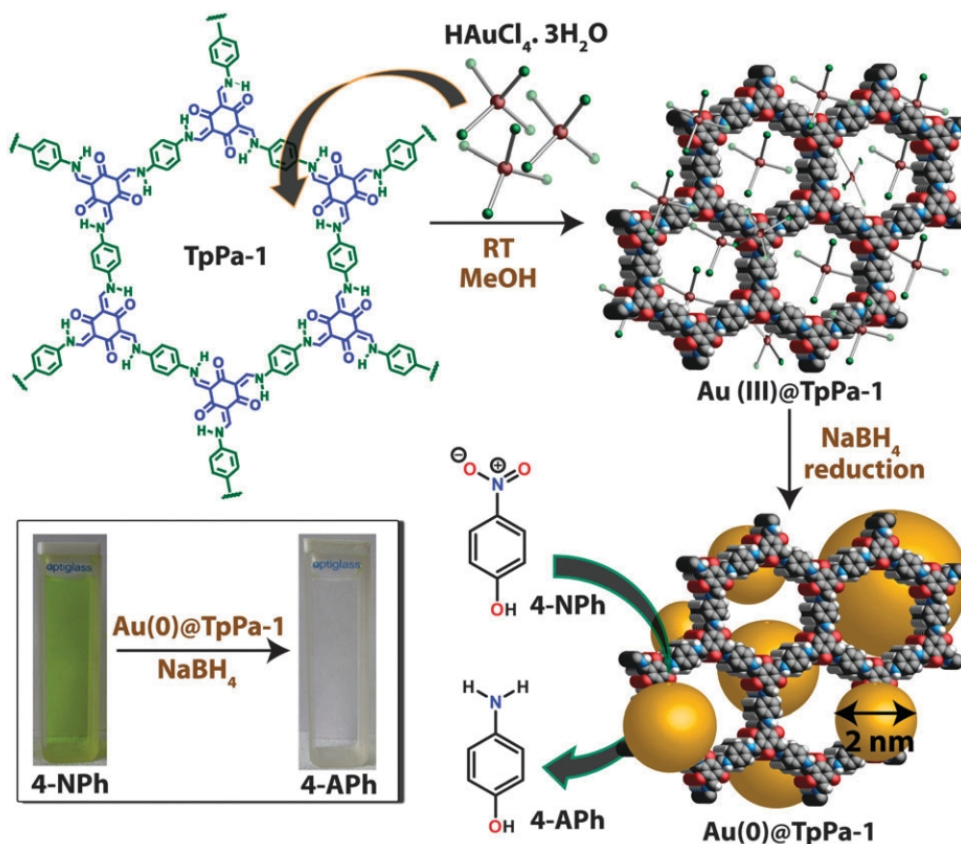


Figure 1.35: Synthesis of the Au(0)@TpPa-1 catalyst using the solution infiltration method for nitrophenol reduction reaction. Inset image: the optical images of the color change observed for the conversion of 4-nitrophenol to 4-aminophenol after the addition of Au(0)@TpPa-1 . Reproduced from ref. 263 with permission of The Royal Society of Chemistry.

the oxidation at distinct spots of the HOPG. This way, after an additional exfoliation step, holey graphene with holes in the nanometer range was obtained.²¹⁸ By immersing the 3D imine COF-300 (made from tetrakis(4-anilyl)methane and terephthalaldehyde) in a solution of 12-phosphomolybdic acid, Gao et al. obtained a catalyst in the epoxidation of olefins such as cyclooctene with *t*-BuOOH.²¹¹

A composite of the COF TpBpy with polymeric phosphonium salt made from ethyldiphenyl(4-vinylphenyl)phosphonium bromide (bearing catalytically active bromide ions) and Cu moieties from Cu(OAc)_2 (for preparation see Section 1.5.3.4) in the pores was tested as a catalyst in the cycloaddition of various epoxides and CO_2 . Highest yields were obtained for a COF that featured both the polymer and the Cu moieties, compared to composites with one component missing or with monomeric phosphonium salt in the

pores. This was attributed to the benefit of flexible catalytic polymer that brings the bromide ions in close proximity to the active Cu sites of the COF.²⁹¹

Nandi et al. formed Ni₃N nanoparticles in a benzimidazole-linked COF prepared by the co-condensation of TPG and 3,3'-diaminobenzidine. To establish the nanoparticles, the COF was mixed with nickel acetate and the mixture was ground with urea followed by heating at 350 °C in air. The turnover frequency for this electrocatalyst for the oxygen evolution reaction was determined to be as high as 0.52 s⁻¹ at an overpotential of 300 mV. Conductivity measurements with the pristine COF and the Ni₃N-COF composite revealed an increase in conductivity by several orders of magnitude upon incorporation of Ni₃N, which was attributed to bandgap-narrowing electronic interactions between the nanoparticles and the COF scaffold.³¹⁸

COFs as organocatalysts. In contrast to serving as well-defined porous host for post-synthetically introduced metal species, the frameworks of COFs themselves have also been successfully applied as catalysts. Fang et al. synthesized the 3D COFs BF-COF-1 and BF-COF-2 from 1,3,5,7-aminoadamantane with TFB and TPG, respectively. The COFs were applied in Knoevenagel condensation reactions of aldehydes with malonitrile and showed excellent size selectivity. While benzaldehyde was converted to more than 95%, only 3-4% were reached with 4-methylbenzaldehyde.¹²⁵ The Knoevenagel condensation of aromatic aldehydes with malonitrile was also catalyzed by the 3D COF LZU-301 (from tetrakis(4-anilyl)methane and (3,3'-bipyridine)-6,6'-dicarbaldehyde). It showed high yields but less size selectivity than BF-COF-1 and BF-COF-2.¹⁵¹

Jiang and coworkers synthesized a tetragonal imine COF (from 5,10,15,20-tetrakis(4'-tetraphenylamino)porphyrin and a mixture of 2,5-bis(2-propynyloxy)terephthalaldehyde and 2,5-dihydroxyterephthalaldehyde) with porphyrin units in the corners and reactive ethynyl units at the edges. Employing the postsynthetic click reaction of these ethynyl groups with pyrrolidine azide, catalytically active moieties were established in the pores. The modified COF catalyzed the Michael addition reaction of nitrostyrenes with aldehydes, although the enantiomeric excess was low.²¹⁹

Developing the system further, this issue could be overcome by applying the same postsynthetic reaction to a hexagonal imine COF made from 2,5-bis(2-propynyloxy)terephthalaldehyde, 2,5-dimethoxyterephthalaldehyde and 1,3,5-tris(4-aminophenyl)benzene. The concentration of pyrrolidine units in the COF was controlled by using different amounts of the alkyne-functionalized linker in the initial COF synthesis. These COFs catalyzed the Michael addition of cyclohexanone and β -nitrostyrene deriva-

tives efficiently and with a high enantiomeric excess, and the reaction was faster when a COF with a low pyrrolidine content was used.¹⁹⁰

The anthracene units in an anthracene pyrene imine-linked COF (made from 1,3,6,8-tetrakis(*p*-formylphenyl)pyrene and 2,6-diaminoanthracene) catalyzed the Diels-Alder reaction of 9-hydroxymethylanthracene and *N*-substituted maleimides at 25°C.¹⁶² A ketone-amine COF (made from 1,3,5-triformylphloroglucinol and 2,5-diaminobenzenesulfonic acid) with sulfonic acid groups at the COFs pore walls was applied as catalyst in the dehydration of fructose and showed good chemoselectivity, and the COF maintained its catalytic activity in several recycling steps although it quickly lost its crystallinity, supposedly due to delamination.²⁸⁰

The postsynthetic introduction of (2-bromoethyl)triethylammonium bromide ionic liquid created charges at the walls of an imine-linked COF (made from 4,4',4'',4'''-(pyrene-1,3,6,8-tetra-yl)tetraaniline and a mixture of 2,5-dihydroxyterephthalaldehyde and terephthalaldehyde). This COF was found to catalyze the *N*-formylation of amines with CO₂ and PhSiH by activating both PhSiH and the amines.³²⁵

Shinde et al. designed an imine-linked COF (made from 2,3-dihydroxyterephthalaldehyde and 5,10,15,20-tetrakis(4-aminophenyl)porphyrin) with porphyrin units at the vertices and catecholic -OH groups at the edges. In a catalyzed reaction the porphyrins and the imines could act as weak basic sites whereas the catechol groups could act as weak acidic sites. With this COF, the cascade reaction of benzaldehydedimethylacetals with malononitrile could be performed in high yields (Figure 1.36).²¹⁷

The same reaction was also catalyzed by the acidic and basic sites in a dual-linkage imine and boroxine 3D COF composed of 1,3,5,7-tetraaminoadamantane and 4-formylphenylboronic acid or 2-fluoro-4-formylphenylboronic acid with the boroxine groups acting as acid sites. Moreover, the cascade reaction was also performed by replacing malononitrile with ethyl cyanoacetate or acetylacetone (producing ethyl trans- α -cyanocinnamate and 3-benzylidene-2,4-pentanedione, respectively), with yields above 90% in all cases.¹⁷³

The cycloaddition of CO₂ and epoxides was performed with a porphyrin imine COF (made from 2,3-dihydroxyterephthalaldehyde and 5,10,15,20-tetrakis(4-aminophenyl)porphyrin) with OH-functional groups at the amine linker serving as catalytic centers. An analogous methoxy-functionalized COF that was examined as a comparison was also catalytically active, although with lower yields and turnover numbers.

The -OH functionalized COF also featured a high regioselectivity in the catalysis of the cycloaddition of CO₂ to aziridines.²¹⁶

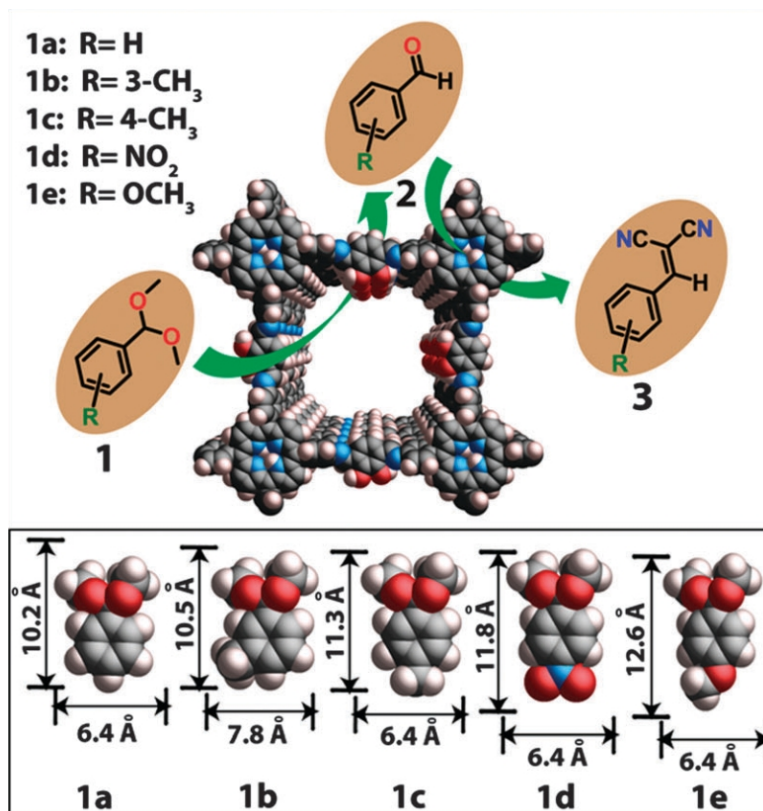


Figure 1.36: The cascade reaction of benzaldehydes with malononitrile with various reactants. Adapted from ref. 217 with permission of The Royal Society of Chemistry.

Chiral COFs. Recently, first chiral COF structures have been introduced, and some have been investigated for their performance in chiral catalysis. The chiral building unit tetraaryl-1,3-dioxolane-4,5-dimethanol (TADDOL) was introduced by Wang et al. in aldehyde linkers to form homochiral imine COFs by co-condensing the TADDOL units with 4,4'-diaminodiphenylmethane. These COFs have been applied in the enantiopure addition of Et₂Zn to aromatic aldehydes. In the first step, Ti(OiPr)₄ was introduced into the COF network to form (TADDOLate)Ti(OiPr)₂ in the COFs. These compounds served as efficient catalysts, converting aromatic aldehydes to aromatic alcohols in high yield and at high enantiomeric excess.³⁰

Xu et al. built a homochiral COF by introducing the linear amine (S)-4,4'-(2-(pyrrolidin-2-yl)-1*H*-benzo[*d*]imidazole-4,7-diyl)dianiline as a chiral building block into a

ketoenamine COF to serve as a catalyst for the asymmetric aldol reaction with various aldehydes. The COF showed good yields and high enantiomeric excess.¹²³

COFs in photocatalysis. To date, only few COF structures have been applied in photocatalysis. Stegbauer et al. synthesized a hydrazine-linked COF from 1,3,5-tris(4-formylphenyl)triazine and 2,5-diethoxy-terephthalohydrazide. In the presence of Pt (introduced as H_2PtCl_6 and reduced *in situ*) and sodium ascorbate or triethanolamine as sacrificial donor, it showed hydrogen evolution from water upon irradiation with visible light, but also amorphization of the COF due to delamination.²⁴⁴ Azine-linked COFs with triphenylarene units having different nitrogen substitutions in the central ring were developed by the same group. These COFs were stable under the photocatalytic hydrogen production conditions and revealed an increasing performance with a higher number of nitrogen atoms present in the central aryl ring, with the highest hydrogen evolution rate of $1703 \mu\text{mol h}^{-1} \text{g}^{-1}$ for N_3 -COF (Figures 1.37 and 1.38).²⁵³

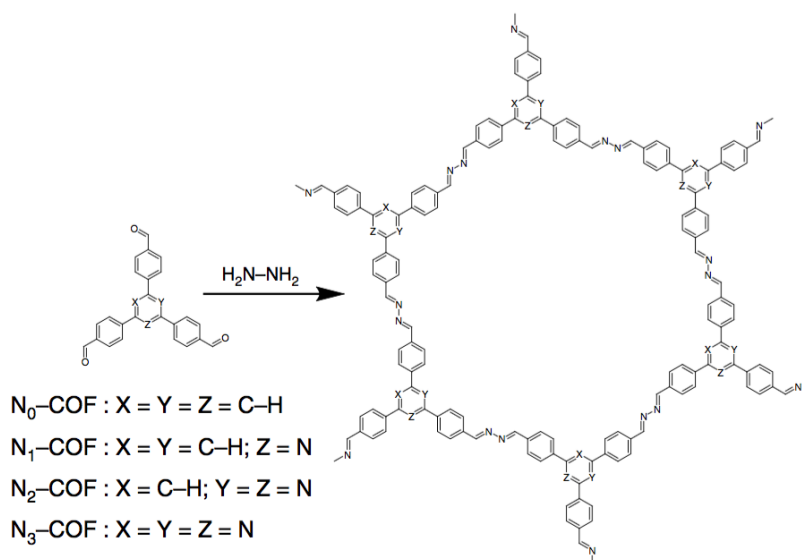


Figure 1.37: Scheme of the synthesis of N_x -COFs from N_x -aldehydes and hydrazine. Adapted from ref. 253. CC-BY 4.0 licence (<https://creativecommons.org/licenses/by/4.0/>).

In contrast, the PTP-COF (from 2,2',2''-(1,3,5-benzenetriyl)tris(pyridine-2-carboxaldehyde) and hydrazine hydrate), in which each of the peripheral phenyl rings was substituted with one nitrogen atom, showed a low hydrogen evolution rate of $83.3 \mu\text{mol h}^{-1} \text{g}^{-1}$ although it contains the same number of nitrogen atoms as N_3 -COF.

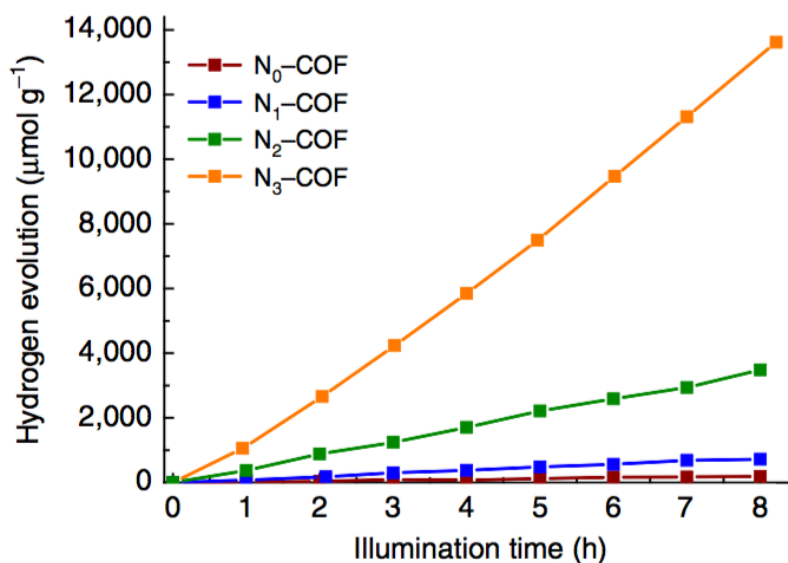


Figure 1.38: Hydrogen production with N_x -COFs as photocatalyst in the presence of triethanolamine as sacrificial electron donor. Adapted from ref. 253. CC-BY 4.0 licence (<https://creativecommons.org/licenses/by/4.0/>).

This difference was attributed to the relatively low BET surface area of PTP COF of only $84 \text{ m}^2 \text{ g}^{-1}$ and to its agglomerated morphology.²⁵⁶

An imine-linked COF, MP-DPh synthesized by Chen et al. (made from 5,10,15,20-tetrakis(4-aminophenyl)porphyrin) and a mixture of 2,3-dihydroxyterephthalaldehyde and terephthalaldehyde contained porphyrin units and aldehyde linkers featuring -OH groups that could undergo hydrogen bonding with the imine nitrogen. This COF showed photocatalytic conversion of molecular oxygen to singlet oxygen that was increasing with an increasing amount of -OH groups in the COF, and a higher photocatalytic activity for porphyrins with $M = \text{H}_2$ than for the Ni or Cu derivatives.²⁰⁴

A hybrid structure of a β -ketoenamine COF with CdS nanoparticles showed an increased photocatalytic activity in the hydrogen evolution reaction (with lactic acid as sacrificial donor) compared to the bare CdS nanoparticles, presumably due to an efficient transfer of the photoelectrons generated by the CdS particles to the COF lattice.²⁷⁷

The squaraine-linked Cu-porphyrin COF CuP-SQ (made from squaric acid and copper(II) 5,10,15,20-tetrakis(4-aminophenyl)porphyrin) showed an increased rate for the photocatalytic generation of singlet oxygen compared to the monomeric CuP.³¹⁶ By synthesizing a MOF-COF hybrid with Ti(IV) units in the structure, Nguyen et al. derived a photocatalyst that showed high performance in the polymerization of methyl methacrylate.¹⁷⁷

Photocatalyzed cross-dehydrogenative C-C coupling reactions were performed between tetraisoquinolines and a variety of reagents with the hydrazone-linked TFB-COF (from TFB and 2,5-dimethoxyterephthalohydrazide) serving as catalyst. High yields and good recyclability were achieved.²³⁹

1.6.4 Electrochemical Energy Storage and Electrical Devices

Proton conductivity. Fuel cells offer an efficient way to convert chemical energy to electricity. Thereby the reaction of hydrogen and oxygen produces water and electrical energy. For a high efficiency, a membrane material is needed that has excellent proton conductivity as well as high chemical and thermal stability.

Banerjee and coworkers were the first to investigate a COF as proton conductive material. They used TPG and 4,4'-azodianiline to synthesize the β -ketoenamine COF Tp-Azo, which is highly stable in acidic environments. While the Tp-Azo COF itself shows almost no proton conductivity, loading its channels with phosphoric acid increased the proton conductivity to $6.7 \times 10^{-5} \text{ S cm}^{-1}$ at 340 K under anhydrous conditions and to $9.9 \times 10^{-4} \text{ S cm}^{-1}$ at 332 K under 98% relative humidity, respectively.²⁹³

Using the mechanochemical synthesis technique, they also prepared the TpBpy COF from the linkers TPG and 2,2'-bipyridine-5,5'-diamine. Loading of the COF pores with H_3PO_4 led to a proton conductivity of $2.5 \times 10^{-3} \text{ S cm}^{-1}$ at 393 K. For this system, a better performance of the mechanochemically synthesized material was observed compared to a solvothermally synthesized COF.²⁸⁹

Two different proton conductivity mechanisms were utilized in the β -ketoenamine COF TpPa-(SO_3H -Py) with a mixture of sulfonic acid and pyridinic groups (made from 1,3,5-triformylphloroglucinol and 2,5-diaminobenzenesulfonic acid). A COF with the sulfonic acid groups only showed a low proton conductivity ($1.7 \times 10^{-5} \text{ S cm}^{-1}$ at 120 °C and anhydrous conditions), which originates from the intrinsic proton conductivity of the sulfonated COF with a moderate increase upon immobilization of phytic acid ($7.5 \times 10^{-5} \text{ S cm}^{-1}$).

The immobilization of phytic acid at the pyridinic sites in a mixed TpPa-(SO_3H -Py) COF provided a proton conductivity of $5 \times 10^{-4} \text{ S cm}^{-1}$, originating from the extrinsic proton conductivity in the phytic acid loaded COF pores. The increase of this value compared to the conductivity in a phytic@TpPa-Py COF ($3 \times 10^{-4} \text{ S cm}^{-1}$) shows the contribution of the sulfonic acid groups in the proton transport and the possibility to improve the proton conductivity of COFs using a combination of different transport mechanisms.²⁸¹

Zhang, Li, and coworkers synthesized the cationic COF EB-COF:Br (made from ethidium bromide and 1,3,5-triformylphloroglucinol) with the counterion Br^- immobilized in the pores. Exchanging these ions with $\text{PW}_{12}\text{O}_{40}^{3-}$ led to a framework with a proton conductivity of $3.32 \times 10^{-3} \text{ S cm}^{-1}$ (98% RH, 298 K).²⁹⁹

By immobilizing triazole and imidazole in the COF TPB-DMTP (made from 1,3,5-tris(4-aminophenyl)benzene and 2,5-dimethoxyterephthalaldehyde) (Figure 1.39), Jiang and coworkers were able to reach high proton conductivities at 130°C and anhydrous conditions of $1.1 \times 10^{-3} \text{ S cm}^{-1}$ and $4.37 \times 10^{-3} \text{ S cm}^{-1}$ for COF with triazole and imidazole, respectively.¹⁹⁵

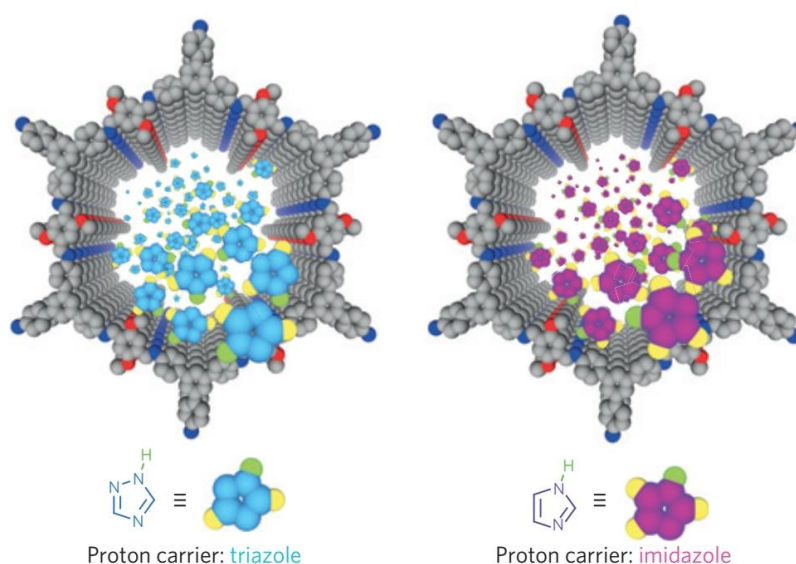


Figure 1.39: TPB-DMTP-COF with triazole and imidazole molecules in the COF channels. Reprinted by permission from Macmillan Publishers Ltd: Nature Materials ref. 195, copyright 2016.

High proton conductivities at 298 K were also achieved with sulfonic acid functionalized COFs. The COF NUS-9 (from TPG and 2,5-diaminobenzenesulfonic acid) features a proton conductivity of $1.5 \times 10^{-4} \text{ S cm}^{-1}$ at 33% RH $1.24 \times 10^{-2} \text{ S cm}^{-1}$ at 97% RH, while NUS-10 (from TPG and 2,5-diaminobenzene-1,4-disulfonic acid) showed even higher conductivities of $2.8 \times 10^{-4} \text{ S cm}^{-1}$ at 33% RH and $3.96 \times 10^{-2} \text{ S cm}^{-1}$ at 97% RH.²⁸²

The quarternary-ammonium-functionalized ketoenamine COF TpBD-MeQA⁺, initially formed from the linkers TPG and 3,3'-dimethylbiphenyl-4,4'-diamine and postsynthetically modified to feature quarternary ammonium groups at the pore walls, was applied as ion exchanger for use in anion exchange membrane fuel cells. It reached a HCO_3^{2-} -conductivity

at 293 K in water of 4.6 S cm^{-1} with Br^- as counterion and 5.3 mS cm^{-1} with OH^- as counterion.²⁸⁷

Redox-active COFs. A number of redox active COFs have been investigated for applications in electrical energy storage. The first redox active COF was synthesized by Dichtel et al., condensing the monomers 2,6-diaminoanthraquinone and 1,3,5-triformylphloroglucinol to the COF DAAQ-TFP whose anthraquinone units undergo 9,10-reduction to 9,10-dihydroxyanthracenes.

Films of this COF were prepared by mixing the COF with carbon black and a binder.²⁷⁴ The capacity of this material was later improved by developing a method to synthesize oriented films of this COF, thereby drastically increasing the capacitance of the DAAQ moieties to 400% compared to the non-oriented films with carbon black as 80-99% of the DAAQ moieties were found to be accessible in the oriented films, compared to only 3% in the non-oriented film.²⁹⁷

Moreover, by polymerization of 3,4-ethylenedioxythiophene in the pores of DAAQ-TFP COF, a 10-fold higher current response relative to pristine COF films was reached, and the material featured cycling stability for over 10000 cycles (Figures 1.40 and 1.41).²⁹⁸

Wang et al. utilized DAAQ-TFP COF (from 1,3,5-tris(4-formylphenyl)benzene and 2,6-diaminoanthraquinone) and the postsynthetically modified DABQ-TFP COF and TEMPO-COF (see Section 1.4.2 for details) in their exfoliated form and manufactured Li-ion cells with these COFs serving as cathode materials.

They found that the specific capacity was increased for the exfoliated material compared to the bulk structure for all three COFs, reaching 145 mA h g^{-1} , 210 mA h g^{-1} , and 115 mA h g^{-1} at 20 mA g^{-1} for exfoliated DAAQ-TFP-COF, DABQ-TFP-COF, and TEMPO-COF, respectively. High Li-ion diffusion coefficients of $6.94 \times 10^{-11} \text{ cm}^2 \text{ s}^{-1}$ for DAAQ-ECOF and $2.48 \times 10^{-11} \text{ cm}^2 \text{ s}^{-1}$ for DAAQ-DFP-COF were measured.²⁰⁰

Khattak et al. utilized the linker diaminopyridine in a ketoenamine COF with TPG for pseudocapacitive energy storage. In the electrochemical process, the pyridyl unit successively accepts two electrons and protons to form dihydropyridine. The specific capacitance of the COF was measured to be 85.3 F g^{-1} at 20 mV s^{-1} in a two-electrode cell, while a COF with PDA as amine linker only showed a capacitance of 33.7 F g^{-1} under the same conditions.²⁷⁶

Chandra et al. studied ketoenamine COFs (made with 1,3,5-triformylphloroglucinol and substituted phenylenediamine or benzidine) with -OH, -OMe and without functionalization at the amine linker in capacitance measurements.

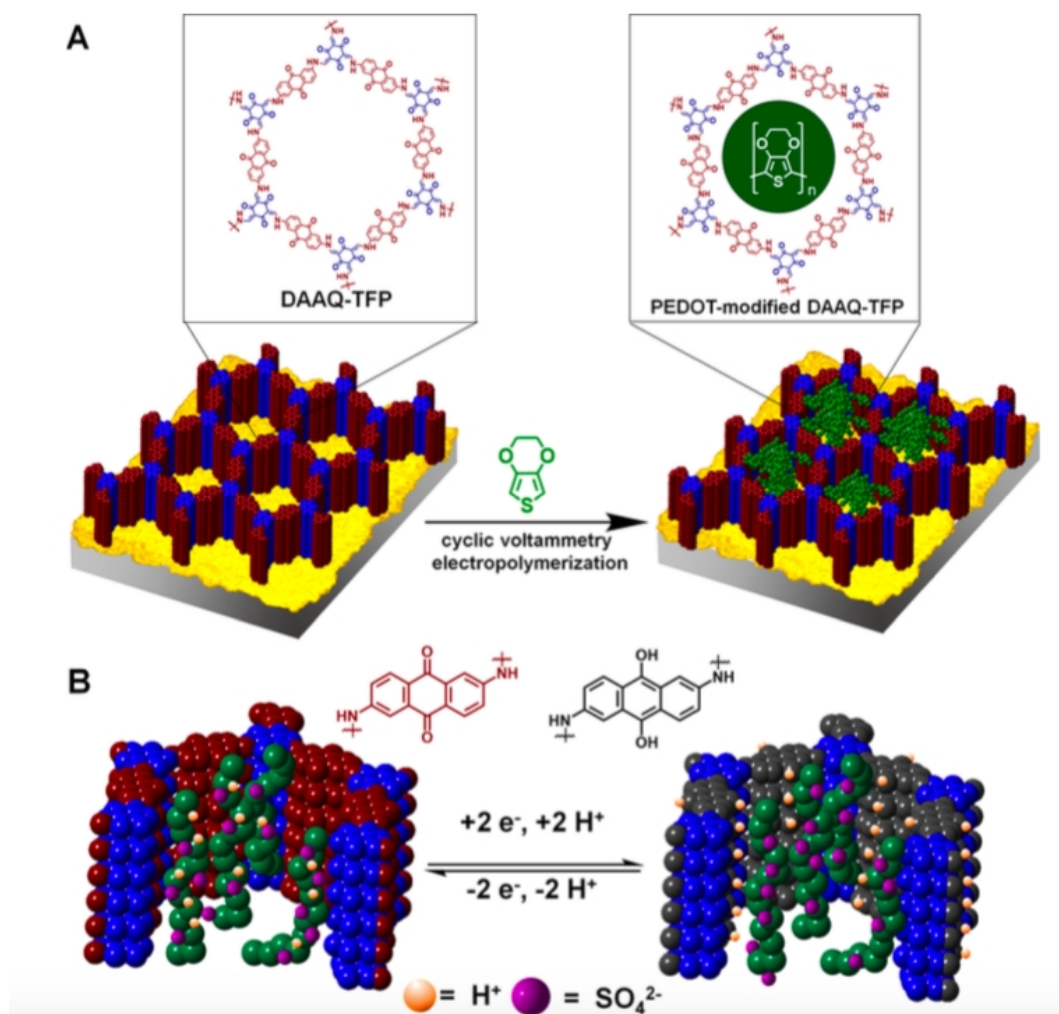


Figure 1.40: Incorporation of PEDOT within a DAAQ-TFP COF film (A) and schematic of oxidation and reduction of the DAAQ moieties (B). Reprinted with permission of the American Chemical Society from ref. 298.

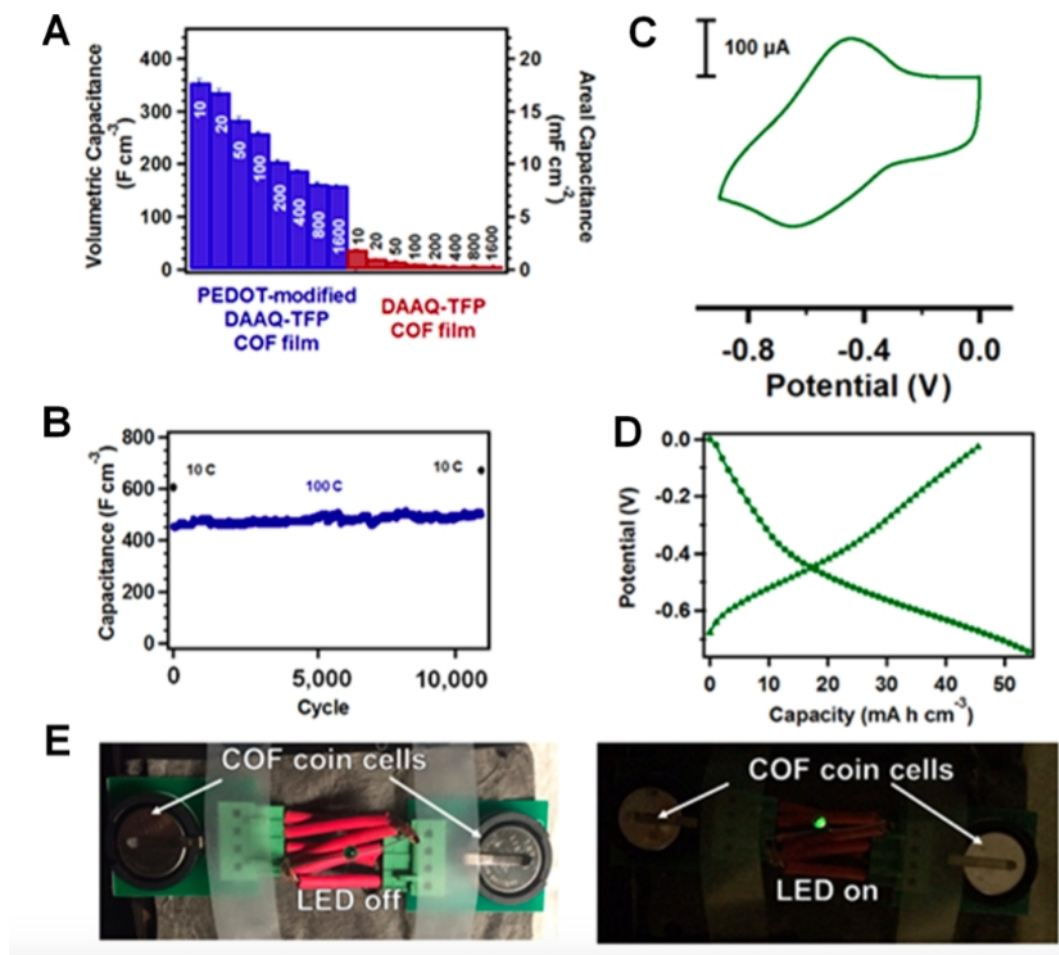


Figure 1.41: Charge storage performance and device integration of a PEDOT-modified DAAQ-TFP film. (A) Average capacitances calculated from 10 cycles of galvanostatic charge-discharge experiments at various C rates (error bars show ± 1 standard deviation). (B) Extended cycling of a PEDOT-modified DAAQ-TFP film showing stability over 10 000 cycles. First three cycles are at a rate of 10 C, then over 10 000 cycles at a rate of 100 C, followed by another three cycles at 10 C showing no loss in capacitance over the cycles. (C) CV in a two-electrode device configuration, in which the counter is a high-surface area carbon electrode. (D) A potential/capacity plot obtained in a two-electrode experiment exhibits well-defined voltage plateaus at the formal potential of the DAAQ moieties. (E) A PEDOT-modified DAAQ-TFP COF working device powering a green LED. Reprinted with permission of the American Chemical Society from ref. 298.

The COF TpPa-(OH)₂, with the functionalized amine linker 2,5-diaminohydroquinone dihydrochloride that can undergo a hydroquinone to benzoquinone conversion upon oxidation showed a very high specific capacitance of 214 F g⁻¹ at a current density of 0.2 A g⁻¹ in two electrode configuration. Thereby the quinone form of the COF was proposed to be stabilized by intramolecular hydrogen bond formation of the quinone oxygen with the adjacent nitrogen in the imine bond.

In comparison, all COFs with -H and -OMe substituted linkers gave low capacitances. The specific capacitance of the COF TpBD(OH)₂, with OH-functionalized benzidine as amine linker, was 86 F g⁻¹ at 2 mV s⁻¹ scan rate, but irreversible decomposition of the radicals formed upon oxidation of this linker led to a distinct capacitance decrease upon repeated cycling.²⁶⁸

Wang et al. grew COF LZU-1 on NH₂-functionalized reduced graphene oxide. The capacitance of this composite was 533 F g⁻¹ (0.2 A g⁻¹ in 1.0 M Na₂SO₄ electrolyte), significantly higher than for each separate component (226 F g⁻¹ for the COF and 190 F g⁻¹ for the graphene oxide). The authors attribute this improvement to an increased effective electrode surface area in the composite.¹³⁰

Multi-wall carbon nanotubes with a coating of COF_{TTA-DHTA}, formed by a solvothermal co-condensation of 4,4',4''-(1,3,5-triazine-2,4,6-triyl)trianiline and 2,5-dihydroxyterephthalaldehyde, were also tested as capacitors. The obtained specific capacitances were 127.5 and 98.7 F g⁻¹ at 0.4 and 2 A g⁻¹, respectively. These values were substantially higher than the capacities of COF or nanotubes alone or of a composite with the COF grown on the nanotubes lacking NH₂ functionalization, supposedly because of a reduced crystallinity of the COF grown on non-functionalized nanotubes.¹⁹⁴

The tetragonal [TEMPO]_x-NiP-COF (for synthesis see Section 1.4.2), featuring post-synthetically introduced organic radicals, was applied as a capacitor. The [TEMPO]_{50%}-NiP-COF with only 50% of the COF linkers modified with the radical featured a capacitance of 124 F g⁻¹ at 100 A g⁻¹, while the fully modified [TEMPO]_{100%}-NiP-COF had a capacitance of 167 F g⁻¹ under the same conditions. The COFs also showed high capacities for higher current densities. An excellent cycling stability was achieved for [TEMPO]_{50%}-NiP-COF.²²¹

The same postsynthetic modification strategy for the incorporation of the TEMPO radical was applied in a hexagonal imine linked COF with 1,3,5-tris(4-aminophenyl)benzene serving as amine. No distinct increase of conductivity was measured in the modified COFs. The radical units were found to electronically interact with each other, showing an increas-

ing level of interaction for higher degrees of modification, while the electronic interaction between COF backbone and the radical side groups was minor.²⁰¹

Finally, the imine-linked TDFP-1 COF (from 1,3,5-tris(4-aminophenyl)triazine and 2,6-diformyl-4-methylphenol) featured a capacitance of 354 F g^{-1} at a scan rate of 2 mV s^{-1} and of 418 F g^{-1} at 0.5 A g^{-1} in $1 \text{ M H}_2\text{SO}_4$. Nyquist impedance measurements revealed an effective charge transfer resistance of $24.27 \text{ } \Omega$.¹⁹⁹

COFs in Li-ion batteries. Rechargeable Li-ion batteries are a prevalent electrochemical cell type in many application areas, including portable devices, tools and electromobility. The use of COFs in Li-ion batteries was first reported by Xu et al. for the boronic ester $\text{D}_{\text{TP}}\text{-A}_{\text{NDI}}\text{-COF}$ built from HHTP and a naphthalene diimide core boronic acid. The naphthalene diimide unit serves as a redox-active component in the lithiation and delithiation process and undergoes enolization upon lithiation.

Incorporation of the imide unit in a COF increased the efficiency compared to the use of the free diimide molecule, as dissolution in the electrolyte is prevented. The COF showed a high charge-transfer resistance, which was overcome by introducing carbon nanotubes in the COF synthesis. The resulting composite was applied as cathode and featured a high capacity of about 70 mA h g^{-1} at a rate of 2.4 C, good performance in high rate charge and discharge cycles and a remarkable cycle stability.¹¹³

The diimide core was also utilized in the form of 2,7-diaminobenzo[*lmn*][3,8]phenanthroline-1,3,6,8(2*H*,7*H*)-tetraone in combination with 1,3,5-triformylbenzene (TFB) and 1,3,5-triformylphloroglucinol (TPG), respectively. With these systems, high capacities (e.g. 80 mA h g^{-1} after 300 cycles at 3.4 C and 89.3 mA h g^{-1} after 200 cycles at 3.7 C with the TFB linker) could be reached without additional carbon nanotube support.²⁴¹

Bai et al. reported capacities of 600 mA h g^{-1} and 593 mA h g^{-1} after 500 cycles for two imine COFs synthesized from TFB with benzidine and the triazine core amine 4,4',4''-(1,3,5-triazine-2,4,6-triyl)trianiline, respectively.¹³⁹

Vazquez-Molina et al. described a method to reach crystallographic alignment in COFs by applying uniaxial pressure to pre-synthesized COF powder material (see Section 1.5.2.3). The resulting COF pellets were impregnated with LiClO_4 ; they exhibited high Li-ion conductivity of 0.15 mS cm^{-1} with COF-5.⁸² Du et al. studied spiroborate-linked COFs with Li as counterion and observed a Li-ion conductivity of $3.05 \times 10^{-5} \text{ S cm}^{-1}$ at RT in a COF blend with polyvinylidene fluoride and propylene carbonate.²⁸

COFs in Li-sulfur batteries. Lithium-sulfur batteries may become an alternative to Li-ion batteries due to their high specific energy, but several stability problems need to be addressed for commercial deployment. To overcome the issue of soluble polysulfides shuttling between anode and cathode, COFs have been investigated as polysulfide traps to improve the cycling stability of the Li-S cells.

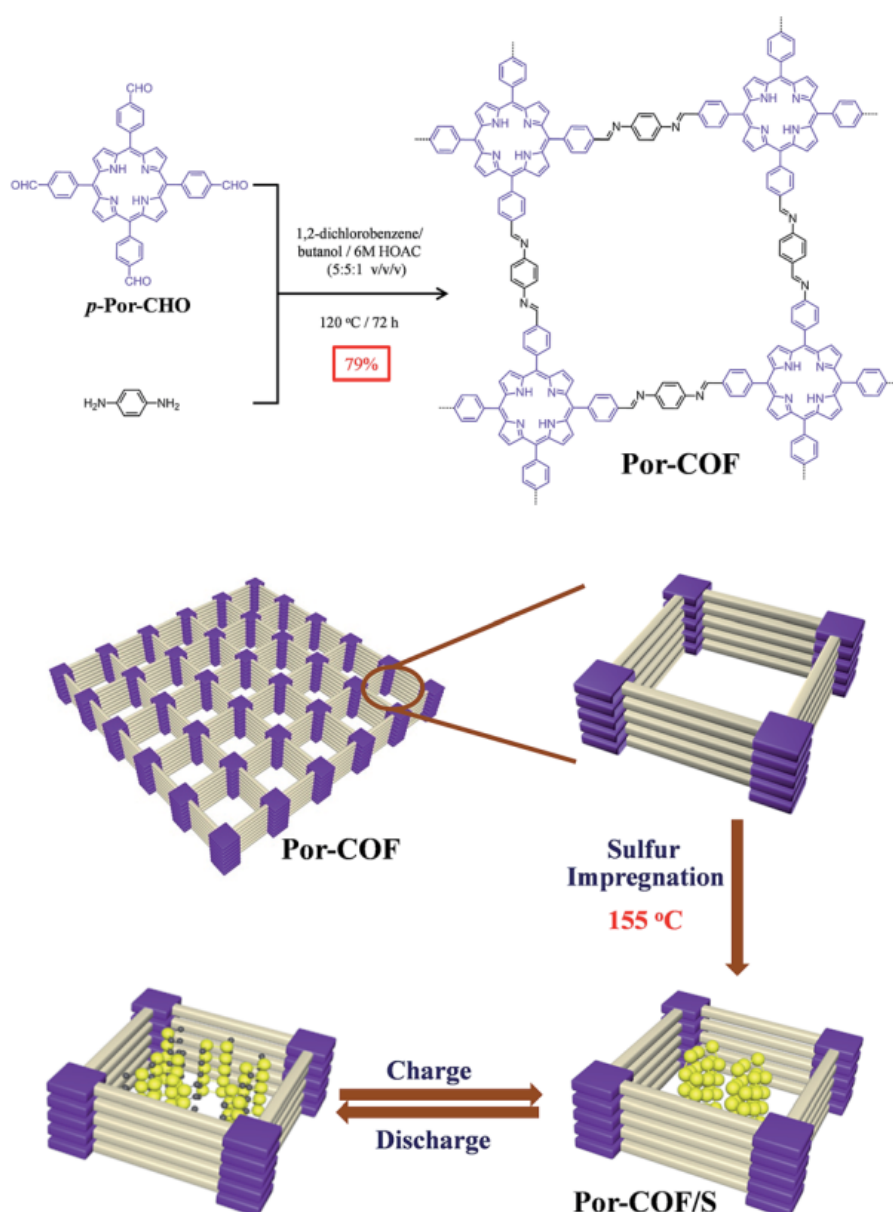


Figure 1.42: Schematic representation of the synthesis and the charge and discharge process of the Por-COF/S composite. Adapted from ref. 233 with permission of The Royal Society of Chemistry.

Yang et al. co-condensed triformylphloroglucinol and 4,4'-azodianiline to form a ketone-amine COF that was then impregnated with sulfur by grinding the COF together with elemental sulfur and subsequent heating to 155 °C for 20 h. Charge-discharge experiments were performed with lithium foil as anode and a mixture of the COF together with conductive carbon (KB600), carboxymethylcellulose sodium and styrene butadiene rubber on an aluminum foil as cathode. The COF showed a high initial discharge capacity of 1536 mA h g⁻¹ at 0.1 C, and after the first drop in capacity in the first few cycles a relatively stable capacity of around 740 mA h g⁻¹, demonstrating the successful stabilizing effect of the COF on the polysulfide moieties.²⁹⁵

Por-COF (from 1,4-phenylenediamine and a porphyrin aldehyde linker) was shown to yield a capacity of 721 mA h g⁻¹ in a Li-sulfur battery after 100 cycles at a rate of 0.5 C (the COF was impregnated with sulfur by grinding and subsequent heating and then mixed with acetylene black and PTFE, pressed onto an aluminum grid and used as cathode, lithium foil was used as anode and reference electrode, see Figure 1.42).²³³

COF-1 was also tested as polysulfide host (in a mixture with carbon black and polyvinylidene fluoride on an aluminum foil) exhibiting a remarkable capacity and cycling stability with 929 mA h g⁻¹ at 0.5 C after 100 cycles, whereas with the triazine COF CTF-1 a significantly lower cycling stability was reported with only 489 mA h g⁻¹ after 100 cycles. The larger pore COFs COF-5 and COF-10 showed even lower performance.⁴⁵

Composites of carbon nanotubes coated with COF-1 were applied as polysulfide trap in Li-S batteries. 84% capacity retention after 300 cycles at a rate of 2.0 C was achieved, compared to only 15% retention without the COF layer on the nanotubes.⁴⁴

COF field effect transistors. As 2D imine COFs feature in-plane conjugation in the COF sheets, they might be an interesting material for designing organic field effect transistors (FETs). This application was first investigated by Feldblum et al. who utilized the imine COF polyTB (from benzene dithiophene carbaldehyde and tris(4-aminophenyl)amine). Films of this COF showed a relatively low field-effect mobility of $3.0 \times 10^{-6} \text{ cm}^2 \text{ V}^{-1} \text{ s}^{-1}$, which was mainly attributed to grain boundaries in the COF film limiting long-range carrier mobility.¹⁸³

Sun et al. found that COF-366 (from tetrakis(*p*-aminophenyl)porphyrin and terephthalaldehyde) selectively grows on hexagonal boron nitride (hBN) as a thin film. FETs containing these films featured a mobility of $0.015 \text{ cm}^2 \text{ V}^{-1} \text{ s}^{-1}$ in the saturated regime and the mobility was shown to be higher on hBN than on a HfO₂/Si surface ($3.4 \times 10^{-4} \text{ cm}^2 \text{ V}^{-1} \text{ s}^{-1}$).²⁰³

To design a vertical field-effect transistor, Sun et al. utilized the COF_{TFPy-PPDA} (from 1,3,6,8-tetrakis(*p*-formylphenyl)pyrene and 1,4-phenylenediamine) on single-layer graphene (SLG). Here, the COF was grown on SLG, which served as source electrode while gold deposited on the COF layer served as drain electrode. High current densities of up to 6.8 A cm⁻² for holes and 4.1 A cm⁻² for electrons were measured and a high current density on/off ratio of > 10⁵ was reached.²³²

1.6.5 Optoelectronics

In recent years, with a focus on potential applications in optoelectronics has markedly expanded. In 2013 we published a review about this nascent development.³⁴⁵

The first semiconducting COF was reported by Jiang and coworkers in 2008. They used the co-condensation of pyrene-2,7-diboronic acid and HHTP to form the boronic ester TP-COF with pyrene moieties in the backbone. Its electrical conductivity was measured using a two-probe method across a 10 μm gap between two Pt electrodes. The *I-V* profile of TP-COF (measured under air at 25 °C) was almost linear, and TP-COF showed a current of 4.3 nA at 2 V bias voltage compared to only 79 pA for a sample where the COF precursors were only mixed. Doping of the COF with iodine led to an increase of the electric current, indicating a p-type semiconducting nature of TP-COF.¹⁷

Self-condensation of the aforementioned pyrene-2,7-diboronic acid resulted in the boroxine-linked PPy-COF. It showed an electrical conductivity similar to TP-COF and a similar increase in current upon doping with iodine, indicating that PPy-COF is also a p-type semiconductor. For photocurrent measurements, PPy-COF was deposited as a film of 100 μm in a sandwich-type electrode assembly between an Al and a semitransparent Au electrode. Upon irradiation with visible light (xenon lamp, > 400 nm), a sharp rise in photocurrent generation was observed. By switching the light on and off, an on/off ratio over 8.0 × 10⁴ was realized. In contrast, TP-COF in which the HHTP moieties are placed between the pyrene units only yielded an on-off ratio of 2.0 × 10⁴.⁵⁶

Incorporation of phthalocyanine moieties in COFs for optoelectronic application was first reported by Ding et al. Here, a boronic ester COF made from BDBA and (2,3,9,10,16,17,23,24-octahydroxyphthalocyaninato)nickel(II) gave the 2D NiPc COF with a tetragonal pore system in which the phthalocyanine units are stacked on top of each other. This stacking led to photoconductivity of the COF whereas the phthalocyanine linker itself did not show any photoresponse. NiPc COF showed p-type semiconducting

properties.¹⁹ By replacing the BDBA with the electron-withdrawing 1,4-benzodithiazole diboronic acid, an n-type semiconducting COF could be synthesized.¹¹⁰

A switching of the nature of the conductivity upon metal insertion was demonstrated for COFs synthesized from porphyrin boronic acids and BDBA. These COFs crystallized in an AA arrangement of the porphyrin units, which allows for columnar interactions in the porphyrin stacks. The metal-free framework, named H₂P-COF is a hole-conducting material. Interestingly, by introducing Zn into the porphyrin units, an ambipolar COF ZnP-COF is formed. If not Zn but Cu is used, the resulting CuP-COF is predominantly electron transporting (Figure 1.43).⁶⁶

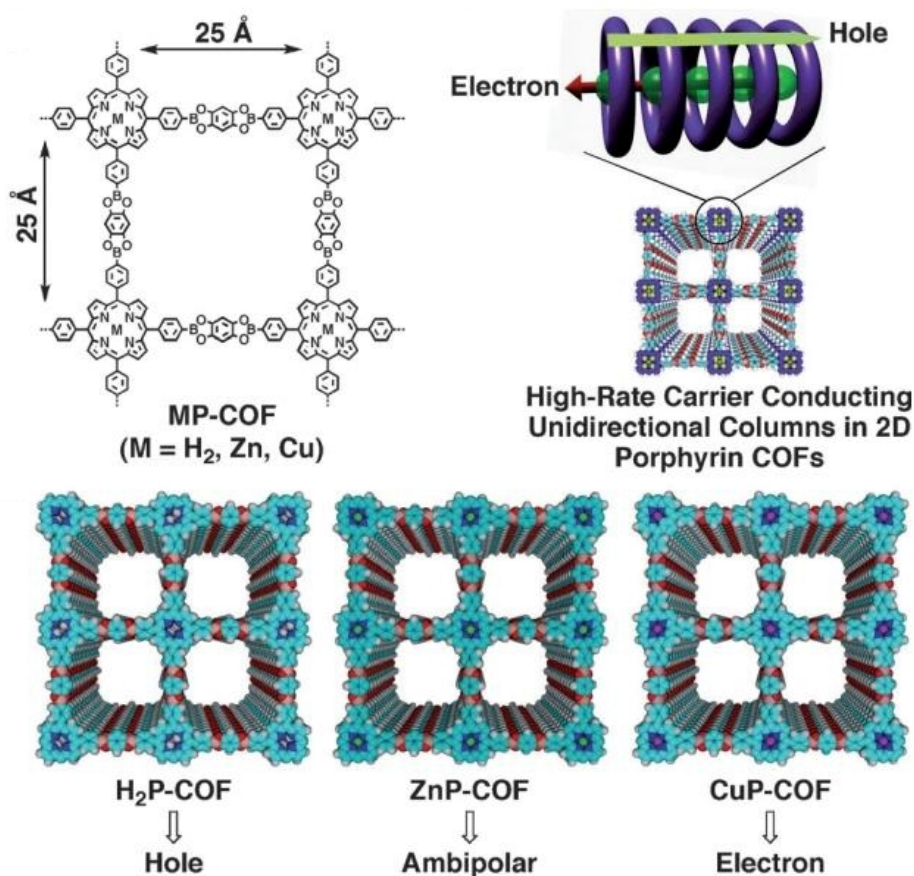


Figure 1.43: MP-COFs with different metals. Adapted with permission from ref. 66. Copyright 2012 John Wiley and Sons.

In contrast, when a phthalocyanine boronic acid was used, a slipped AA arrangement of the COF layers was obtained, and thus the columnar interactions were reduced. The Pc-COFs with Cu, Zn or Co as complexed metal ions were all mainly hole transporting,

but the metal ions lowered the electron density in the phthalocyanine units following the trend $\text{Cu} < \text{Zn} < \text{Co}$, thereby influencing the mobility.⁹⁸

Yaghi and coworkers reported a porphyrin boronic ester COF made from a boronic acid functionalized porphyrin unit and 2,3,4,5-tetrahydroxyanthracene. Pulse-radiolysis time-resolved microwave conductivity measurements revealed a high charge carrier mobility of $3.0 \text{ cm}^2 \text{ V}^{-1} \text{ s}^{-1}$ in the framework. An even higher value of $8.1 \text{ cm}^2 \text{ V}^{-1} \text{ s}^{-1}$ was measured for an imine COF formed by the co-condensation of terephthalaldehyde and amino-functionalized porphyrin.

However, these high mobilities were found only for short-range motion, presumably within individual crystalline domains, while the long-range mobility values (from time-of-flight (TOF) transient, measured on $1.5 \text{ }\mu\text{m}$ thick films of COF and poly(methylmethacrylate) with Al and indium tin oxide electrodes) were significantly lower, indicating that the charge carrier movement over longer distances is limited by grain boundaries.⁷¹

Two COFs with tetrathiafulvalene (TTF) serving as a linker (TTF-Ph-COF with the linker PDA and TTF-Py-COF with the linker 1,3,6,8-tetrakis(4-aminophenyl)pyrene) were investigated by flash-photolysis time-resolved microwave conductivity. The TTF-Ph-COF showed a charge carrier mobility of $0.2 \text{ cm}^2 \text{ V}^{-1} \text{ s}^{-1}$, while it was only $0.08 \text{ cm}^2 \text{ V}^{-1} \text{ s}^{-1}$ for TTF-Py-COF, probably due to less efficient layer stacking in the latter COF.²⁶

Several investigations have been focused on the synthesis of COFs that combine donor and acceptor units in their lattice. The defined arrangement of the building blocks in the COF structure could conceptually lead to highly ordered heterojunctions in the COF lattice. In 2012 the group of Jiang reported a boronic ester COF in which HHTP represents the electron donor and 1,4-benzothiadiazole diboronic acid the electron acceptor.¹⁰²

This concept was later expanded to the $\text{D}_{\text{ZnPc}}\text{-A}_{\text{NDI}}\text{-COF}$ that was built from the electron donating Zn-phthalocyanine and electron withdrawing naphthalene diimide. In this structure, the neighboring donor-acceptor pairings enable an effective charge separation over long distances. This led to a charge carrier lifetime of 1.8 and 1500 μs at 280 and 80 K, respectively, determined from time-resolved electron spin resonance spectroscopy (TR-ESR) measurements.¹¹⁶

The formation of donor-acceptor heterojunction COFs with HHTP as an electron donor and naphthalene diimide or pyromellitic anhydride as electron acceptor demonstrated the importance of donor-acceptor matching for the design of COF superheterojunctions. While in the COF with naphthalene diimide separated columns of acceptor and donor units are

present, the COF with pyromellitic dianhydride forms a through-bond charge transfer complex.⁸⁸

A systematic study of donor-acceptor combinations in COFs made from metallophthalocyanines and diimides indicated in all investigated structures charge separation and charge migration along the columns of the electron donor and acceptor units, respectively. The lifetimes of the charge-separated states were found to be increasing depending on the metal centers in the series $\text{Zn} < \text{Ni} < \text{Cu}$, while the nature or length of the used aromatic diimide acceptor played a minor role, as revealed by transient absorption spectroscopy.¹¹⁵

Our group prepared a donor-acceptor COF thin film utilizing an HHTP acceptor and a porphyrin donor as linkers to build a donor-acceptor heterojunction COF structure that was used as active layer in a solar cell. Upon irradiation with simulated solar light, it featured an open-circuit voltage of 312 mV and a short-circuit current density of $44.6 \mu\text{A cm}^{-2}$. In comparison, the short circuit current density of a cell with the two COF precursors mixed as a blend was more than 30 times smaller than with the COF, demonstrating the advantage of the defined alignment of donor and acceptor in the COF.¹¹²

A different approach for the formation of a donor-acceptor heterojunction with a COF was reported by our group in 2013. Thereby, the electron donating TT-COF, comprising thienothiophene units was synthesized as a thin film, and the COF pores were filled with the electron accepting fullerene derivative [6,6]-phenyl- C_{61} -butyric acid methyl ester (PCBM). TT-COF showed efficient charge transfer towards PCBM, demonstrating the benefit of the concept of filling an electron-donor network with an electron acceptor. TT-COF:PCBM was tested as active layer in a photovoltaic device and revealed an open-circuit voltage of 0.62 V and a power conversion efficiency of 0.053%.¹⁰⁴

Moreover, we developed oriented films based on a benzodithiophene (BDT) COF, presenting honeycomb-like networks of vertically arranged pores on the substrate. Filling these BDT-COF films with [60]PCBM or [70]PCBM yielded donor-acceptor interpenetrated systems that showed an efficient energy transfer from the benzodithiophene units to the PCBM.¹⁰⁶

Further investigation of the directional charge carrier transport in oriented BTD-COF films (using hole-only devices) revealed a dependence of the charge transport on the film thickness, with higher hole mobility values for thinner films ($3 \times 10^{-8} \text{ cm}^2 \text{ V}^{-1} \text{ s}^{-1}$ for a film of 80-100 nm in thickness), supposedly due to defects in the COF stacks. Additionally, illumination of the film led to a threefold increase of the the hole mobility, demonstrating the photoactive nature of BDT-COF.¹⁰⁸

The intrinsic hole mobility of a COF built from a hexabenzocoronene amine and terephthalaldehyde was calculated to be as high as $0.7 \text{ cm}^2 \text{ V}^{-1} \text{ s}^{-1}$, as determined by direct current integration.²⁷

A delocalization of the π -clouds over the COF sheets was realized in CS-COF, a phenazine-linked COF that is formed from triphenylene hexamine and tert-butylpyrene tetraone. CS-COF was investigated applying flash photolysis time-resolved microwave conductivity and time-of-flight measurements and was found to be a hole conducting framework with a remarkable intrinsic mobility of $4.2 \text{ cm}^2 \text{ V}^{-1} \text{ s}^{-1}$.

The pores (1.6 nm in diameter) of the electron-donating COF network were filled with fullerene molecules to build a bicontinuous donor-acceptor system. This system showed photoconductivity and was tested as an active layer in solar cells. A power conversion efficiency of 0.9% was achieved, although the COF film was non-oriented. An open-circuit voltage as high as 0.98 V was measured, which was attributed to the low HOMO-level of CS-COF (-5.7 eV) (Figure 1.44).³²⁰

In contrast to filling the COF pores with the electron acceptor, Chen, et al. demonstrated a postsynthetic reaction of an azide-functionalized Zn-phthalocyanine COF with alkyne-functionalized fullerenes, thereby covalently attaching the electron acceptor unit to the COF lattice. They found that the fullerene units are necessary for charge separation and that the efficiency of charge separation is increased for a higher fullerene content.²¹

Following a different approach, the π -electron donating tetrathiafulvalene was used as aldehyde building block and co-condensed with PDA in an imine COF. The resulting COF TTF-COF showed conductivity upon doping with iodine to up to $1.8 \times 10^{-6} \text{ S cm}^{-1}$ at 25 °C, determined by constant-voltage two-probe measurements.²²⁹

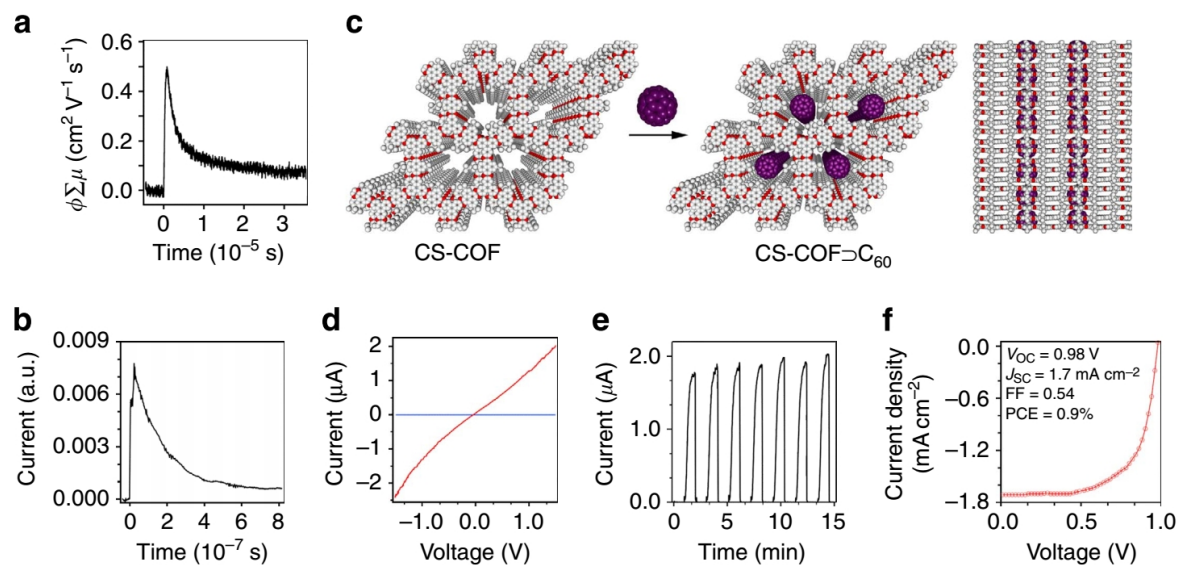


Figure 1.44: Carrier mobility and photoelectric properties of CS-COF. (a) Conductivity transient using flash photolysis time-resolved microwave conductivity methods on excitation with a 355-nm laser pulse. (b) Time-of-flight transient current integration for CS-COF with a 355-nm laser pulse at a power of 34 mJ cm^{-2} per pulse. (c) Schematic representation of synthesis of CS-COF \supset C₆₀ by sublimed crystallization of fullerenes in the open one-dimensional channels (white: carbon; red: nitrogen; purple: fullerene). A side view of CS-COF \supset C₆₀ is also shown. (d) I-V curve of a 50-nm-thick CS-COF \supset C₆₀/PMMA film sandwiched between Al and Au electrodes at bias voltages ranging from -1.5 to 1.5 V in air at 25 °C. (e) Photocurrent switching at a bias voltage of 1.5 V in air at 25 °C, with repetitive light on-off actions on the 50-nm-thick CS-COF \supset C₆₀/PMMA film. (f) J-V curve of the photovoltaic cell under irradiation with air mass 1.5 conditions. Reprinted by permission from Macmillan Publishers Ltd: Nature Communications ref. 320, copyright 2013.

By preparing TTF-COF as oriented thin film, the conductivity of the doped COF could be dramatically increased to $2.8 \times 10^{-3} \text{ S cm}^{-1}$ (determined by two-probe measurements). This demonstrates the advantage of an oriented arrangement for charge carrier transport.²²⁸ A related effect was found for thin films of the aforementioned TT-COF that showed a significantly increased photoresponse compared to the non-oriented COF.¹⁰⁵

For a range of COFs, an increased conductivity was observed upon incorporation of a dopant in the pores, indicating a charge transfer between the COF host material and the guest molecules. For example, this was found in the azodioxy linked POR-COF made from a protected tetrakis-(arylhydroxylamine)porphyrin. The electrical conductivity of the undoped COF was $4.6 \times 10^{-11} \text{ S cm}^{-1}$ (I-V-curves from two-probe measurement, room temperature, air) while it was increased to $1.52 \times 10^{-7} \text{ S cm}^{-1}$ upon doping with I_2 .³¹⁹

When the imine-linked COF FL-COF-1 (made from 2,7-diaminofluorene and 1,3,5-triformylbenzene), bearing fluorene units in the amine linker, was doped with iodine, the conductivity was significantly increased to $1.0 \times 10^{-4} \text{ S cm}^{-1}$ at RT, and a high Seebeck coefficient of $2450 \mu\text{V K}^{-1}$ was measured, but the COF was amorphized.¹²² Charge transfer was also observed between the boronic ester-linked T-COF-4 (from HHTP and thieno[3,2-*b*]thiophene-2,5-diboronic acid) and the electron acceptor molecule tetracyanoquinodimethane (TCNQ).¹⁰³

1.6.6 Sensing

The confined space of COF pores and their defined pore environment make COFs promising materials for sensing applications. However, in view of the great structural variety of COFs, surprisingly few examples have been reported to date. Dalapati et al. reported an azine-linked COF (made from hydrazine and 1,3,6,8-tetrakis(4-formylphenyl)pyrene with four aldehyde groups) that was tested for fluorescence quenching upon addition of nitroaromatic compounds. It was shown to be very sensitive and selective towards the explosive 2,4,6-trinitrophenol.²⁵

The same principle was investigated with the imine COF 3D-Py-COF (made from tetrakis(*p*-aminophenyl)methane and 1,3,6,8-tetrakis(4-formylphenyl)pyrene with four aldehyde groups). It showed fluorescence quenching upon addition of picric acid, with a 75% reduction of the fluorescence at a picric acid concentration of 20 ppm (Figure 1.45).³²

A high selectivity towards 2,4,6-trinitrophenol was also found for delaminated sheets of the imide-linked PI-COF (from tetrakis(4-aminophenyl)porphyrin and 3,4,9,10-

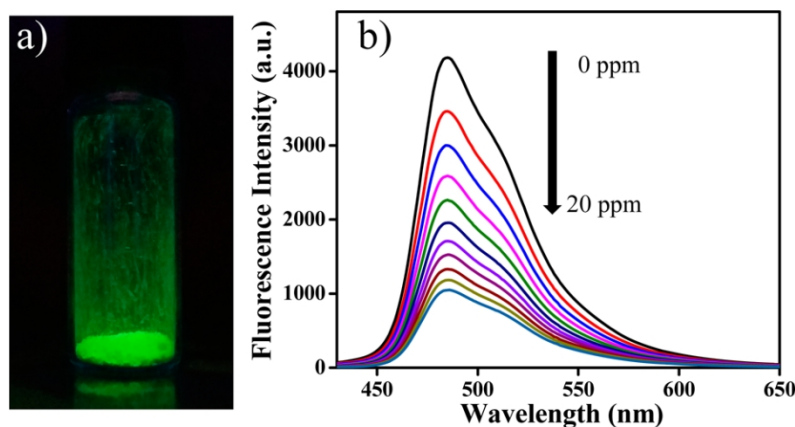


Figure 1.45: Fluorescent behavior of 3D-Py-COF. (a) Photography of the 3D-Py-COF powder under UV light irradiation. (b) Fluorescence quenching upon addition of PA (0-20 ppm) in DMF ($\lambda_{\text{ex}} = 408 \text{ nm}$). Reprinted with permission from ref. 32. Copyright 2016 American Chemical Society.

perylene-tetracarboxylic dianhydride). A significantly higher quenching constant of $1 \times 10^{-7} \text{ M}^{-1}$ for the sheets than for the bulk COF was measured.³⁰⁸

The boronic ester COF TPE-Ph (from 1,2,4,5-tetrahydroxybenzene and tetraphenylethylene-tetraboronic acid) with the ETTA unit as the boronic acid building block showed fluorescence quenching upon addition of ammonia, with a substantial fluorescence decrease of 30% at an ammonia content of 1 ppm (measured in toluene).²⁴

The ketoenamine COFs 3BD and 3'PD derived from a Michael addition-elimination reaction (from amines and β -ketoenols, see Table 1.26 for details) featured fluorescence quenching with nitro- and peroxide-based explosives with a detection onset of $\approx 1 \mu\text{M}$ for triacetone triperoxide. The fluorescence quenching with this compound presumably originated from the oxidation of the enamine units.³⁰⁴ The imine-linked TAT-COF-2 (from 2,7,12-triformyl-5,10,15-triethyltriindole and 1,4-phenylenediamine) showed a change in fluorescence intensity with a variety of compounds, with nitrobenzene, 2-nitrotoluene and phenol leading to efficient fluorescence quenching.¹⁵²

Delaminated sheets of the COF TfpBDH (from pyromellitic-*N,N'*-bisaminoimide and 1,3,5-tris(4-formylphenyl)benzene) featured fluorescence quenching with nitroaromatic compounds. Thereby the quenching was significantly stronger with 2,4,6-trinitrophenol than with other nitroaromatic analytes, supposedly resulting from charge transfer of the picrate anion (TNP^-) to the COF.²⁴³ The concept of quenched fluorescence was also applied for Hg^{2+} detection.

The hydrazone COF LZU-8, synthesized from an (ethylthio)propoxy-functionalized hydrazide and TFB, features a strong fluorescence, which is effectively quenched in the presence of Hg^{2+} -ions. Here, the thiol units served as sensitive receptors for Hg^{2+} , leading to a decrease in fluorescence of 83% in a 33 μM Hg^{2+} solution. Due to this specific interaction, the COF responded selectively to Hg^{2+} ions and was also usable in aqueous solution. Furthermore, the removal of Hg^{2+} from the COF framework was demonstrated, showing the recyclability of this material.²⁴⁰

Likewise, the azine-linked COF JLU-3 from hydrazine and a hydroxyl-functionalized triformylbenzene was used as Cu^{2+} detector *via* fluorescence quenching upon interaction of the Cu^{2+} -ions with the COF framework. Removal of the Cu^{2+} -ions with a chelating agent turned on the fluorescence again, demonstrating the COF's recyclability. COF-JLU-3 showed the strongest quenching effect with Cu^{2+} , and less response towards Co^{2+} , Fe^{3+} , and Ni^{2+} .²⁵⁷

1.6.7 Drug Delivery

Recently, first examples of the successful application of COF particles as carriers for drug delivery have been reported. Fang et al. synthesized 3D imide COFs from pyromellitic dianhydride and the amines 1,3,5,7-tetraaminoadamantane and tetrakis(4-aminophenyl)methane, respectively.

They were loaded with Ibuprofen, captopril or caffeine and showed a slow release of these drugs over several days *in vitro*.³⁰⁷ Bai et al. were the first to report the cell uptake of drug-loaded COF particles and drug release in the cells. For this purpose, they synthesized two imine COFs co-condensing TFB with benzidine to form PI-2-COF and with TAPP to form PI-3-COF (with particle diameters of ≈ 50 nm). Both COFs were successfully loaded with the anticancer drug 5-fluorouracil (by immersing the COFs in a solution of 5-fluorouracil), captopril or ibuprofen and taken up by cells of the MCF-7 cell line (Figure 1.46).¹³⁸

Triazine triphenyl aldehyde and triazine triphenylamine were co-condensed by Vyas et al. to form the imine COF TTI-COF. H-bonding interactions of the imine groups of the COF with the anti-cancer drug Quercetin were utilized to bind the drug in the COF pores. The loaded COF particles were taken up by human breast carcinoma cells and led to a lower proliferation rate compared to the bare drug.¹⁵⁰

The mixed ketoenamine- and hydrazone-linked COF TpASH (from 4-aminobenzohydrazide and TPG) was postsynthetically modified in a three-step

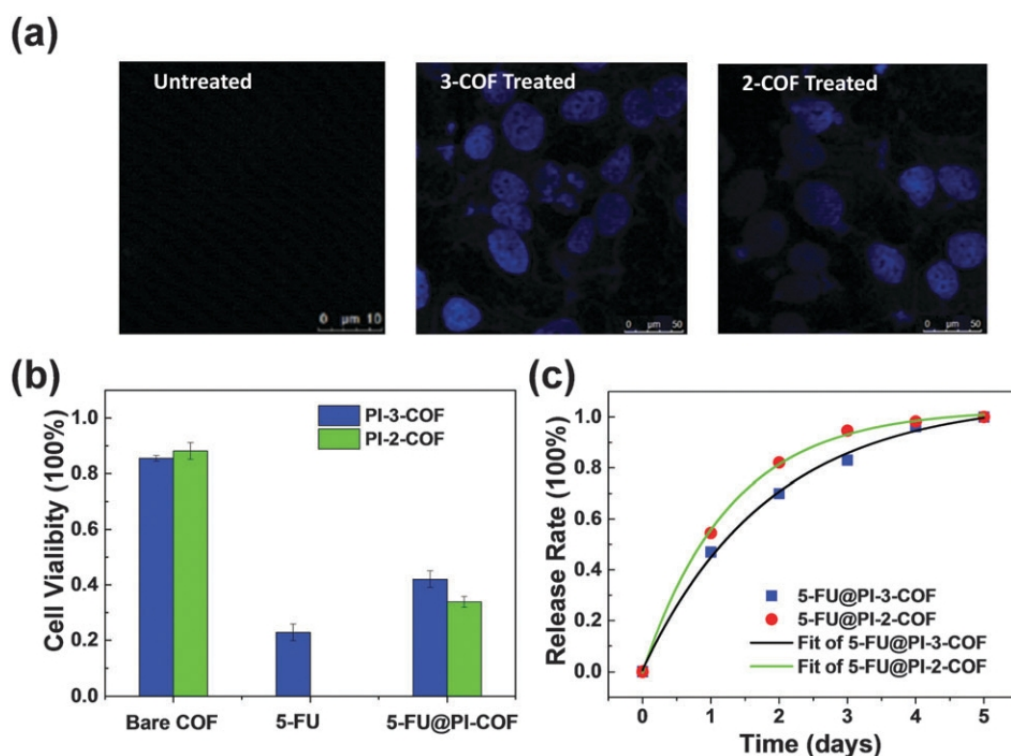


Figure 1.46: (a) Confocal images of cells before and after the treatment with drug-loaded COFs. (b) Quantitative MTT analysis showing the cell viability when incubated with bare COFs, 5-FU, and 5-FU loaded COFs for 24 h. Corresponding concentrations are $100 \mu\text{g mL}^{-1}$, $16 \mu\text{g mL}^{-1}$ and $100 \mu\text{g mL}^{-1}$. (c) Release profiles of two 5-FU loaded COFs at $100 \mu\text{g mL}^{-1}$ and corresponding fitting curves. Reproduced from ref. 138 with permission of The Royal Society of Chemistry.

route to establish a functionalization with folic acid and a delamination of the COF to produce nanosheets. These functionalized COFs were applied in the targeted delivery of 5-fluorouracil in MDA-MB-231 cell lines and showed preferential uptake into cancer cells, as the latter feature an overexpression of folate receptors. The loaded COFs were also shown to induce cell death *via* apoptosis.²⁵⁹

1.7 Conclusion and Perspectives

In this article, we have provided a comprehensive overview over the structural diversity of covalent organic frameworks developed so far, the relevant synthesis techniques and the accessible variety of COF morphologies, as well as a discussion on demonstrated and potential applications. In the past few years, the structural diversity of COFs has greatly expanded, alongside with a broadening of the scope of applications of COFs.

Novel building block structures and geometries have given rise to the development of numerous COFs with dual or triple pore geometries and new pore shapes. The post-synthetic modification of as-synthesized COFs has proven to be a versatile method to circumvent structural or synthetic limitations for the incorporation of functional groups and bulky moieties.

Important knowledge about factors controlling packing behavior and crystallinity of COFs as well as insights into the mechanisms of COF formation have been gained, but many questions are still open. It is anticipated that novel strategies to lock in the spatial positions of building blocks in COFs and thus to achieve improved stacking order will give rise to a pronounced enhancement of their performance in optoelectronics and related applications.

The development of new linkage motifs as well as new building blocks in recent years will open up numerous possibilities for the design of new COF structures and we expect to see a rapid increase of new structures. Importantly, chemically stable COF linkages open up whole new fields of applications under harsh conditions, including heterogeneous catalysis and electrochemical applications. The ability to design an enormous structural space of porous organic frameworks with variable pore diameters and to precisely position almost arbitrary molecular moieties with a broad range of functionalities offers great intellectual challenges and inspiration for intriguing applications - we have just begun to open the door to this exciting world.

Bibliography

- [1] C. S. Diercks and O. M. Yaghi. *Science*, **2017**, 355.
- [2] N. Huang, P. Wang, and D. Jiang. *Nat. Rev. Mater.*, **2016**, 1, 16068.
- [3] J. W. Colson and W. R. Dichtel. *Nat. Chem.*, **2013**, 5, 453–65.
- [4] S.-Y. Ding and W. Wang. *Chem. Soc. Rev.*, **2013**, 42, 548–568.
- [5] M. E. Davis. *Chem. Mater*, **2014**, 26, 239–245.
- [6] Y. Li and J. Yu. *Chem. Rev.*, **2014**, 114, 7268–7316.
- [7] C. Baerlocher, L. B. McCusker, and D. H. Olson. *Atlas of Zeolite Framework Types (Sixth Edition)*. Amsterdam: Elsevier Science B.V., **2007**.
- [8] W. Lu, Z. Wei, Z.-Y. Gu, T.-F. Liu, J. Park, J. Park, J. Tian, M. Zhang, Q. Zhang, T. Gentle Iii, M. Bosch, and H.-C. Zhou. *Chem. Soc. Rev.*, **2014**, 43, 5561–5593.
- [9] H. Furukawa, K. E. Cordova, M. O’Keeffe, and O. M. Yaghi. *Science*, **2013**, 341.
- [10] S. Kaskel, ed. *The Chemistry of Metal-Organic Frameworks. Synthesis, Characterization, and Applications*. Weinheim, Germany: Wiley-VCH Verlag GmbH & Co. KGaA, **2017**.
- [11] T. Ben and S. Qiu. *CrystEngComm*, **2013**, 15, 17–26.
- [12] D. Ramimoghadam, E. M. Gray, and C. J. Webb. *Int. J. Hydrogen Energy*, **2016**, 41, 16944–16965.
- [13] N. B. McKeown and P. M. Budd. *Chem. Soc. Rev.*, **2006**, 35, 675–683.
- [14] A. P. Côté, A. I. Benin, N. W. Ockwig, M. O’Keeffe, A. J. Matzger, and O. M. Yaghi. *Science*, **2005**, 310, 1166–1170.
- [15] A. P. Côté, H. M. El-Kaderi, H. Furukawa, J. R. Hunt, and O. M. Yaghi. *J. Am. Chem. Soc.*, **2007**, 129, 12914–12915.
- [16] E. L. Spitler, B. T. Koo, J. L. Novotney, J. W. Colson, F. J. Uribe-Romo, G. D. Gutierrez, P. Clancy, and W. R. Dichtel. *J. Am. Chem. Soc.*, **2011**, 133, 19416–19421.

- [17] S. Wan, J. Guo, J. Kim, H. Ihee, and D. Jiang. *Angew. Chem., Int. Ed.*, **2008**, *47*, 8826–8830.
- [18] Q. Sun, B. Aguila, J. Perman, L. D. Earl, C. W. Abney, Y. Cheng, H. Wei, N. Nguyen, L. Wojtas, and S. Ma. *J. Am. Chem. Soc.*, **2017**, *139*, 2786–2793.
- [19] X. Ding, J. Guo, X. Feng, Y. Honsho, J. Guo, S. Seki, P. Maitarad, A. Saeki, S. Nagase, and D. Jiang. *Angew. Chem., Int. Ed.*, **2011**, *50*, 1289–1293.
- [20] E. L. Spitler, J. W. Colson, F. J. Uribe-Romo, A. R. Woll, M. R. Giovino, A. Saldivar, and W. R. Dichtel. *Angew. Chem., Int. Ed.*, **2012**, *51*, 2623–2627.
- [21] L. Chen, K. Furukawa, J. Gao, A. Nagai, T. Nakamura, Y. Dong, and D. Jiang. *J. Am. Chem. Soc.*, **2014**, *136*, 9806–9809.
- [22] N. Huang, L. Zhai, D. E. Coupry, M. A. Addicoat, K. Okushita, K. Nishimura, T. Heine, and D. Jiang. *Nat. Commun.*, **2016**, *7*, 12325.
- [23] X. Chen, M. Addicoat, E. Jin, H. Xu, T. Hayashi, F. Xu, N. Huang, S. Irle, and D. Jiang. *Sci. Rep.*, **2015**, *5*, 14650.
- [24] S. Dalapati, E. Jin, M. Addicoat, T. Heine, and D. Jiang. *J. Am. Chem. Soc.*, **2016**, *138*, 5797–5800.
- [25] S. Dalapati, S. Jin, J. Gao, Y. Xu, A. Nagai, and D. Jiang. *J. Am. Chem. Soc.*, **2013**, *135*, 17310–3.
- [26] S. Jin, T. Sakurai, T. Kowalczyk, S. Dalapati, F. Xu, H. Wei, X. Chen, J. Gao, S. Seki, S. Irle, and D. Jiang. *Chem. - Eur. J.*, **2014**, *20*, 14608–14613.
- [27] S. Dalapati, M. Addicoat, S. Jin, T. Sakurai, J. Gao, H. Xu, S. Irle, S. Seki, and D. Jiang. *Nat. Commun.*, **2015**, *6*, 7786.
- [28] Y. Du, H. Yang, J. M. Whiteley, S. Wan, Y. Jin, S.-H. Lee, and W. Zhang. *Angew. Chem., Int. Ed.*, **2016**, *55*, 1737–1741.
- [29] X. Feng, Y. Dong, and D. Jiang. *CrystEngComm*, **2013**, *15*, 1508–1511.
- [30] X. Wang, X. Han, J. Zhang, X. Wu, Y. Liu, and Y. Cui. *J. Am. Chem. Soc.*, **2016**, *138*, 12332–12335.
- [31] J. R. Hunt, C. J. Doonan, J. D. LeVangie, A. P. Côté, and O. M. Yaghi. *J. Am. Chem. Soc.*, **2008**, *130*, 11872–3.
- [32] G. Lin, H. Ding, D. Yuan, B. Wang, and C. Wang. *J. Am. Chem. Soc.*, **2016**, *138*, 3302–3305.

- [33] D. N. Bunck and W. R. Dichtel. *Angew. Chem., Int. Ed.*, **2012**, *51*, 1885–1889.
- [34] H. M. El-Kaderi, J. R. Hunt, J. L. Mendoza-Cortes, A. P. Côté, R. E. Taylor, M. O’Keeffe, and O. M. Yaghi. *Science*, **2007**, *316*, 268–272.
- [35] J. F. Dienstmaier, D. D. Medina, M. Dogru, P. Knochel, T. Bein, W. M. Heckl, and M. Lackinger. *ACS Nano*, **2012**, *6*, 7234–7242.
- [36] Y. Li and R. T. Yang. *AIChE J.*, **2008**, *54*, 269–279.
- [37] M. A. A. Musa, C.-Y. Yin, and R. M. Savory. *Mater. Chem. Phys.*, **2010**, *123*, 5–8.
- [38] J. F. Dienstmaier, A. M. Gigler, A. J. Goetz, P. Knochel, T. Bein, A. Lyapin, S. Reichlmaier, W. M. Heckl, and M. Lackinger. *ACS Nano*, **2011**, *5*, 9737–45.
- [39] S.-T. Yang, J. Kim, H.-Y. Cho, S. Kim, and W.-S. Ahn. *RSC Adv.*, **2012**, *2*, 10179–10181.
- [40] H. Oh, S. B. Kalidindi, Y. Um, S. Bureekaew, R. Schmid, R. A. Fischer, and M. Hirscher. *Angew. Chem., Int. Ed.*, **2013**, *52*, 13219–13222.
- [41] S. B. Kalidindi, C. Wiktor, A. Ramakrishnan, J. Wessing, A. Schneemann, G. Van Tendeloo, and R. A. Fischer. *Chem. Commun.*, **2013**, *49*, 463–465.
- [42] D. Cui, J. M. MacLeod, M. Ebrahimi, D. F. Perepichka, and F. Rosei. *Chem. Commun.*, **2015**, *51*, 16510–16513.
- [43] J. Plas, O. Ivasenko, N. Martsinovich, M. Lackinger, and S. De Feyter. *Chem. Commun.*, **2016**, *52*, 68–71.
- [44] J. Yoo, S.-J. Cho, G. Y. Jung, S. H. Kim, K.-H. Choi, J.-H. Kim, C. K. Lee, S. K. Kwak, and S.-Y. Lee. *Nano Lett.*, **2016**, *16*, 3292–3300.
- [45] Z. A. Ghazi, L. Zhu, H. Wang, A. Naeem, A. M. Khattak, B. Liang, N. A. Khan, Z. Wei, L. Li, and Z. Tang. *Adv. Energy Mater.*, **2016**, *6*, 1601250.
- [46] Y. Chen and Z. Chen. *Talanta*, **2017**, *165*, 188–193.
- [47] Y. Du, D. Calabro, B. Wooler, Q. Li, S. Cundy, P. Kamakoti, D. Colmyer, K. Mao, and P. Ravikovitch. *J. Phys. Chem. C*, **2014**, *118*, 399–407.
- [48] Y. Du, K. Mao, P. Kamakoti, B. Wooler, S. Cundy, Q. Li, P. Ravikovitch, and D. Calabro. *J. Mater. Chem. A*, **2013**, *1*, 13171–13178.
- [49] Y. Du, D. Calabro, B. Wooler, P. Kortunov, Q. Li, S. Cundy, and K. Mao. *Chem. Mater.*, **2015**, *27*, 1445–1447.

- [50] D. Cui, J. M. MacLeod, M. Ebrahimi, and F. Rosei. *CrystEngComm*, **2017**, *19*, 4927–4932.
- [51] G. Li, K. Zhang, and T. Tsuru. *ACS Appl. Mater. Interfaces*, **2017**, *9*, 8433–8436.
- [52] S. Spitzer, A. Rastgoo-Lahrood, K. Macknapp, V. Ritter, S. Sotier, W. M. Heckl, and M. Lackinger. *Chem. Commun.*, **2017**, *53*, 5147–5150.
- [53] T. Pham, K. A. Forrest, M. Mostrom, J. R. Hunt, H. Furukawa, J. Eckert, and B. Space. *Phys. Chem. Chem. Phys.*, **2017**, *19*, 13075–13082.
- [54] N. A. A. Zwaneveld, R. Pawlak, M. Abel, D. Catalin, D. Gigmes, D. Bertin, and L. Porte. *J. Am. Chem. Soc.*, **2008**, *130*, 6678–6679.
- [55] C.-Z. Guan, D. Wang, and L.-J. Wan. *Chem. Commun.*, **2012**, *48*, 24, 2943–2945.
- [56] S. Wan, J. Guo, J. Kim, H. Ihee, and D. Jiang. *Angew. Chem., Int. Ed.*, **2009**, *48*, 5439–5442.
- [57] D. D. Medina, J. M. Rotter, Y. Hu, M. Dogru, V. Werner, F. Auras, J. T. Markiewicz, P. Knochel, and T. Bein. *J. Am. Chem. Soc.*, **2015**, *137*, 1016–1019.
- [58] C. Liu, W. Zhang, Q. Zeng, and S. Lei. *Chem. - Eur. J.*, **2016**, *22*, 6768–6773.
- [59] S. B. Kalidindi, H. Oh, M. Hirscher, D. Esken, C. Wiktor, S. Turner, G. Van Tendeloo, and R. A. Fischer. *Chem. - Eur. J.*, **2012**, *18*, 10848–10856.
- [60] S. B. Kalidindi, K. Yusenko, and R. A. Fischer. *Chem. Commun.*, **2011**, *47*, 8506–8.
- [61] S. D. Brucks, D. N. Bunck, and W. R. Dichtel. *Polymer*, **2014**, *55*, 330–334.
- [62] D. N. Bunck and W. R. Dichtel. *Chem. Commun.*, **2013**, *49*, 2457–2459.
- [63] R. W. Tilford, W. R. Gemmill, H.-C. zur Loye, and J. J. Lavigne. *Chem. Mater.*, **2006**, *18*, 5296–5301.
- [64] R. W. Tilford, I. Mugavero Sam J., P. J. Pellechia, and J. J. Lavigne. *Adv. Mater.*, **2008**, *20*, 2741–2746.
- [65] L. M. Lanni, R. W. Tilford, M. Bharathy, and J. J. Lavigne. *J. Am. Chem. Soc.*, **2011**, *133*, 13975–13983.
- [66] X. Feng, L. Liu, Y. Honsho, A. Saeki, S. Seki, S. Irle, Y. Dong, A. Nagai, and D. Jiang. *Angew. Chem., Int. Ed.*, **2012**, *51*, 2618–22.

- [67] X. Feng, L. Chen, Y. Dong, and D. Jiang. *Chem. Commun.*, **2011**, *47*, 1979–1981.
- [68] H. Ma, H. Ren, S. Meng, Z. Yan, H. Zhao, F. Sun, and G. Zhu. *Chem. Commun.*, **2013**, *49*, 9773–9775.
- [69] N. Huang, X. Ding, J. Kim, H. Ihee, and D. Jiang. *Angew. Chem., Int. Ed.*, **2015**, *54*, 8704–8707.
- [70] M. Dogru, A. Sonnauer, A. Gavryushin, P. Knochel, and T. Bein. *Chem. Commun.*, **2011**, *47*, 1707–1709.
- [71] S. Wan, F. Gandara, A. Asano, H. Furukawa, A. Saeki, S. K. Dey, L. Liao, M. W. Ambrogio, Y. Y. Botros, X.-F. Duan, S. Seki, J. F. Stoddart, and O. M. Yaghi. *Chem. Mater.*, **2011**, *23*, 4094–4097.
- [72] S. S. Han, H. Furukawa, O. M. Yaghi, and I. Goddard William A. *J. Am. Chem. Soc.*, **2008**, *130*, 11580–11581.
- [73] N. L. Campbell, R. Clowes, L. K. Ritchie, and A. I. Cooper. *Chem. Mater.*, **2009**, *21*, 204–206.
- [74] J. W. Colson, A. R. Woll, A. Mukherjee, M. P. Levendorf, E. L. Spitler, V. B. Shields, M. G. Spencer, J. Park, and W. R. Dichtel. *Science*, **2011**, *332*, 228–31.
- [75] B. J. Smith and W. R. Dichtel. *J. Am. Chem. Soc.*, **2014**, *136*, 8783–8789.
- [76] B. J. Smith, N. Hwang, A. D. Chavez, J. L. Novotney, and W. R. Dichtel. *Chem. Commun.*, **2015**, *51*, 7532–7535.
- [77] J. T. Yoo, S. H. Lee, S. Hirata, C. R. Kim, C. K. Lee, T. Shiraki, N. Nakashima, and J. K. Shim. *Chem. Lett.*, **2015**, *44*, 560–562.
- [78] T. Bao, P. Tang, D. Kong, Z. Mao, and Z. Chen. *J. Chromatogr. A*, **2016**, *1445*, 140–8.
- [79] M. Calik, T. Sick, M. Dogru, M. Döblinger, S. Datz, H. Budde, A. Hartschuh, F. Auras, and T. Bein. *J. Am. Chem. Soc.*, **2016**, *138*, 1234–1239.
- [80] Y.-B. Huang, P. Pachfule, J.-K. Sun, and Q. Xu. *J. Mater. Chem. A*, **2016**, *4*, 4273–4279.
- [81] R. P. Bisbey, C. R. DeBlase, B. J. Smith, and W. R. Dichtel. *J. Am. Chem. Soc.*, **2016**, *138*, 11433–11436.
- [82] D. A. Vazquez-Molina, G. S. Mohammad-Pour, C. Lee, M. W. Logan, X. Duan, J. K. Harper, and F. J. Uribe-Romo. *J. Am. Chem. Soc.*, **2016**, *138*, 9767–9770.

- [83] B. J. Smith, L. R. Parent, A. C. Overholts, P. A. Beaucage, R. P. Bisbey, A. D. Chavez, N. Hwang, C. Park, A. M. Evans, N. C. Gianneschi, and W. R. Dichtel. *ACS Cent. Sci.*, **2017**, *3*, 58–65.
- [84] S. Rager, M. Dogru, V. Werner, A. Gavryushin, M. Götz, H. Engelke, D. D. Medina, P. Knochel, and T. Bein. *CrystEngComm*, **2017**, *19*, 4886–4891.
- [85] E. L. Spitler, M. R. Giovino, S. L. White, and W. R. Dichtel. *Chem. Sci.*, **2011**, *2*, 1588–1593.
- [86] A. Nagai, Z. Guo, X. Feng, S. Jin, X. Chen, X. Ding, and D. Jiang. *Nat. Commun.*, **2011**, *2*, 1542/1–1542/8.
- [87] C. J. Doonan, D. J. Tranchemontagne, T. G. Glover, J. R. Hunt, and O. M. Yaghi. *Nat. Chem.*, **2010**, *2*, 235–238.
- [88] S. Jin, K. Furukawa, M. Addicoat, L. Chen, S. Takahashi, S. Irle, T. Nakamura, and D. Jiang. *Chem. Sci.*, **2013**, *4*, 4505–4511.
- [89] L. Yu, Z.-B. Li, and D. Wang. *Chem. Commun.*, **2016**, *52*, 13771–13774.
- [90] L. M. Salonen, D. D. Medina, E. Carbo-Argibay, M. G. Goesten, L. Mafra, N. Guldris, J. M. Rotter, D. G. Stroppa, and C. Rodriguez-Abreu. *Chem. Commun.*, **2016**, *52*, 7986–7989.
- [91] J.-T. Yu, Z. Chen, J. Sun, Z.-T. Huang, and Q.-Y. Zheng. *Journal of Materials Chemistry*, **2012**, *22*, 5369–5373.
- [92] J. Zhen, S. Ding, W. Wang, J. Liu, J. Sun, Z. Huang, and Q. Zheng. *Chin. J. Chem.*, **2016**, *34*, 783–787.
- [93] L. A. Baldwin, J. W. Crowe, M. D. Shannon, C. P. Jaroniec, and P. L. McGrier. *Chem. Mater.*, **2015**, *27*, 6169–6172.
- [94] H. Yang, Y. Du, S. Wan, G. D. Trahan, Y. Jin, and W. Zhang. *Chem. Sci.*, **2015**, *6*, 4049–4053.
- [95] J. W. Crowe, L. A. Baldwin, and P. L. McGrier. *J. Am. Chem. Soc.*, **2016**, *138*, 10120–10123.
- [96] Z. Kahveci, T. Islamoglu, G. A. Shar, R. Ding, and H. M. El-Kaderi. *CrystEngComm*, **2013**, *15*, 1524–1527.
- [97] E. L. Spitler and W. R. Dichtel. *Nat. Chem.*, **2010**, *2*, 672–677.

- [98] X. Ding, X. Feng, A. Saeki, S. Seki, A. Nagai, and D. Jiang. *Chem. Commun.*, **2012**, *48*, 8952–8954.
- [99] J. W. Colson, J. A. Mann, C. R. De Blase, and W. R. Dichtel. *J. Polym. Sci., Part A: Polym. Chem.*, **2015**, *53*, 378–384.
- [100] V. S. P. K. Neti, X. Wu, M. Hosseini, R. A. Bernal, S. Deng, and L. Echegoyen. *CrystEngComm*, **2013**, *15*, 7157–7160.
- [101] J. Zhang, L. Wang, N. Li, J. Liu, W. Zhang, Z. Zhang, N. Zhou, and X. Zhu. *CrystEngComm*, **2014**, *16*, 6547–6551.
- [102] X. Feng, L. Chen, Y. Honsho, O. Saengsawang, L. Liu, L. Wang, A. Saeki, S. Irle, S. Seki, Y. Dong, and D. Jiang. *Adv. Mater.*, **2012**, *24*, 3026–3031.
- [103] G. H. V. Bertrand, V. K. Michaelis, T.-C. Ong, R. G. Griffin, and M. Dincă. *Proc. Natl. Acad. Sci. U. S. A.*, **2013**, *110*, 4923–4928.
- [104] M. Dogru, M. Handloser, F. Auras, T. Kunz, D. Medina, A. Hartschuh, P. Knochel, and T. Bein. *Angew. Chem., Int. Ed.*, **2013**, *52*, 2920–2924.
- [105] Y. Chen, H. Cui, J. Zhang, K. Zhao, D. Ding, J. Guo, L. Li, Z. Tian, and Z. Tang. *RSC Adv.*, **2015**, *5*, 92573–92576.
- [106] D. D. Medina, V. Werner, F. Auras, R. Tautz, M. Dogru, J. Schuster, S. Linke, M. Döblinger, J. Feldmann, P. Knochel, and T. Bein. *ACS Nano*, **2014**, *8*, 4042–4052.
- [107] M. S. Lohse, J. M. Rotter, J. T. Margraf, V. Werner, M. Becker, S. Herbert, P. Knochel, T. Clark, T. Bein, and D. D. Medina. *CrystEngComm*, **2016**, *18*, 4295–4302.
- [108] D. D. Medina, M. L. Petrus, A. N. Jumabekov, J. T. Margraf, S. Weinberger, J. M. Rotter, T. Clark, and T. Bein. *ACS Nano*, **2017**, *11*, 2706–2713.
- [109] S. Duhović and M. Dincă. *Chem. Mater.*, **2015**, *27*, 5487–5490.
- [110] X. Ding, L. Chen, Y. Honsho, X. Feng, O. Saengsawang, J. Guo, A. Saeki, S. Seki, S. Irle, S. Nagase, V. Parasuk, and D. Jiang. *J. Am. Chem. Soc.*, **2011**, *133*, 14510–14513.
- [111] C. Liu, Y. Yu, W. Zhang, Q. Zeng, and S. Lei. *Chem. - Eur. J.*, **2016**, *22*, 18412–18418.

- [112] M. Calik, F. Auras, L. M. Salonen, K. Bader, I. Grill, M. Handloser, D. D. Medina, M. Dogru, F. Löbermann, D. Trauner, A. Hartschuh, and T. Bein. *J. Am. Chem. Soc.*, **2014**, *136*, 17802–17807.
- [113] F. Xu, S. Jin, H. Zhong, D. Wu, X. Yang, X. Chen, H. Wei, R. Fu, and D. Jiang. *Sci. Rep.*, **2015**, *5*, 8225.
- [114] V. S. P. K. Neti, X. Wu, S. Deng, and L. Echegoyen. *CrystEngComm*, **2013**, *15*, 6892–6895.
- [115] S. Jin, M. Supur, M. Addicoat, K. Furukawa, L. Chen, T. Nakamura, S. Fukuzumi, S. Irle, and D. Jiang. *J. Am. Chem. Soc.*, **2015**, *137*, 7817–7827.
- [116] S. Jin, X. Ding, X. Feng, M. Supur, K. Furukawa, S. Takahashi, M. Addicoat, M. E. El-Khouly, T. Nakamura, S. Irle, S. Fukuzumi, A. Nagai, and D. Jiang. *Angew. Chem., Int. Ed.*, **2013**, *52*, 2017–2021.
- [117] I. Berlanga, M. L. Ruiz-González, J. M. González-Calbet, J. L. G. Fierro, R. Mas-Ballesté, and F. Zamora. *Small*, **2011**, *7*, 1207–1211.
- [118] L. A. Baldwin, J. W. Crowe, D. A. Pyles, and P. L. McGrier. *J. Am. Chem. Soc.*, **2016**, *138*, 15134–15137.
- [119] F. J. Uribe-Romo, J. R. Hunt, H. Furukawa, C. Klöck, M. O’Keeffe, and O. M. Yaghi. *J. Am. Chem. Soc.*, **2009**, *131*, 4570–4571.
- [120] L. Wang, B. Dong, R. Ge, F. Jiang, J. Xiong, Y. Gao, and J. Xu. *Microporous Mesoporous Mater.*, **2016**, *224*, 95–99.
- [121] L. Xu, X. Zhou, Y. Yu, W. Q. Tian, J. Ma, and S. Lei. *ACS Nano*, **2013**, *7*, 8066–8073.
- [122] L. Wang, B. Dong, R. Ge, F. Jiang, and J. Xu. *ACS Appl. Mater. Interfaces*, **2017**, *9*, 7108–7114.
- [123] H.-S. Xu, S.-Y. Ding, W.-K. An, H. Wu, and W. Wang. *J. Am. Chem. Soc.*, **2016**, *138*, 11489–11492.
- [124] L. Zou, X. Yang, S. Yuan, and H.-C. Zhou. *CrystEngComm*, **2017**, *19*, 4868–4871.
- [125] Q. Fang, S. Gu, J. Zheng, Z. Zhuang, S. Qiu, and Y. Yan. *Angew. Chem., Int. Ed.*, **2014**, *53*, 2878–2882.
- [126] S.-Y. Ding, J. Gao, Q. Wang, Y. Zhang, W.-G. Song, C.-Y. Su, and W. Wang. *J. Am. Chem. Soc.*, **2011**, *133*, 19816–19822.

- [127] Y. Peng, W. K. Wong, Z. Hu, Y. Cheng, D. Yuan, S. A. Khan, and D. Zhao. *Chem. Mater.*, **2016**, *28*, 5095–5101.
- [128] G. Das, D. Balaji Shinde, S. Kandambeth, B. P. Biswal, and R. Banerjee. *Chem. Commun.*, **2014**, *50*, 12615–12618.
- [129] P. Wang, M. Kang, S. Sun, Q. Liu, Z. Zhang, and S. Fang. *Chin. J. Chem.*, **2014**, *32*, 838–843.
- [130] P. Wang, Q. Wu, L. Han, S. Wang, S. Fang, Z. Zhang, and S. Sun. *RSC Adv.*, **2015**, *5*, 27290–27294.
- [131] X. Niu, S. Ding, W. Wang, Y. Xu, Y. Xu, H. Chen, and X. Chen. *J. Chromatogr. A*, **2016**, *1436*, 109–117.
- [132] L. Chen, L. Zhang, Z. Chen, H. Liu, R. Luque, and Y. Li. *Chem. Sci.*, **2016**, *7*, 6015–6020.
- [133] H. Wang, B. He, F. Liu, C. Stevens, M. A. Brady, S. Cai, C. Wang, T. P. Russell, T.-W. Tan, and Y. Liu. *J. Mater. Chem. C*, **2017**, *5*, 5090–5095.
- [134] X.-H. Liu, C.-Z. Guan, S.-Y. Ding, W. Wang, H.-J. Yan, D. Wang, and L.-J. Wan. *J. Am. Chem. Soc.*, **2013**, *135*, 10470–10474.
- [135] L. Xu, X. Zhou, W. Q. Tian, T. Gao, Y. F. Zhang, S. Lei, and Z. F. Liu. *Angew. Chem., Int. Ed.*, **2014**, *53*, 9564–9568.
- [136] J. Sun, X. Zhou, and S. Lei. *Chem. Commun.*, **2016**, *52*, 8691–8694.
- [137] Q. Gao, L. Bai, Y. Zeng, P. Wang, X. Zhang, R. Zou, and Y. Zhao. *Chem. - Eur. J.*, **2015**, *21*, 16818–16822.
- [138] L. Bai, S. Z. F. Phua, W. Q. Lim, A. Jana, Z. Luo, H. P. Tham, L. Zhao, Q. Gao, and Y. Zhao. *Chem. Commun.*, **2016**, *52*, 4128–4131.
- [139] L. Bai, Q. Gao, and Y. Zhao. *J. Mater. Chem. A*, **2016**, *4*, 14106–14110.
- [140] J. Dong, Y. Wang, G. Liu, Y. Cheng, and D. Zhao. *CrystEngComm*, **2017**, *19*, 4899–4904.
- [141] A. de la Peña Ruigómez, D. Rodríguez-San-Miguel, K. C. Stylianou, M. Cavallini, D. Gentili, F. Liscio, S. Milita, O. M. Roscioni, M. L. Ruiz-González, C. Carbonell, D. MasPOCH, R. Mas-Ballesté, J. L. Segura, and F. Zamora. *Chem. - Eur. J.*, **2015**, *21*, 10666–10670.

- [142] J. Romero, D. Rodríguez-San-Miguel, A. Ribera, R. Mas-Ballesté, T. F. Otero, I. Manet, F. Licio, G. Abellán, F. Zamora, and E. Coronado. *J. Mater. Chem. A*, **2017**, *5*, 4343–4351.
- [143] D. Rodríguez-San-Miguel, A. Abrishamkar, J. A. R. Navarro, R. Rodríguez-Trujillo, D. B. Amabilino, R. Mas-Ballesté, F. Zamora, and J. Puigmartí-Luis. *Chem. Commun.*, **2016**, *52*, 9212–9215.
- [144] D. Rodríguez-San-Miguel, J. J. Corral-Pérez, E. Gil-González, D. Cuellas, J. Arauzo, V. M. Monsalvo, V. Carcelén, and F. Zamora. *CrystEngComm*, **2017**, *19*, 4872–4876.
- [145] Q. Gao, L. Bai, X. Zhang, P. Wang, P. Li, Y. Zeng, R. Zou, and Y. Zhao. *Chin. J. Chem.*, **2015**, *33*, 90–94.
- [146] D. Mullangi, V. Dhavale, S. Shalini, S. Nandi, S. Collins, T. Woo, S. Kurungot, and R. Vaidhyanathan. *Adv. Energy Mater.*, **2016**, *6*, n/a.
- [147] D. Mullangi, S. Shalini, S. Nandi, B. Choksi, and R. Vaidhyanathan. *J. Mater. Chem. A*, **2017**, *5*, 8376–8384.
- [148] L. Zhai, N. Huang, H. Xu, Q. Chen, and D. Jiang. *Chem. Commun.*, **2017**, *53*, 4242–4245.
- [149] X.-H. Liu, Y.-P. Mo, J.-Y. Yue, Q.-N. Zheng, H.-J. Yan, D. Wang, and L.-J. Wan. *Small*, **2014**, *10*, 4934–4939.
- [150] V. S. Vyas, M. Vishwakarma, I. Moudrakovski, F. Haase, G. Savasci, C. Ochsenfeld, J. P. Spatz, and B. V. Lotsch. *Adv. Mater.*, **2016**, *28*, 8749–8754.
- [151] Y.-X. Ma, Z.-J. Li, L. Wei, S.-Y. Ding, Y.-B. Zhang, and W. Wang. *J. Am. Chem. Soc.*, **2017**, *139*, 4995–4998.
- [152] Y.-F. Xie, S.-Y. Ding, J.-M. Liu, W. Wang, and Q.-Y. Zheng. *J. Mater. Chem. C*, **2015**, *3*, 10066–10069.
- [153] S. Lin, Y. Hou, X. Deng, H. Wang, S. Sun, and X. Zhang. *RSC Adv.*, **2015**, *5*, 41017–41024.
- [154] L. Xu, S.-Y. Ding, J. Liu, J. Sun, W. Wang, and Q.-Y. Zheng. *Chem. Commun.*, **2016**, *52*, 4706–4709.
- [155] J.-R. Song, J. Sun, J. Liu, Z.-T. Huang, and Q.-Y. Zheng. *Chem. Commun.*, **2014**, *50*, 788–791.

- [156] L. H. Li, X. L. Feng, X. H. Cui, Y. X. Ma, S. Y. Ding, and W. Wang. *J. Am. Chem. Soc.*, **2017**, *139*, 6042–6045.
- [157] Y. Fan, Q. Wen, T.-G. Zhan, Q.-Y. Qi, J.-Q. Xu, and X. Zhao. *Chem. - Eur. J.*, **2017**, *23*, 5668–5672.
- [158] S.-L. Cai, K. Zhang, J.-B. Tan, S. Wang, S.-R. Zheng, J. Fan, Y. Yu, W.-G. Zhang, and Y. Liu. *ACS Macro Lett.*, **2016**, *5*, 1348–1352.
- [159] Z.-F. Pang, S.-Q. Xu, T.-Y. Zhou, R.-R. Liang, T.-G. Zhan, and X. Zhao. *J. Am. Chem. Soc.*, **2016**, *138*, 4710–4713.
- [160] M. G. Rabbani, A. K. Sekizkardes, Z. Kahveci, T. E. Reich, R. Ding, and H. M. El-Kaderi. *Chem. - Eur. J.*, **2013**, *19*, 3324–3328.
- [161] X. Chen, N. Huang, J. Gao, H. Xu, F. Xu, and D. Jiang. *Chem. Commun.*, **2014**, *50*, 6161–6163.
- [162] Y. Wu, H. Xu, X. Chen, J. Gao, and D. Jiang. *Chem. Commun.*, **2015**, *51*, 10096–10098.
- [163] X. Chen, J. Gao, and D. Jiang. *Chem. Lett.*, **2015**, *44*, 1257–1259.
- [164] W. Leng, R. Ge, B. Dong, C. Wang, and Y. Gao. *RSC Adv.*, **2016**, *6*, 37403–37406.
- [165] T.-Y. Zhou, S.-Q. Xu, Q. Wen, Z.-F. Pang, and X. Zhao. *J. Am. Chem. Soc.*, **2014**, *136*, 15885–15888.
- [166] Y. Tian, S.-Q. Xu, R.-R. Liang, C. Qian, G.-F. Jiang, and X. Zhao. *CrystEngComm*, **2017**, *19*, 4877–4881.
- [167] Z.-F. Pang, T.-Y. Zhou, R.-R. Liang, Q.-Y. Qi, and X. Zhao. *Chem. Sci.*, **2017**, *8*, 3866–3870.
- [168] S.-Q. Xu, T.-G. Zhan, Q. Wen, Z.-F. Pang, and X. Zhao. *ACS Macro Lett.*, **2016**, *5*, 99–102.
- [169] C. Qian, S. Q. Xu, G. F. Jiang, T. G. Zhan, and X. Zhao. *Chem. - Eur. J.*, **2016**, *22*, 17784–17789.
- [170] Z.-J. Yin, S.-Q. Xu, T.-G. Zhan, Q.-Y. Qi, Z.-Q. Wu, and X. Zhao. *Chem. Commun.*, **2017**, *53*, 7266–7269.
- [171] C. Qian, Q.-Y. Qi, G.-F. Jiang, F.-Z. Cui, Y. Tian, and X. Zhao. *J. Am. Chem. Soc.*, **2017**, *139*, 6736–6743.

- [172] Y. Zeng, R. Zou, Z. Luo, H. Zhang, X. Yao, X. Ma, R. Zou, and Y. Zhao. *J. Am. Chem. Soc.*, **2015**, *137*, 1020–1023.
- [173] H. Li, Q. Pan, Y. Ma, X. Guan, M. Xue, Q. Fang, Y. Yan, V. Valtchev, and S. Qiu. *J. Am. Chem. Soc.*, **2016**, *138*, 14783–14788.
- [174] J.-Y. Yue, Y.-P. Mo, S.-Y. Li, W.-L. Dong, T. Chen, and D. Wang. *Chem. Sci.*, **2017**, *8*, 2169–2174.
- [175] Y. Liu, Y. Ma, Y. Zhao, X. Sun, F. Gandara, H. Furukawa, Z. Liu, H. Zhu, C. Zhu, K. Suenaga, P. Oleynikov, A. S. Alshammari, X. Zhang, O. Terasaki, and O. M. Yaghi. *Science*, **2016**, *351*, 365–369.
- [176] A. Dutta, K. Koh, A. G. Wong-Foy, and A. J. Matzger. *Angew. Chem., Int. Ed.*, **2015**, *54*, 3983–3987.
- [177] H. L. Nguyen, F. Gandara, H. Furukawa, T. L. H. Doan, K. E. Cordova, and O. M. Yaghi. *J. Am. Chem. Soc.*, **2016**, *138*, 4330–4333.
- [178] W. Huang, Y. Jiang, X. Li, X. Li, J. Wang, Q. Wu, and X. Liu. *ACS Appl. Mater. Interfaces*, **2013**, *5*, 8845–8849.
- [179] Y. Jiang, W. Huang, J. Wang, Q. Wu, H. Wang, L. Pan, and X. Liu. *J. Mater. Chem. A*, **2014**, *2*, 8201–8204.
- [180] L. Ascherl, T. Sick, J. T. Margraf, S. H. Lapidus, M. Calik, C. Hettstedt, K. Karaghiosoff, M. Döblinger, T. Clark, K. W. Chapman, F. Auras, and T. Bein. *Nat. Chem.*, **2016**, *8*, 310–316.
- [181] J. Zhen, S. Ding, J. Liu, Z. Huang, W. Wang, and Q. Zheng. *CrystEngComm*, **2016**, *18*, 1039–1045.
- [182] M. Matsumoto, R. R. Dasari, W. Ji, C. H. Feriante, T. C. Parker, S. R. Marder, and W. R. Dichtel. *J. Am. Chem. Soc.*, **2017**, *139*, 4999–5002.
- [183] J. I. Feldblyum, C. H. McCreery, S. C. Andrews, T. Kurosawa, E. J. G. Santos, V. Duong, L. Fang, A. L. Ayzner, and Z. Bao. *Chem. Commun.*, **2015**, *51*, 13894–13897.
- [184] Z.-J. Li, S.-Y. Ding, H.-D. Xue, W. Cao, and W. Wang. *Chem. Commun.*, **2016**, *52*, 7217–7220.
- [185] S.-B. Yu, H. Lyu, J. Tian, H. Wang, D.-W. Zhang, Y. Liu, and Z.-T. Li. *Polym. Chem.*, **2016**, *7*, 3392–3397.

- [186] J.-Y. Yue, X.-H. Liu, B. Sun, and D. Wang. *Chem. Commun.*, **2015**, *51*, 14318–14321.
- [187] B. J. Smith, A. C. Overholts, N. Hwang, and W. R. Dichtel. *Chem. Commun.*, **2016**, *52*, 3690–3693.
- [188] G. Lin, C. Gao, Q. Zheng, Z. Lei, H. Geng, Z. Lin, H. Yang, and Z. Cai. *Chem. Commun.*, **2017**, *53*, 3649–3652.
- [189] P. J. Waller, S. J. Lyle, T. M. Osborn Popp, C. S. Diercks, J. A. Reimer, and O. M. Yaghi. *J. Am. Chem. Soc.*, **2016**, *138*, 15519–15522.
- [190] H. Xu, J. Gao, and D. Jiang. *Nat. Chem.*, **2015**, *7*, 905–912.
- [191] S. Kandambeth, V. Venkatesh, D. B. Shinde, S. Kumari, A. Halder, S. Verma, and R. Banerjee. *Nat. Commun.*, **2015**, *6*, 6786.
- [192] B. P. Biswal, S. Kandambeth, S. Chandra, D. B. Shinde, S. Bera, S. Karak, B. Garai, U. K. Kharul, and R. Banerjee. *J. Mater. Chem. A*, **2015**, *3*, 23664–23669.
- [193] Y.-P. Mo, X.-H. Liu, B. Sun, H.-J. Yan, D. Wang, and L.-J. Wan. *Phys. Chem. Chem. Phys.*, **2017**, *19*, 539–543.
- [194] B. Sun, J. Liu, A. Cao, W. Song, and D. Wang. *Chem. Commun.*, **2017**, *53*, 6303–6306.
- [195] H. Xu, S. Tao, and D. Jiang. *Nat. Mater.*, **2016**, *15*, 722–6.
- [196] X. Shi, Y. Yao, Y. Xu, K. Liu, G. Zhu, L. Chi, and G. Lu. *ACS Appl. Mater. Interfaces*, **2017**, *9*, 7481–7488.
- [197] N. Huang, L. Zhai, H. Xu, and D. Jiang. *J. Am. Chem. Soc.*, **2017**, *139*, 2428–2434.
- [198] A. Halder, S. Kandambeth, B. P. Biswal, G. Kaur, N. C. Roy, M. Addicoat, J. K. Salunke, S. Banerjee, K. Vanka, T. Heine, S. Verma, and R. Banerjee. *Angew. Chem., Int. Ed.*, **2016**, *55*, 7806–10.
- [199] P. Bhanja, K. Bhunia, S. K. Das, D. Pradhan, R. Kimura, Y. Hijikata, S. Irle, and A. Bhaumik. *ChemSusChem*, **2017**, *10*, 921–929.
- [200] S. Wang, Q. Wang, P. Shao, Y. Han, X. Gao, L. Ma, S. Yuan, X. Ma, J. Zhou, X. Feng, and B. Wang. *J. Am. Chem. Soc.*, **2017**, *139*, 4258–4261.
- [201] B. K. Hughes, W. A. Braunecker, D. C. Bobela, S. U. Nanayakkara, O. G. Reid, and J. C. Johnson. *J. Phys. Chem. Lett.*, **2016**, *7*, 3660–3665.

- [202] F. Auras, L. Ascherl, A. H. Hakimioun, J. T. Margraf, F. C. Hanusch, S. Reuter, D. Bessinger, M. Döblinger, C. Hettstedt, K. Karaghiosoff, S. Herbert, P. Knochel, T. Clark, and T. Bein. *J. Am. Chem. Soc.*, **2016**, *138*, 16703–16710.
- [203] B. Sun, J. Li, W.-L. Dong, M.-L. Wu, and D. Wang. *J. Phys. Chem. C*, **2016**, *120*, 14706–14711.
- [204] X. Chen, M. Addicoat, E. Jin, L. Zhai, H. Xu, N. Huang, Z. Guo, L. Liu, S. Irle, and D. Jiang. *J. Am. Chem. Soc.*, **2015**, *137*, 3241–3247.
- [205] Y. Hu, N. Goodeal, Y. Chen, A. M. Ganose, R. G. Palgrave, H. Bronstein, and M. O. Blunt. *Chem. Commun.*, **2016**, *52*, 9941–9944.
- [206] X. Chen, M. Addicoat, S. Irle, A. Nagai, and D. Jiang. *J. Am. Chem. Soc.*, **2013**, *135*, 546–549.
- [207] R. Tanoue, R. Higuchi, K. Ikebe, S. Uemura, N. Kimizuka, A. Z. Stieg, J. K. Gimzewski, and M. Kunitake. *J. Nanosci. Nanotechnol.*, **2014**, *14*, 2211–2216.
- [208] S. Lin, C. S. Diercks, Y.-B. Zhang, N. Kornienko, E. M. Nichols, Y. Zhao, A. R. Paris, D. Kim, P. Yang, O. M. Yaghi, and C. J. Chang. *Science*, **2015**, *349*, 1208–1213.
- [209] W. Ma, P. Yu, T. Ohsaka, and L. Mao. *Electrochem. Commun.*, **2015**, *52*, 53–57.
- [210] J. Fu, S. Das, G. Xing, T. Ben, V. Valtchev, and S. Qiu. *J. Am. Chem. Soc.*, **2016**, *138*, 7673–7680.
- [211] W. Gao, X. Sun, H. Niu, X. Song, K. Li, H. Gao, W. Zhang, J. Yu, and M. Jia. *Microporous Mesoporous Mater.*, **2015**, *213*, 59–67.
- [212] S. Kandambeth, D. B. Shinde, M. K. Panda, B. Lukose, T. Heine, and R. Banerjee. *Angew. Chem., Int. Ed.*, **2013**, *52*, 13052–13056.
- [213] N. Huang, X. Chen, R. Krishna, and D. Jiang. *Angew. Chem., Int. Ed.*, **2015**, *54*, 2986–2990.
- [214] J. L. Mendoza-Cortes, W. A. Goddard, H. Furukawa, and O. M. Yaghi. *J. Phys. Chem. Lett.*, **2012**, *3*, 2671–2675.
- [215] X.-H. Liu, J.-Y. Yue, Y.-P. Mo, Y. Yao, C. Zeng, T. Chen, H.-J. Yan, Z.-H. Wang, D. Wang, and L.-J. Wan. *J. Phys. Chem. C*, **2016**, *120*, 15753–15757.
- [216] V. Saptal, D. B. Shinde, R. Banerjee, and B. M. Bhanage. *Catal. Sci. Technol.*, **2016**, *6*, 6152–6158.

- [217] D. B. Shinde, S. Kandambeth, P. Pachfule, R. R. Kumar, and R. Banerjee. *Chem. Commun.*, **2015**, *51*, 310–313.
- [218] W. Seo, D. L. White, and A. Star. *Chem. - Eur. J.*, **2017**, *23*, 5652–5657.
- [219] H. Xu, X. Chen, J. Gao, J. Lin, M. Addicoat, S. Irle, and D. Jiang. *Chem. Commun.*, **2014**, *50*, 1292–1294.
- [220] N. Huang, R. Krishna, and D. Jiang. *J. Am. Chem. Soc.*, **2015**, *137*, 7079–7082.
- [221] F. Xu, H. Xu, X. Chen, D. Wu, Y. Wu, H. Liu, C. Gu, R. Fu, and D. Jiang. *Angew. Chem., Int. Ed.*, **2015**, *54*, 6814–6818.
- [222] Y. Hou, X. Zhang, J. Sun, S. Lin, D. Qi, R. Hong, D. Li, X. Xiao, and J. Jiang. *Microporous Mesoporous Mater.*, **2015**, *214*, 108–114.
- [223] Y.-B. Zhang, J. Su, H. Furukawa, Y. Yun, F. Gandara, A. Duong, X. Zou, and O. M. Yaghi. *J. Am. Chem. Soc.*, **2013**, *135*, 16336–16339.
- [224] H. Lu, C. Wang, J. Chen, R. Ge, W. Leng, B. Dong, J. Huang, and Y. Gao. *Chem. Commun.*, **2015**, *51*, 15562–15565.
- [225] Y. Xin, C. Wang, Y. Wang, J. Sun, and Y. Gao. *RSC Adv.*, **2017**, *7*, 1697–1700.
- [226] N. Huang, P. Wang, M. A. Addicoat, T. Heine, and D. Jiang. *Angew. Chem., Int. Ed.*, **2017**, *56*, 4982–4986.
- [227] W. Leng, Y. Peng, J. Zhang, H. Lu, X. Feng, R. Ge, B. Dong, B. Wang, X. Hu, and Y. Gao. *Chem. - Eur. J.*, **2016**, *22*, 9087–9091.
- [228] S.-L. Cai, Y.-B. Zhang, A. B. Pun, B. He, J. Yang, F. M. Toma, I. D. Sharp, O. M. Yaghi, J. Fan, S.-R. Zheng, W.-G. Zhang, and Y. Liu. *Chem. Sci.*, **2014**, *5*, 4693–4700.
- [229] H. Ding, Y. Li, H. Hu, Y. Sun, J. Wang, C. Wang, C. Wang, G. Zhang, B. Wang, W. Xu, and D. Zhang. *Chem. - Eur. J.*, **2014**, *20*, 14614–14618.
- [230] W.-l. Dong, L. Wang, H.-m. Ding, L. Zhao, D. Wang, C. Wang, and L.-J. Wan. *Langmuir*, **2015**, *31*, 11755–11759.
- [231] W.-L. Dong, S.-Y. Li, J.-Y. Yue, C. Wang, D. Wang, and L.-J. Wan. *Phys. Chem. Chem. Phys.*, **2016**, *18*, 17356–17359.
- [232] B. Sun, C.-H. Zhu, Y. Liu, C. Wang, L.-J. Wan, and D. Wang. *Chem. Mater.*, **2017**, *29*, 4367–4374.

- [233] H. Liao, H. Wang, H. Ding, X. Meng, H. Xu, B. Wang, X. Ai, and C. Wang. *J. Mater. Chem. A*, **2016**, *4*, 7416–7421.
- [234] Y. Tian, S.-Q. Xu, C. Qian, Z.-F. Pang, G.-F. Jiang, and X. Zhao. *Chem. Commun.*, **2016**, *52*, 11704–11707.
- [235] S.-Q. Xu, R.-R. Liang, T.-G. Zhan, Q.-Y. Qi, and X. Zhao. *Chem. Commun.*, **2017**, *53*, 2431–2434.
- [236] F. J. Uribe-Romo, C. J. Doonan, H. Furukawa, K. Oisaki, and O. M. Yaghi. *J. Am. Chem. Soc.*, **2011**, *133*, 11478–11481.
- [237] M. Wu, G. Chen, J. Ma, P. Liu, and Q. Jia. *Talanta*, **2016**, *161*, 350–358.
- [238] M. Wu, G. Chen, P. Liu, W. Zhou, and Q. Jia. *J. Chromatogr. A*, **2016**, *1456*, 34–41.
- [239] W. Liu, Q. Su, P. Ju, B. Guo, H. Zhou, G. Li, and Q. Wu. *ChemSusChem*, **2017**, *10*, 664–669.
- [240] S.-Y. Ding, M. Dong, Y.-W. Wang, Y.-T. Chen, H.-Z. Wang, C.-Y. Su, and W. Wang. *J. Am. Chem. Soc.*, **2016**, *138*, 3031–3037.
- [241] D.-H. Yang, Z.-Q. Yao, D. Wu, Y.-H. Zhang, Z. Zhou, and X.-H. Bu. *J. Mater. Chem. A*, **2016**, *4*, 18621–18627.
- [242] D. N. Bunck and W. R. Dichtel. *J. Am. Chem. Soc.*, **2013**, *135*, 14952–14955.
- [243] G. Das, B. P. Biswal, S. Kandambeth, V. Venkatesh, G. Kaur, M. Addicoat, T. Heine, S. Verma, and R. Banerjee. *Chem. Sci.*, **2015**, *6*, 3931–3939.
- [244] L. Stegbauer, K. Schwinghammer, and B. V. Lotsch. *Chem. Sci.*, **2014**, *5*, 2789–2793.
- [245] W. Zhang, P. Jiang, Y. Wang, J. Zhang, Y. Gao, and P. Zhang. *RSC Adv.*, **2014**, *4*, 51544–51547.
- [246] Y. Zhang, X. Shen, X. Feng, H. Xia, Y. Mu, and X. Liu. *Chem. Commun.*, **2016**, *52*, 74, 11088–91.
- [247] Z. Kang, Y. Peng, Y. Qian, D. Yuan, M. A. Addicoat, T. Heine, Z. Hu, L. Tee, Z. Guo, and D. Zhao. *Chem. Mater.*, **2016**, *28*, 1277–1285.
- [248] S. B. Alahakoon, C. M. Thompson, A. X. Nguyen, G. Occhialini, G. T. McCandless, and R. A. Smaldone. *Chem. Commun.*, **2016**, *52*, 2843–2845.

- [249] Y. Zhu, S. Wan, Y. Jin, and W. Zhang. *J. Am. Chem. Soc.*, **2015**, *137*, 13772–13775.
- [250] Z. Li, X. Feng, Y. Zou, Y. Zhang, H. Xia, X. Liu, and Y. Mu. *Chem. Commun.*, **2014**, *50*, 13825–13828.
- [251] M. Shan, B. Seoane, E. Rozhko, A. Dikhtiarenko, G. Clet, F. Kapteijn, and J. Gascon. *Chem. Eur. J.*, **2016**, *22*, 14467–14470.
- [252] L. Stegbauer, M. W. Hahn, A. Jentys, G. Savasci, C. Ochsenfeld, J. A. Lercher, and B. V. Lotsch. *Chem. Mater.*, **2015**, *27*, 7874–7881.
- [253] V. S. Vyas, F. Haase, L. Stegbauer, G. Savasci, F. Podjaski, C. Ochsenfeld, and B. V. Lotsch. *Nat. Commun.*, **2015**, *6*, 8508.
- [254] S. B. Alahakoon, G. T. McCandless, A. A. K. Karunathilake, C. M. Thompson, and R. A. Smaldone. *Chem. - Eur. J.*, **2017**, *23*, 4255–4259.
- [255] S. B. Alahakoon, G. Occhialini, G. T. McCandless, A. A. K. Karunathilake, S. O. Nielsen, and R. A. Smaldone. *CrystEngComm*, **2017**, *19*, 4882–4885.
- [256] F. Haase, T. Banerjee, G. Savasci, C. Ochsenfeld, and B. V. Lotsch. *Faraday Discuss.*, **2017**, *201*, 247–264.
- [257] Z. Li, Y. Zhang, H. Xia, Y. Mu, and X. Liu. *Chem. Commun.*, **2016**, *52*, 6613–6616.
- [258] Z. Li, Y. Zhi, X. Feng, X. Ding, Y. Zou, X. Liu, and Y. Mu. *Chem. - Eur. J.*, **2015**, *21*, 12079–12084.
- [259] S. Mitra, H. S. Sasmal, T. Kundu, S. Kandambeth, K. Illath, D. Diaz Diaz, and R. Banerjee. *J. Am. Chem. Soc.*, **2017**, *139*, 4513–4520.
- [260] S. Kandambeth, A. Mallick, B. Lukose, M. V. Mane, T. Heine, and R. Banerjee. *J. Am. Chem. Soc.*, **2012**, *134*, 19524–19527.
- [261] S. Chandra, S. Kandambeth, B. P. Biswal, B. Lukose, S. M. Kunjir, M. Chaudhary, R. Babarao, T. Heine, and R. Banerjee. *J. Am. Chem. Soc.*, **2013**, *135*, 17853–17861.
- [262] B. P. Biswal, S. Chandra, S. Kandambeth, B. Lukose, T. Heine, and R. Banerjee. *J. Am. Chem. Soc.*, **2013**, *135*, 5328–5331.
- [263] P. Pachfule, S. Kandambeth, D. Diaz Diaz, and R. Banerjee. *Chem. Commun.*, **2014**, *50*, 3169–3172.

- [264] P. Pachfule, M. K. Panda, S. Kandambeth, S. M. Shivaprasad, D. D. Diaz, and R. Banerjee. *J. Mater. Chem. A*, **2014**, *2*, 7944–7952.
- [265] P. Pachfule, S. Kandambeth, A. Mallick, and R. Banerjee. *Chem. Commun.*, **2015**, *51*, 11717–11720.
- [266] J. Thote, H. Barike Aiyappa, R. Rahul Kumar, S. Kandambeth, B. P. Biswal, D. Balaji Shinde, N. Chaki Roy, and R. Banerjee. *IUCrJ*, **2016**, *3*, 402–407.
- [267] S. Karak, S. Kandambeth, B. P. Biswal, H. S. Sasmal, S. Kumar, P. Pachfule, and R. Banerjee. *J. Am. Chem. Soc.*, **2017**, *139*, 1856–1862.
- [268] S. Chandra, D. Roy Chowdhury, M. Addicoat, T. Heine, A. Paul, and R. Banerjee. *Chem. Mater.*, **2017**, *29*, 2074–2080.
- [269] H. Wei, S. Chai, N. Hu, Z. Yang, L. Wei, and L. Wang. *Chem. Commun.*, **2015**, *51*, 12178–12181.
- [270] B. P. Biswal, H. D. Chaudhari, R. Banerjee, and U. K. Kharul. *Chem. - Eur. J.*, **2016**, *22*, 4695–4699.
- [271] H. Wang, F. Jiao, F. Gao, X. Zhao, Y. Zhao, Y. Shen, Y. Zhang, and X. Qian. *Anal. Bioanal. Chem.*, **Mar. 2017**, *409*, 2179–2187.
- [272] S. He, T. Zeng, S. Wang, H. Niu, and Y. Cai. *ACS Appl. Mater. Interfaces*, **2017**, *9*, 2959–2965.
- [273] H. Wang, F. Jiao, F. Gao, J. Huang, Y. Zhao, Y. Shen, Y. Zhang, and X. Qian. *J. Mater. Chem. B*, **2017**, *5*, 4052–4059.
- [274] C. R. DeBlase, K. E. Silberstein, T.-T. Truong, H. D. Abruna, and W. R. Dichtel. *J. Am. Chem. Soc.*, **2013**, *135*, 16821–16824.
- [275] X. Gou, Q. Zhang, Y. Wu, Y. Zhao, X. Shi, X. Fan, L. Huang, and G. Lu. *RSC Adv.*, **2016**, *6*, 39198–39203.
- [276] A. M. Khattak, Z. Ali Ghazi, B. Liang, N. Ali Khan, A. Iqbal, L. Li, and Z. Tang. *J. Mater. Chem. A*, **2016**, *4*, 16312–16317.
- [277] J. Thote, H. B. Aiyappa, A. Deshpande, D. Diaz Diaz, S. Kurungot, and R. Banerjee. *Chem. - Eur. J.*, **2014**, *20*, 15961–15965.
- [278] L. Xu, J. Xu, B. Shan, X. Wang, and C. Gao. *J. Membr. Sci.*, **2017**, *526*, 355–366.
- [279] H. Wang, F. Jiao, F. Gao, Y. Lv, Q. Wu, Y. Zhao, Y. Shen, Y. Zhang, and X. Qian. *Talanta*, **2017**, *166*, 133–140.

- [280] Y. Peng, Z. Hu, Y. Gao, D. Yuan, Z. Kang, Y. Qian, N. Yan, and D. Zhao. *ChemSusChem*, **2015**, *8*, 3348.
- [281] S. Chandra, T. Kundu, K. Dey, M. Addicoat, T. Heine, and R. Banerjee. *Chem. Mater.*, **2016**, *28*, 1489–1494.
- [282] Y. Peng, G. Xu, Z. Hu, Y. Cheng, C. Chi, D. Yuan, H. Cheng, and D. Zhao. *ACS Appl. Mater. Interfaces*, **2016**, *8*, 18505–18512.
- [283] S. Kandambeth, B. P. Biswal, H. D. Chaudhari, K. C. Rout, H. S. Kunjattu, S. Mitra, S. Karak, A. Das, R. Mukherjee, U. K. Kharul, and R. Banerjee. *Adv. Mater.*, **2017**, *29*, 1603945/1–1603945/9.
- [284] C.-X. Yang, C. Liu, Y.-M. Cao, and X.-P. Yan. *Chem. Commun.*, **2015**, *51*, 12254–12257.
- [285] J. Tan, S. Namuangruk, W. Kong, N. Kungwan, J. Guo, and C. Wang. *Angew. Chem., Int. Ed.*, **2016**, *55*, 13979–13984.
- [286] Y. Li, C.-X. Yang, and X.-P. Yan. *Chem. Commun.*, **2017**, *53*, 2511–2514.
- [287] H. Guo, J. Wang, Q. Fang, Y. Zhao, S. Gu, J. Zheng, and Y. Yan. *CrystEngComm*, **2017**, *19*, 4905–4910.
- [288] M. S. Lohse, T. Stassin, G. Naudin, S. Wuttke, R. Ameloot, D. De Vos, D. D. Medina, and T. Bein. *Chem. Mater.*, **2016**, *28*, 626–631.
- [289] D. B. Shinde, H. B. Aiyappa, M. Bhadra, B. P. Biswal, P. Wadge, S. Kandambeth, B. Garai, T. Kundu, S. Kurungot, and R. Banerjee. *J. Mater. Chem. A*, **2016**, *4*, 2682–2690.
- [290] H. B. Aiyappa, J. Thote, D. B. Shinde, R. Banerjee, and S. Kurungot. *Chem. Mater.*, **2016**, *28*, 4375–4379.
- [291] Q. Sun, B. Aguila, J. Perman, N. Nguyen, and S. Ma. *J. Am. Chem. Soc.*, **2016**, *138*, 15790–15796.
- [292] M. Bhadra, H. S. Sasmal, A. Basu, S. P. Midya, S. Kandambeth, P. Pachfule, E. Balaraman, and R. Banerjee. *ACS Appl. Mater. Interfaces*, **2017**, *9*, 13785–13792.
- [293] S. Chandra, T. Kundu, S. Kandambeth, R. Babarao, Y. Marathe, S. M. Kunjir, and R. Banerjee. *J. Am. Chem. Soc.*, **2014**, *136*, 6570–6573.
- [294] R. Ge, D. Hao, Q. Shi, B. Dong, W. Leng, C. Wang, and Y. Gao. *J. Chem. Eng. Data*, **2016**, *61*, 1904–1909.

- [295] X. Yang, B. Dong, H. Zhang, R. Ge, Y. Gao, and H. Zhang. *RSC Adv.*, **2015**, *5*, 86137–86143.
- [296] M. A. Khayum, S. Kandambeth, S. Mitra, S. B. Nair, A. Das, S. S. Nagane, R. Mukherjee, and R. Banerjee. *Angew. Chem., Int. Ed.*, **2016**, *55*, 15604–15608.
- [297] C. R. DeBlase, K. Hernandez-Burgos, K. E. Silberstein, G. G. Rodriguez-Calero, R. P. Bisbey, H. D. Abruna, and W. R. Dichtel. *ACS Nano*, **2015**, *9*, 3178–3183.
- [298] C. R. Mulzer, L. Shen, R. P. Bisbey, J. R. McKone, N. Zhang, H. D. Abruna, and W. R. Dichtel. *ACS Cent. Sci.*, **2016**, *2*, 667–673.
- [299] H. Ma, B. Liu, B. Li, L. Zhang, Y.-G. Li, H.-Q. Tan, H.-Y. Zang, and G. Zhu. *J. Am. Chem. Soc.*, **2016**, *138*, 5897–5903.
- [300] R. Gomes and A. Bhaumik. *RSC Adv.*, **2016**, *6*, 28047–28054.
- [301] X. Zhu, S. An, Y. Liu, J. Hu, H. Liu, C. Tian, S. Dai, X. Yang, H. Wang, C. W. Abney, and S. Dai. *AIChE J.*, **2017**, *63*, 3470–3478.
- [302] L.-H. Liu, C.-X. Yang, and X.-P. Yan. *J. Chromatogr. A*, **2017**, *1479*, 137–144.
- [303] H.-L. Qian, C.-X. Yang, X.-P. Yan, and X.-P. Yan. *Nat. Commun.*, **2016**, *7*, 12104.
- [304] M. R. Rao, Y. Fang, S. De Feyter, and D. F. Perepichka. *J. Am. Chem. Soc.*, **2017**, *139*, 2421–2427.
- [305] Q. Fang, Z. Zhuang, S. Gu, R. B. Kaspar, J. Zheng, J. Wang, S. Qiu, and Y. Yan. *Nat. Commun.*, **2014**, *5*, 4503pp.
- [306] G.-Y. Lee, J. Lee, S. Kim, T. Park, H. T. Vo, and H. Lee. *Sci. Rep.*, **2017**, *7*, 557.
- [307] Q. Fang, J. Wang, S. Gu, R. B. Kaspar, Z. Zhuang, J. Zheng, H. Guo, S. Qiu, and Y. Yan. *J. Am. Chem. Soc.*, **2015**, *137*, 8352–8355.
- [308] C. Zhang, S. Zhang, Y. Yan, F. Xia, A. Huang, and Y. Xian. *ACS Appl. Mater. Interfaces*, **2017**, *9*, 13415–13421.
- [309] P. Kuhn, M. Antonietti, and A. Thomas. *Angew. Chem., Int. Ed.*, **2008**, *47*, 3450–3453.
- [310] M. J. Bojdys, J. Jeromenok, A. Thomas, and M. Antonietti. *Adv. Mater.*, **2010**, *22*, 2202–2205.
- [311] S. Ren, M. J. Bojdys, R. Dawson, A. Laybourn, Y. Z. Khimyak, D. J. Adams, and A. I. Cooper. *Adv. Mater.*, **2012**, *24*, 2357–2361.

- [312] P. Puthiaraj, Y.-R. Lee, S. Zhang, and W.-S. Ahn. *J. Mater. Chem. A*, **2016**, *4*, 16288–16311.
- [313] Y. Ying, D. Liu, J. Ma, M. Tong, W. Zhang, H. Huang, Q. Yang, and C. Zhong. *J. Mater. Chem. A*, **2016**, *4*, 13444–13449.
- [314] P. Wen, C. Zhang, Z. Yang, R. Dong, D. Wang, M. Fan, and J. Wang. *Tribol. Int.*, **2017**, *111*, 57–65.
- [315] K. T. Jackson, T. E. Reich, and H. M. El-Kaderi. *Chem. Commun.*, **2012**, *48*, 8823–8825.
- [316] A. Nagai, X. Chen, X. Feng, X. Ding, Z. Guo, and D. Jiang. *Angew. Chem., Int. Ed.*, **2013**, *52*, 3770–3774.
- [317] D. A. Pyles, J. W. Crowe, L. A. Baldwin, and P. L. McGrier. *ACS Macro Lett.*, **2016**, *5*, 1055–1058.
- [318] S. Nandi, S. K. Singh, D. Mullangi, R. Illathvalappil, L. George, C. P. Vinod, S. Kurungot, and R. Vaidhyanathan. *Adv. Energy Mater.*, **2016**, *6*, 1601189.
- [319] B. Nath, W.-H. Li, J.-H. Huang, G.-. E. Wang, Z.-h. Fu, M.-S. Yao, and G. Xu. *CrystEngComm*, **2016**, *18*, 4259–4263.
- [320] J. Guo, Y. Xu, S. Jin, L. Chen, T. Kaji, Y. Honsho, M. A. Addicoat, J. Kim, A. Saeki, H. Ihee, S. Seki, S. Irle, M. Hiramoto, J. Gao, and D. Jiang. *Nat. Commun.*, **2013**, *4*, 3736/1–3736/8.
- [321] X. Zhuang, W. Zhao, F. Zhang, Y. Cao, F. Liu, S. Bi, and X. Feng. *Polym. Chem.*, **2016**, *7*, 4176–4181.
- [322] Y. Zhu, M. Qiao, W. Peng, Y. Li, G. Zhang, F. Zhang, Y. Li, and X. Fan. *J. Mater. Chem. A*, **2017**, *5*, 9272–9278.
- [323] Y. Du, K. Mao, P. Kamakoti, P. Ravikovitch, C. Paur, S. Cundy, Q. Li, and D. Calabro. *Chem. Commun.*, **2012**, *48*, 4606–4608.
- [324] S. Zhao, B. Dong, R. Ge, C. Wang, X. Song, W. Ma, Y. Wang, C. Hao, X. Guo, and Y. Gao. *RSC Adv.*, **2016**, *6*, 38774–38781.
- [325] B. Dong, L. Wang, S. Zhao, R. Ge, X. Song, Y. Wang, and Y. Gao. *Chem. Commun.*, **2016**, *52*, 7082–5.
- [326] W. Zhou, H. Wu, and T. Yildirim. *Chem. Phys. Lett.*, **2010**, *499*, 103–107.
- [327] B. Lukose, A. Kuc, and T. Heine. *Chem. - Eur. J.*, **2011**, *17*, 2388–2392.

- [328] X.-H. Liu, C.-Z. Guan, D. Wang, and L.-J. Wan. *Adv. Mater.*, **2014**, *26*, 6912–6920.
- [329] S. B. Kalidindi and R. A. Fischer. *Phys. Status Solidi B*, **2013**, *250*, 1119–1127.
- [330] Y. Zeng, R. Zou, and Y. Zhao. *Adv. Mater.*, **2016**, *28*, 2855–2873.
- [331] H. Furukawa and O. M. Yaghi. *J. Am. Chem. Soc.*, **2009**, *131*, 8875–8883.
- [332] Y. Pramudya and J. L. Mendoza-Cortes. *J. Am. Chem. Soc.*, **2016**, *138*, 15204–15213.
- [333] J. L. Mendoza-Cortes, S. S. Han, and I. Goddard William A. *J. Phys. Chem. A*, **2012**, *116*, 1621–1631.
- [334] F. Gao, J. T. Sun, and S. Meng. *Nanoscale*, **2015**, *7*, 6319–24.
- [335] F. Gao, Z. Ding, and S. Meng. *Sci Rep*, **2013**, *3*, 1882.
- [336] L. Xia and Q. Liu. *J. Solid State Chem.*, **2016**, *244*, 1–5.
- [337] J.-H. Guo, H. Zhang, and Y. Miyamoto. *Phys. Chem. Chem. Phys.*, **2013**, *15*, 8199–8207.
- [338] J.-H. Guo, H. Zhang, Z.-P. Liu, and X.-L. Cheng. *J. Phys. Chem. C*, **2012**, *116*, 15908–15917.
- [339] J.-h. Guo, X.-L. Cheng, S.-J. Li, and G. Chen. *J. Phys. Chem. C*, **2016**, *120*, 17153–17164.
- [340] X.-Y. Liu, H. Jie, J.-X. Yu, Z.-X. Li, and Z.-Q. Fan. *Chin. Phys. B*, **2014**, *23*, 067303/1–067303/8.
- [341] E. Ganz and M. Dornfeld. *J. Phys. Chem. C*, **2014**, *118*, 5657–5663.
- [342] E. Ganz and M. Dornfeld. *J. Phys. Chem. C*, **2012**, *116*, 3661–3666.
- [343] J.-h. Guo, H. Zhang, Y. Tang, and X. Cheng. *Phys. Chem. Chem. Phys.*, **2013**, *15*, 2873–2881.
- [344] R. Kadam and N. L. Panwar. *Renewable Sustainable Energy Rev.*, **2017**, *73*, 892–903.
- [345] M. Dogru and T. Bein. *Chem. Commun.*, **2014**, *50*, 5531–5546.

Chapter 2

Characterization Methods

2.1 X-ray Diffraction and Scattering

X-ray diffraction (XRD) is a versatile and widely used technique for the analysis of crystalline materials, providing information about lattice constants and geometry, crystallite domain sizes and defects. X-rays are produced when electrons are accelerated in a magnetic field and hit the anode.

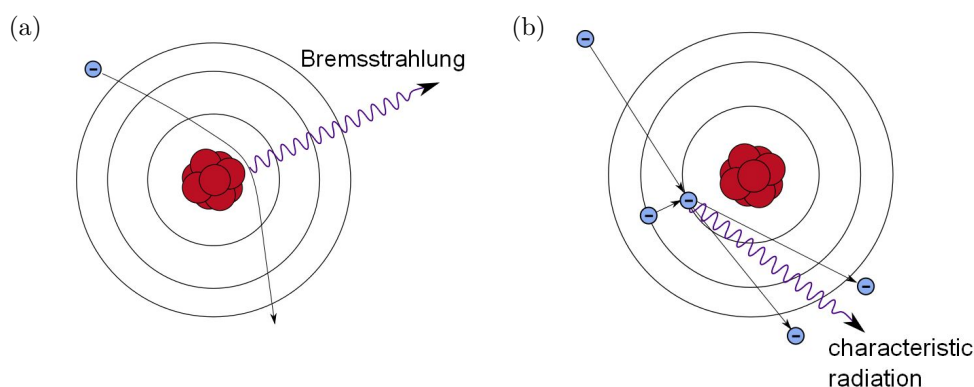


Figure 2.1: Generation of X-rays: (a) Bremsstrahlung. (b) Characteristic radiation.

The resulting spectrum is a spectrum of continuous radiation called "Bremsstrahlung" that is emitted when electrons slow down due to deflection in the electric field of an atomic nucleus (see Figure 2.1a) and sharp peaks that originate from characteristic X-ray radiation. The latter is emitted when high-energy particles hit inner shell electrons of an atom. The resulting vacancy is filled by an outer shell electron under emission of photons with an energy that corresponds to the energy difference of the higher and lower energy state of this electron (see Figure 2.1b).

Thus, each element has a set of characteristic X-ray frequencies. For X-ray diffraction analysis, one type of the characteristic radiation is filtered to yield monochromatic X-rays. The most commonly used radiation is $K\alpha$ radiation (from electronic transition from the

second so-called L-shell to the innermost, so-called K-shell). This is usually the most intense X-ray radiation generated.¹

If electromagnetic waves interact with periodic lattices, constructive interference can occur when Bragg's law is satisfied:²

$$n\lambda = 2d\sin\theta \quad (2.1)$$

with the interplanar distance d , the scattering angle θ , the wavelength of the incident beam λ , and a positive integer n . The diffraction at a periodical lattice is depicted in Figure 2.2.

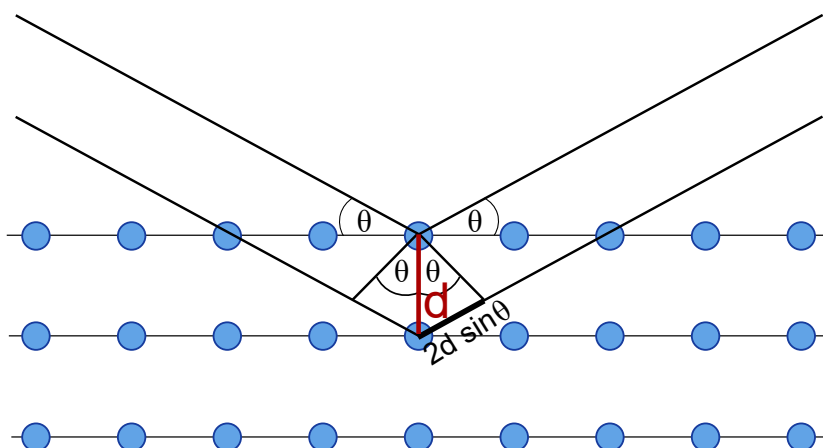


Figure 2.2: Schematic representation of Bragg diffraction at a periodical lattice.

The relation between the peak broadening in XRD patterns and the size of crystallites was first described by Scherrer.³ It can be experimentally used to determine the domain size in a polycrystalline material, see Equation (2.2).⁴

$$D = \frac{k\lambda}{B\cos\theta_B} \quad (2.2)$$

Here, D denotes the mean size of the crystalline domains, k represents a shape factor, λ is the wavelength of the incident beam, B corresponds to the full width at half maximum (FWHM) corrected for instrumental broadening and θ_B is the diffraction angle.

X-ray diffraction under grazing incident angles (GID) can, among others, be applied for the investigation of the crystallinity and preferential orientation in thin films. The setup

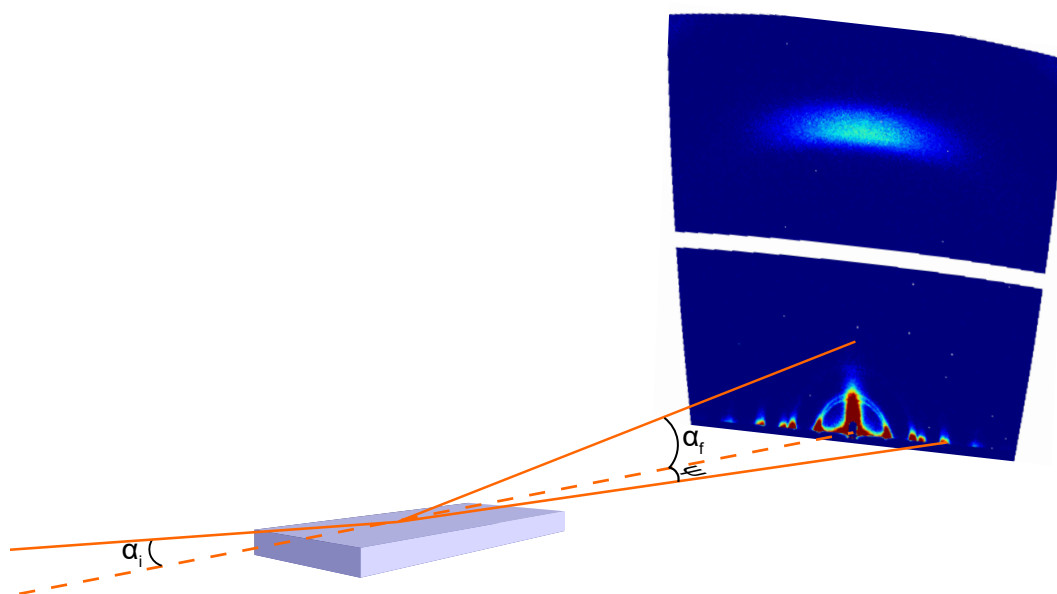


Figure 2.3: Schematic representation of the GID geometry.

of a GID experiment is depicted in Figure 2.3. The X-ray beam hits the sample surface in a very small angle in respect to the sample surface, typically $\alpha_i < 1^\circ$. Diffraction on the surface occurs that is detected utilizing a 2D detector. With this setup, diffraction can be detected as a function of both, the exit angle α_f (out-of-plane angle) and the in-plane angle ψ .⁵

2.2 Vibrational Spectroscopy

2.2.1 Infrared Spectroscopy

In infrared (IR) spectroscopy, radiation in the infrared range is passed through a sample and is absorbed in certain wavelengths. These wavelengths correspond to the vibrational energies of the vibrational modes of the molecule. In general, a molecule has different vibrational modes.

Vibrations that alter the distance between the atoms while their angle remains constant are called stretching vibrations and vibrations with an angular change but constant atomic distance are termed bending vibrations. The stretching vibrational modes can be further classified as symmetric or antisymmetric⁶ (see Figure 2.4 for the vibrational modes of H_2O). In order to be visible in IR spectroscopy, the respective vibration has to change the dipole moment of the molecule. Vibrations that do not affect the dipole moment are IR-inactive.

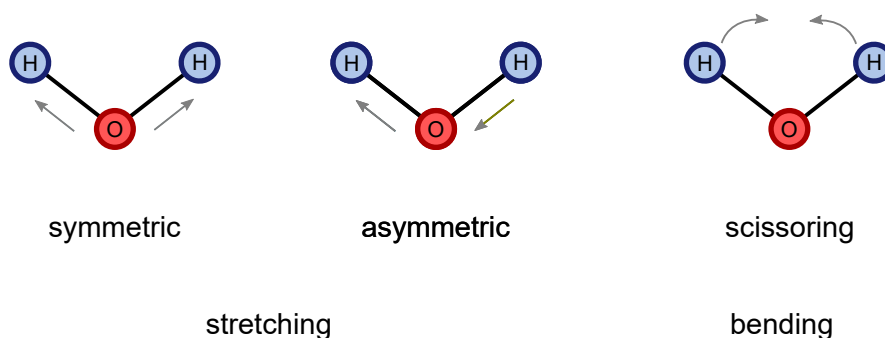


Figure 2.4: Basic modes of vibration for the H_2O molecule.

2.2.2 Raman Spectroscopy

Raman spectroscopy utilizes the Raman effect, that is the inelastic scattering of a photon. If a photon interacts with a molecule, elastic or inelastic scattering can occur. In the case of elastic scattering, the wavelength of the radiation is unchanged. This process is called Rayleigh scattering and accounts for the predominant part of scattering events. A small fraction of photons is however scattered in an inelastic fashion.

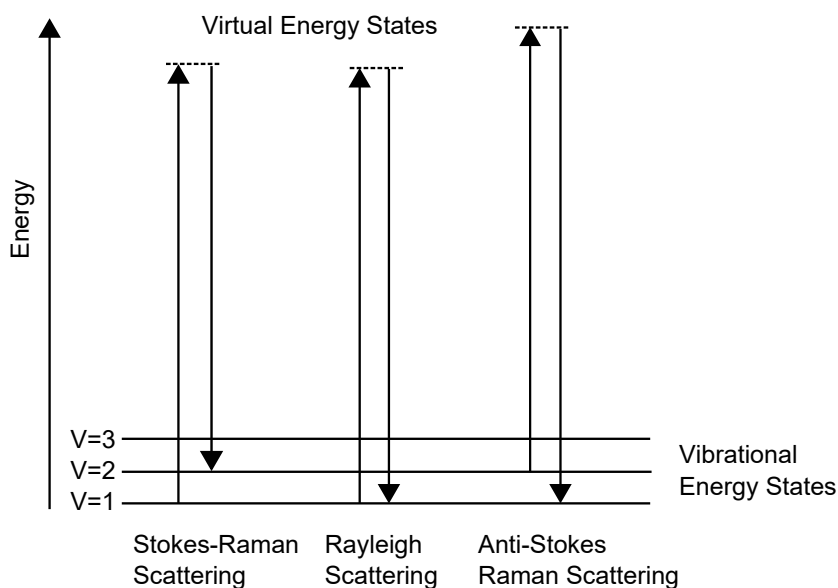


Figure 2.5: Energy-level diagram showing the energy transitions for Rayleigh and Raman scattering.

A part of the photons is inducing vibrations when interacting with the molecule, thereby losing a part of its energy. These photons are then visible at longer wavelengths and are called Stokes Raman lines. If the photons absorb vibrational energy from the

molecule, they appear at shorter wavelengths to form the anti Stokes Raman lines.⁷ All three processes are depicted in Figure 2.5.

The condition for Raman activity is a change of the polarizability of the molecule. Consequently, the vibration of a molecule can be either IR-active or Raman-active or both. In a molecule with a center of symmetry, the rule of mutual exclusion states that no normal modes can be both IR-and Raman active.⁸

2.3 UV-vis Spectroscopy

The valence electrons of molecules can be excited by radiation in the ultraviolet (UV) and visible (vis) region. Thereby the electrons are excited to energetically higher anti-bonding molecular orbitals. This excitation can occur with σ -, π - and non-bonding n -electrons as $\sigma\text{-}\sigma^*$, $\pi\text{-}\pi^*$, $n\text{-}\sigma^*$, and $n\text{-}\pi^*$ transitions, see Figure 2.6.

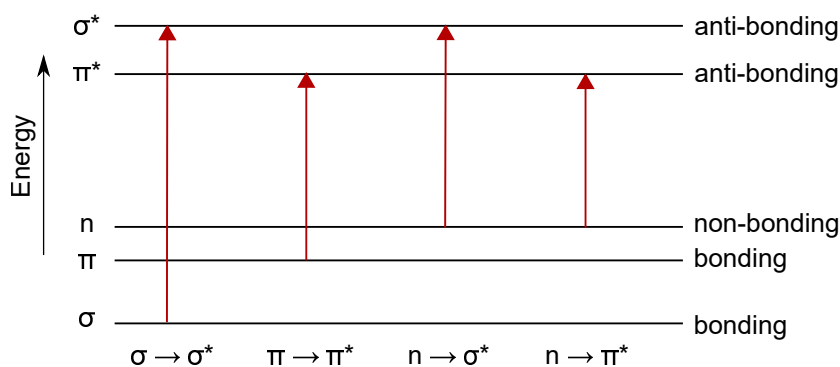


Figure 2.6: Electron transitions in molecules with π -, σ - and n -electrons.⁹

In an experimental setup, the attenuation of the incident light upon transition through the sample is determined. Deviations originating from stray light, reflection or absorption of the sample holder, e.g. a cuvette, are eliminated by reference measurements. With UV-vis spectroscopy, the concentration of a UV-vis absorbing substance can be determined by applying the Beer-Lambert law (Equation (2.3)):

$$\lg \frac{I_0}{I} = \epsilon \cdot d \cdot c \quad (2.3)$$

with the intensity of the incident light I_0 , the intensity of the transmitted light I , the sample thickness d , and the concentration c . The value of the extinction coefficient ϵ is determined from calibration curves and specific for a particular wavelength.¹⁰ UV-vis

spectra are furthermore accessible from powders *via* diffuse reflectance measurements. If the scattering at the sample surface is significantly larger than the absorption and the amount of reflection is negligible, the Kubelka-Munk function (Equation (2.4)) can be applied.¹¹

$$\frac{K}{S} = \frac{(1 - R)^2}{2R} \quad (2.4)$$

Here, K represents the absorption coefficient, S corresponds to the scattering coefficient, and R describes the diffuse reflectance.

2.4 Atomic Emission Spectroscopy

When Kirchhoff and Bunsen introduced the spectroscopic analysis of elements in 1860, they reported three properties of their emission that laid the foundation for the development of atomic emission and atomic absorption spectroscopy. First, atoms that absorb light at a given wavelength also emit light at the same wavelength. Second, the line spectra that can be recorded from the emission or absorption are characteristic for an element. Third, the lines that can be observed stem from free atoms rather than their compounds.¹²

In atomic emission spectroscopy (AES), atoms are excited in a flame, spark, or in ICP-AES in an inductively coupled plasma (ICP). This plasma is established by three concentric quartz tubes that are placed in the middle of the coils of an arrangement of radio frequency coils. Typically, argon is used as gas and ignited with a Tesla coil discharge. Upon ignition, free charge carriers of Ar^+ are created and form a conductive gas. By applying a high frequency field, avalanche ionization occurs establishing a stable plasma.⁶ In a typical ICP-AES setup the sample is directly brought into the flame and the emitted light is separated into its different wavelengths by a diffraction grating. The light intensities at the different wavelengths are then measured with a photodetector.

2.5 Nuclear Magnetic Resonance Spectroscopy

Nuclei with an odd number of protons and/or neutrons such as ^1H , ^{11}B , ^{13}C , and ^{15}N feature a nuclear spin p with the value:

$$p = \hbar \cdot \sqrt{l(l+1)} \quad (2.5)$$

with the reduced Planck constant \hbar and the nuclear spin quantum number l .

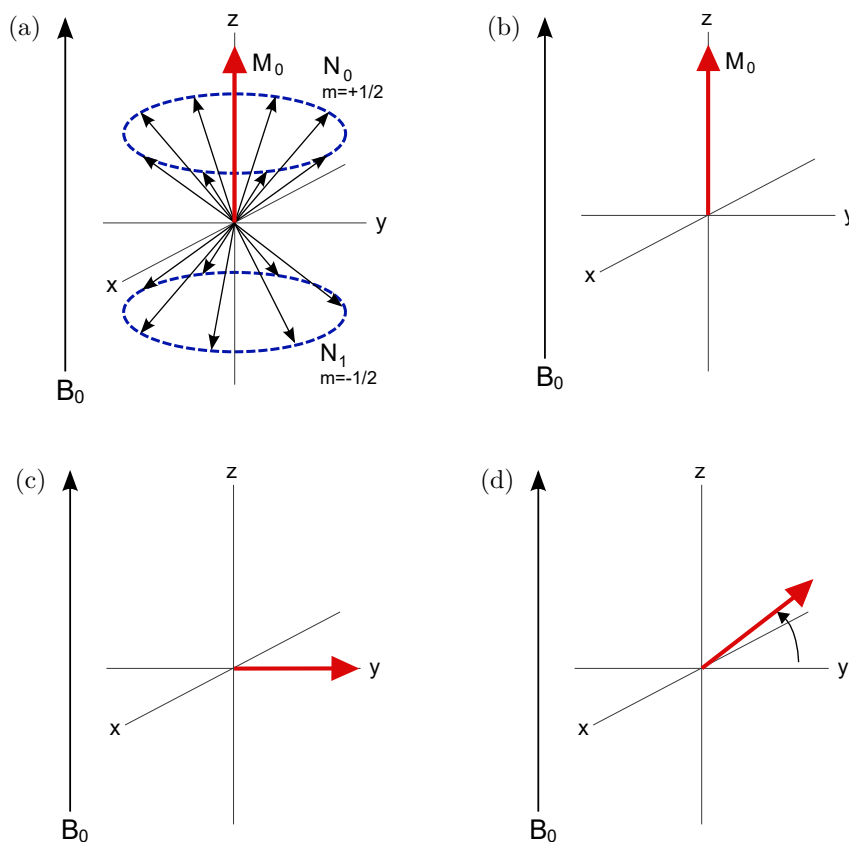


Figure 2.7: (a) Schematic representation of the magnetic vector double cone and the overall magnetization originating from excess spin population, (b) magnetization vector M_0 in static magnetization, (c) orientation of the magnetization vector at a 90° pulse, (d) relaxation after the pulse.

In the absence of a magnetic field these spins are energetically equal. If an external magnetic field is applied, the energy levels split. For example for $l = 1/2$, two levels are established. The nuclear magnetic vector precesses about the external field axis and can be depicted as a double cone. As the number of spins in the ground state is slightly higher than in the excited state, an overall magnetization is realized (Figures 2.7a and 2.7b). Absorption and emission of electromagnetic radiation leads to transitions between these states. In a nuclear magnetic resonance (NMR) experiment, electromagnetic radiation is applied to induce these transitions until the system is saturated, i.e. both energy levels are equally populated. In this condition, the magnetic vector is tilted in the y -direction and the resulting magnetization in y -direction can be detected (Figure 2.7c). When the radiation stops, the vector relaxes back into its original position (Figure 2.7d).

The resonance frequencies of the nuclei are influenced by their chemical environment, hence they provide information about the structure of the molecule. In liquid NMR,

the sample is measured in solution and the mobility of the molecules in the solution suppresses line-broadening from dipole-dipole interactions. When a solid material has to be investigated, this mobility is not available and a measurement as such would result in a large line broadening. To overcome this issue, magic-angle spinning (MAS) has been developed. In a MAS experiment, the sample is brought into a tube that is rotated in the NMR spectrometer at the so-called "magic angle" of 54.74° with respect to the magnetic field. At this angle, the contributions of the dipolar interactions between the nuclei are largely eliminated.

2.6 Electron Microscopy

In electron microscopy, an accelerated electron beam is used to illuminate the sample. Depending on the setup, different measurement techniques can be realized. In transmission electron microscopy (TEM) the focussed electron beam transmits through a very thin sample. The general operation principle of TEM is the same as for a light microscope, but electrons are shone through the sample instead of light. As the wavelength of the electrons used here is smaller than that of visible light, the resolution of a TEM is significantly, that means by several orders of magnitude, higher than in a light microscope. With this method, resolution down to the atomic scale is possible. In a TEM instrument (see Figure 2.8) the electron beam is focused on a small area of the sample by condenser lenses. The fraction of the electron beam that is transmitted through the sample is focused by the objective lens and projected onto a fluorescent phosphor screen. Furthermore, when the electron beam passes the sample, scattering occurs and a diffraction pattern of the sample can be collected.¹³

In scanning electron microscopy (SEM, see Figure 2.8 for a schematic setup with a secondary electron detector), an accelerated electron beam is focused onto a small sample area and interacts with the sample under emission of a range of signals, which can be applied to characterize the sample.¹⁴ Secondary electrons are emitted when the electrons of the beam remove electrons from the K-shell of the sample atoms. These secondary electrons are emitted only from the first few nanometers in depth from the sample surface. This detection mode is therefore applied to collect information about the sample topography. In order to obtain a topographic image of a certain area of the specimen, the electron beam scans the sample surface in a raster fashion. Detection of secondary electrons is the method that is used in this thesis. Other measurement modes are possible, for example the detection of high-energy backscattered electrons that emerge from elastic interactions

with the sample atoms (see Figure 2.1a) and are distinct for different chemical compositions of the sample. In energy-dispersive X-ray spectroscopy (EDX), characteristic X-ray radiation (see Section 2.1) is emitted from the specimen and provides information about the elemental composition of the sample.¹⁵

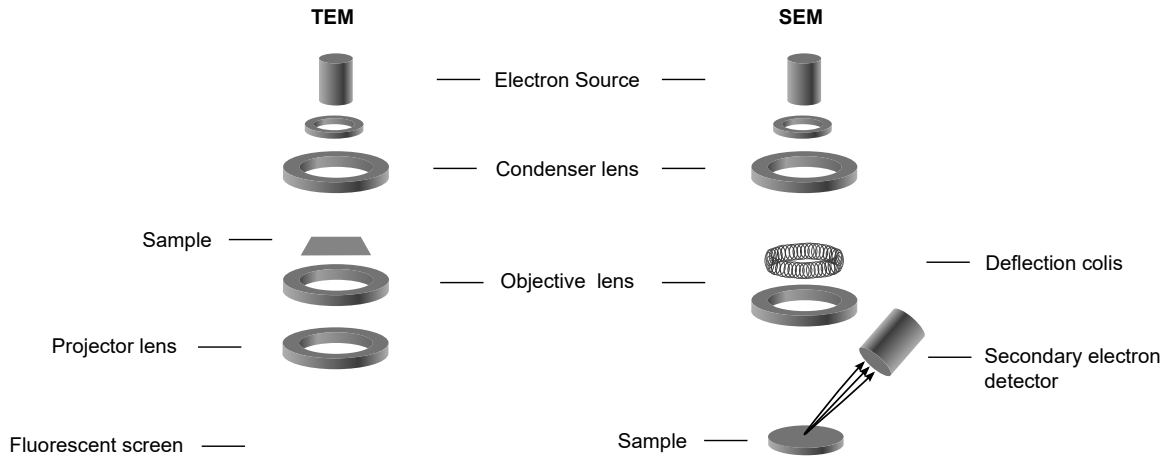


Figure 2.8: Schematic setup of a transmission electron microscope (left) and a scanning electron microscope (right).

2.7 Sorption

Nitrogen sorption under constant pressure is a measurement that is widely used to determine the surface areas and pore sizes of porous materials. The equilibrium curve at $T = \text{const.}$ is the adsorption isotherm. It has different shapes, depending on the size distribution and types of pores in the material. The pore size of a material roughly classifies it as microporous (<2 nm), mesoporous (2 nm to 50 nm) or macroporous (>50 nm). Experimentally, a sorption isotherm is obtained at constant temperature by applying increasing and subsequently decreasing pressure of the probe gas to the evacuated porous substance and measuring the equilibrium pressure after adsorption of the probe gas on the surface of the substrate, thus obtaining the adsorption and desorption branch of an adsorption isotherm.

The isotherm types correspond to different pore sizes and shapes and were classified by IUPAC in 1985 and refined in 2015.^{16,17} Figure 2.9 depicts the main isotherm shapes from the 2015 IUPAC report. Type I corresponds to microporous materials and features a steep rise at low pressure and a generally concave form (to the argument p/p_0) of the isotherm. The overall uptake of the material is limited by the accessible volume of the micropores.

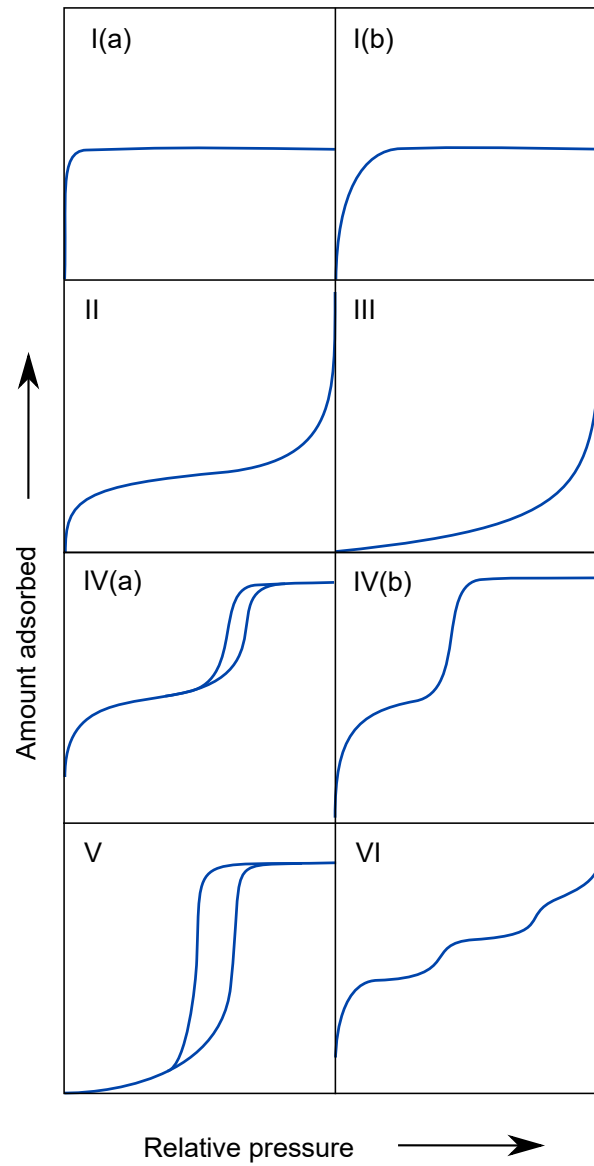


Figure 2.9: Classification of physisorption isotherms according to IUPAC. Adapted from ref. 16.

In Type I(a) only very narrow micropores of < 1 nm in width are present while Type I(b) accounts for larger micropores and a broader range of pore size distribution, also possibly including small mesopores. Isotherms of Type II correspond to non-porous or macroporous solids. On these materials, an unrestricted multilayer formation is possible, leading to a rise of the curve after the monolayer formation has occurred. If the adsorbent-adsorbate interactions are relatively weak, no distinctive monolayer formation takes place before multilayer adsorption begins. Therefore, the curve is convex already at low p/p_0 . This form is classified as Type III.

For mesoporous solids - the dominating type of material used in this work - the adsorption isotherm follows the form of the Type II isotherm in the low pressure region. For higher pressure pore condensation takes place, leading to filling of the mesopores with the probing gas, culminating in a plateau indicating saturation of the surface. If a hysteresis is present, this curve is classified as Type IV (a) indicating mesopores above a critical width that depends on the probe gas (around 4 nm for nitrogen). The reason for the hysteresis lies in a delayed condensation due to metastability of the adsorbed monolayer. Pore blocking may also lead to a delayed emptying of the pores during desorption. Smaller pores or those with conical shape give rise to an isotherm of Type IV(b), without hysteresis. If both, a low adsorbent-adsorbate interaction and pore condensation are present, the result is an isotherm of Type V, with a shape similar to that of Type III, but featuring a plateau at high p/p_0 and a hysteresis. Finally, if a stepwise formation of several layers on a non-porous, highly uniform substrate takes place, the result is an isotherm of Type VI, with several steps.

For the evaluation of the surface area from the experimentally obtained adsorption isotherm, a range of models have been developed, which use different approaches for the description of the adsorbent-adsorbate interactions. The two models that are applied in Covalent Organic Framework research are the Langmuir and the Brunauer-Emmett-Teller model. The Langmuir model assumes that only a monolayer is formed at the surface and no interaction between different adsorbent molecules is present, i.e. the interaction between the adsorber and the adsorbent is strong, while the adsorbent-adsorbent interaction is negligible. For example, this behavior is represented by chemisorption processes. In the Langmuir model the adsorption isotherm is described as follows:

$$k_i = k_{max} \frac{p_i}{p_i + b} \quad (2.6)$$

Here, k_i is the surface concentration and k_{max} is the maximum surface concentration of the adsorbent and p_i represents the gas pressure. The parameter b is related to the molar free standard adsorption enthalpy $\Delta_A G^\circ$:

$$b = [p_i] \exp\left(\frac{\Delta_A G^\circ}{RT}\right) \quad (2.7)$$

with the ideal gas constant R and the temperature T .

For high pressure p_i , the surface is saturated with adsorbent and $k_i = k_{max}$, corresponding to a full monolayer on the surface.¹⁸ In contrast to this, the Brunauer-Emmett-Teller equation also accounts for multilayer adsorption. It is described as:

$$v = \frac{v_m c_B p}{(p_0 - p) \left[1 + (c_B - 1) \frac{p}{p_0}\right]} \quad (2.8)$$

Here, v_m corresponds to the volume of one adsorbed monolayer, p_0 describes the saturation pressure of the adsorbate while p is assigned to the equilibrium partial pressure of the adsorbate and c_B is the BET constant.

For the determination of the BET surface area, Equation (2.8) is brought into its linearized form

$$\frac{p}{v(p_0 - p)} = \frac{1}{v_m c_B} + \frac{c - 1}{v_m c_B} \frac{p}{p_0} \quad (2.9)$$

A plot of $p/v(p_0 - p)$ against p/p_0 gives $(c - 1)/v_m c_B$ as slope from which v_m can be determined.¹⁹

Assumptions include the energetic homogeneity of the surface, the possibility for multilayer growth and the absence of interactions of the adsorbent molecules within the adsorbent layer. Although not all of these conditions are always fulfilled in the investigated materials, the BET method is the standard analysis method for the determination of the

surface area in mesoporous and microporous solids and hence the method applied in this work.

The adsorption isotherm can furthermore be used to determine the pore size distribution of a mesoporous material.¹⁶ For that purpose, a commonly used model is one that was derived by Barrett, Joyner and Halenda (BJH) from the Kelvin equation for cylindrical pores:

$$\ln \frac{p}{p_0} = \frac{2\gamma V_m}{(r_p - t_c)RT} \quad (2.10)$$

with the molar volume of the liquid V_m , the surface tension γ , the pore radius r_p and the thickness of the adsorbed multilayer film t_c .

In addition to the Kelvin equation, the BJH method applies a standard isotherm, called t -curve, to take into account the pre-adsorbed multilayer film. As this model does not properly include the surface curvature in mesoporous materials and ignores the enhanced surface forces, it underestimates the pore sizes of narrow mesopores. Because of these limitations, today density functional theory (DFT) and Monte Carlo (MC) simulations are applied to determine the pore size distribution. Both methods provide a molecular level description of the distribution of the adsorbent molecules on the solid surface. Non-local DFT (NLDFT) models calculate theoretical isotherms for the given adsorbent/adsorptive pair and are available for a broad range of materials.

A limitation of the above methods is that these models assume a homogeneous surface of the porous material, thus deviating in most cases from the nature of the experimentally investigated materials. In order to account for the heterogeneity of the adsorbent, new methods such as Quenched Solid Density Functional Theory (QSDFT) have been developed recently, taking into account surface roughness and chemical inhomogeneity, and leading to significantly improved pore size distribution calculations.²⁰ Because of their improved modelling, QSDFT models have been applied for the pore size distribution determination in this work.

2.8 Contact Angle Measurement

Contact angle measurements determine the wettability of a surface. In the sessile drop method, a small droplet of the liquid is placed on the surface applying a microliter syringe and the droplet is viewed by a camera. From the recorded images, the angle between

droplet and surface is determined. According to Youngs' equation (Equation (2.11)) the contact angle of a droplet θ_Y on a surface is determined by the interplay of three interfacial tensions: liquid-vapor γ_{lv} , solid-vapor γ_{sv} , and solid-liquid γ_{sl} (Section 2.8).

$$\gamma_{lv} \cos\theta_Y = \gamma_{sv} - \gamma_{sl} \quad (2.11)$$

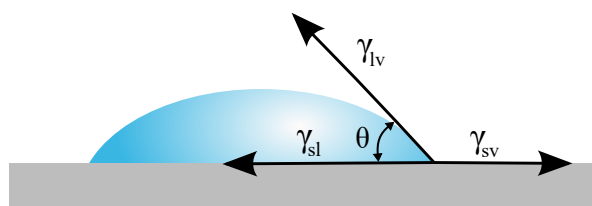


Figure 2.10: Illustration of the contact angle and the interfacial tensions.

If the wettability of the surface is very high, the droplet will spread over the surface with a contact angle close to 0° , while for a very poor wettability, the contact angle will be close to 180° .²¹

2.9 Thermogravimetric Analysis

In thermogravimetric analysis (TGA), the change of the sample mass upon heating at a defined heating rate is monitored. With this method, the thermal stability of materials and their content of volatile components can be determined. For this technique, a high weighting accuracy is necessary. TGA measurements are carried out by first placing the sample in the sample pan of a precision balance. Then, a controlled heating rate is applied and the sample chamber is purged with an either inert or reactive gas, usually N_2 or synthetic air. For analysis, the sample weight is plotted as a function of time or temperature. From this graph, temperatures of changes in the sample like desolvatization, oxidation, decomposition or phase transitions can be identified.

Bibliography

- [1] P. Atkins. *Physikalische Chemie*. 4th ed. Wiley-VCH, Weinheim, **2006**, 778–779.
- [2] W. H. Bragg and W. L. Bragg. *Proc. R. Soc. London, Ser. A*, **1913**, *88*, 428–438.
- [3] P. Scherrer. *Nachrichten von der Gesellschaft der Wissenschaften zu Göttingen, Mathematisch-Physikalische Klasse*, **1918**, 98–100.
- [4] G. Cao. *Nanostructures and Nanomaterials*. Imperial College Press, London, **2004**, 331.
- [5] P. Müller-Buschbaum. “A Basic Introduction to Grazing Incidence Small-Angle X-Ray Scattering”. In: *Applications of Synchrotron Light to Scattering and Diffraction in Materials and Life Sciences*. Springer Berlin/Heidelberg, **2009**, 61–89.
- [6] M. Otto. *Analytische Chemie*. Wiley-VCH, Weinheim, **1995**, 237.
- [7] M. Otto. *Analytische Chemie*. Wiley-VCH, Weinheim, **1995**, 234–235.
- [8] B. Z. Manfred Hesse Herbert Meier. *Spektroskopische Methoden in der organischen Chemie*. Thieme, Stuttgart, **2002**, 33–34.
- [9] M. Otto. *Analytische Chemie*. Wiley-VCH, Weinheim, **1995**, 277.
- [10] K. Cammann, ed. *Instrumentelle Analytische Chemie*. Spektrum Akademischer Verlag GmbH Heidelberg/Berlin, **2001**, 5/5–5/6.
- [11] M. Otto. *Analytische Chemie*. Wiley-VCH, Weinheim, **1995**, 194–196.
- [12] G. Kirchhoff and R. Bunsen. *Ann. Phys.*, **1860**, *186*, 161–189.
- [13] B. Fultz and J. Howe. *Transmission Electron Microscopy and Diffractometry of Materials*. Springer-Verlag Berlin/Heidelberg, **2008**, 60–63.
- [14] M. von Ardenne. *Z. Phys.*, **1938**, *109*, 553–572.
- [15] D. Brandon and W. Kaplan. *Microstructural Characterization of Materials*. John Wiley & Sons Ltd, Chichester, England, **2008**, 262–264.
- [16] M. Thommes, K. Kaneko, A. V. Neimark, J. P. Olivier, F. Rodriguez-Reinoso, J. Rouquerol, and K. S. Sing. *Pure Appl. Chem.*, **2015**, *87*, 1051–1069.
- [17] K. S. W. Sing. *Pure Appl. Chem.*, **1985**, *7*, 603–619.

- [18] G. Brezesinski and H.-J. Mögel. *Grenzflächen und Kolloide*. Spektrum Akademischer Verlag Heidelberg, **1993**, 42–43.
- [19] S. Brunauer, P. H. Emmett, and E. Teller. *J. Am. Chem. Soc.*, **1938**, *60*, 309–319.
- [20] M. Thommes and K. A. Cychoz. *Adsorption*, **2014**, *20*, 233–250.
- [21] Y. Yuan and T. R. Lee. “Contact Angle and Wetting Properties”. In: *Surface Science Techniques*. Springer Berlin/Heidelberg, **2013**, 3–34.

Chapter 3

From Benzodithiophene to Diethoxy-benzodithiophene Covalent Organic Frameworks - Structural Investigations

This chapter is based on the following publication:

Maria S. Lohse, Julian M. Rotter, Johannes T. Margraf, Veronika Werner, Matthias Becker, Simon Herbert, Paul Knochel, Timothy Clark, Thomas Bein, Dana D. Medina, *CrystEngComm* **2016**, *18*, 4295–4302.



Image prepared by Christoph Hohmann, Nanosystems Initiative Munich (NIM)

Abstract

The incorporation of side groups into a covalent organic framework (COF) backbone can be of significant importance for developing new frameworks with enhanced properties. Here we present a novel π -stacked thiophene-based COF containing a benzodithiophene building unit modified with ethoxy side chains. The resulting BDT-OEt COF is a crystalline mesoporous material featuring high surface area and accessible hexagonal pores. We further synthesized a series of COFs containing both BDT and BDT-OEt building units at different ratios. The impact of the gradual incorporation of the BDT-OEt building units into the COF backbone on the crystallinity and porosity was investigated. Furthermore, molecular dynamic simulations shed light on the possible processes governing the COF assembly from molecular building blocks.

3.1 Introduction

The self-organization of π -stacked organic layers into highly ordered three-dimensional porous structures endows covalent organic frameworks (2D COFs) with interesting properties for diverse applications, including chemical separations, catalysis and optoelectronics.¹⁻⁷ The extended organic layers constituting a 2D COF are generally obtained by the copolymerization of rigid building units having complimentary geometries through the formation of strong yet reversible covalent bonds. Boroxines and boronic esters, obtained by condensation reactions of boronic acids and diols, are commonly utilized as integral COF assembly motifs and thereby enable the growth of planar two-dimensional layers.⁸

Along with the condensation reactions, stacking of the formed organic layers takes place through dispersive forces.⁹ Therefore, 2D COFs connected through boronate esters feature an assembly of organic building units (or linkers) in a columnar fashion. This permits the formation of supramolecular structures having long-range order, one-dimensional channels and high surface areas.¹⁰⁻¹⁵ Tuning the structural and physical properties of a COF while maintaining its key features, namely porosity and crystallinity, can pose significant synthetic challenges. For example, incorporating building units having a large conjugated π -system into a framework can be highly desirable for enhanced light absorption properties.^{11,16} However, such attractive building units tend to exhibit poor solubility under the reaction conditions, often leading to poor crystallinity of the resulting COF.¹⁷

To overcome solubility limitations, a modification of the building units with solubilizing agents such as alkyl side chains can be considered. In the final COF structure the solubilizing side chains are oriented orthogonally to the COF pore walls and therefore need to be compatible with the stacking of the COF layers. In addition, these groups can play an important role in defining the electronic properties of the COF. Electron donating or electron withdrawing side groups can have a strong impact on the COF optical bandgap, and they can affect the fine balance between the Coulomb repulsion and the weak attractive London dispersion interactions holding the COF layers together. In an early study, Lavigne and co-workers reported the synthesis of a boronate ester-linked COF-18 series where the catechol building units were modified with linear alkyl side chains ranging from methyl to propyl groups. The impact of the integrated alkyl side chains on guest molecule uptake was investigated.¹⁸ In a later study, enhanced stability towards humidity of the propyl modified COF structure was shown within the COF-18 series.¹⁹ However, the overall long-range order of the COF-18 series was significantly diminished with the elongation of the side groups.

Jiang and co-workers introduced an azide-modified benzo diboronic acid (BDBA) for the purpose of COF backbone postmodification. In that report, the overall crystallinity of the modified COF-5 was maintained as the azide units having a planar configuration were extended along the plane of the COF layers.²⁰ Dichtel and co-workers introduced an effective crystallization route for boronate ester linked COFs starting from saturated homogeneous precursor solutions.^{9,21}

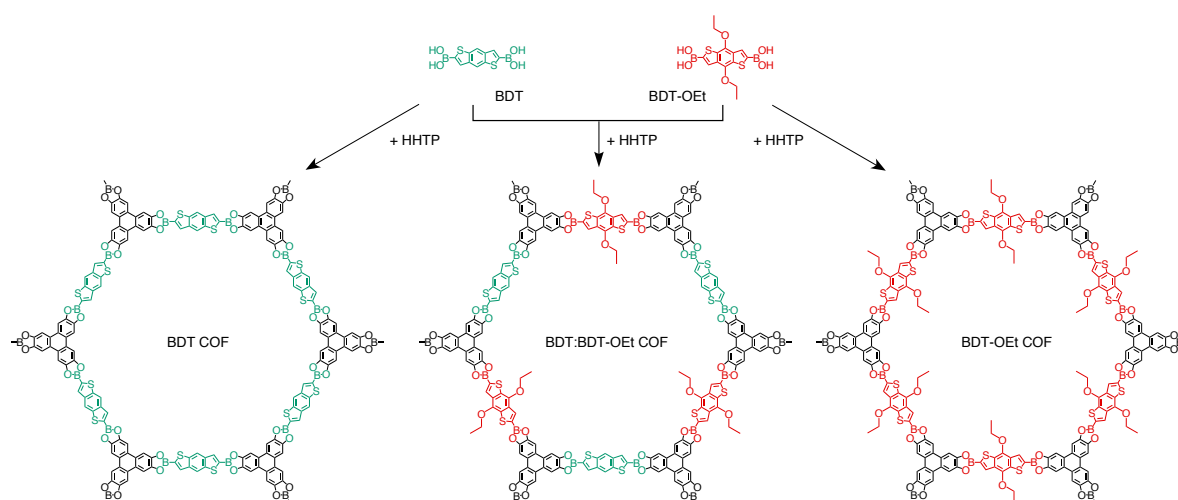


Figure 3.1: Schematic representation of the synthesis of BDT COF (left), BDT : BDT-OEt 1 : 1 COF (middle), and BDT-OEt COF (right).

Applying this method, COF structures having high surface area and long-range order were obtained. This crystallization route illustrates the importance of the COF precursor's solubility under reaction conditions. Recently, we reported the synthesis under solvothermal conditions of oriented thin films of an electron donor COF based on benzodithiophene units, BDT COF.²² We also introduced a novel vapor-assisted conversion approach for the direct deposition of BDT COF films under mild thermal conditions.²³ Herein, we describe the synthesis of a highly porous boronate ester linked BDT-OEt COF containing (4,8-diethoxybenzo[1,2-*b*:4,5-*b'*]dithiophene-2,6-diyl)diboronic acid.

The BDT core is modified with electron-donating ethoxy side chains thereby expanding the family of thiophene-based COFs.^{7,22,24,25} We synthesized a series of COFs consisting of BDT and BDT-OEt building unit mixtures and studied their structural properties (Figure 3.1). The impact of the gradual layer perturbation imposed by the increased fraction of incorporated BDT-OEt building units into the COF backbone on the crystallinity and porosity was investigated. Furthermore, molecular dynamic simulations shed light on the possible processes governing the COF assembly from molecular building units.

3.2 Results and Discussion

A novel BDT-OEt COF featuring a BDT core decorated with ethoxy side chains was synthesized through the co-condensation of (4,8-diethoxybenz[1,2-*b*:4,5-*b'*]dithiophene-2,6-diyl)diboronic acid and HHTP (2,3,6,7,10,11-hexahydroxytriphenylene) under solvothermal conditions (for more details see Experimental section).

Powder X-ray diffraction data of the newly synthesized BDT-OEt COF clearly indicate the formation of a crystalline framework. The diffraction pattern reveals an intensive reflection at 2.78° corresponding to the (100) plane. Additional reflections observed at 4.85° , 5.58° , 7.38° , 9.71° and $\approx 25.7^\circ$ (broad) are attributed to the (110), (200), (120), (220) and (001) planes, respectively (Figure 3.2). The obtained d-values correspond to lattice parameters of $a = b = 3.66$ nm for an ideal hexagonal BDT-OEt COF structure. Effective crystallite domain sizes of 21 nm in diameter for BDT-OEt COF were calculated using the Scherrer equation for reflection broadening.

Molecular mechanics simulations for the possible COF layer arrangements were carried out using Materials Studio software and the Forcite module. Assuming a hexagonal symmetry, the BDT-OEt COF unit cell was constructed in the $P6$ space group corresponding to an ideal eclipsed AA COF layer arrangement, and featuring a completely open pore system (Section 3.4.7).

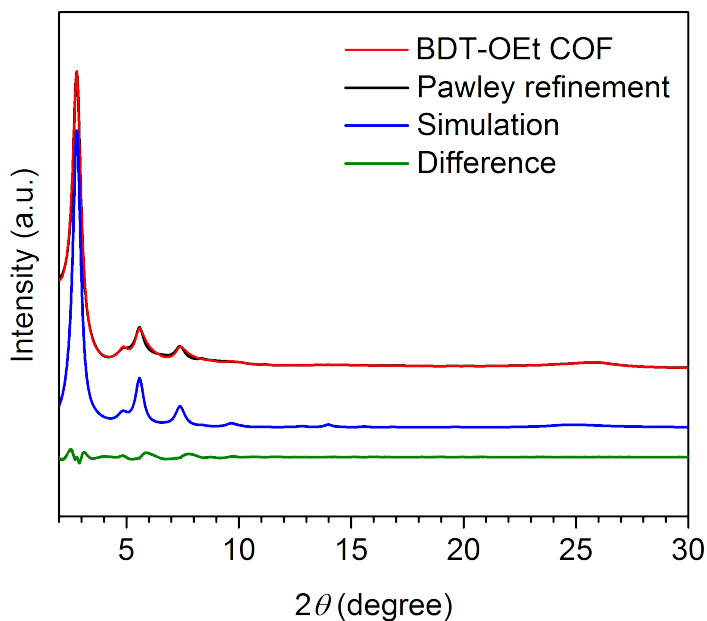


Figure 3.2: XRD patterns of BDT-OEt COF: experimental (red), Pawley refinement (black), simulated pattern (blue), and difference plot (green).

To obtain the final unit cell parameters and the crystallite domain sizes, Pawley refinement was employed. For this purpose, the geometry optimized BDT-OEt COF unit cell was refined against the experimental powder X-ray diffraction pattern. Lattice parameters of $a = b = 3.65$ nm, $c = 0.365$ nm and crystallite sizes of 20 nm in diameter were obtained.

The simulated powder diffraction pattern corrected for reflection broadening is in very good agreement with the experimentally observed pattern with regard to reflection positions and relative intensities (Figure 3.2). Additionally, we simulated the BDT-OEt COF unit cell in the triclinic $P1$ space group where no symmetry constraints are imposed. After geometry optimization and Pawley refinement, the refined unit cell reveals an eclipsed configuration with tilted COF layers.²⁶

This layer configuration produced a nearly identical simulated diffraction pattern, and therefore the exact eclipsed layer arrangement cannot be determined based on the experimental diffraction pattern (see Figure 3.15). To confirm the eclipsed layer arrangement for the BDT-OEt COF, we also simulated the X-ray diffraction pattern for an alternative hexagonal unit cell with $P6_3$ space group corresponding to a staggered, AB layer arrangement (Figure 3.18a). Based on the comparison of the simulated AA and AB patterns with the experimentally obtained pattern, we conclude that BDT-OEt crystallizes with an eclipsed layer arrangement allowing for an open pore system. In previous reports, the

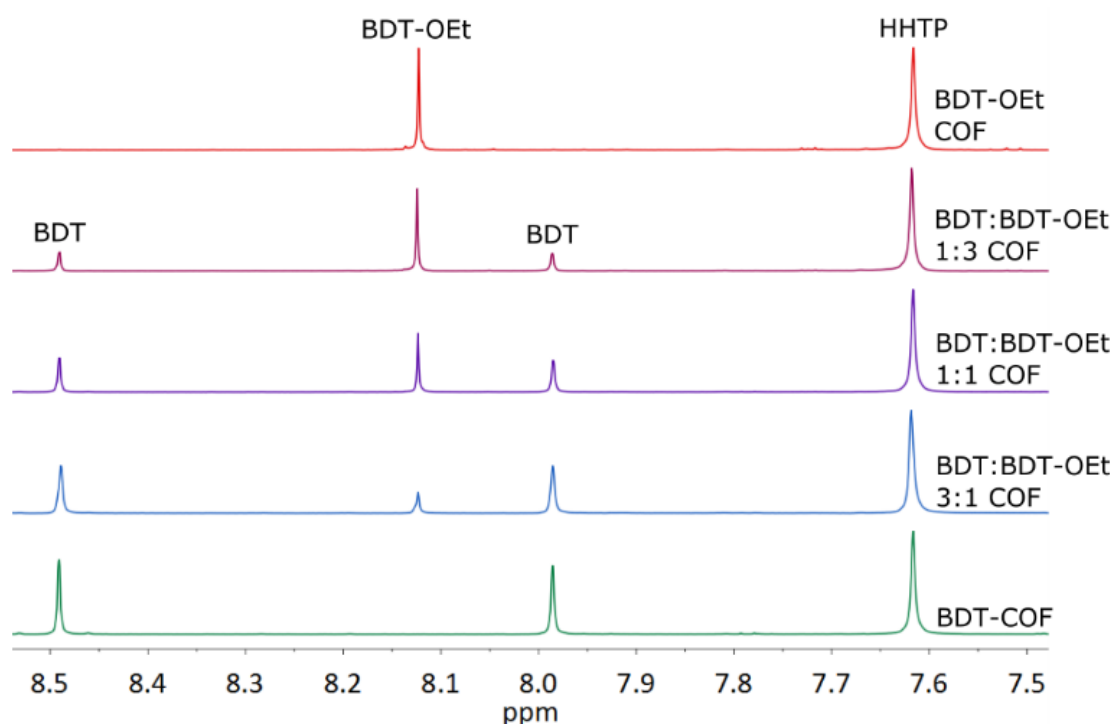


Figure 3.3: ^1H -NMR spectra of the hydrolyzed COFs showing the stoichiometric incorporation of BDT and BDT-OEt linkers into the respective frameworks.

side groups decorating the pore walls were considered as an amorphous contribution to the X-ray scattering data, having no preferred orientation in the pore due to their free rotation.^{18,20,27}

To investigate the preferred orientation of the ethoxy groups in the pores, several separate molecular dynamics simulations were carried out (Figure 3.6). Independent of the initial orientation of the groups, which can either face the adjacent hydrogen or sulfur atom of the BDT core or alternate between these two cases, nearly all ethoxy-groups rotated to face the sulfur atom within less than 1 ns.

The ethoxy groups retained their position, indicating that the groups can in principle rotate at room temperature, and that the sulfur-facing position is favoured in the crystal (Figure 3.6). This was confirmed by DFT calculations at the PBE+D level, which indicate that the sulfur-facing geometry is more stable by 0.2 eV (corresponding to a Boltzmann population ratio of approx. 4×10^{-4} for the hydrogen-facing geometry at room tempera-

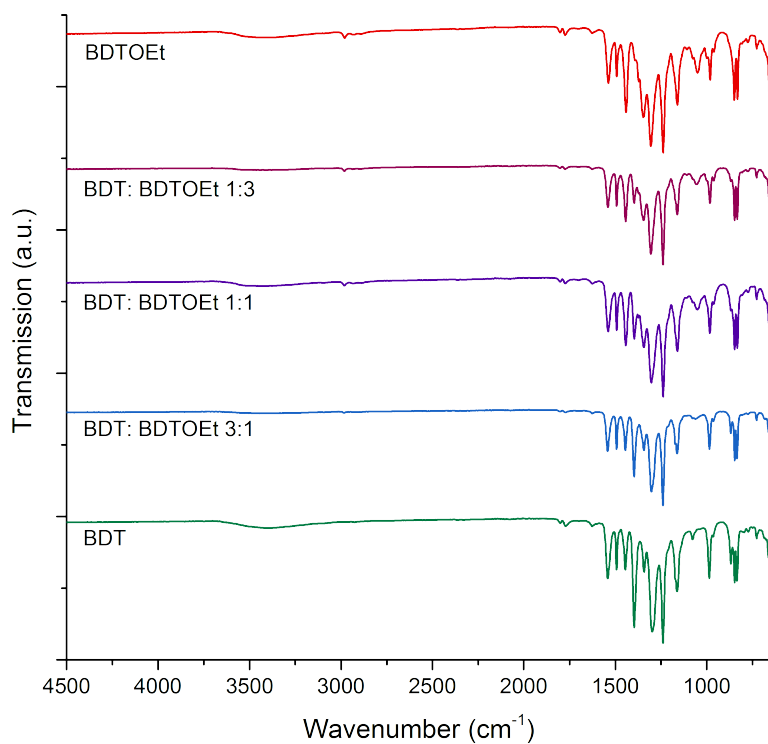


Figure 3.4: FT-IR plots of BDT COF, BDT:BDT-OEt COFs and BDT-OEt COF.

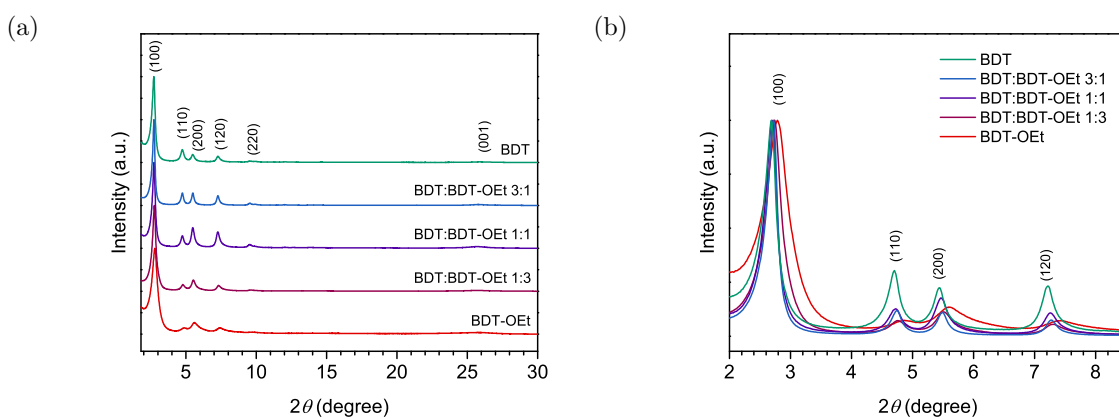


Figure 3.5: PXRD patterns of BDT COF, BDT : BDT-OEt COFs, and BDT-OEt COF: (a) stacked plot, (b) low angle region.

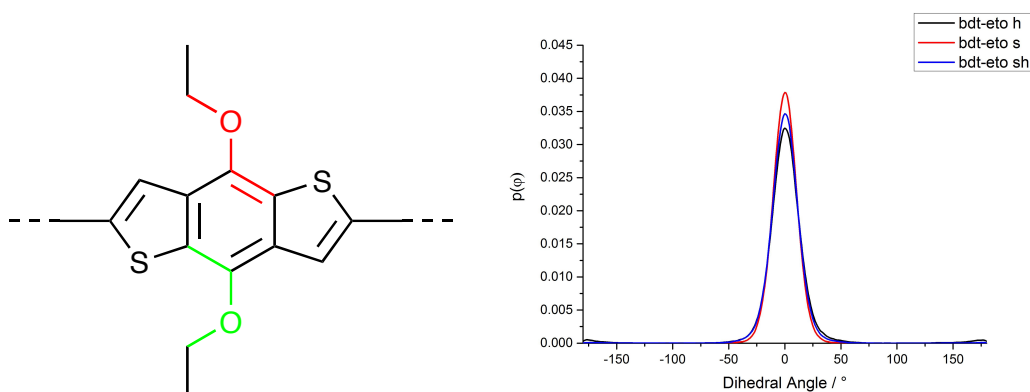


Figure 3.6: Left: Molecular structure of the ethoxy-substituted BDT unit. The possible initial orientations for the dihedral angle are shown in red (facing hydrogen, 180°) and green (facing sulfur, 0°). Right: Probability distribution of the dihedral angle sampled over 10 ns. Almost all dihedrals reorient to face the sulfur atom within the equilibration period of 0.1 ns, independent of the starting orientation (s = sulfur, h = hydrogen, sh = mixed).

ture). This preference can be attributed to the electrostatic attraction between the sulfur lone-pairs and the ethoxy hydrogen atoms.

Nitrogen sorption analysis of an activated BDT-OEt COF powder reveals a type IV sorption isotherm, with a distinct nitrogen uptake at relative low partial pressures, typical for a mesoporous material (Figure 3.8e).

The Brunauer–Emmett–Teller (BET) surface area was calculated to be as high as $1844 \text{ m}^2 \text{ g}^{-1}$ ($p/p_0 = 0.05\text{--}0.13$ in the adsorption branch) and the pore volume to be $1.07 \text{ m}^3 \text{ g}^{-1}$. These values are in good agreement with the simulated Connolly surface area of $2075 \text{ m}^2 \text{ g}^{-1}$ and calculated pore volume of $1.06 \text{ m}^3 \text{ g}^{-1}$ for a BDTOEt COF with an eclipsed layer arrangement. BDT-OEt COF exhibits a narrow pore size distribution as derived from the sorption isotherm with a pore size of 2.9 nm corresponding to a defined mesoporous structure (Figure 3.7).

An aggregation process of COF crystallites into larger domains was discussed as a crucial non-reversible step for the formation of COF precipitates.⁹ Scanning electron microscopy (SEM) micrographs of BDT-OEt COF bulk material indicate that the small BDT-OEt COF crystallites aggregate into micrometer spherical agglomerates upon COF powder precipitation (Figure 3.9). Transmission electron microscopy (TEM) images reveal an intergrowth of small BDT-OEt COF crystallites into larger polycrystalline domains.

In contrast to the BDT COF, less regular fairly short COF channels can be observed (Figure 3.9e). These observations are in accordance with the reflection broadening ob-

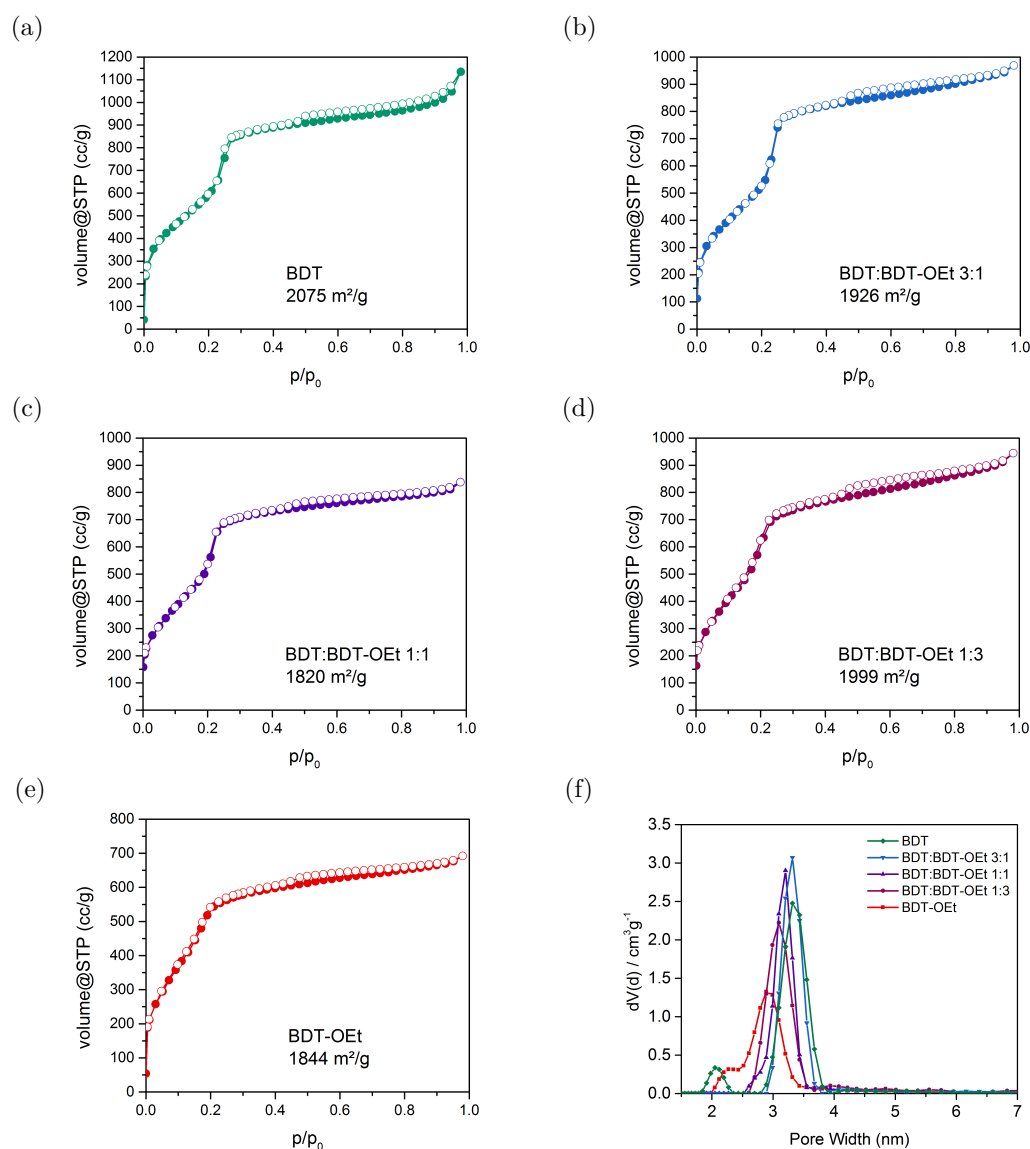


Figure 3.7: (a) to (e) Nitrogen sorption isotherms of the COF powders. (f) Detail of the pore size distributions of BDT COF, mixed BDT : BDT-OEt COFs and BDT-OEt COF showing the decrease of the main pore diameter upon the incorporation of ethoxy side chains into the COF structure.

served in the X-ray analysis and suggest that the incorporation of ethoxy side chains can influence the COF growth process in both the ab-plane and the stacking direction.

Thermogravimetric analysis (TGA) of the COF powder displays a major mass loss at 400°C that is attributed to framework decomposition (Figure 3.11e). The formation of a boronate ester motif in the COF framework was confirmed by FT-IR and solid-state NMR spectroscopy. IR-bands at 1346 and 1238 cm^{-1} are attributed to the B-O and C-O vibrational modes of the ester formed (Figure 3.4).

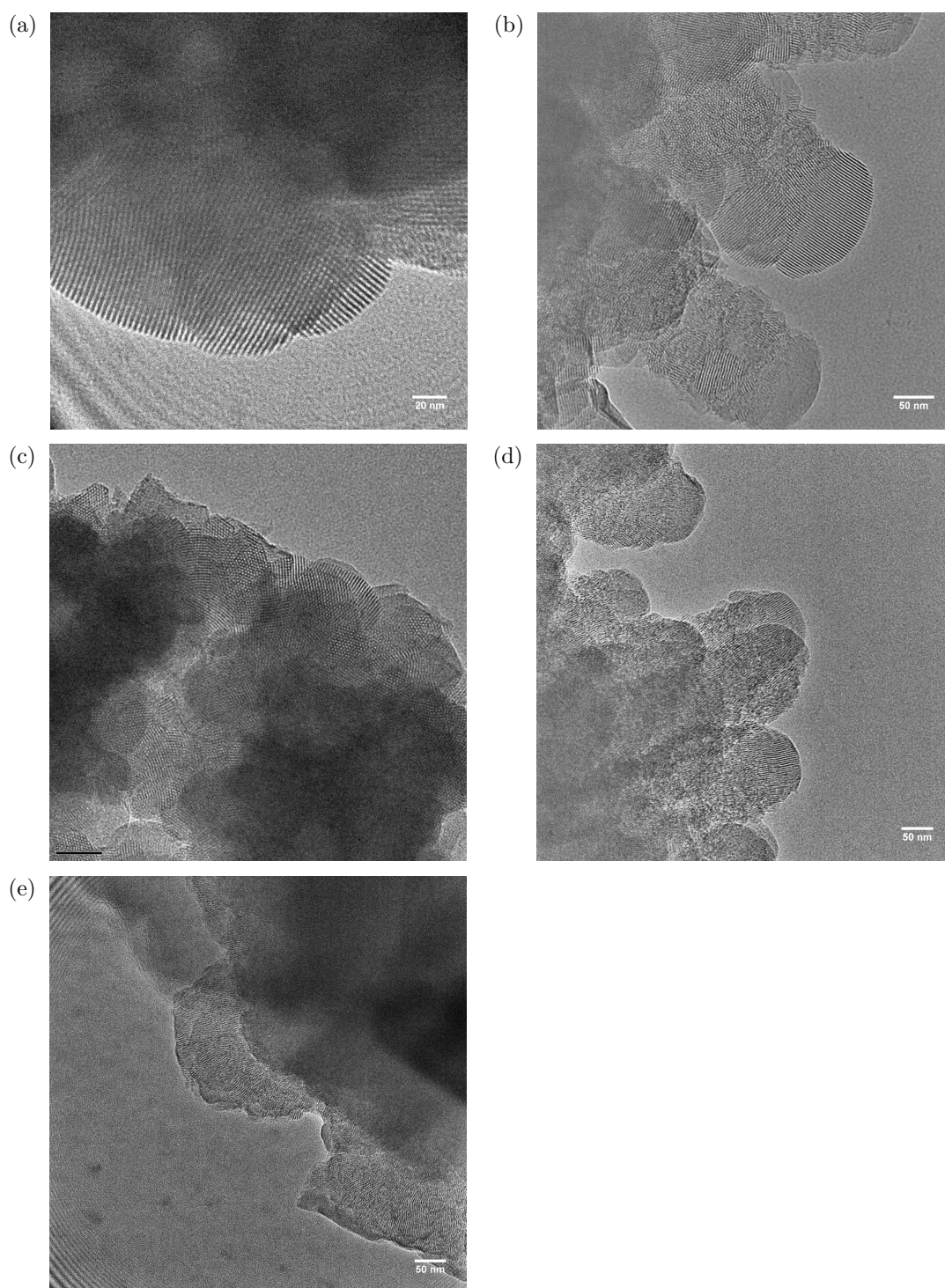


Figure 3.8: TEM micrographs of (a) BDT COF, (b) BDT:BDT-OEt 3 : 1 COF, (c) BDT:BDT-OEt 1 : 1 COF, (d) BDT:BDT-OEt 1 : 3 COF, (e) BDT-OEt COF, respectively.

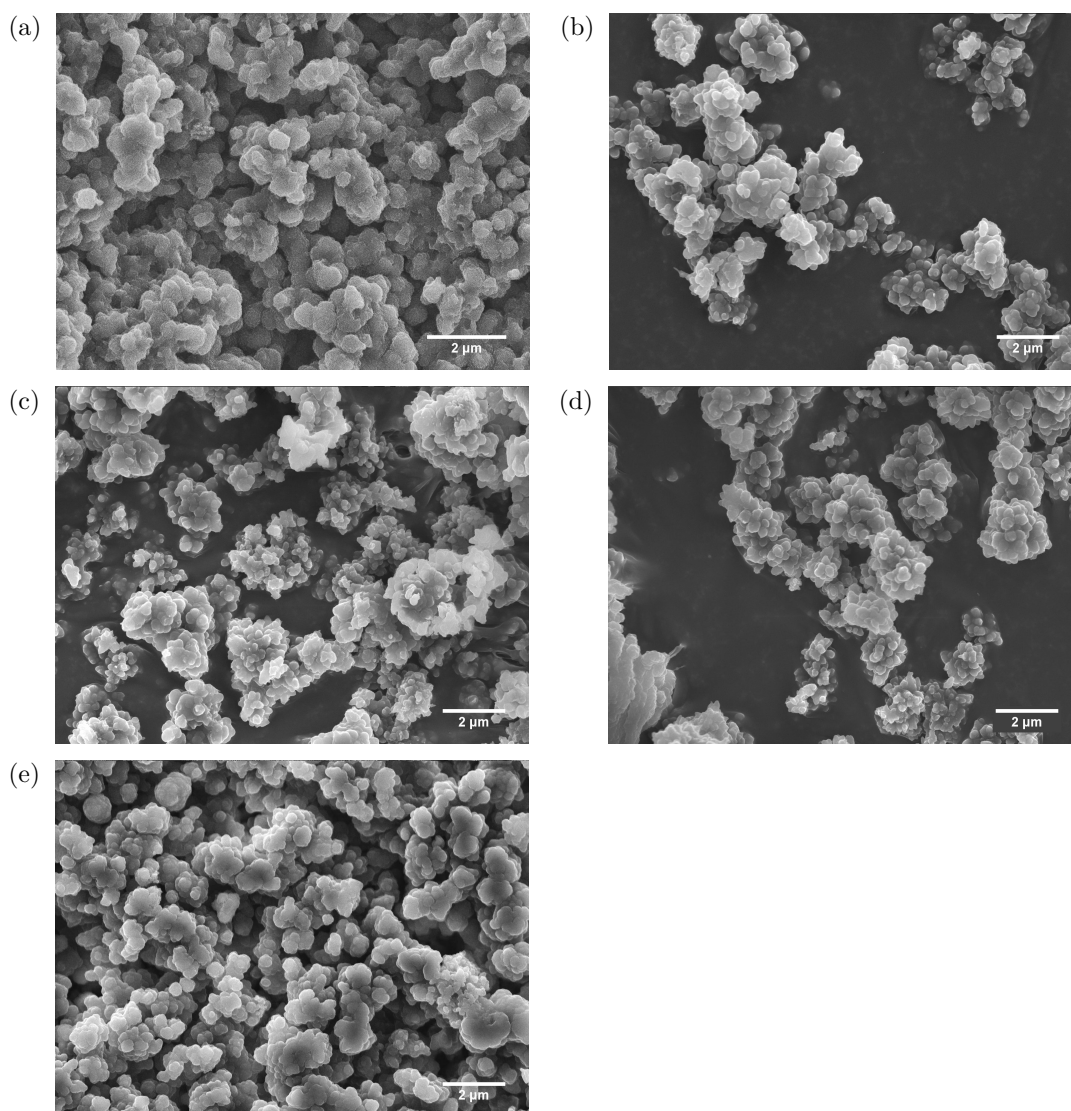


Figure 3.9: SEM micrographs of (a) BDT COF, (b) BDT:BDT-OEt 3 : 1 COF, (c) BDT:BDT-OEt 1 : 1 COF, (d) BDT:BDT-OEt 1 : 3 COF, (e) BDT-OEt COF, respectively.

In the ^{11}B solid-state NMR spectrum of BDT-OEt COF, a strong peak at 20.9 ppm confirms the presence of a trigonal-planar boron atom of a boronate ester (Figure 3.11a). In the ^{13}C solid-state NMR spectrum, the signals at 13.2 ppm and 67.7 ppm are attributed to the methyl and methylene carbon atoms in the ethoxy side chain (Figure 3.11b). Boronate ester linked COFs consisting of building unit mixtures have been introduced in a series of COF-5 structures modified with azide side chains as a platform for a gradual post synthetic modification *via* click chemistry.²⁰

Herein, we aim at investigating the structural changes imposed by ethoxy groups on a well-defined and highly crystalline COF structure such as the BDT COF. For this pur-

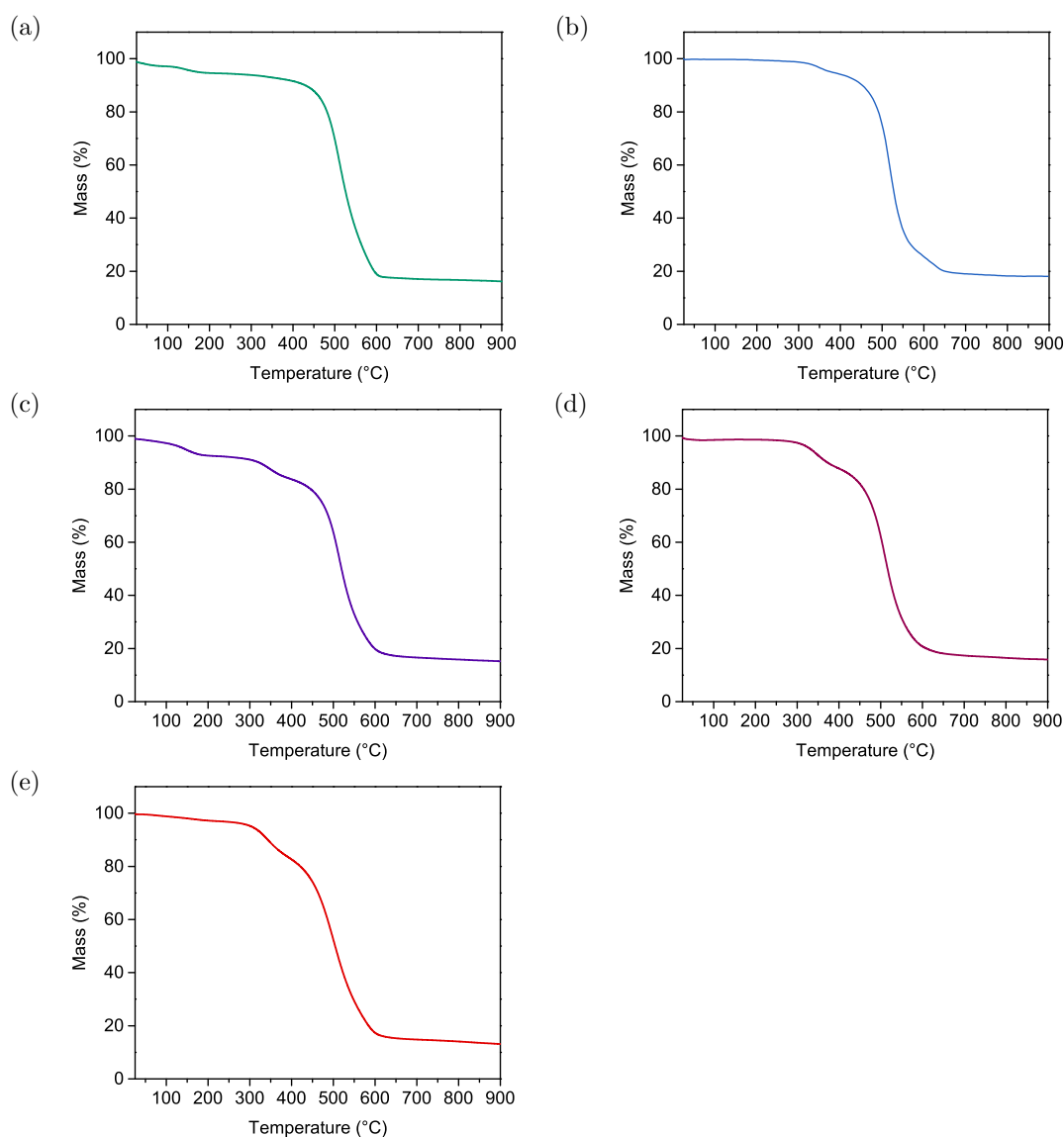


Figure 3.10: TGA traces of (a) BDT COF, (b) BDT:BDT-OEt 3 : 1 COF, (c) BDT:BDT-OEt 1 : 1 COF, (d) BDT:BDT-OEt 1 : 3 COF, (e) BDT-OEt COF, respectively.

pose, we synthesised a series of COFs where both building units BDT and BDT-OEt are randomly distributed within the COF backbone at different ratios. The BDT : BDT-OEt COF series was synthesised under solvothermal conditions similarly to the synthesis of BDT-OEt COF, with BDT : BDT-OEt building unit ratios of 1 : 0, 3 : 1, 1 : 1, 1 : 3 and 0 : 1 (for more information see Experimental).

Powder X-ray diffraction patterns of the obtained BDT : BDT-OEt COFs confirmed the formation of a series of crystalline frameworks (Figure 3.5a). Upon the incorporation of ethoxy side chains into the BDT COF backbone, gradual changes in the BDT : BDT-

OEt COF diffraction patterns were observed. The relative intensities of the (110) and (200) planes change with the increased fraction of BDT-OEt building units.

This is in excellent agreement with the simulated diffraction patterns of BDT and BDT-OEt COFs and further confirms the successful incorporation of BDT-OEt into the frameworks (Figure 3.18b). A broadening of the X-ray reflections is evident in BDT-OEt-rich COFs. The effective crystallite domain sizes calculated for BDT : BDT-OEt 3 : 1 and BDT : BDT-OEt 1 : 3 COFs are 95 nm and 47 nm, respectively. Therefore, we attribute the reflection broadening to a regular decrease in the crystallite domain sizes with increasing the BDT-OEt building unit content.

A gradual small shift of the reflections corresponding to the *ab* plane to higher 2θ values with the higher integrated fraction of BDT-OEt building units is observed as well (Figure 3.5b). Interestingly, the broad reflection at $\approx 25.7^\circ$, attributed to the layer stacking, maintained its position and its relative intensity. The gradual shift to higher 2θ values implies that the incorporation of ethoxy groups into the frameworks induced structural modifications expressed in the unit cell parameters. This can be either attributed to a gradual shrinkage of the hexagonal unit cell or to a gradual increase of layer dynamics resulting in a *P1* like structure (Figure 3.15c).²⁶

Molecular dynamics simulations regarding the layer interactions provided further insights into the effect of the ethoxy groups on the dynamics and order of the system. A comparison of the sulfur–sulfur radial distribution functions $g_{SS}(r)$ for the ethoxy substituted and pristine BDT COF reveals a significant increase in short-range disorder in the former COF (Figure 3.12). This is evident from the broadening and shifted position towards larger distances of the first peak $g_{SS}(r)$ corresponding to the closest sulfur–sulfur distance between adjacent layers.

The increased short-range disorder is attributed mainly to increased movement of the layers in the *ab*-plane, since more displaced geometries are stabilized by the interactions between the ethoxy groups. Interestingly, the average interlayer distance in the simulations increases when the ethoxy groups are present, which might be expected due to the spatial demands of the ethyl groups. However, this trend regarding the interlayer distances is not observed in the experimental pattern.

The impact of the gradual incorporation of the ethoxy side chains on the pore accessibility of the frameworks was investigated by nitrogen sorption. The BDT : BDT-OEt COF series retained the typical type IV isotherms for mesoporous materials.

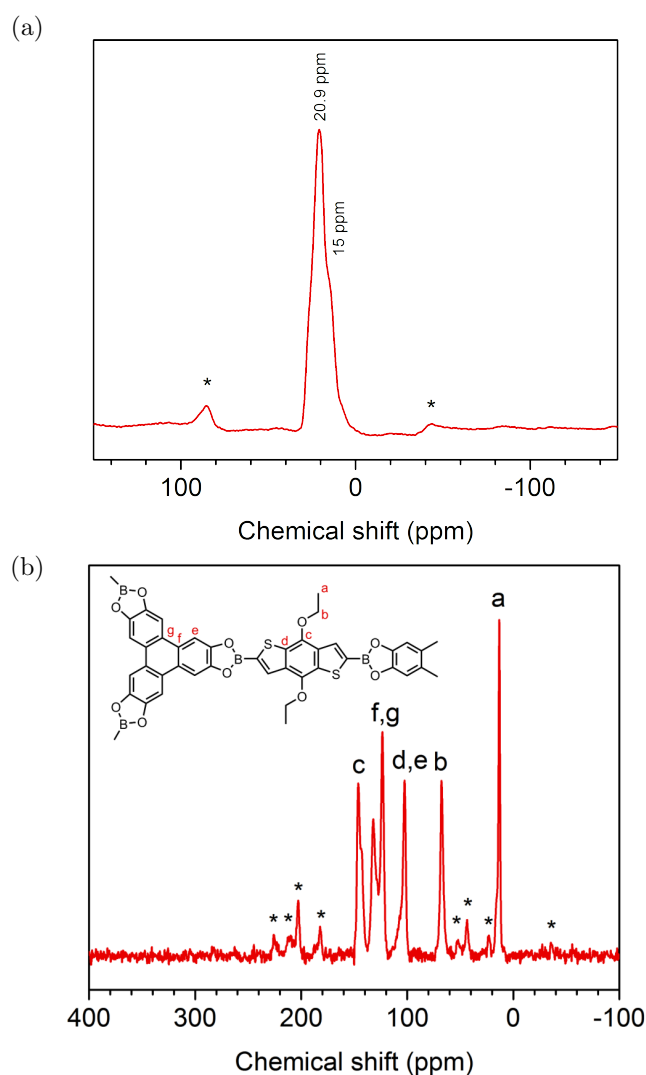


Figure 3.11: (a) ^{11}B ssNMR spectrum of BDT-OEt COF showing a boronic ester peak at 20.9 ppm. The shoulder peak at 15 ppm is attributed to free boronic acid groups present as terminal moieties of the framework. Asterisks indicate spinning side bands. (b) ^{13}C ssNMR spectrum of BDT-OEt COF. Asterisks indicate spinning side bands.

The relative partial pressure of the slope of the nitrogen uptake is shifted to lower values as expected for the gradually increasing pore occupancy with ethoxy side chains.

Pore size distribution evaluation revealed a gradual decrease of the pore size upon the incorporation of ethoxy side chains. In all the BDT : BDT-OEt COF structures only one type of pore is present, indicating a random integration of the ethoxy groups into the frameworks, as opposed to the formation of phase-separated domains. High surface areas were calculated for the BDT : BDT-OEt COF series. This clearly illustrates that incorporation of BDT-OEt building units into the framework does not affect the accessible surface areas and pores of the BDT : BDT-OEt COF (Figure 3.7).

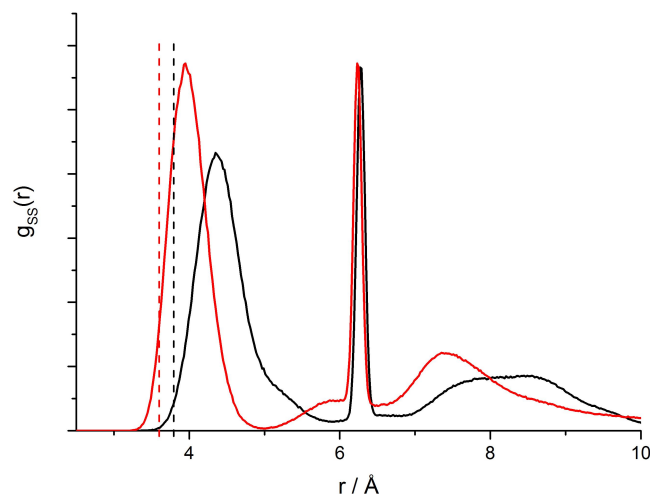


Figure 3.12: Sulfur-sulfur radial distribution functions of the ethoxy substituted (black) and pristine (red) BDT-COF. The vertical, dotted lines indicate the respective average interlayer distance.

The solubility of the respective building units under the reaction conditions plays an important role regarding their incorporation into the COF backbone. If a significant solubility difference would exist, their ratio in the frameworks might deviate from the initial stoichiometric mixture. To determine the final BDT : BDT-OEt ratio incorporated into the frameworks, samples of the respective BDT : BDT-OEt COF series were hydrolysed in wet DMSO-d₆ for ¹H NMR spectroscopy.

Integrating the proton signals of the building units showed that the observed intensities are in very good agreement with the intended stoichiometric ratios of BDT, BDT-OEt and HHTP building units for all COFs. Therefore defects in the form of precursor deficiencies within the frameworks are not observed (Figure 3.3 and Section 3.4.8). SEM micrographs reveal a similar overall morphology for all investigated COFs.

Small unevenly shaped particles form large aggregates, comparable with the morphology we observed for BDT-OEt COF (Figure 3.9). In TEM images, BDT-rich COFs show intergrown cauliflower morphology. Depending on the crystallite orientation, ordered channels or the typical honeycomb structure are visible. BDT-OEt-rich COFs feature smaller crystallite domain sizes and shorter COF channels (Figure 3.8).

TGA traces were recorded to determine the thermal stability of the COF series. For all COFs, the major mass loss attributed to the decomposition of the framework takes place at 400 °C, showing a similar thermal stability of all investigated frameworks (Figure 3.10).

These analyses confirm that with BDT and BDT-OEt building units, COFs can be formed from freely selected ratios of the respective boronic acids. While mixing these building units in a COF leads to structural changes in the framework, a highly porous, crystalline and thermally stable framework is generated in all cases.

3.3 Conclusion

In conclusion, a novel ethoxy-functionalized benzodithiophene based COF, namely BDT-OEt COF, was synthesized under solvothermal conditions. BDT-OEt COF features crystallinity, mesoporosity and high surface area. A series of COFs consisting of both BDT and BDT-OEt building units in different ratios was synthesized. Highly crystalline, mesoporous frameworks were obtained for all BDT : BDT-OEt COFs.

A nearly linear evolution from BDT to BDT-OEt COF was observed with regard to pore size and crystallite domain size upon the gradual incorporation of BDT-OEt building units into the COF backbone. Furthermore, we show that the final building unit ratios in the framework can be predetermined prior to the COF synthesis. Therefore, the COF backbones and chemical pore environment can be finely tuned towards desired properties while an eclipsed layer arrangement is retained.

Molecular dynamics simulations and DFT calculations shed light on the preferred orientation of the ethoxy groups in the pores. Furthermore, the simulations illustrate that the incorporation of ethoxy chains facilitates a subtle lateral displacement of the BDT COF layers relative to each other.

3.4 Experimental

3.4.1 Materials

All materials (if not otherwise noted) were purchased from Aldrich, Fluka, Acros or TCI Europe in the common purities *purum* and *puriss*. All materials were used as received without further purification.

3.4.2 Synthesis of 4,8-diethoxybenzo[1,2-*b*:4,5-*b'*]dithiophene (1)

The reaction was performed based on a literature procedure.²⁸ A mixture of benzo[1,2-*b*:4,5-*b'*]dithiophene-4,8-dione (1.10 g, 4.99 mmol, 1.0 equiv.), zinc dust (0.981 g, 15.0 mmol, 3.0 equiv.), NaOH (10 mL) and EtOH (10 mL) was stirred at 95 °C for 2 h. Ethyl *p*-toluenesulfonate (3.00 g, 15.0 mmol, 3.0 equiv.) was added and the resulting solution

was stirred at 95 °C for additional 3 h. The reaction mixture was allowed to cool down to room temperature and was diluted with dichloromethane (DCM) (70 mL). The aqueous layer was extracted with DCM (4×100 mL) and the combined organic fractions were dried over Na₂SO₄. After filtration, the solvents were evaporated *in vacuo*.

The crude product was purified by flash column chromatography (silica, isohexane/DCM = 3 : 1) to afford **1** as a colorless solid (0.675 g, 49%). Mp: 96.9-102.6 °C. ¹H NMR (400 MHz, CDCl₃) δ/ppm = 7.46 (d, *J* = 5.5 Hz, 2H), 7.35 (d, *J* = 5.5 Hz, 2H), 4.35 (q, *J* = 7.0 Hz, 4H), 1.47 (t, *J* = 7.0 Hz, 6H). ¹³C NMR (100 MHz, CDCl₃) δ/ppm = 144.3, 131.8, 130.4, 126.0, 120.3, 69.4, 16.1. IR (cm⁻¹): $\tilde{\nu}$ = 3100, 2980, 2873, 1892, 1515, 1477, 1436, 1372, 1347, 1199, 1106, 1085, 1029, 977, 873, 810, 752, 736, 695, 661. MS (70 eV, EI) *m/z*(%) = 278 (27, M⁺), 223 (11), 222 (13), 221 (100), 111 (37), 44 (31), 43 (80). HRMS for C₁₄H₁₄O₂S₂ (278.0435) found: 278.0428.

3.4.3 Synthesis of 2,6-dibromo-4,8-diethoxybenzo[1,2-*b*:4,5-*b'*]-dithiophene (**2**)

In a dry argon flushed Schlenk-flask, equipped with a magnetic stirring bar and septum, **1** (1.39 g, 5.0 mmol, 1.0 equiv.) was dissolved in *N,N*-dimethylformamide (25 mL) and cooled down to 0 °C. *N*-Bromosuccinimide (1.78 g, 10.0 mmol, 2.0 equiv.) was added in one portion and the resulting solution was warmed to room temperature and stirred for 4 h. The reaction mixture was diluted with water (100 mL) and extracted with Et₂O (3×30 mL). The combined organic layers were washed with water (6×100 mL) and dried over Na₂SO₄.

After filtration, the solvents were evaporated *in vacuo*. The crude product was purified by flash column chromatography (silica, isohexane) to give **2** as a colorless solid (1.50 g, 69%). Mp: 158.7-161.9 °C. ¹H NMR (400 MHz, CDCl₃) δ/ppm = 7.41 (s, 2H), 4.26 (q, *J* = 7.0 Hz, 4H), 1.44 (t, *J* = 7.0 Hz, 6H). ¹³C NMR (100 MHz, CDCl₃) δ/ppm = 142.3, 131.4, 131.1, 123.2, 115.0, 69.7, 16.0. IR (cm⁻¹): $\tilde{\nu}$ = 2980, 2927, 2886, 1905, 1520, 1479, 1442, 1370, 1350, 1265, 1170, 1104, 1042, 999, 935, 894, 873, 809, 689, 668. MS (70 eV, EI) *m/z* (%) = 434 (23, M⁺), 409 (25), 407 (44), 405 (22), 381 (54), 380 (18), 379 (100), 378 (14), 377 (47), 300 (30), 298 (28), 191 (16), 189 (11), 109 (11), 61 (12), 45 (11), 43 (70). HRMS for C₁₄H₁₂O₂Br₂S₂ (433.8640) found: 433.8649.

3.4.4 Synthesis of 4,8-diethoxybenzo[1,2-*b*:4,5-*b'*]-dithiophene-2,6-diyl diboronic acid (**3**)

In a dry argon flushed Schlenkflask, equipped with a magnetic stirring bar and septum, **2** (434 mg, 1.00 mmol, 1.0 equiv.) was dissolved in tetrahydrofuran (THF) (8 mL) and cooled down to -40°C . *n*-BuLi (1.06 mL, 2.5 mmol, 2.5 equiv., 2.35 M in hexane) was added and the resulting solution was stirred for 1.5 h and cooled down to -85°C . Then, triisopropyl borate (0.69 mL, 3.0 mmol, 3.0 equiv.) was added and the reaction mixture was allowed to warm to room temperature and stirred overnight. The solution was diluted with half-concentrated aq NH_4Cl solution (25 mL). The alkaline solution was acidified to pH 6 (with 2.0 M HCl) and extracted with a 3 : 1 THF : diethyl ether mixture (3×150 mL). The combined organic layers were dried over Na_2SO_4 . After filtration, the solvents were evaporated *in vacuo*. The crude product was suspended in isohexane (70 mL) and the mixture was stirred at room temperature for 5 h.

The precipitate was filtered off and dried *in vacuo*. **3** was obtained as green solid (184 mg, 50%) and was used without further purification. Mp: $71.9\text{--}274.3^{\circ}\text{C}$. ^1H NMR (400 MHz, acetone- d_6) δ/ppm = 8.14 (s, 2H), 4.39 (q, $J = 7.2$ Hz, 4H), 1.47 (t, $J = 7.2$ Hz, 6H). ^{13}C (75 MHz, acetone- d_6) δ/ppm = 145.5, 135.1, 134.5, 130.3, 70.4, 16.8. IR (cm^{-1}): $\tilde{\nu} = 3209, 2978, 1532, 1445, 1373, 1344, 1320, 1161, 1084, 1046, 989, 959, 850, 788, 700$. HRMS for $\text{C}_{14}\text{H}_{15}\text{O}_6\text{B}_2\text{S}_2$ (365.0496) found: 365.0501.

3.4.5 COF synthesis

A 25 mL Schott Duran glass bottle with a Teflon sealed polybutylene terephthalate cap was equipped with 2,3,6,7,10,11-hexahydroxytriphenylene, HHTP (11 mg, 0.034 mmol) and a total of 0.051 mmol of BDT : BDT-OEt linkers in molar ratios of 1 : 0, 3 : 1, 1 : 1, 1 : 3, and 0 : 1. The reaction mixture was suspended in 1.5 mL of a 1 : 1 (v/v) solution of mesitylene/dioxane and heated for 72 h at 100°C . Afterwards, the green precipitate was isolated by filtration and dried *in vacuo* for 72 h at 150°C .

3.4.6 Computational details

The models were defined as periodic supercells containing ten COF layers. MD simulations were performed in the isothermal-isobaric ensemble (at 25 °C and 1 atm), using the Dreiding forcefield as implemented in Forcite Plus and a timestep of 1 fs.²⁹ This forcefield has been shown to provide high quality descriptions of polythiophenes in the condensed phase.³⁰ The average temperature was kept constant using the Andersen thermostat during equilibration and the Nosé–Hoover–Langevin thermostat during production runs. Isotropic pressure was kept constant using the Berendsen barostat. Charges for the periodic COF network were calculated using the QEq scheme.³¹

Long range electrostatic and van der Waals interactions were treated *via* the Ewald summation method, with a 6 Å cutoff on the repulsive contribution to the van der Waals energy. In all dynamics runs, the system was equilibrated for 0.1 ns and results were collected over 10 ns. DFT calculations were performed with CASTEP,³² using the PBE functional and the D2 dispersion correction as implemented in the DFT-SEDC code.^{33–35} We used a plane wave basis set with a 340 eV cutoff and ultrasoft pseudopotentials.³⁶ k -point sampling was performed with a $1 \times 1 \times 6$ Monkhorst–Pack grid.³⁷

3.4.7 Characterization

Fourier-transform infrared spectra were measured with a Bruker Equinox 55 equipped with a PIKE MIRacle ATR-unit at room temperature in the scan range 650–4000 cm^{-1} . Nitrogen sorption was measured with 20–25 mg sample using a Quantachrome AUTOSORB-1 station at 77.3 K after degassing the sample for at least 12 h under vacuum at 150 °C. The Brunauer–Emmett–Teller (BET) surface areas were calculated from the adsorption branch in the range of $p/p_0 = 0.05 - 0.13$. Pore sizes were calculated with a QSDFT adsorption model of N_2 on carbon (cylindrical, adsorption branch). Powder X-ray diffraction (PXRD) measurements were carried out in reflection mode on a Bruker D8 Discover diffractometer with Ni-filtered $\text{K}\alpha$ radiation ($\lambda = 1.54060 \text{ \AA}$) and a position-sensitive detector (LynxEye). Molecular geometry optimization was performed with Accelrys MS Modeling 4.4 using the universal and Dreiding forcefield method. The final hexagonal unit cell was calculated with the geometric parameters from the optimized structure. For the Pawley refinement and simulation of the PXRD patterns the Reflex module was used (a software package implemented in MS Modeling 4.4).

Scanning electron microscopy (SEM) was performed on a JEOL 6500F instrument at an acceleration voltage of 2–5 kV. The samples were coated with a thin carbon layer by

carbon fiber flash evaporation at high vacuum. Transmission electron microscopy (TEM) data were obtained with a FEI Titan Themis 60–300 microscope at an acceleration voltage of 300 kV. Cross-polarized ^{11}B and ^{13}C solid-state NMR (ssNMR) measurements were performed on a Bruker Avance III-500 spectrometer in a 4 mm ZrO_2 rotor with a spinning rate of 10 kHz. Thermogravimetric analyses (TGA) were recorded on a Netzsch STA 440 C TG/DSC. The measurements proceeded at a heating rate of 10 $^\circ\text{C}/\text{min}$ up to 900 $^\circ\text{C}$, in a stream of synthetic air of about 25 mL min^{-1} . Hydrolyzed COF ^1H NMR solution spectra were recorded on a Bruker Avance III-400 MHz spectrometer. 5 mg of COF powder was dissolved in DMSO- d_6 containing 5% D_2O in every case. A relaxation delay of 8 s was employed to increase the precision of aromatic signal integration.

Appendix

BDT-OEt COF simulated structures

Molecular mechanics simulations for the BDT-OEt COF unit cell were carried out using Materials Studio software 4.4 and the Forcite module. First, we constructed a bare hexagonal $P6$ space group unit cell with lattice parameters reported for the BDT-COF. Based on the functional groups and the geometry of the BDT-OEt COF precursor molecules, the repeating unit was constructed and placed in the bare hexagonal unit cell to obtain the complete unit cell. The geometry of the BDT-OEt COF layer was optimized in the unit cell using the Dreiding forcefield and the QEq correction for weak interactions. The Reflex package in the Materials Studio software allows for Pawley refinement for the simulated unit cell parameters according to the experimental PXRD. The simulated unit cell parameters were refined against the experimental PXRD. The refinement parameters R_p and R_{wp} are 3.37% and 4.95%, respectively, the final unit cell parameters are $a = b = 36.56 \pm 0.04 \text{ \AA}$, $c = 3.65 \pm 0.04 \text{ \AA}$.

Table 3.1: Refined crystal data of BDT-OEt COF.

Formula	$C_{78}O_{18}B_6S_6H_{48}$
Formula weight	1530.49 g/mol
Crystal system	Hexagonal
Space group	$P6$
Unit cell dimensions	$a = b = 36.56 \text{ \AA}$ $c = 3.65 \text{ \AA}$
Cell Volume	4234.14 \AA^3

Table 3.2: Fractional atomic coordinates of BDT-OEt COF.

Atom	Wyck.	x	y	z
C1	6d	0.58577	0.36594	0.44433
C2	6d	0.58777	0.32954	0.44062
C3	6d	0.49211	0.45890	0.47547
C4	6d	0.56198	0.47912	0.46663
C5	6d	0.54195	0.53395	0.48791
C6	6d	0.66044	0.40711	0.44743
C7	6d	0.62166	0.40426	0.44828
O8	6d	0.55181	0.37005	0.44579
B9	6d	0.56817	0.41435	0.45221
O10	6d	0.61299	0.43536	0.45323
C11	6d	0.54370	0.43609	0.45827
C12	6d	0.53300	0.49234	0.47430
S13	6d	0.48972	0.41092	0.45743
C14	6d	0.66425	0.37067	0.44362
C15	6d	0.62683	0.33073	0.44244
H16	6d	0.55974	0.30310	0.43696
H17	6d	0.59341	0.49907	0.46773
H18	6d	0.68480	0.43656	0.45058
O19	6d	0.58285	0.56389	0.51939
C20	6d	0.60015	0.60358	0.69692
C21	6d	0.64333	0.61313	0.83124
H22	6d	0.58033	0.60202	0.92893
H23	6d	0.60269	0.62792	0.50983
H24	6d	0.66339	0.61603	0.59942
H25	6d	0.63977	0.58737	1.00418
H26	6d	0.65821	0.64193	0.99045

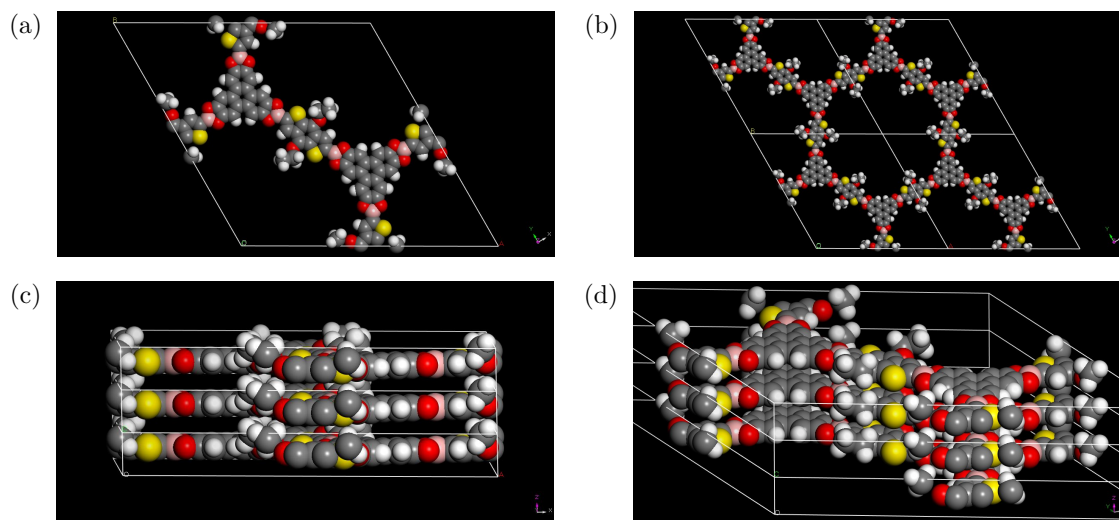


Figure 3.13: (a) and (b) Simulation of BDT-OEt COF unit cells calculated in an eclipsed arrangement in the $P6$ space group. Top: top view on ab plane, bottom: four BDT-OEt COF unit cells fused to form the hexagonal pore. (c) and (d) Simulation of BDT-OEt COF unit cell in an eclipsed arrangement in the $P6$ space group viewed along the c -axis with an interlayer distance of 3.65 Å.

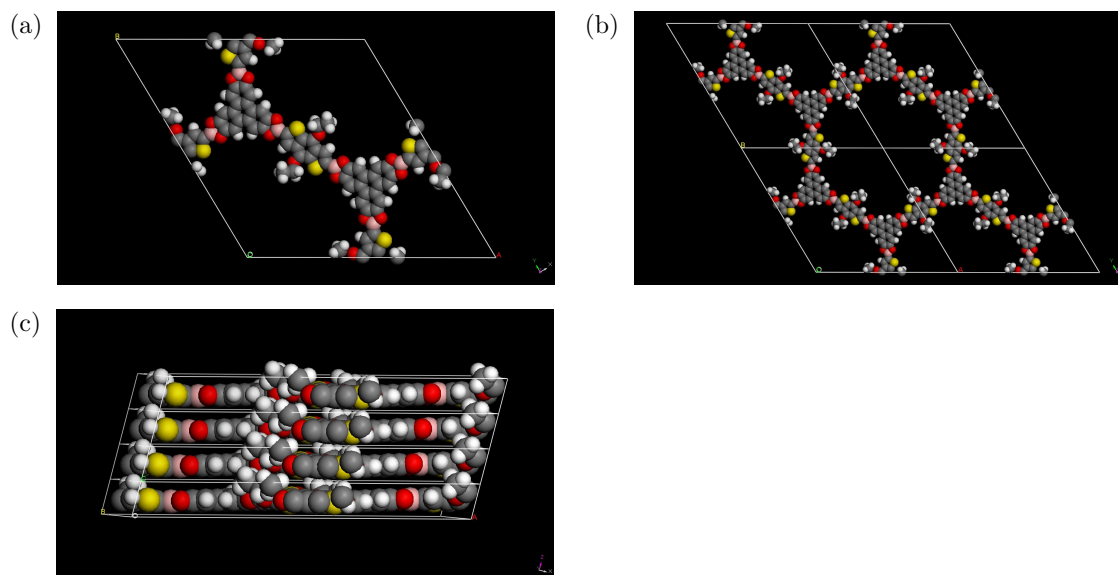


Figure 3.14: Simulation of BDT-OEt COF unit cells calculated in an eclipsed arrangement in the $P1$ space group. (a) top view on ab plane, (b) four BDT-OEt COF unit cells fused to form the hexagonal pore, (c) view along the c -axis.

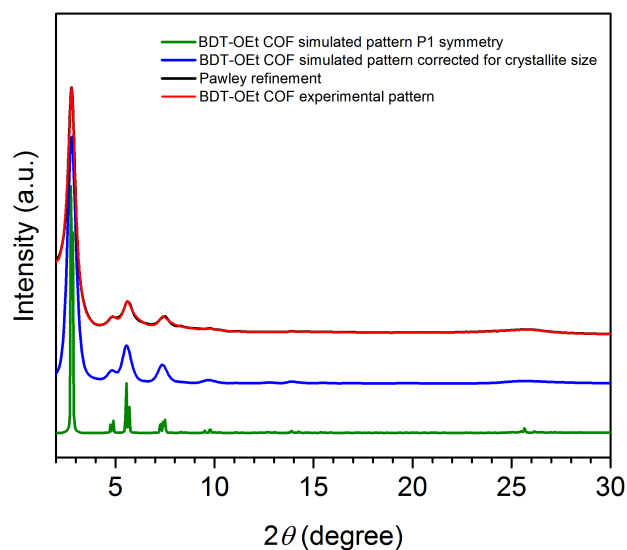


Figure 3.15: XRD patterns of BDT-OEt COF in $P1$ space group: experimental (red), Pawley refinement (black), simulated pattern corrected for crystallite size (blue), and simulated pattern (green). For Pawley refinement: The refinement parameters R_p and R_{wp} are 2.87% and 2.16%, respectively, the refined unit cell parameters are $a = 37.15 \text{ \AA} \pm 0.04$, $b = 37.17 \pm 0.04 \text{ \AA}$, $c = 3.58 \pm 0.04 \text{ \AA}$; $\alpha = 90.31^\circ$, $\beta = 77.44^\circ$, $\gamma = 120.35^\circ$.

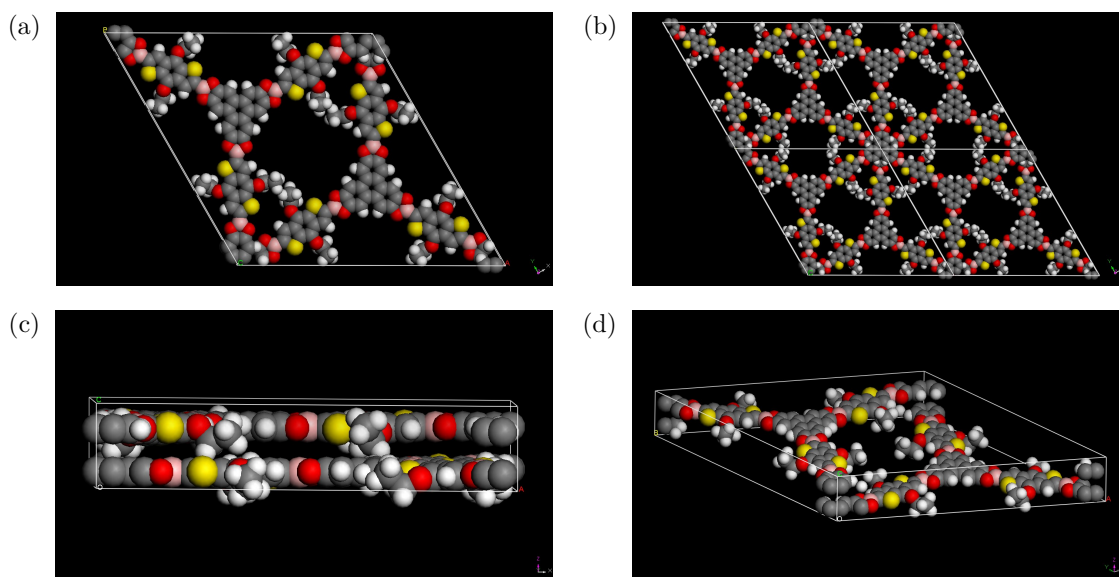


Figure 3.16: Simulation of BDT-OEt COF unit cells calculated in a staggered arrangement with $P6_3$ space group. (a) Top view on ab plane, (b) four BDT-OEt COF unit cells fused to form the pore system, (c) and (d) view along the c -axis.

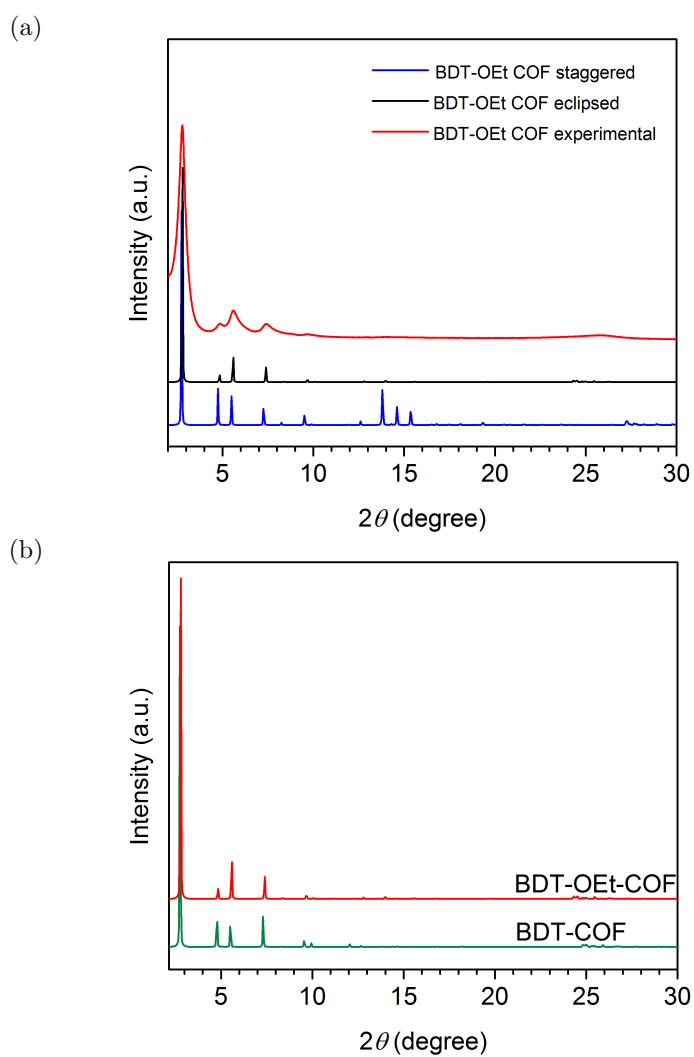
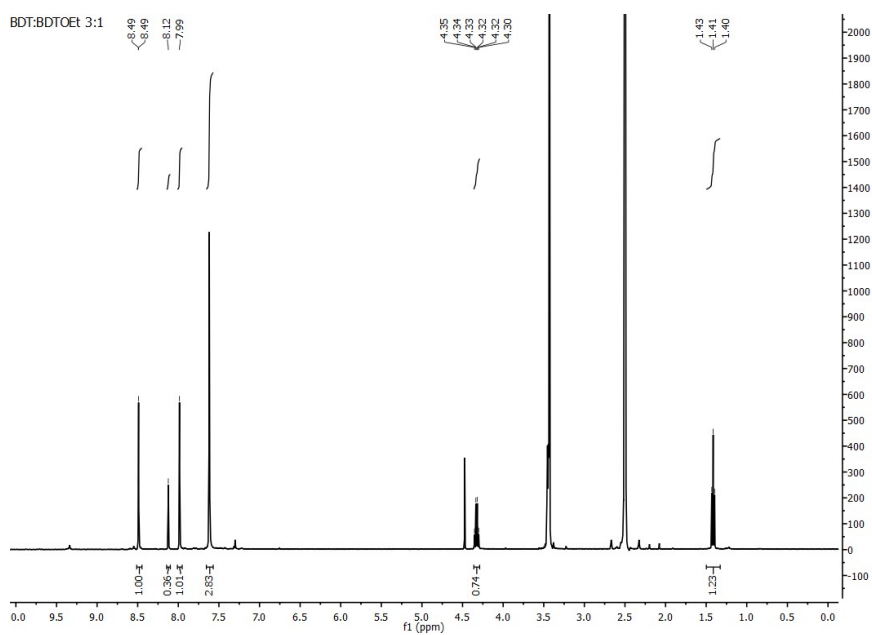
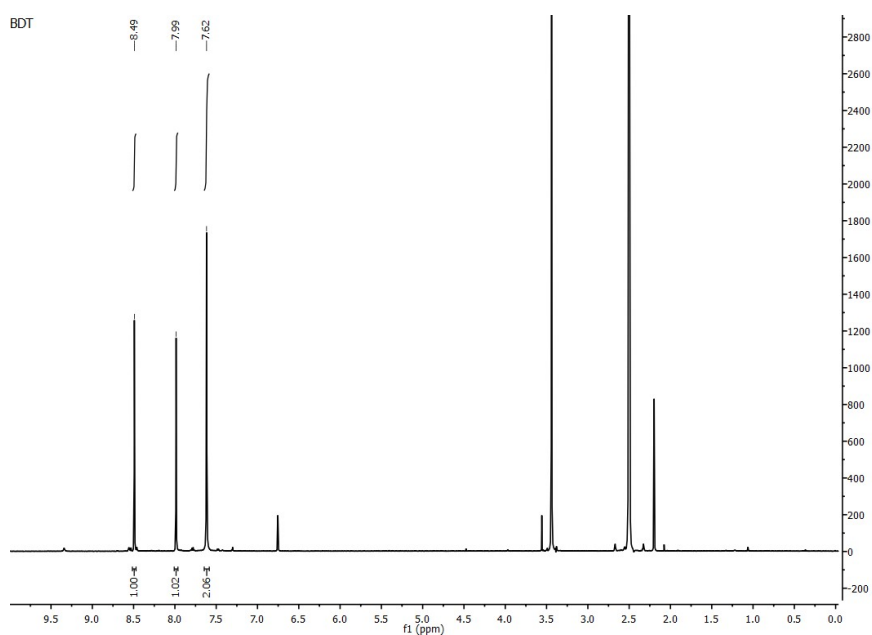
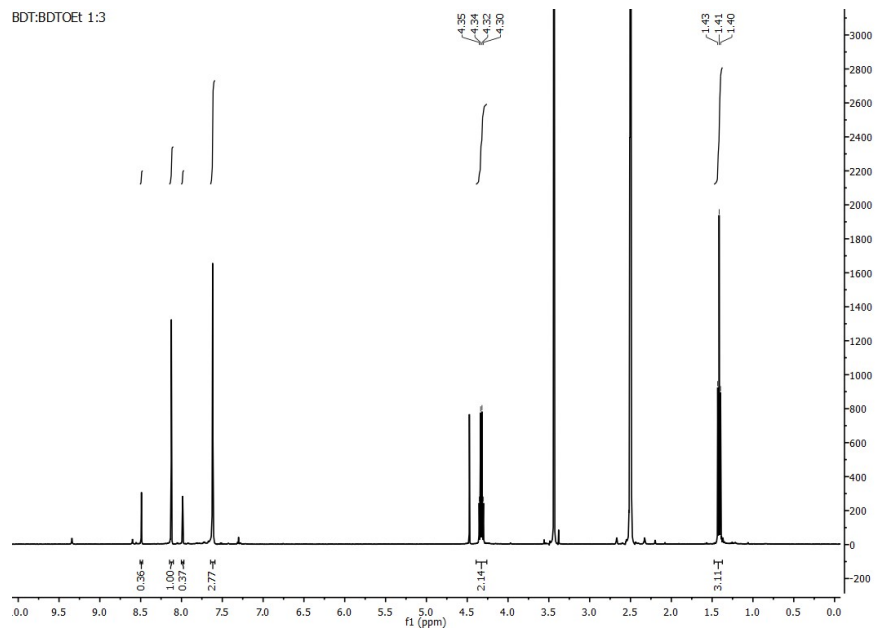
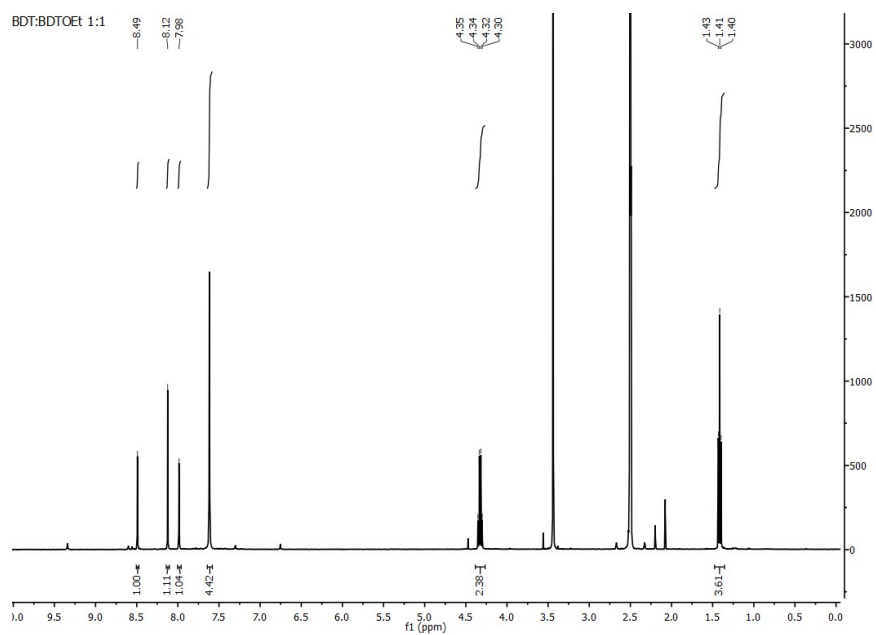
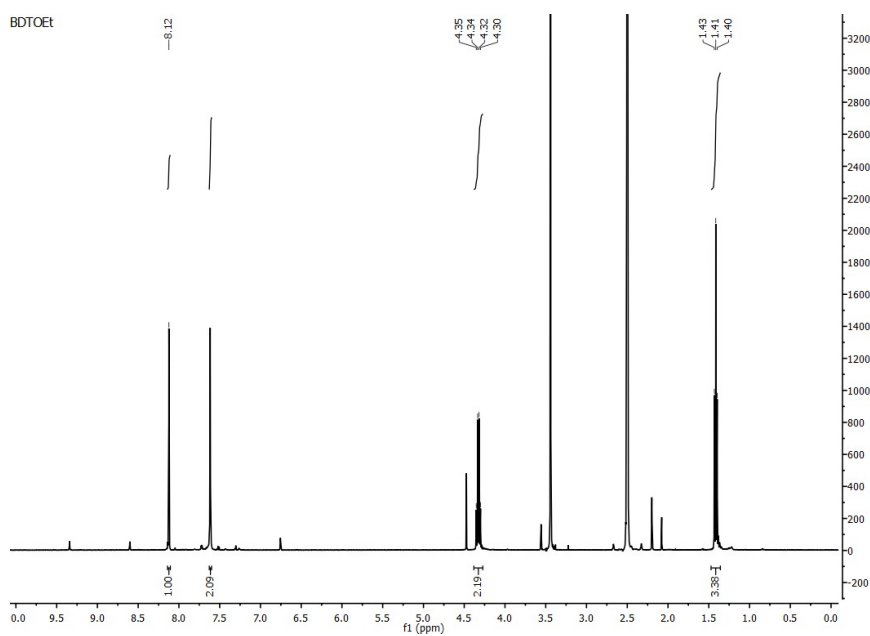


Figure 3.17: (a) XRD patterns of BDT-OEt COF: experimental (red), simulated AA eclipsed arrangement (black), and simulated AB staggered arrangement (blue). (b) Comparison of simulated XRD patterns of BDT COF (green) and BDT-OEt COF (red).

NMR spectra of hydrolysed COFs







Bibliography

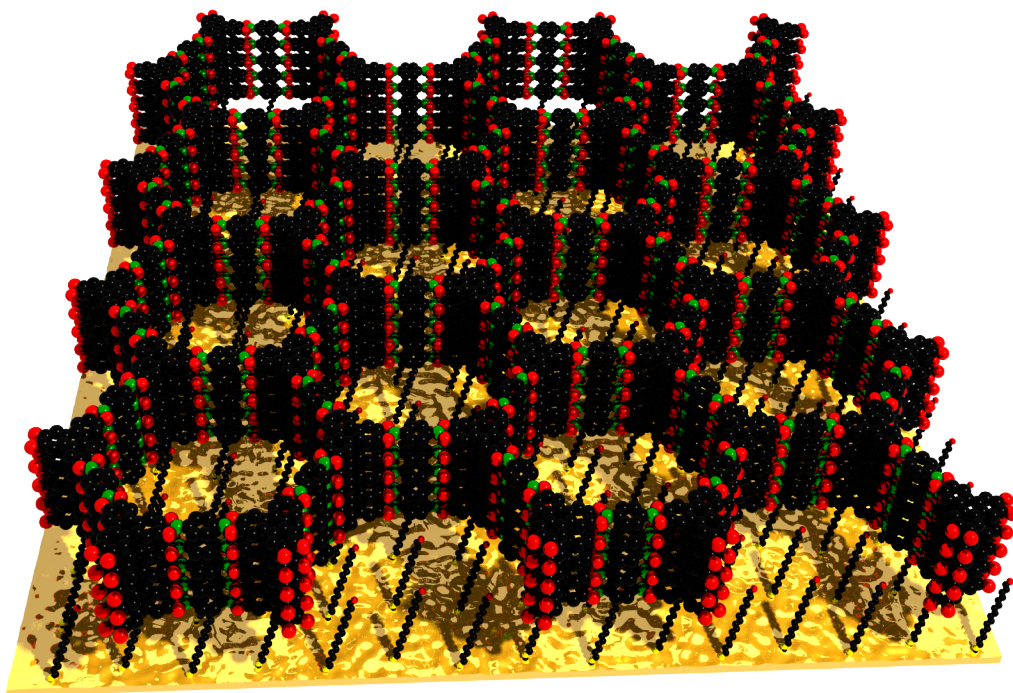
- [1] A. P. Côté, A. I. Benin, N. W. Ockwig, M. O’Keeffe, A. J. Matzger, and O. M. Yaghi. *Science*, **2005**, *310*, 1166–1170.
- [2] N. Huang, X. Chen, R. Krishna, and D. Jiang. *Angew. Chem., Int. Ed.*, **2015**, *54*, 2986–2990.
- [3] H. Xu, J. Gao, and D. Jiang. *Nat. Chem.*, **2015**, *7*, 905–912.
- [4] S. Lin, C. S. Diercks, Y.-B. Zhang, N. Kornienko, E. M. Nichols, Y. Zhao, A. R. Paris, D. Kim, P. Yang, O. M. Yaghi, and C. J. Chang. *Science*, **2015**, *349*, 1208–1213.
- [5] C. R. DeBlase, K. E. Silberstein, T.-T. Truong, H. D. Abruna, and W. R. Dichtel. *J. Am. Chem. Soc.*, **2013**, *135*, 16821–16824.
- [6] M. S. Lohse, T. Stassin, G. Naudin, S. Wuttke, R. Ameloot, D. De Vos, D. D. Medina, and T. Bein. *Chem. Mater.*, **2016**, *28*, 626–631.
- [7] M. Dogru, M. Handloser, F. Auras, T. Kunz, D. Medina, A. Hartschuh, P. Knochel, and T. Bein. *Angew. Chem., Int. Ed.*, **2013**, *52*, 2920–2924.
- [8] J. W. Colson and W. R. Dichtel. *Nat. Chem.*, **2013**, *5*, 453–65.
- [9] B. J. Smith and W. R. Dichtel. *J. Am. Chem. Soc.*, **2014**, *136*, 8783–8789.
- [10] L. Chen, K. Furukawa, J. Gao, A. Nagai, T. Nakamura, Y. Dong, and D. Jiang. *J. Am. Chem. Soc.*, **2014**, *136*, 9806–9809.
- [11] S. Jin, X. Ding, X. Feng, M. Supur, K. Furukawa, S. Takahashi, M. Addicoat, M. E. El-Khouly, T. Nakamura, S. Irle, S. Fukuzumi, A. Nagai, and D. Jiang. *Angew. Chem., Int. Ed.*, **2013**, *52*, 2017–2021.
- [12] S. Jin, K. Furukawa, M. Addicoat, L. Chen, S. Takahashi, S. Irle, T. Nakamura, and D. Jiang. *Chem. Sci.*, **2013**, *4*, 4505–4511.
- [13] J. Guo, Y. Xu, S. Jin, L. Chen, T. Kaji, Y. Honsho, M. A. Addicoat, J. Kim, A. Saeki, H. Ihee, S. Seki, S. Irle, M. Hiramoto, J. Gao, and D. Jiang. *Nat. Commun.*, **2013**, *4*, 3736/1–3736/8.

- [14] E. L. Spitler, J. W. Colson, F. J. Uribe-Romo, A. R. Woll, M. R. Giovino, A. Saldivar, and W. R. Dichtel. *Angew. Chem., Int. Ed.*, **2012**, *51*, 2623–2627.
- [15] H. Yang, Y. Du, S. Wan, G. D. Trahan, Y. Jin, and W. Zhang. *Chem. Sci.*, **2015**, *6*, 4049–4053.
- [16] M. Calik, F. Auras, L. M. Salonen, K. Bader, I. Grill, M. Handloser, D. D. Medina, M. Dogru, F. Löbermann, D. Trauner, A. Hartschuh, and T. Bein. *J. Am. Chem. Soc.*, **2014**, *136*, 17802–17807.
- [17] S. Jin, M. Supur, M. Addicoat, K. Furukawa, L. Chen, T. Nakamura, S. Fukuzumi, S. Irle, and D. Jiang. *J. Am. Chem. Soc.*, **2015**, *137*, 7817–7827.
- [18] R. W. Tilford, I. Mugavero Sam J., P. J. Pellechia, and J. J. Lavigne. *Adv. Mater.*, **2008**, *20*, 2741–2746.
- [19] L. M. Lanni, R. W. Tilford, M. Bharathy, and J. J. Lavigne. *J. Am. Chem. Soc.*, **2011**, *133*, 13975–13983.
- [20] A. Nagai, Z. Guo, X. Feng, S. Jin, X. Chen, X. Ding, and D. Jiang. *Nat. Commun.*, **2011**, *2*, 1542/1–1542/8.
- [21] B. J. Smith, N. Hwang, A. D. Chavez, J. L. Novotney, and W. R. Dichtel. *Chem. Commun.*, **2015**, *51*, 7532–7535.
- [22] D. D. Medina, V. Werner, F. Auras, R. Tautz, M. Dogru, J. Schuster, S. Linke, M. Döblinger, J. Feldmann, P. Knochel, and T. Bein. *ACS Nano*, **2014**, *8*, 4042–4052.
- [23] D. D. Medina, J. M. Rotter, Y. Hu, M. Dogru, V. Werner, F. Auras, J. T. Markiewicz, P. Knochel, and T. Bein. *J. Am. Chem. Soc.*, **2015**, *137*, 1016–1019.
- [24] G. H. V. Bertrand, V. K. Michaelis, T.-C. Ong, R. G. Griffin, and M. Dincă. *Proc. Natl. Acad. Sci. U. S. A.*, **2013**, *110*, 4923–4928.
- [25] S. Duhović and M. Dincă. *Chem. Mater.*, **2015**, *27*, 5487–5490.
- [26] E. L. Spitler, B. T. Koo, J. L. Novotney, J. W. Colson, F. J. Uribe-Romo, G. D. Gutierrez, P. Clancy, and W. R. Dichtel. *J. Am. Chem. Soc.*, **2011**, *133*, 19416–19421.
- [27] H. Xu, X. Chen, J. Gao, J. Lin, M. Addicoat, S. Irle, and D. Jiang. *Chem. Commun.*, **2014**, *50*, 1292–1294.
- [28] D. W. Slocum and P. L. Gierer. *J. Org. Chem.*, **1976**, *41*, 3668–3673.

-
- [29] S. L. Mayo, B. D. Olafson, and W. A. Goddard. *J. Phys. Chem.*, **1990**, *94*, 8897–8909.
- [30] O. Alexiadis and V. G. Mavrantzas. *Macromolecules*, **2013**, *46*, 2450–2467.
- [31] A. K. Rappe and W. A. Goddard. *J. Phys. Chem.*, **1991**, *95*, 3358–3363.
- [32] S. J. Clark, M. D. Segall, C. J. Pickard, P. J. Hasnip, M. I. J. Probert, K. Refson, and M. C. Payne. *Z. Kristallogr.*, **2005**, *220*, 567.
- [33] J. P. Perdew, K. Burke, and M. Ernzerhof. *Phys. Rev. Lett.*, **1996**, *77*, 3865–3868.
- [34] S. Grimme. *J. Comp. Chem.*, **2006**, *27*, 1787–1799.
- [35] E. R. McNellis, J. Meyer, and K. Reuter. *Phys. Rev. B*, **2009**, *80*, 205414.
- [36] D. Vanderbilt. *Phys. Rev. B*, **1990**, *41*, 7892–7895.
- [37] H. J. Monkhorst and J. D. Pack. *Phys. Rev. B*, **1976**, *13*, 5188–5192.

Chapter 4

Highly Oriented COF Thin Films Grown on SAM-modified Substrates



Abstract

The control over the oriented growth of covalent organic frameworks (COFs) as thin films can be essential for the potential application of these systems in areas such as optoelectronics or chemical sensing. Herein, we examine the impact of the chemical modification of the substrate on the growth of COF-5 thin films. For that purpose, we modify gold substrates with self-assembled monolayers (SAMs) with the terminal functional groups -OH, -CH₃, and -COOH and subsequently grow COF-5 in a solvothermal synthesis route as thin film on these substrates and on bare gold. Crystalline thin films with a preferential orientation of the domains in which the COF pores are aligned perpendicularly to the substrate surface is achieved for all substrates. We demonstrate that a particularly high degree of orientation can be achieved on substrates modified with OH-SAM or COOH-SAM, indicating a growth-directing effect of these functional groups.

4.1 Introduction

By co-condensing rigid organic linkers in reversible condensation reactions, covalent organic frameworks (COFs) can be formed featuring a defined arrangement of the organic building blocks and permanent porosity.¹⁻⁶ When flat molecular linkers are applied in the COF synthesis, the COF crystallizes in 2D sheets that can form stacks due to π - π interactions between the layers.

The growth of COFs as thin films plays a major role on the way to the successful application of these materials, e.g as potential components of solar cells. The formation of such films with a preferred orientation of the COF domains in contrast to a random alignment has shown to improve their performance in a range of applications, for example as capacitive electrode,⁷ field-effect transistor,⁸ and photoelectric device.⁹

The growth of oriented and thin COF films has been accomplished on a range of substrates like graphene,¹⁰ or on oxide substrates (indium doped tin oxide, nickel oxide, and molybdenum oxide).^{11,12} Early on, the solvent composition was found to play an important role in achieving oriented thin films instead of a random alignment of the COF crystallites, as shown by Dichtel and coworkers with a series of Zn-phthalocyanine COFs.¹³ A continuous flow COF thin film synthesis was found to allow for control over the film thickness.¹⁴

The boronic ester-linked phthalocyanine ZnPc-PBBA COF was shown to selectively grow on single-layered graphene and not on bare fused SiO₂ when a methanol and 1,4-dioxane solvent mixture was used.¹⁵ In all these films the crystallites were oriented with

the *c*-direction being aligned perpendicularly to the substrate plane but recently, thin films of COF-5 were grown from a colloidal solution of COF-5. In these films, the *c*-direction of the COF crystallites has a preferential orientation parallel to the substrate surface plane.¹⁶ Despite these investigations, there is still a range of questions open regarding the key factors of the growth of COFs as thin oriented films, among them the characteristics of the substrate.

In this work we investigate the impact of the functional modification of the substrate on the oriented growth of COF thin films. For that purpose we use self-assembled monolayers (SAMs). These are formed from molecules that consist of a long alkyl chain and a functional group at one end, while the other end bears a thiol group that is able to bind to a gold surface.

As these molecules arrange on the substrate in the form of dense self-assembled monolayers with the functional groups pointing towards the layer surface, a dense and defined coverage of the substrate with different functionalities can be achieved.¹⁷ By growing COF-5 in a solvothermal synthesis route as thin film on these substrates, we study the influence of substrate functionalization on the orientation of the domains in COF thin films.

4.2 Results and Discussion

Gold coated glass substrates were modified with SAMs to alter the surface functionalization. For this purpose we placed clean gold substrates (for cleaning procedure see Section 4.4.3) for 3 days in 1 mM mesitylene : 1,4-dioxane 1 : 1 (v/v) solutions of the thiols 16-mercaptohexadecan-1-ol and 1-hexadecanethiol, to grow self-assembled monolayers on the gold substrate hereafter denoted as OH-SAM and CH₃-SAM, respectively. The formation of the SAMs on gold substrates was examined by water contact angle measurements, see Figure 4.1. The unmodified gold substrate exhibited a contact angle of 94°. Upon modification with 16-mercaptohexadecan-1-ol the contact angle was reduced to 62°, while the substrate with CH₃-SAM had a contact angle of 90°.

Films of COF-5 were grown on these substrates by solvothermal co-condensation of 2,3,6,7,10,11-hexahydroxytriphenylene (HHTP) and 1,4-benzenediboronic acid (BDDBA) in a mesitylene : dioxane 1 : 1 (v/v) mixture at 100 °C for 24 h. In order to reduce the precipitation of COF-5 particles formed in solution onto the films, the substrates were placed face-down in the reaction mixture. X-ray diffraction (XRD) detector scan measurements were conducted to investigate the crystallinity of the COF films. In the XRD pattern of COF-5 grown on OH-SAM (Figure 4.2a), a distinct signal is visible at

26°, which can be attributed to the (001) plane of the COF and represents the stacking distance of the COF layers, while all other reflections of COF-5 are absent. This is a first indication for a preferential orientation of the COF sheets parallel to the substrate surface.

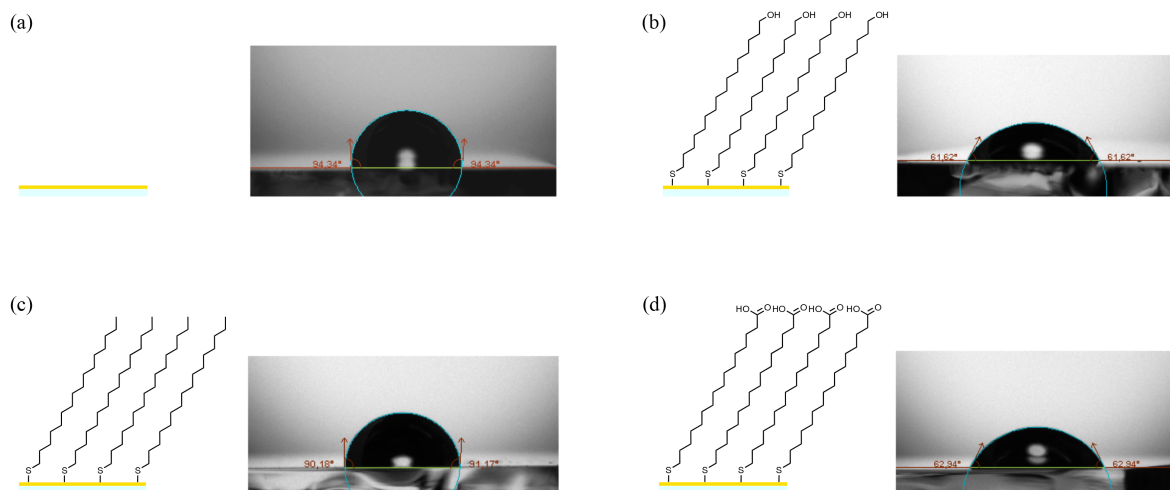


Figure 4.1: Contact angle measurements of functionalized gold substrates: (a) bare gold, (b) OH-SAM, (c) CH₃-SAM, (d) COOH-SAM.

To further confirm the preferential orientation of the COF crystallites, grazing incidence diffraction (GID) analysis was performed. Figure 4.3b shows the 2D-GID data for the film grown on OH-SAM. In the image, a signal at $q(y) = 17.5 \text{ nm}^{-1}$ is visible that corresponds to the (001) reflection of the COF. When this signal is located at a spot at $q(z) = 0$, it establishes a low angular spread and an alignment of the crystallites with the c -direction of the COF crystallites perpendicular to the substrate plane while a full arc would correspond to a random orientation. Furthermore, signals aligned at $q(y) = 0$ are visible at 2.33, 4.07, 4.75, and 6.26 nm^{-1} that correspond to the (100), (110), (200), (210), (220) planes of the COF lattice and are in good agreement with previously reported values for COF-5.¹⁰

These observations reveal a highly oriented alignment of the COF crystallites on OH-SAM. Scanning electron microscopy (SEM) micrographs show the formation of a film that fully covers the substrate, while large particles are also visible that sit on the dense film (Figure 4.4d). The film has a thickness of approx. 90 nm (Figure 4.4c).

On a substrate without SAM and on CH₃-SAM, the (011) reflection at 26° is also present in the XRD detector scan measurement (see Figure 4.2a), but in GID measurements, the higher angular spread of the (001) reflection is visible, evincing a less oriented growth of COF-5 on these substrates (Figures 4.3a and 4.3c). Particularly on CH₃-SAM,

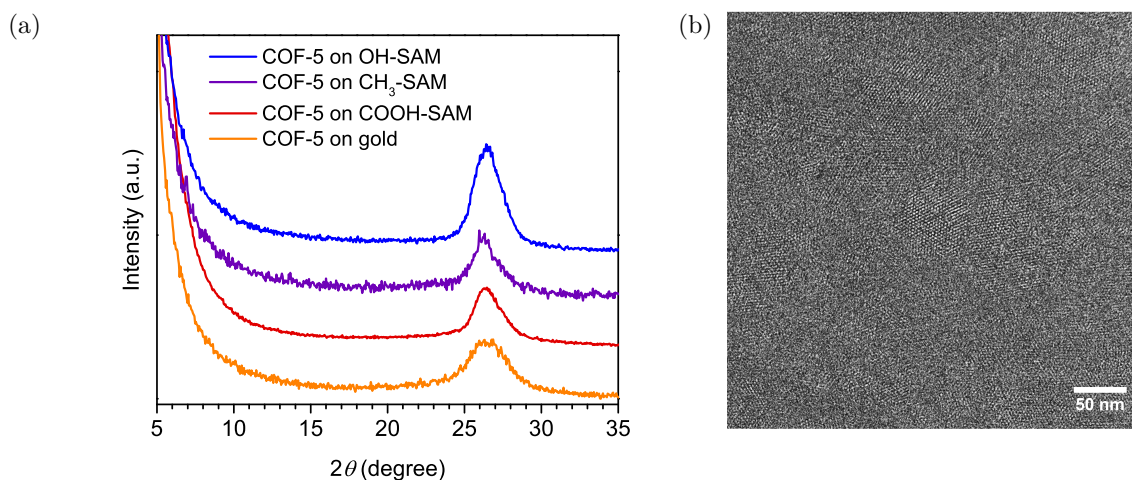


Figure 4.2: (a) Detector scan XRD measurements of COF-5 grown on bare gold and gold substrates functionalized with OH-SAM, CH₃-SAM, and COOH-SAM. (b) TEM image of a COF-5 thin film grown on OH-SAM.

the signals in GID are also weak and the reflections at the (210) plane at 4.75 nm^{-1} and at the (200) plane at 6.26 nm^{-1} are not visible (Figure 4.3c). This may also result from the reduced COF film thickness of 40 nm that we observed in SEM investigations on CH₃-SAM (Figure 4.4e).

On bare gold, the COF film thickness was 120 nm (Figure 4.4a), comparable to the film on OH-SAM. For both films, SEM top view images revealed the presence of agglomerates on the films, furthermore the film on bare gold exhibited cracks (Figures 4.4b and 4.4f).

The COF film grown on OH-SAM was investigated by transmission electron microscopy (TEM). For this measurement the COF film was removed from the substrate with a fine blade and transferred to a copper grid. The hexagonal structure of the COF pores is visible (Figure 4.2b) corresponding to an alignment of the COF crystallites *c*-axis perpendicular to the substrate surface plane. We attribute the absence of this pattern in some areas to the high thickness of the film with multiple COF crystallites lying on top of each other and having slightly varying orientations.

The highly oriented growth of the COF on OH-SAM in a way that the COF sheets are aligned parallel to the substrate surface plane may appear somewhat counter-intuitive, as the OH groups are pointing towards the substrate surface normal and thus could provide anchoring points for an upright growth of the COF sheets. In contrast, in this work we found a beneficial influence of the OH groups towards a highly ordered flat arrangement of the COF sheets. This might be induced by a reversible binding and cleavage of the boronic acid linker to the SAM molecules thereby slowing down the COF formation and

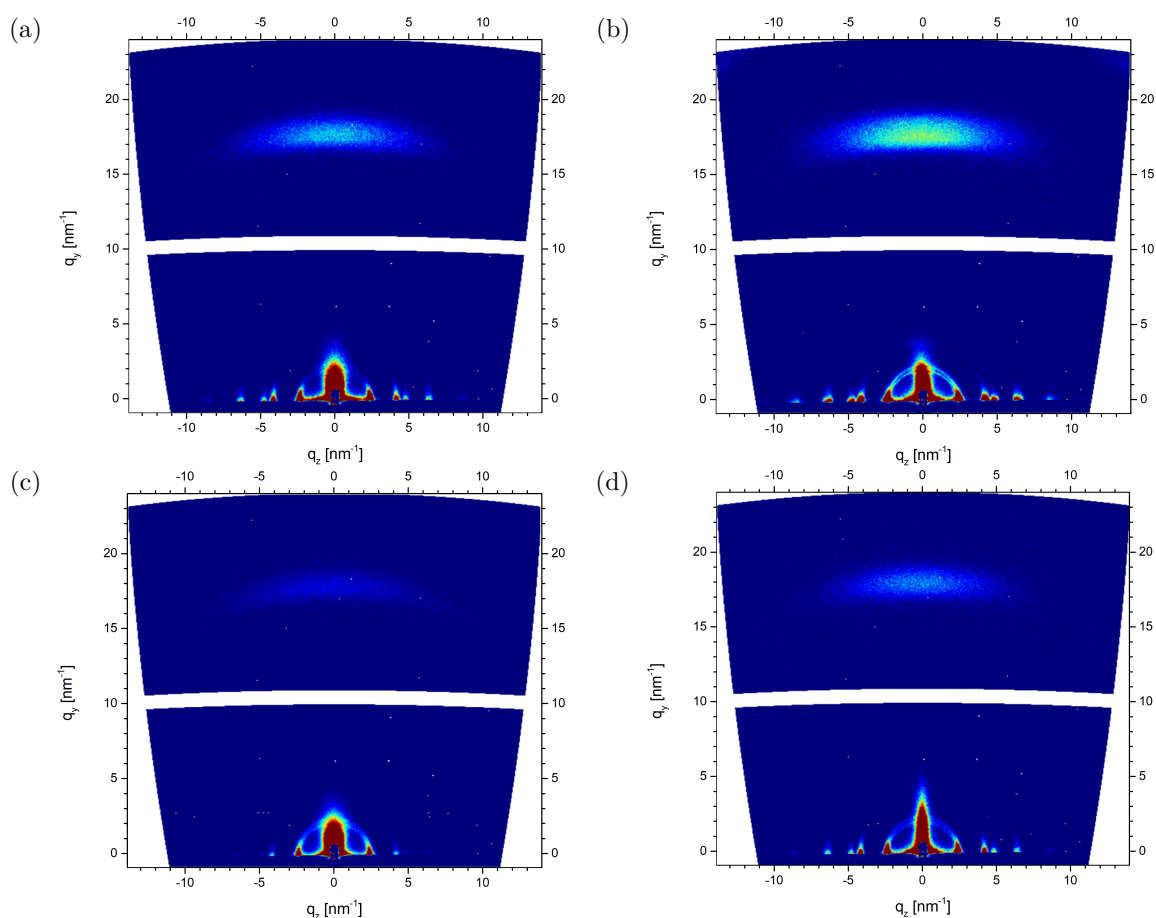


Figure 4.3: 2D-GID analysis for COF-5 grown on: (a) gold substrate without SAM, (b) OH-SAM, (c) CH₃-SAM, (d) COOH-SAM. All images are normalized to have the same colour range between minimal and maximal intensity.

enabling an improved alignment of the crystallites. Recently, Wang et al. investigated the growth of imine-linked COFs as thin films and found a high degree of orientation for films grown on an NH₂-terminated SAM,¹⁸ an observation that is in line with our results.

In order to further explore the impact of SAM structure on COF orientation, an additional modification with 16-mercaptohexadecanoic acid, forming a carboxylic acid-functionalized SAM (hereafter denoted as COOH-SAM), was investigated for COF growth. Combining boronic acids and carboxylic acids can lead to the formation of mixed anhydrides of the form RC(O)OB(OH)₂R.¹⁹ A surface functionalization with a carboxylic acid may thus also act in an orientation-directing way.

COF-5 was grown on COOH-SAM in the same solvothermal synthesis route as the other films. Gold films with COOH-SAM exhibited a contact angle of 63° (Figure 4.1d), evincing the successful SAM formation. In the XRD detector scan pattern of the COF-5

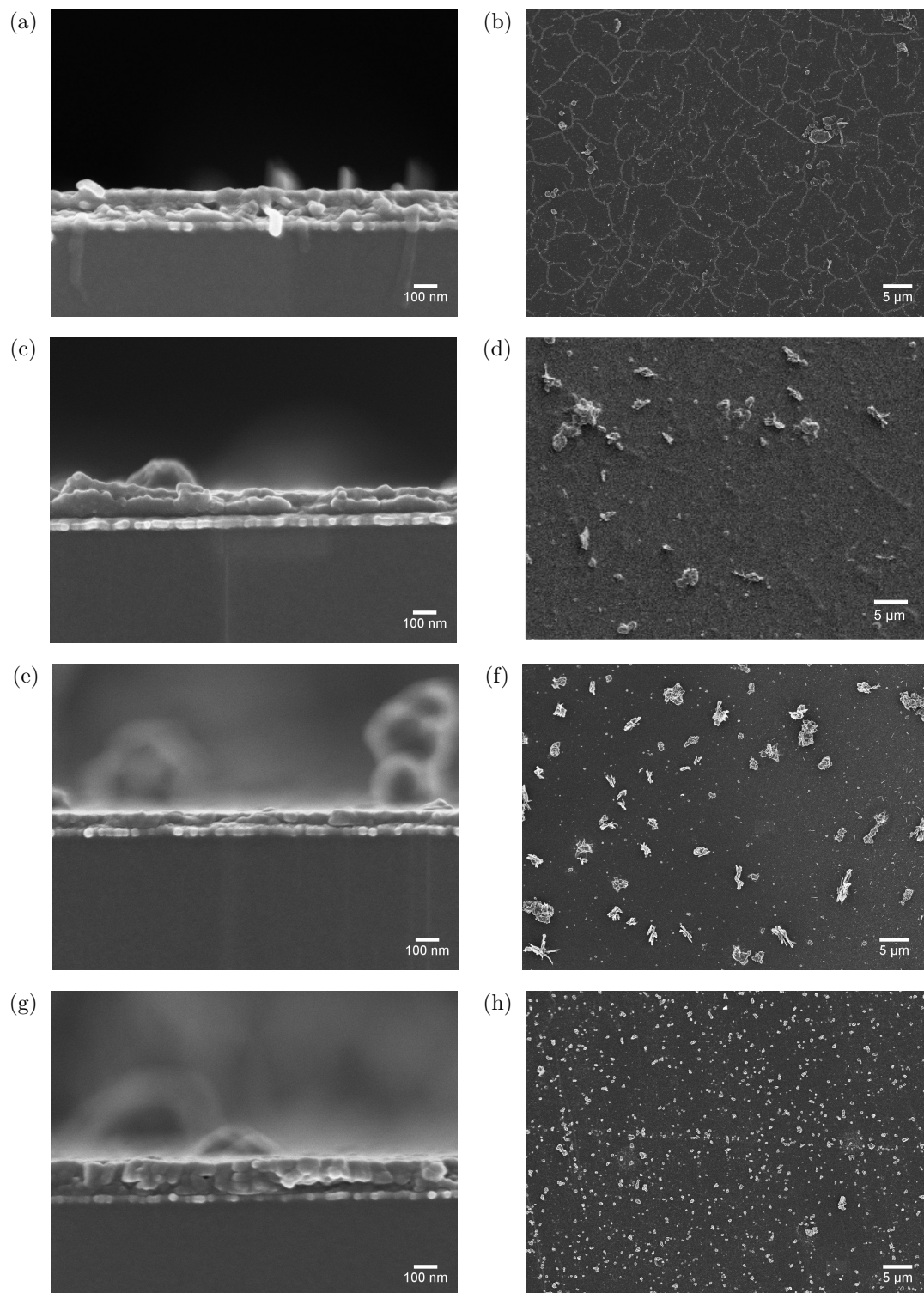


Figure 4.4: Scanning electron microscopy images in cross section (left) and top view (right) of COF-5 grown on (a) and (b): bare gold, (c) and (d): OH-SAM, (e) and (f) CH₃-SAM, (g) and (h): COOH-SAM.

grown on COOH-SAM, the signal at 26° is the only visible peak, indicating a preferential flat alignment of the COF layers (Figure 4.2a).

The COF-5 film on COOH-SAM has a thickness of 130 nm, and shows agglomerates on the flat film that are smaller than on the other films, as determined from SEM micrographs (Figures 4.4g and 4.4h). A GID measurement of the COF-5 film on COOH-SAM exhibits a narrow angular spread of the signal at $q(y) = 17.5 \text{ nm}^{-1}$ that is comparable to the measurement of the film on OH-SAM. We therefore conclude that COOH-SAM also exerts a beneficial effect towards the oriented growth of the COF, similar to OH-SAM-modified substrates.

4.3 Conclusion

Herein we investigated the influence of the functionalization of self-assembled monolayers on gold on the growth of COF-5 as thin films on these substrates. For that purpose, we first modified gold substrates with self-assembling monolayers exhibiting different terminal functionalization. Subsequently, we grew COF-5 in a solvothermal route as thin film on the functionalized substrates and on bare gold. It was found that all investigated substrates, made of bare gold or featuring surface modification with SAM presenting -OH, -CH₃, or -COOH head groups, allowed for the growth of crystalline COF-5 films.

The crystallites featured preferential orientation with their *c*-direction being aligned perpendicular to the substrate surface plane. This alignment was present on all substrates but it was more pronounced on OH- and COOH-functionalized substrates than on CH₃-SAM or bare gold, indicating a growth-directing impact of the surface functionalization with carboxylic acid or hydroxyl groups on the crystallite growth.

4.4 Experimental

All materials (if not otherwise noted) were purchased from Aldrich, Fluka, or Acros in the common purities purum and puriss and used as received without further purification. 2,3,6,7,10,11-Hexahydroxytriphenylene (HHTP) was purchased from TCI Europe. 1,4-Dioxane was purchased from Acros in 99.5% purity.

4.4.1 Methods and Characterization

Oxygen plasma cleaning was performed applying a Diener Electronic from Plasma-Surface-Technology. The deposition of Ti and Au onto glass slides was conducted using a MBraun

Labmaster Pro SP equipped with an Inficon SQC-310C deposition controller. The instrument was placed in a nitrogen-filled glove box.

Contact angle measurements were performed on an attension instrument from Biolin Scientific. A droplet of water was placed on the substrate while recording images. Analysis of the images was performed with the software one attension applying a Young-Laplace analysis mode and an air-to-water interface.

Detector scan X-ray diffraction (XRD) measurements were carried out in reflection mode on a Bruker D8 Discover diffractometer with Ni-filtered $K\alpha$ radiation ($\lambda = 1.54060 \text{ \AA}$) and a position-sensitive detector (LynxEye) with the X-ray tube placed at a constant angle of $0.5^\circ 2\theta$. Two-dimensional grazing-incident wide-angle X-ray diffraction measurements were conducted with an Anton-Paar SAXSpace system equipped with a Cu $K\alpha$ microfocus source at 50 kV and 1 mA with an Eiger Dectris R 1M 2D detector.

Scanning electron microscopy (SEM) was performed on a JEOL 6500F instrument at acceleration voltages of 2-5 kV. The samples were coated with a thin carbon layer by carbon fiber flash evaporation at high vacuum. Transmission electron microscopy (TEM) data were obtained with an FEI Titan Themis at an acceleration voltage of 300 kV.

4.4.2 Preparation of Gold Substrates

The gold substrates were prepared following a procedure that was developed earlier in our group.²⁰ The microscope glass slides (Menzel, 76 mm \times 26 mm) were placed in a custom-made Teflon holder and cleaned successively by ultrasonic treatment in acetone, 2-propanol, a 1 : 100 Hellmanex to water mixture, water and 2-propanol (Chromasolv), followed by oxygen plasma cleaning for 30 min.

Subsequently, 10 nm of titanium and 100 or 40 nm of gold were thermally deposited under high vacuum onto the microscope glass slides. Afterwards the microscope slides were cut into 1.2 cm \times 1 cm pieces.

4.4.3 Growth of Self-Assembled Monolayers on Gold Substrates

The gold substrates were cleaned by ultrasonic treatment in absolute ethanol and methanol for 10 min each and subsequently dried in a stream of pressurized air. Afterward the slides were placed in 20 mL of a 1 mM solution of the respective SAM (16-mercaptohexadecan-1-ol, 1-hexadecanethiol, or 16-mercaptohexadecanoic acid) in mesitylene : dioxane 1 : 1 (v/v) and left undisturbed for 3 days. Then the slides were transferred to a fresh vial with 20 mL mesitylene : dioxane 1 : 1 (v/v) and stored until use.

4.4.4 Solvothermal COF-5 Film Growth

In a typical reaction, a 40 mL glass vial with rolled rim was placed in a 100 ml Schott Duran glass bottle and charged with 5 mL mesitylene : dioxane 1 : 1 (v/v). Benzene-1,4-diboronic acid, BDBA (46 mg, 0.28 mmol) and 2,3,6,7,10,11-hexahydroxytriphenylene, HHTP (55 mg, 0.17 mmol) were added successively with minimum turbulence of the liquid. The mixture was left to stand for 10 minutes to allow for a complete precipitation of the solid material. Two clean gold-coated glass substrates were placed with the gold side showing down in a custom-made, Π -shaped Teflon holder equipped with three slide compartments. The Teflon holder was slowly transferred to the glass vial. Subsequently, 1 mL mesitylene was added and the reaction mixture was heated for 24 h at 70 °C. Afterwards, the substrates were removed from solution and dried under a stream of N₂.

Bibliography

- [1] A. P. Côté, A. I. Benin, N. W. Ockwig, M. O’Keeffe, A. J. Matzger, and O. M. Yaghi. *Science*, **2005**, *310*, 1166–1170.
- [2] S.-Y. Ding and W. Wang. *Chem. Soc. Rev.*, **2013**, *42*, 548–568.
- [3] X. Feng, X. Ding, and D. Jiang. *Chem. Soc. Rev.*, **2012**, *41*, 6010–6022.
- [4] J. W. Colson and W. R. Dichtel. *Nat. Chem.*, **2013**, *5*, 453–65.
- [5] N. Huang, P. Wang, and D. Jiang. *Nat. Rev. Mater.*, **2016**, *1*, 16068.
- [6] P. J. Waller, F. Gándara, and O. M. Yaghi. *Acc. Chem. Res.*, **2015**, *48*, 3053–3063.
- [7] C. R. DeBlase, K. Hernandez-Burgos, K. E. Silberstein, G. G. Rodriguez-Calero, R. P. Bisbey, H. D. Abruna, and W. R. Dichtel. *ACS Nano*, **2015**, *9*, 3178–3183.
- [8] B. Sun, C.-H. Zhu, Y. Liu, C. Wang, L.-J. Wan, and D. Wang. *Chem. Mater.*, **2017**, *29*, 4367–4374.
- [9] Y. Chen, H. Cui, J. Zhang, K. Zhao, D. Ding, J. Guo, L. Li, Z. Tian, and Z. Tang. *RSC Adv.*, **2015**, *5*, 92573–92576.
- [10] J. W. Colson, A. R. Woll, A. Mukherjee, M. P. Levendorf, E. L. Spitler, V. B. Shields, M. G. Spencer, J. Park, and W. R. Dichtel. *Science*, **2011**, *332*, 228–31.
- [11] D. D. Medina, V. Werner, F. Auras, R. Tautz, M. Dogru, J. Schuster, S. Linke, M. Döblinger, J. Feldmann, P. Knochel, and T. Bein. *ACS Nano*, **2014**, *8*, 4042–4052.
- [12] M. Calik, F. Auras, L. M. Salonen, K. Bader, I. Grill, M. Handloser, D. D. Medina, M. Dogru, F. Löbermann, D. Trauner, A. Hartschuh, and T. Bein. *J. Am. Chem. Soc.*, **2014**, *136*, 17802–17807.
- [13] E. L. Spitler, J. W. Colson, F. J. Uribe-Romo, A. R. Woll, M. R. Giovino, A. Saldivar, and W. R. Dichtel. *Angew. Chem., Int. Ed.*, **2012**, *51*, 2623–2627.
- [14] R. P. Bisbey, C. R. DeBlase, B. J. Smith, and W. R. Dichtel. *J. Am. Chem. Soc.*, **2016**, *138*, 11433–11436.
- [15] J. W. Colson, J. A. Mann, C. R. De Blase, and W. R. Dichtel. *J. Polym. Sci., Part A: Polym. Chem.*, **2015**, *53*, 378–384.

-
- [16] B. J. Smith, L. R. Parent, A. C. Overholts, P. A. Beaucage, R. P. Bisbey, A. D. Chavez, N. Hwang, C. Park, A. M. Evans, N. C. Gianneschi, and W. R. Dichtel. *ACS Cent. Sci.*, **2017**, *3*, 58–65.
- [17] J. C. Love, L. A. Estroff, J. K. Kriebel, R. G. Nuzzo, and G. M. Whitesides. *Chem. Rev.*, **Apr. 2005**, *105*, 1103–1170.
- [18] H. Wang, B. He, F. Liu, C. Stevens, M. A. Brady, S. Cai, C. Wang, T. P. Russell, T.-W. Tan, and Y. Liu. *J. Mater. Chem. C*, **2017**, *5*, 5090–5095.
- [19] K. Ishihara and Y. Lu. *Chem. Sci.*, **2016**, *7*, 1276–1280.
- [20] F. M. Hinterholzinger, S. Wuttke, P. Roy, T. Preuße, A. Schaate, P. Behrens, A. Godt, and T. Bein. *Dalton Trans.*, **2012**, *41*, 3899–3901.

Chapter 5

Sequential Pore Wall Modification in a Covalent Organic Framework for Application in Lactic Acid Adsorption

This chapter is based on the following publication:

Maria S. Lohse, Timothée Stassin, Guillaume Naudin, Stefan Wuttke, Rob Ameloot, Dirk De Vos, Dana D. Medina, Thomas Bein, *Chemistry of Materials* **2016**, *28*, 626–631.



Image prepared by Christoph Hohmann, Nanosystems Initiative Munich (NIM).

Abstract

Here we describe the synthesis and postsynthetic modification of the stable β -ketoenamine TpBD(NH₂)₂ covalent organic framework (COF), having primary amine groups integrated into the pore walls. For this purpose we initially synthesized the nitro version of this COF, TpBD(NO₂)₂. Afterward, TpBD(NO₂)₂ was reduced to afford the desired framework having primary amine functionality. We demonstrate the accessibility of the primary amine groups and the robustness of the framework by a second modification step, the aminolysis of acetic anhydride, to obtain the corresponding amide form TpBD(NHCOCH₃)₂. Taking advantage of the high stability of these frameworks under acidic conditions, we study the liquid-phase adsorption of lactic acid, revealing the strong impact of a pore wall modification on the adsorption performance

5.1 Introduction

Postsynthetic modification (PSM) of porous materials offers an effective route to incorporate functional groups into the pores and thus tailor the structural and chemical environment of the pores. This method is already established for inorganic porous materials such as zeolites^{1,2} and hybrid materials such as metal-organic frameworks (MOFs).^{3,4} Recently, two-dimensional covalent organic frameworks (2D COFs), an emerging class of porous materials, have attracted much attention in this respect due to their unique ordered channel structure and their relatively large accessible pore apertures.⁵⁻⁸ Typically, in a PSM scheme the framework must consist of organic building blocks with reactive functional groups that can serve as anchoring points for further covalent modifications.

The direct incorporation of such functional groups into 2D COFs can be challenging and is generally limited to those which do not inhibit the COF formation or interfere with the π - π -interactions establishing the COF stacks.⁹⁻²⁰

To date, only few PSM reactions have been investigated for COFs, for example, using click reactions on azide,²¹ allyl,²² and ethynyl.²³⁻²⁵ Hydroxyl groups were also modified with succinic anhydride.²⁶ Association of nitrogen compounds with boron atoms was demonstrated in boron-based COFs.²⁷⁻²⁹

For the development of a wider range of postsynthetic reactions, a nucleophilic functional group such as a primary amine in a chemically stable COF is highly desirable. However, it cannot be easily incorporated as a side group in COFs that are formed from

aldehydes, boronic acids, or anhydrides as it is prone to react with the building units and therefore is likely to inhibit the COF formation.

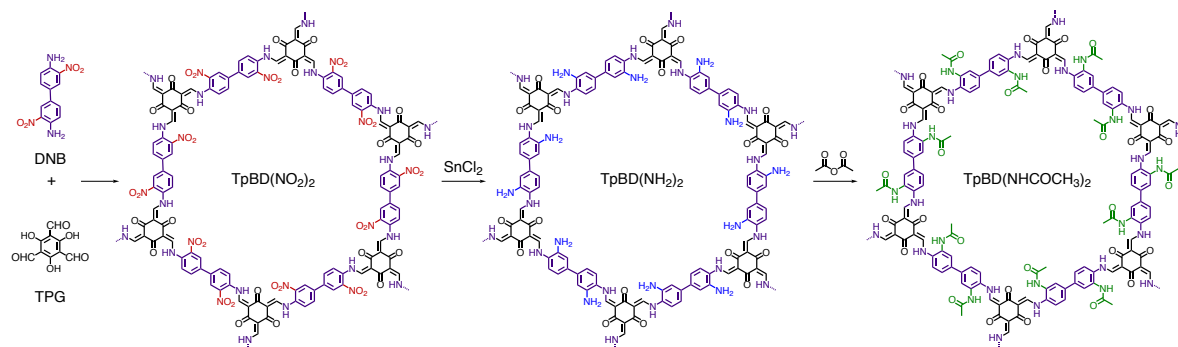


Figure 5.1: Schematic representation of the synthesis of TpBD(NO₂)₂ and postsynthetic modification to TpBD(NH₂)₂ and TpBD(NHCOCH₃)₂.

Imine-based COFs made from diamines and 1,3,5-triformylphloroglucinol that undergo a keto-enol tautomerization upon lattice formation to form β -ketoenamines showed high chemical stability in acidic as well as basic environments.¹⁴ The uniform pore size combined with the possibility to fine-tune the chemical environment of the pore interior by postsynthetic modification further suggests COFs of this type to be promising candidates for selective adsorption processes. Moreover, the exceptional stability of these materials in acidic solutions calls for applications where stability under low pH conditions is limiting the use of other types of adsorbents.

Of particular interest is the adsorptive recovery of lactic acid, a major precursor for biodegradable plastics.³⁰ Typically, lactic acid is being produced by fermentation of carbohydrate substrates, but its isolation from the broth generates stoichiometric amounts of precipitated salt waste. While the demand for lactic acid is drastically increasing, this separation problem is the main bottleneck limiting the further upscaling of the production process.^{31–33}

Therefore, new materials for selective adsorption of lactic acid are in great demand. Here we present a novel approach for the synthesis of a β -ketoenamine COF bearing an amine functional group in the pores through a postsynthetic reduction reaction. For this purpose, we initially synthesized the chemically stable β -ketoenamine COF TpBD(NO₂)₂ featuring nitro functionalities in the pores serving as protective groups for the final desired amino groups. The nitro groups were then reduced to afford an amine functionalized COF, TpBD(NH₂)₂. To demonstrate the accessibility of the amino groups in the pores, a sequential postsynthetic modification step, the aminolysis of acetic anhydride,

was performed to obtain the amide functionalized COF, TpBD(NHCOCH₃)₂ (Figure 5.1). Thereby, a two-step postsynthetic modification in a COF is demonstrated for the first time. The systematically modified frameworks were then applied in the batch adsorption of lactic acid and the influence of the pore chemical environment on the lactic acid uptake was studied.

5.2 Results and Discussion

The PXRD pattern of TpBD(NO₂)₂ shows an intensive reflection at 3.5° corresponding to the (100) plane. The reflections at 6.0°, 9.4°, and ≈ 26° are attributed to the (110), (210), and (001) planes, respectively (Figure 5.2a). It is in agreement with the reported theoretical prediction of an AA stacking arrangement.¹⁵

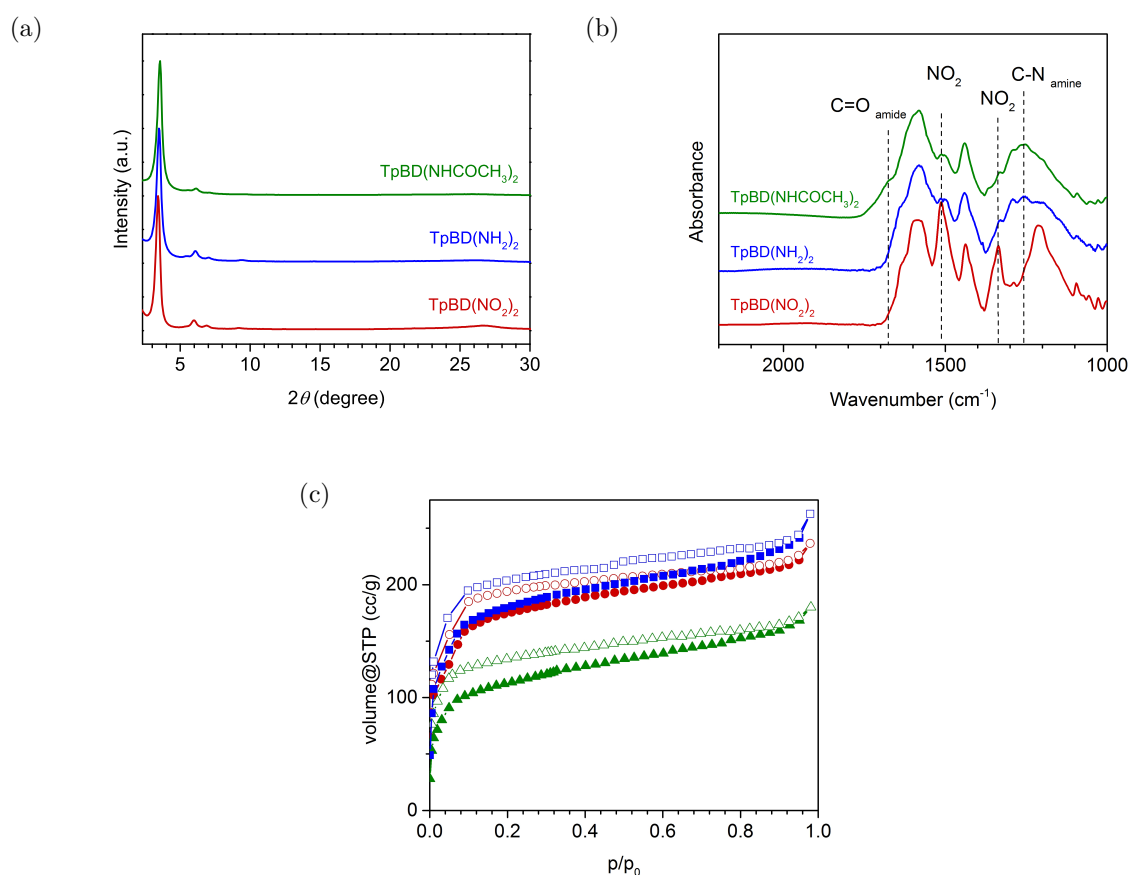


Figure 5.2: (a) PXRD patterns, and (b) FT-IR spectra of TpBD(NO₂)₂ (red), TpBD(NH₂)₂ (blue), and TpBD(NHCOCH₃)₂ (green). (c) Nitrogen sorption isotherms with adsorption branch (closed symbols) and desorption branch (open symbols) of TpBD(NO₂)₂ (red circles), TpBD(NH₂)₂ (blue squares) and TpBD(NHCOCH₃)₂ (green triangles).

Nitrogen sorption measurements of $\text{TpBD}(\text{NO}_2)_2$ provided an isotherm that is a combination of type I and type IV which indicates pores in the intersection between the microporous and mesoporous range (Figure 5.2c). This is in agreement with the calculated pore size distribution corresponding to mesopores of ≈ 2.3 nm in diameter as well as micropores of >1.6 nm in diameter (see Figure 5.3a).

The BET surface area is calculated to be as high as $639 \text{ m}^2 \text{ g}^{-1}$. With a porous and crystalline nitro-functionalized framework available, we proceeded to reduce the nitro groups to the desired primary amines. In the reduction step, tin(II)chloride dihydrate ($\text{SnCl}_2 \times 2\text{H}_2\text{O}$) was employed as a reducing agent. The PXRD pattern of the obtained material exhibits a diffraction pattern comparable to the one of $\text{TpBD}(\text{NO}_2)_2$ with an intensive reflection at 3.5° (Figure 5.2a).

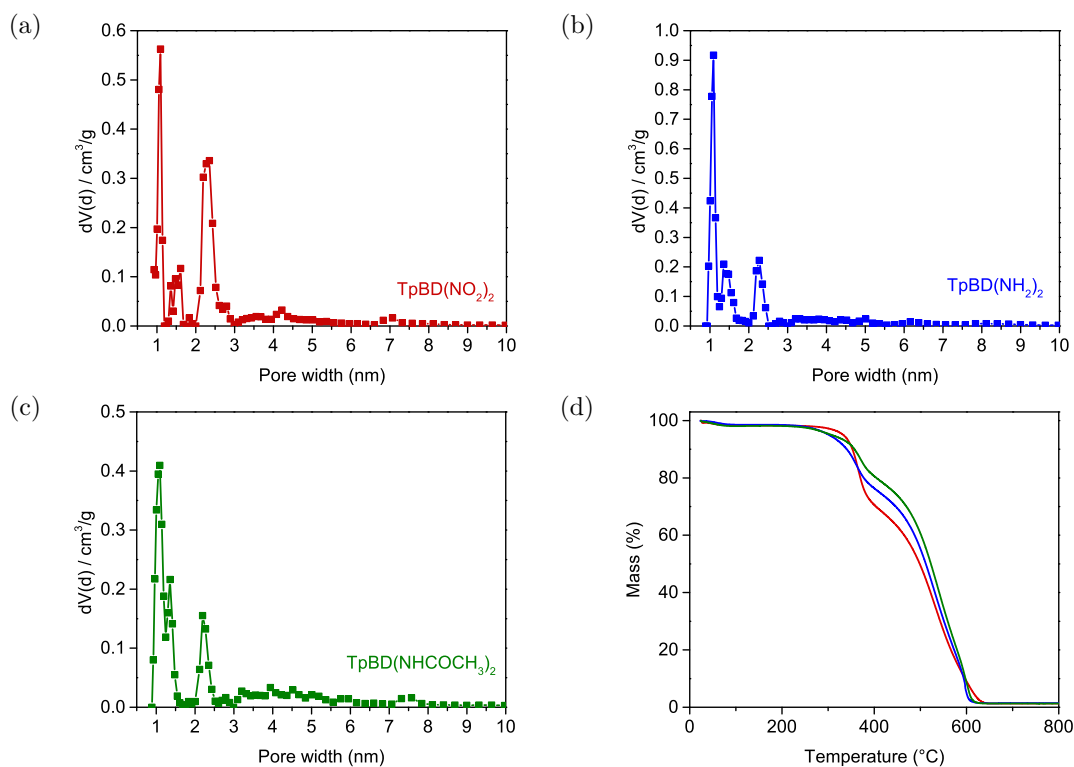


Figure 5.3: Differential pore size distribution plot of (a) $\text{TpBD}(\text{NO}_2)_2$, (b) $\text{TpBD}(\text{NH}_2)_2$, and (c) $\text{TpBD}(\text{NHCOCH}_3)_2$. (d) Thermogravimetric traces of $\text{TpBD}(\text{NO}_2)_2$ (red), $\text{TpBD}(\text{NH}_2)_2$ (blue), and $\text{TpBD}(\text{NHCOCH}_3)_2$ (green).

Nitrogen sorption measurements were conducted to verify pore accessibility after the reductive treatment. They provided an isotherm similar to the one of $\text{TpBD}(\text{NO}_2)_2$, at the intersection of micro- and mesoporosity (Figure 5.2c). The BET surface area was calculated to be as high as $643 \text{ m}^2 \text{ g}^{-1}$. This confirms that porosity is retained after the reduction process. SEM micrographs of $\text{TpBD}(\text{NH}_2)_2$ show spherical particles of \approx

5 μm in diameter that are decorated with thin rods. This is comparable to the observed morphology of $\text{TpBD}(\text{NO}_2)_2$ (Figure 5.4).

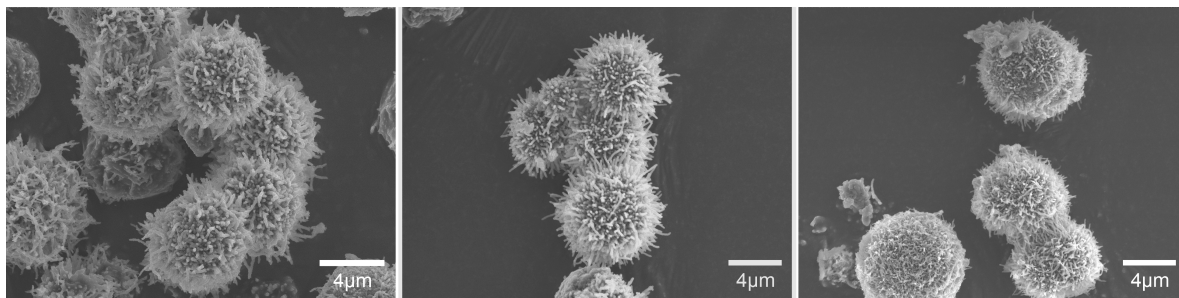


Figure 5.4: Scanning electron microscopy images of $\text{TpBD}(\text{NO}_2)_2$ (left), $\text{TpBD}(\text{NH}_2)_2$ (middle) and $\text{TpBD}(\text{NHCOCH}_3)_2$ (right).

In transmission electron microscopy (TEM) images, $\text{TpBD}(\text{NH}_2)_2$ exhibits a polycrystalline structure with random crystal orientation. Projections along the c -axis show the typical hexagonal pattern representing the 1D channels along this axis (Figure 5.5b). The same structure was observed for $\text{TpBD}(\text{NO}_2)_2$ (Figure 5.5a). Thermogravimetric analysis (TGA) indicates a major mass loss at 450 $^\circ\text{C}$, attributed to the decomposition of the framework, confirming that $\text{TpBD}(\text{NH}_2)_2$ is as thermally stable as $\text{TpBD}(\text{NO}_2)_2$ (Figure 5.3d).

On the basis of the above we can conclude that no distinct structural changes occurred during the reduction of the nitro group-containing COF to the amine functionalized COF. Determination of the tin content in the framework after the reduction by atomic emission spectroscopy revealed a tin concentration of 0.2 - 0.3 wt%, indicating a successful removal of the residual tin species (see Table 5.1). This observation is in line with the thermogravimetric analysis as no significant residual mass is observed after the decomposition of the framework.

Table 5.1: ICP-OES elemental analysis determination of residual tin concentration in $\text{TpBD}(\text{NH}_2)_2$ at three different characteristic emission wavelengths. Samples were prepared independently and measured twice.

Sample Number	Measurement	Sn 189.927 (mg/g)	Sn 235.485 (mg/g)	Sn 242.950 (mg/g)
1	1	2.26	3.10	2.99
	2	2.69	2.75	2.74
2	1	2.28	2.68	2.86
	2	1.81	1.90	2.05

To study the postsynthetic modification and the amine formation, IR spectroscopy was performed. Upon reduction to the amine, the characteristic NO_2 stretching vibrations of

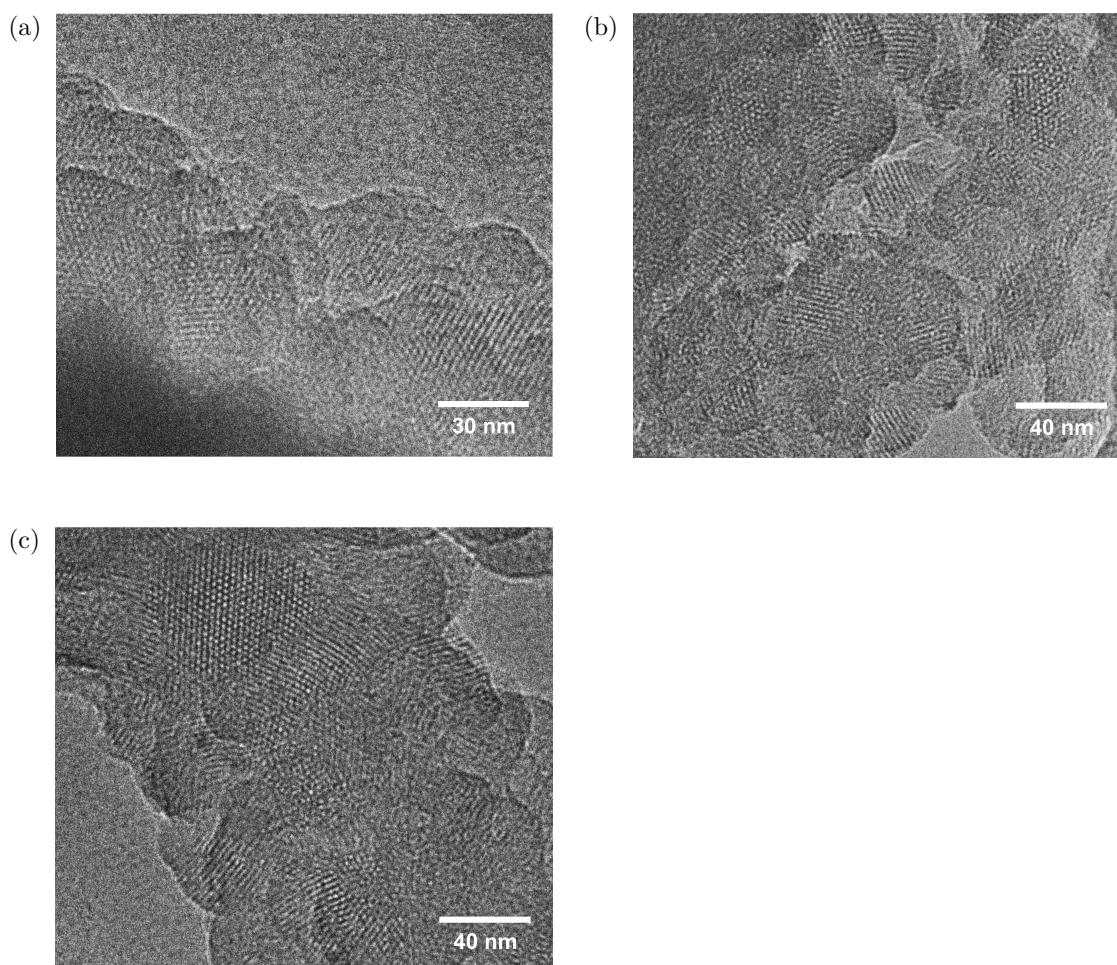


Figure 5.5: Transmission electron microscopy images of (a) $\text{TpBD}(\text{NO}_2)_2$, (b) $\text{TpBD}(\text{NH}_2)_2$, and (c) $\text{TpBD}(\text{NHCOCH}_3)_2$.

the nitro group of $\text{TpBD}(\text{NO}_2)_2$ at 1511 cm^{-1} (asymmetric) and 1336 cm^{-1} (symmetric) are strongly reduced, and a signal at 1291 cm^{-1} that corresponds to the C-N stretch vibration of a primary amine arises in the IR spectrum. This supports the successful reduction of the nitro group to the corresponding primary amine (Figure 5.2b). To further investigate the amine formation, we acquired cross-polarized ^{15}N solid-state NMR spectra (ssNMR). $\text{TpBD}(\text{NO}_2)_2$ shows one signal at ppm, corresponding to the secondary amine connecting the COF backbone. However, in $\text{TpBD}(\text{NH}_2)_2$ a second signal is present at -344 ppm, which is assigned to the aromatic primary amine (Figure 5.6a).

We can therefore conclude that we have successfully achieved the NH_2 -pore functionalization in the COF. To address the accessibility of the amino groups for postsynthetic modification in the pore system, we performed a sequential aminolysis reaction of pure acetic anhydride to form an amide bond at the pore walls.³⁴ PXRD measurement confirmed a crystalline TpBD COF structure (Figure 5.2a). All previously assigned reflections are

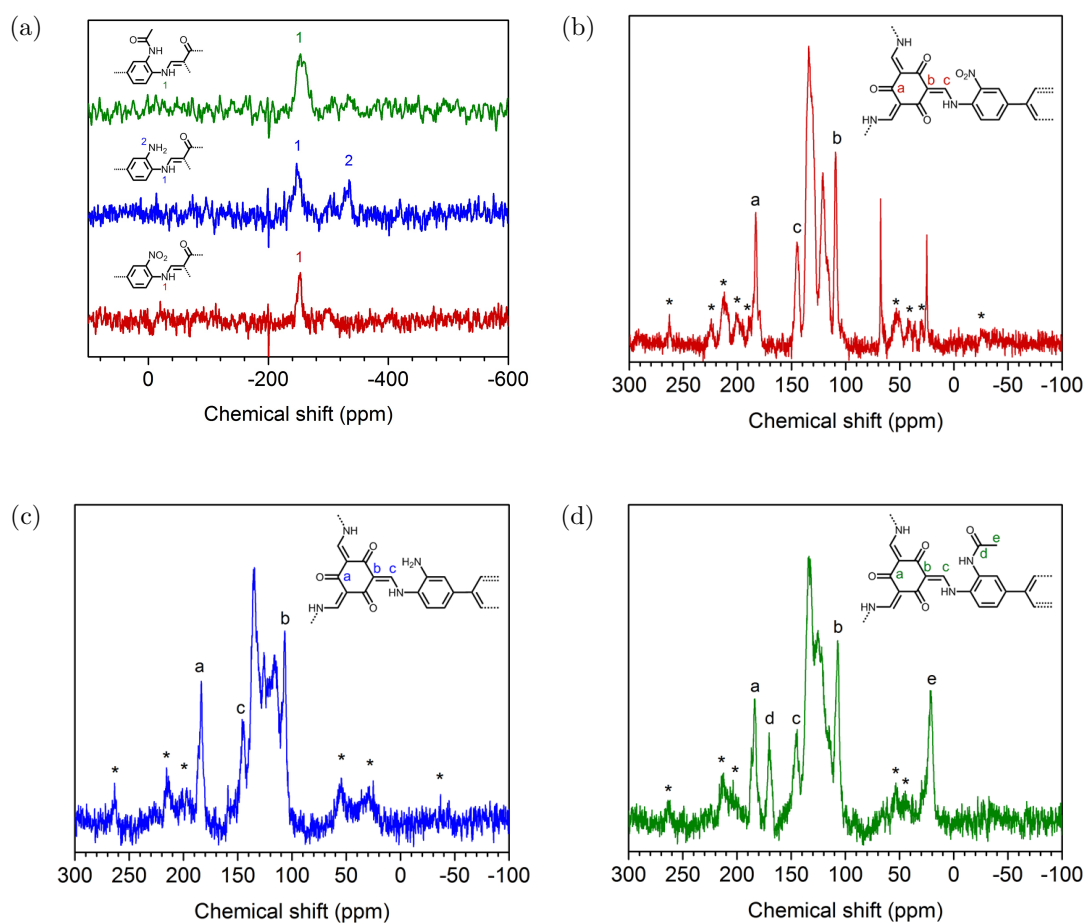


Figure 5.6: (a) ^{15}N solid state NMR spectra of $\text{TpBD}(\text{NO}_2)_2$ (red), $\text{TpBD}(\text{NH}_2)_2$ (blue) and $\text{TpBD}(\text{NHCOCH}_3)_2$ (green). ^{13}C solid state NMR spectra of $\text{TpBD}(\text{NO}_2)_2$ (b), $\text{TpBD}(\text{NH}_2)_2$ (c), $\text{TpBD}(\text{NHCOCH}_3)_2$ (d).

present in the X-ray diffraction pattern of $\text{TpBD}(\text{NHCOCH}_3)_2$. SEM analysis of the COF powder revealed that the general TpBD -COF morphology of a spherical shape decorated with thin rods was maintained during the different treatment steps (Figure 5.4). TEM analysis showed the typical honeycomb structure of a highly ordered COF material (Figure 5.5c). TGA measurements indicate a thermal stability that is similar to the nitro and the amino COF forms (see Figure 5.3d).

The successful formation of intra-COF amide bonds was investigated by IR and ss-NMR spectroscopy. In the IR spectrum of $\text{TpBD}(\text{NHCOCH}_3)_2$ a vibrational mode appears at 1674 cm^{-1} that is characteristic for C=O stretch vibrations of amides (Figure 5.2b). ^{15}N solid state NMR measurements reveal only one signal in the spectrum of $\text{TpBD}(\text{NHCOCH}_3)_2$ at -252 ppm, which can be assigned to a secondary amine. The signal of the primary amine, which was present at -334 ppm in $\text{TpBD}(\text{NH}_2)_2$, has completely disappeared as a result of the amide formation (Figure 5.6a). In the ^{13}C ssNMR spec-

trum, the amide side group is visible (see Figure 5.6d). Nitrogen sorption measurements of $\text{TpBD}(\text{NHCOCH}_3)_2$ provide a Type I isotherm, which is characteristic for microporous materials (Figure 5.2c). This observation corresponds with the pore size distribution calculation predicting some mesopores and a large contribution of micropores (Figure 5.3c). As a result of the presence of additional groups in the pores, the BET surface area is reduced to $519 \text{ m}^2 \text{ g}^{-1}$ upon postsynthetic modification with acetic anhydride.

After the successful synthesis of TpBD COF with different functional groups in the pore system, we examined these chemically very stable networks in an acidic adsorption application, the batch adsorption of lactic acid. For each of the three functionalized COFs, a lactic acid adsorption isotherm was measured (Figure 5.7a). These isotherms were recorded by high-performance liquid chromatography from aqueous solutions at their natural pH (pH 2.2 for a 0.1 M lactic acid solution). Different isotherm shapes can clearly be observed for the three materials. $\text{TpBD}(\text{NH}_2)_2$ and $\text{TpBD}(\text{NHCOCH}_3)_2$ display type I isotherms with uptakes of up to 6.6 and 4.0 wt%, respectively.

In contrast, the isotherm of $\text{TpBD}(\text{NO}_2)_2$ is linear with a highest measured uptake of 2.5 wt%. After the adsorption experiments the respective COFs were collected by centrifugation and washed with water and acetone. PXRD measurements indicate that the COFs maintained their crystalline structure throughout the adsorption experiment (Section 5.2).

While the high concentration range of the isotherm yields information about the capacity of the COF for lactic acid, the slope of the isotherm linear fit in the low concentration range reflects the affinity of the frameworks for lactic acid (Figure 5.7b). Interestingly, the affinity follows the same trend as the uptake with the highest value observed for $\text{TpBD}(\text{NH}_2)_2$ (3.4 L mol^{-1}), followed by $\text{TpBD}(\text{NHCOCH}_3)_2$ (1.7 L mol^{-1}) and $\text{TpBD}(\text{NO}_2)_2$ (0.1 L mol^{-1}). As lactic acid is a small polar molecule with both H-bond donor and acceptor atoms, one can link the different adsorption performances of the materials to their different H-bonding properties. Therefore, the presence of H-bond donating and accepting amino groups lining the pores results in a substantially higher affinity for lactic acid compared to a host with nitro groups offering only H-bond acceptor properties. These results clearly show that lactic acid adsorption can be tuned by the chemical pore environment.

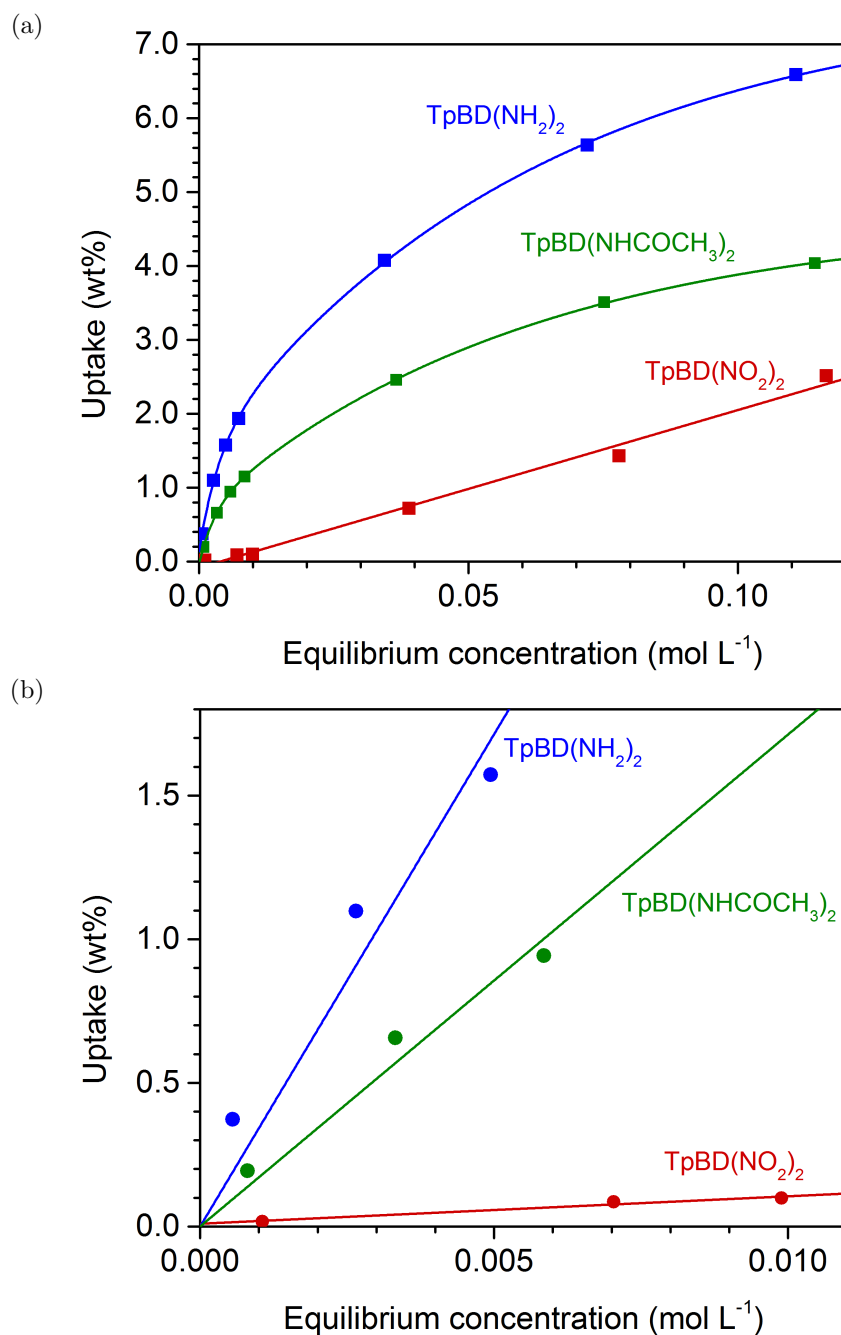


Figure 5.7: (a) Lactic acid adsorption isotherms from aqueous solutions at natural pH, and (b) detail of the low concentration range and linear fit of the lactic acid adsorption isotherms of TpBD(NO₂)₂ (red), TpBD(NH₂)₂ (blue) and TpBD(NHCOCH₃)₂ (green).

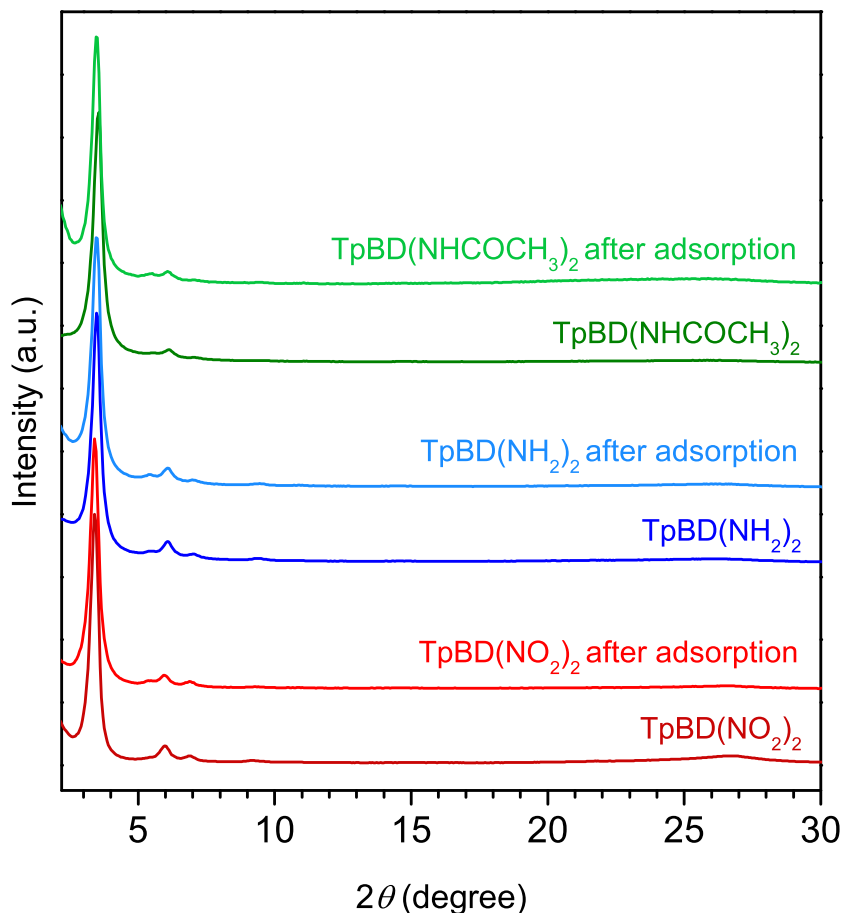


Figure 5.8: PXRD patterns of the TpBD-COFs before and after batch adsorption of lactic acid. Subsequent to the adsorption experiments the powders were collected by centrifugation, washed with water and acetone and PXRD patterns were recorded.

5.3 Conclusion

We have demonstrated the synthesis of a NH₂-pore-functionalized COF through a postsynthetic reduction step as well as the further chemical modification of this functional group. For this purpose, we synthesized the chemically stable imine-based covalent organic framework TpBD(NO₂)₂. The reduction of the nitro groups led to the TpBD(NH₂)₂ framework while retaining the crystallinity and porosity of the original COF. We further investigated a subsequent modification step of TpBD(NH₂)₂ with acetic anhydride, resulting in the amide functionalized TpBD(NHCOCH₃)₂.

Lactic acid adsorption experiments showed that the affinity for lactic acid could be successfully increased by postsynthetic modification of the functional side groups in the

COF pores. To the best of our knowledge, this study represents the first demonstration of a two-step postsynthetic modification in a covalent organic framework. Our model reaction also shows that TpBD(NH₂)₂ is a promising platform for further modification experiments and that multistep postsynthetic modification protocols are a feasible route for pore wall functionalization in COFs.

The successful uptake of lactic acid from diluted aqueous solutions combined with the striking influence of the pore-wall functional groups on the affinity for the adsorbate reveals the great potential of pore functionalization of COF materials for liquid-phase adsorption processes. A large increase in affinity of the framework for lactic acid upon reduction of the nitro group to the amine also demonstrates the benefit of a primary amine functionalization in a COF for H-bonding interactions with adsorbates. We are currently expanding the postsynthetic reaction pathway to a broader range of reactions and the incorporation of additional functionalities.

5.4 Experimental

All materials (if not otherwise noted) were purchased from Aldrich, Fluka, or Acros in the common purities purum and puriss and used as received without further purification. The building block TPG was synthesized according to a method described by Yelamaggad et al. Analytical data were found to match literature data.³⁵

5.4.1 COF Synthesis of TpBD(NO₂)₂

The nitro functionalized COF TpBD(NO₂)₂ was previously reported by Banerjee and co-workers.¹⁵ It is synthesized through a condensation reaction of 1,3,5-triformylphloroglucinol (TPG) and 3,3'-dinitrobenzidine (DNB) in a mesitylene and 1,4-dioxane solvent mixture in the presence of 3 M aqueous acetic acid under solvothermal conditions. Here, we synthesized TpBD(NO₂)₂ using anisole as a single solvent in the presence of 12 M acetic acid. 1,3,5-Triformylphloroglucinol (50.4 mg, 0.23 mmol) and 3,3'-dinitrobenzidine (85.5 mg, 0.31 mmol) followed by 8 mL of dry anisole and 2 mL of 12 M AcOH were placed in a 25 mL Schott Duran glass bottle with a Teflon sealed PBT cap.

The reaction mixture was heated for 96 h at 120 °C. A reddish brown precipitate was filtered off and washed with 100 mL of acetone. The obtained COF powder was resuspended in 5 mL of anisole in a 25 mL Schott Duran glass bottle and heated at 120 °C for 24 h. Afterward the COF powder was filtered and washed with 100 mL of acetone to afford the COF in 90% yield.

5.4.2 Postsynthetic Modifications

5.4.2.1 Reduction of TpBD(NO₂)₂ to TpBD(NH₂)₂

A total of 3 g of SnCl₂ × 2H₂O was dissolved in 5 mL of dry THF and added to 150 mg of TpBD(NO₂)₂ in a 100 mL round bottomed flask. The reaction mixture was heated under reflux for 3 h. The brown solid was centrifuged and suspended in 10 mL of 1 M hydrochloric acid. Afterward, the precipitate was washed 10 times with 70 mL of 1 M hydrochloric acid, 3 times with 70 mL of water, and one time with acetone (100 mL). Then the obtained reddish brown COF powder was resuspended in 5 mL of anisole in a 25 mL Schott Duran glass bottle. The suspension was heated at 120 °C for 24 h. Finally, the COF powder was filtered and washed with 100 mL of acetone.

5.4.2.2 Postsynthetic Modification to TpBD(NHCOCH₃)₂

A total of 150 mg of TpBD(NH₂)₂ was placed in a round bottomed flask in a preheated oil bath at 100 °C. Acetic anhydride was added, and the mixture was allowed to react at 100 °C under reflux conditions for 10 min. Afterward, the product was allowed to cool down to room temperature, filtered off, and washed with water and acetone to yield a brown powder. Subsequently, it was resuspended in 5 mL of anisole in a 25 mL Schott Duran glass bottle and heated at 120 °C for 24 h. Then the COF powder was collected by filtration and washed with 100 mL of acetone.

5.4.3 Batch Adsorption

Liquid-phase batch adsorption experiments were carried out at 25 °C in 1.8 mL glass vials filled with 25 mg of adsorbent and 1.8 mL of a lactic acid solution in demineralized water. In a standard procedure, the materials TpBD(R)₂ (R = NO₂, NH₂, NHCOCH₃) were pretreated at 100 °C in an oven overnight under atmospheric conditions. Uptakes were directly calculated from high performance liquid chromatography (HPLC) data obtained with an Agilent 1200 HPLC equipped with a Bio-Rad Aminex HPX-87H column (300 × 7.8 mm) at 30 °C with 35 mM H₃PO₄ in Milli-Q water as mobile phase flowing at a rate of 0.6 mL min⁻¹. The column was connected to a UV-detector operating at a wavelength of 212 nm. Adsorption isotherms were constructed by plotting the uptake, in weight %, versus the residual concentration in solution. The initial slopes of the isotherms were determined by fitting a straight line through the first data points including the origin.

5.4.4 Characterization

Fourier transform infrared (FT-IR) spectra were recorded on a Thermo Scientific Nicolet 6700 spectrometer in the scan range 650-4000 cm^{-1} . The samples were prepared as KBr pellets. Nitrogen sorption was measured with a Quantachrome AUTOSORB-1 station at 77.3 K after degassing the sample for at least 12 h under vacuum at 120 °C. The Brunauer-Emmett-Teller (BET) surface areas were calculated from the adsorption branch. The range for the calculation was $p/p_0 = 0.05-0.2$ for $\text{TpBD}(\text{NO}_2)_2$ and $\text{TpBD}(\text{NH}_2)_2$ and $p/p_0 = 0.005-0.1$ for $\text{TpBD}(\text{NHCOCH}_3)_2$. Pore sizes were calculated with a QSDFT adsorption model of N_2 on carbon (cylindrical/slit pore model, adsorption branch). Powder X-ray diffraction (PXRD) measurements were carried out in reflection mode on a Bruker D8 Discover diffractometer with Ni-filtered $\text{K}\alpha$ -radiation ($\lambda = 1.54060 \text{ \AA}$) and a position-sensitive detector (LynxEye).

Scanning electron microscopy (SEM) was performed on a JEOL 6500F instrument at acceleration voltages of 2-5 kV. The samples were coated with a thin carbon layer by carbon fiber flash evaporation at high vacuum. Transmission electron microscopy (TEM) data were obtained with a FEI Titan Themis at an acceleration voltage of 300 kV. Atomic emission spectroscopy for the tin content determination was performed on a Varian Vista RL Simultaneous ICP-AES instrument equipped with a CCD detector. The samples were dissolved in aqua regia. UV-vis spectra were recorded using a PerkinElmer Lambda 1050 spectrometer equipped with a 150 mm integrating sphere and InGaAs detector. Diffuse reflectance spectra were collected with a Praying Mantis (Harrick) accessory and were referenced to barium sulfate as a white standard.

Cross-polarized ^{13}C and ^{15}N solid-state NMR (ssNMR) measurements were performed on a Bruker Avance III-500 spectrometer in a 4 mm ZrO_2 rotor with a spinning rate of 10 kHz. Thermogravimetric analyses (TGA) were recorded on a Netzsch STA 440 C TG/DSC. The measurements proceeded at a heating rate of 10 °C/min up to 900 °C, in a stream of synthetic air of about 25 mL min^{-1} .

5.5 Appendix

5.5.1 FT-IR spectra

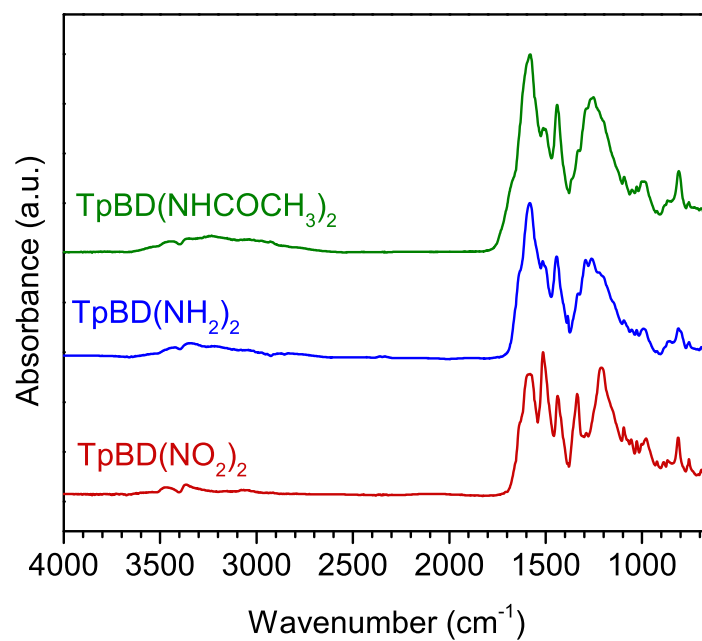


Figure 5.9: FT-IR spectra of $\text{TpBD}(\text{NO}_2)_2$ (red), $\text{TpBD}(\text{NH}_2)_2$ (blue) and $\text{TpBD}(\text{NHCOCH}_3)_2$ (green).

Table 5.2: Assignment of IR bands

Wavenumber (cm^{-1})	Assignment
1679	C=O (amide)
1587	C=C (at Tp linker)
1511	NO_2 (asym)
1336	NO_2 (sym)
1291	C-N (primary amine)
1210	C-N (backbone)

5.5.2 UV-Vis spectra

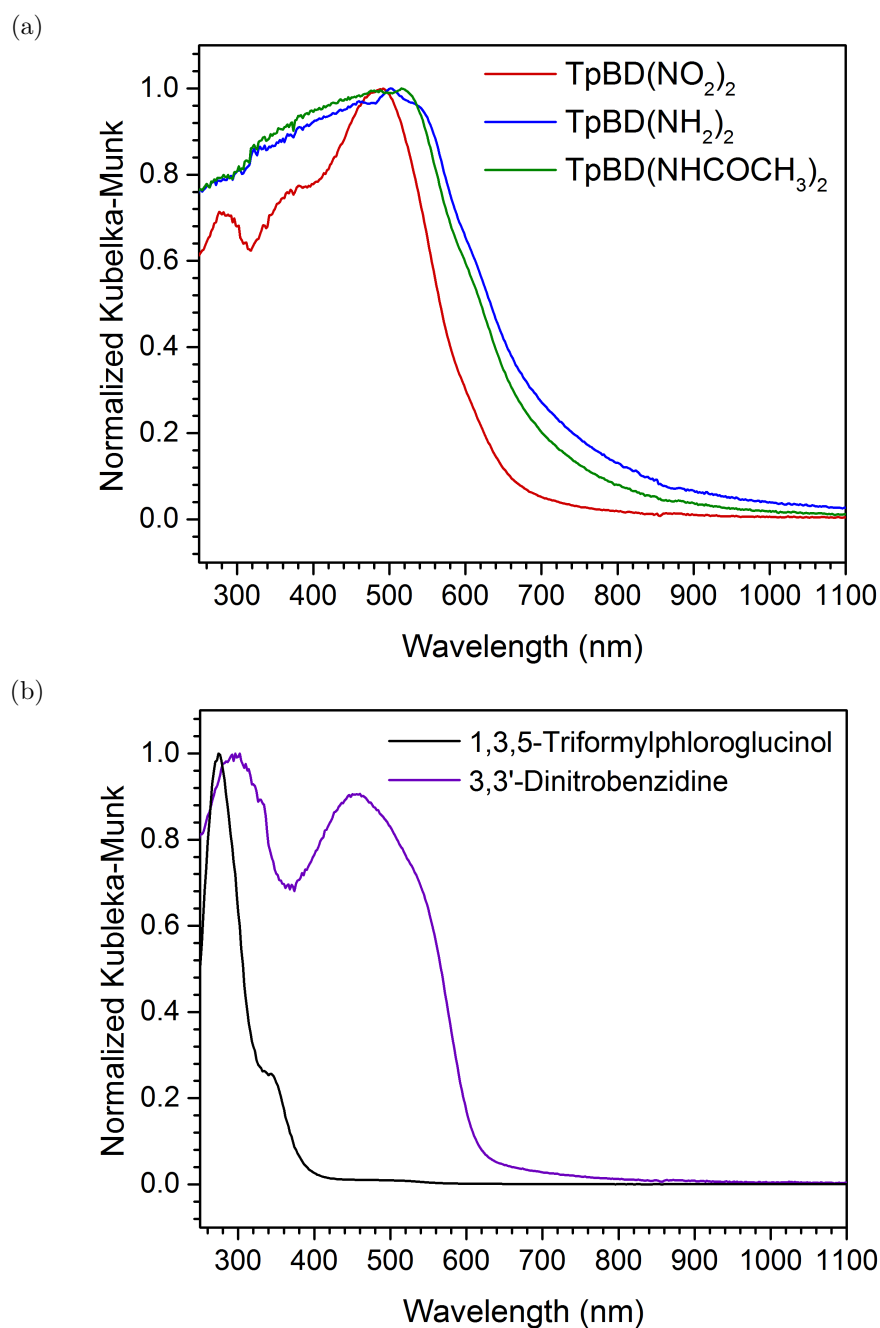


Figure 5.10: UV-Vis spectra of (a) TpBD(NO₂)₂ (red), TpBD(NH₂)₂ (blue) and TpBD(NHCOCH₃)₂ (green), and (b) the building blocks of TpBD(NO₂)₂, recorded from powders in diffuse reflectance.

5.5.3 COF synthesis attempt with 3,3'-diaminobenzidine as an alternative route to TpBD(NH₂)₂

To test the possibility of a direct synthesis of TpBD(NH₂)₂ *via* an amine functionalized linker, we performed a COF synthesis with 3,3'-diaminobenzidine (Figure 5.12), the amino functionalized equivalent of 3,3'-dinitrobenzidine under the same conditions as used for the synthesis of TpBD(NO₂)₂. For this purpose, 1,3,5-triformylphloroglucinol (50.4 mg, 0.23 mmol) and 3,3'-diaminobenzidine (85.5 mg, 0.31 mmol) were placed a 25 ml Schott Duran glass bottle with a teflon sealed PBT cap. To this mixture, 8 ml dry anisole and 2 ml 12M AcOH were added and the reaction mixture was heated for 96 h at 120 °C. A dark brown precipitate was filtered off and washed with 100 ml acetone. Subsequent PXRD measurement confirmed the expected non-crystalline structure of the product (see Figure 5.11).

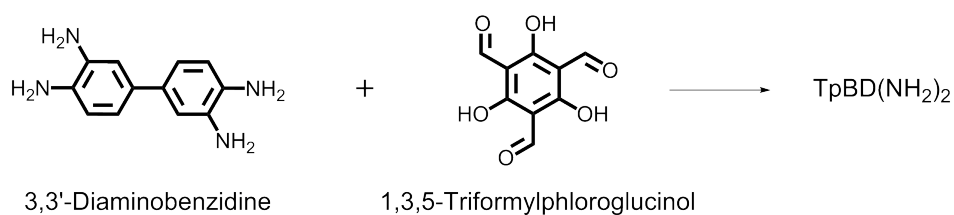


Figure 5.11: Reaction scheme for a proposed direct synthesis of TpBD(NH₂)₂.

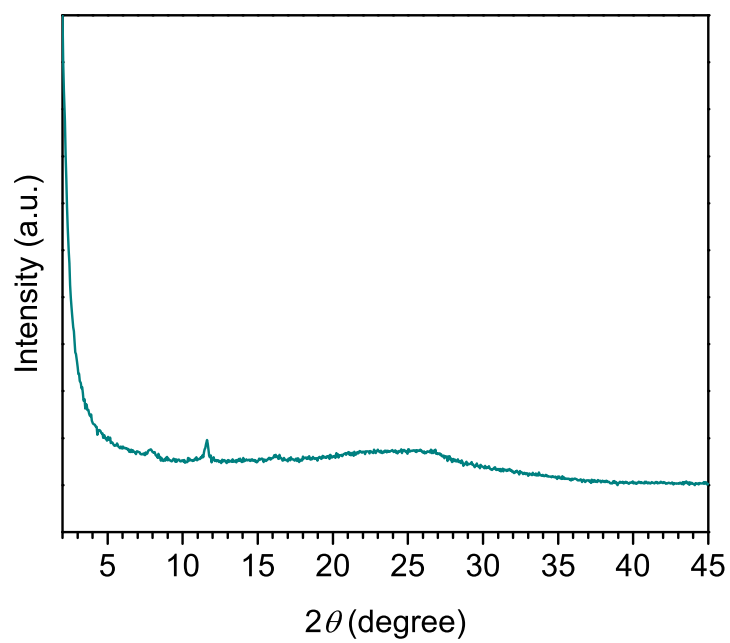


Figure 5.12: PXRD pattern of the reaction product formed from 3,3'-diaminobenzidine and 1,3,5-triformylphloroglucinol.

Bibliography

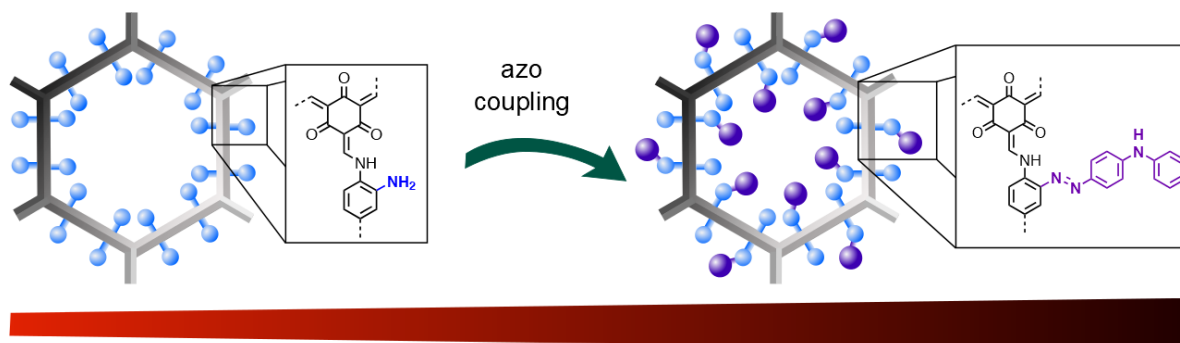
- [1] V. Valtchev, G. Majano, S. Mintova, and J. Perez-Ramirez. *Chem. Soc. Rev.*, **2013**, *42*, 263–290.
- [2] C. Martinez and A. Corma. *Coord. Chem. Rev.*, **2011**, *255*, 1558–1580.
- [3] S. M. Cohen. *Chem. Sci.*, **2010**, *1*, 32–36.
- [4] S. M. Cohen. *Chem. Rev.*, **2012**, *112*, 970–1000.
- [5] A. P. Côté, H. M. El-Kaderi, H. Furukawa, J. R. Hunt, and O. M. Yaghi. *J. Am. Chem. Soc.*, **2007**, *129*, 12914–12915.
- [6] F. J. Uribe-Romo, C. J. Doonan, H. Furukawa, K. Oisaki, and O. M. Yaghi. *J. Am. Chem. Soc.*, **2011**, *133*, 11478–11481.
- [7] D. D. Medina, V. Werner, F. Auras, R. Tautz, M. Dogru, J. Schuster, S. Linke, M. Döblinger, J. Feldmann, P. Knochel, and T. Bein. *ACS Nano*, **2014**, *8*, 4042–4052.
- [8] D. D. Medina, J. M. Rotter, Y. Hu, M. Dogru, V. Werner, F. Auras, J. T. Markiewicz, P. Knochel, and T. Bein. *J. Am. Chem. Soc.*, **2015**, *137*, 1016–1019.
- [9] X. Chen, M. Addicoat, E. Jin, L. Zhai, H. Xu, N. Huang, Z. Guo, L. Liu, S. Irle, and D. Jiang. *J. Am. Chem. Soc.*, **2015**, *137*, 3241–3247.
- [10] D. B. Shinde, S. Kandambeth, P. Pachfule, R. R. Kumar, and R. Banerjee. *Chem. Commun.*, **2015**, *51*, 310–313.
- [11] L. M. Lanni, R. W. Tilford, M. Bharathy, and J. J. Lavigne. *J. Am. Chem. Soc.*, **2011**, *133*, 13975–13983.
- [12] X. Chen, M. Addicoat, S. Irle, A. Nagai, and D. Jiang. *J. Am. Chem. Soc.*, **2013**, *135*, 546–549.
- [13] W. Huang, Y. Jiang, X. Li, X. Li, J. Wang, Q. Wu, and X. Liu. *ACS Appl. Mater. Interfaces*, **2013**, *5*, 8845–8849.
- [14] S. Kandambeth, A. Mallick, B. Lukose, M. V. Mane, T. Heine, and R. Banerjee. *J. Am. Chem. Soc.*, **2012**, *134*, 19524–19527.

- [15] S. Chandra, S. Kandambeth, B. P. Biswal, B. Lukose, S. M. Kunjir, M. Chaudhary, R. Babarao, T. Heine, and R. Banerjee. *J. Am. Chem. Soc.*, **2013**, *135*, 17853–17861.
- [16] R. W. Tilford and J. J. Lavigne. *Polymer*, **2008**, *49*, 308.
- [17] B. J. Smith and W. R. Dichtel. *J. Am. Chem. Soc.*, **2014**, *136*, 8783–8789.
- [18] B. J. Smith, N. Hwang, A. D. Chavez, J. L. Novotney, and W. R. Dichtel. *Chem. Commun.*, **2015**, *51*, 7532–7535.
- [19] D. N. Bunck and W. R. Dichtel. *Angew. Chem., Int. Ed.*, **2012**, *51*, 1885–1889.
- [20] S. D. Brucks, D. N. Bunck, and W. R. Dichtel. *Polymer*, **2014**, *55*, 330–334.
- [21] A. Nagai, Z. Guo, X. Feng, S. Jin, X. Chen, X. Ding, and D. Jiang. *Nat. Commun.*, **2011**, *2*, 1542/1–1542/8.
- [22] D. N. Bunck and W. R. Dichtel. *Chem. Commun.*, **2013**, *49*, 2457–9.
- [23] H. Xu, X. Chen, J. Gao, J. Lin, M. Addicoat, S. Irle, and D. Jiang. *Chem. Commun.*, **2014**, *50*, 1292–1294.
- [24] F. Xu, H. Xu, X. Chen, D. Wu, Y. Wu, H. Liu, C. Gu, R. Fu, and D. Jiang. *Angew. Chem., Int. Ed.*, **2015**, *54*, 6814–6818.
- [25] N. Huang, R. Krishna, and D. Jiang. *J. Am. Chem. Soc.*, **2015**, *137*, 7079–7082.
- [26] N. Huang, X. Chen, R. Krishna, and D. Jiang. *Angew. Chem., Int. Ed.*, **2015**, *54*, 2986–2990.
- [27] Y. Du, D. Calabro, B. Wooler, P. Kortunov, Q. Li, S. Cundy, and K. Mao. *Chem. Mater.*, **2015**, *27*, 1445–1447.
- [28] Y. Du, K. Mao, P. Kamakoti, P. Ravikovitch, C. Paur, S. Cundy, Q. Li, and D. Calabro. *Chem. Commun.*, **2012**, *48*, 4606–4608.
- [29] H. Oh, S. B. Kalidindi, Y. Um, S. Bureekaew, R. Schmid, R. A. Fischer, and M. Hirscher. *Angew. Chem., Int. Ed.*, **2013**, *52*, 13219–13222.
- [30] R. A. Auras, L.-T. Lim, S. E. M. Selke, and H. Tsuji. *Poly(lactic acid): Synthesis, Structures, Properties, Processing, and Applications*. Hoboken, New Jersey: John Wiley & Sons, **2010**.
- [31] R. Datta and M. Henry. *J. Chem. Technol. Biot.*, **2006**, *81*, 1119–1129.

-
- [32] H. G. Joglekar, I. Rahman, S. Babu, B. D. Kulkarni, and A. Joshi. *Sep. Purif. Technol.*, **2006**, *52*, 1–17.
- [33] M. Dusselier, P. Van Wouwe, A. Dewaele, E. Makshina, and B. F. Sels. *Energ. Environ. Sci.*, **2013**, *6*, 1415–1442.
- [34] H. Hintz and S. Wuttke. *Chem. Mater.*, **2014**, *26*, 6722–6728.
- [35] C. V. Yelamaggad, A. S. Achalkumar, D. S. S. Rao, and S. K. Prasad. *J. Org. Chem.*, **2009**, *74*, 3168–3171.

Chapter 6

Postsynthetic Azo Coupling in a Chemically Stable β -ketoenamine COF



Abstract

The optical absorption over a broad range of the visible spectrum is one of the key factors for the potential application of covalent organic frameworks (COFs) in optoelectronic devices. Herein we report the postsynthetic extension of the optical absorption range of a covalent organic framework *via* azo coupling. For this purpose, the previously reported amino-functionalized COF TpBD(NH₂)₂ was subjected to azo coupling with *N,N*-dimethylaniline (DMA) and diphenylamine (DPA), respectively. The degree of modification could be tuned from an only partial conversion of the amino groups to a quantitative azo group formation by varying the amount of coupling agent. The impact of the formation of azo moieties in the COF pores on the optical absorption was investigated. When diphenylamine is used as coupling partner, a strong bathochromic shift of the COF absorption can be observed, demonstrating the applicability of postsynthetic modification for the shift of optical absorption in COFs.

6.1 Introduction

COFs are a class of porous organic structures synthesized by reversible reactions leading to a regular arrangement of their molecular building blocks. They feature a regular pore structure with a defined pore environment.¹⁻⁶ Although the selection of the geometry and functionalization of the building units enables the fine-tuning of the physical and chemical properties of the resulting networks, the choice of building blocks for COF synthesis is limited to those that do not interfere with the COF formation reaction, and that exhibit sufficient solubility in the reaction medium. In the case of two-dimensional (2D) COFs relying on stacking of building blocks via π - π -interactions, this restricts the incorporation of spatially demanding side groups that may inhibit the π - π -interactions and thereby the stacking of the 2D COF sheets. The postsynthetic modification of covalent organic frameworks is a powerful strategy to address this challenge. Thereby, a COF is first synthesized with a functional group that is relatively small and inactive in the COF formation reaction. This functionality then serves as starting point for a one- or multiple-step modification of the already established COF lattice.

To date, the scope of modification reactions reported for COFs is still quite limited. Frequently used reactions are the click reaction of azides with alkynes,⁷⁻¹³ the thiol-ene reaction between an allyl and a thiol,^{14,15} and reactions using a hydroxyl group as starting point which is then modified with succinic anhydride in a ring opening reaction,¹⁶ with

carbonyl chlorides,¹⁷ with glycidol under epoxy ring opening¹⁸ or with an alkyl bromide in a Williamson ether synthesis, respectively.¹⁹

Recently, we reported the reduction of the nitro groups of the COF TpBD(NO₂)₂ to primary aromatic amines in the COF TpBD(NH₂)₂ as a feasible route to establish these versatile functional groups in a chemically stable COF.²⁰ The amino groups were then applied in lactic acid adsorption and for the further reaction with acetic anhydride to establish amide groups, representing the first two-step postsynthetic modification in a COF.

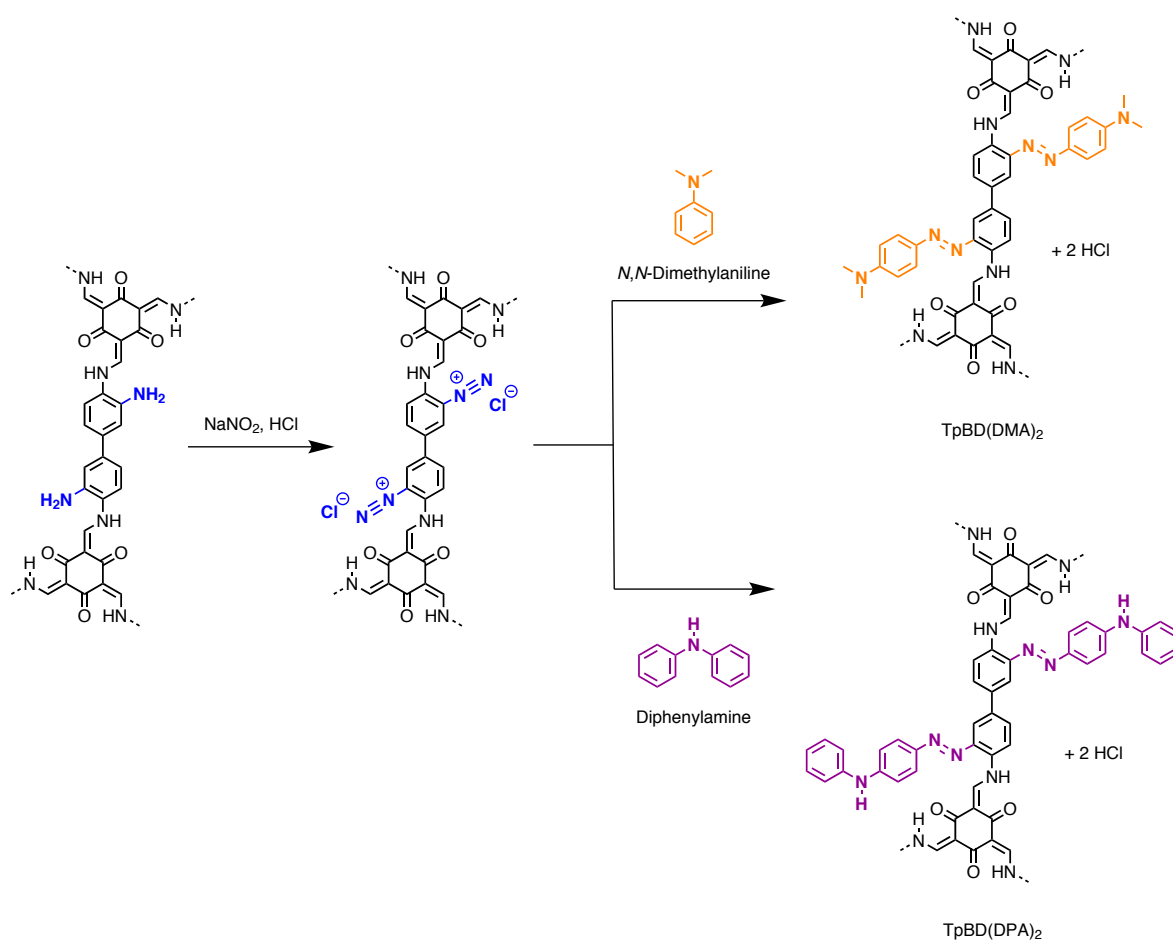


Figure 6.1: Schematic representation of the azo coupling reaction of TpBD(NH₂)₂ with *N,N*-dimethylaniline to TpBD(DMA)₂ and with diphenylamine to TpBD(DPA)₂.

COFs have received considerable attention because of their potential application in various fields such as gas storage,^{21,22} catalysis,^{12,23,24} and electrochemical energy storage.^{25–27} The covalent construction and the stacking in regular columns have made 2D COFs especially interesting for potential applications in optoelectronics.^{28,29} For example, to control

light harvesting behavior, a broadening of the absorption range in covalent organic frameworks may be achieved by a suitable postsynthetic modification reaction.

Herein we aim to increase the optical absorption range of a COF by postsynthetic azo coupling. For this purpose, the stable COF $\text{TpBD}(\text{NH}_2)_2$ bearing primary aromatic amines is applied as starting material. In the first step, sodium nitrite serves as diazotation agent to establish diazonium units at the COF pore walls. In a second step, these moieties are coupled with *N,N*-dimethylaniline and diphenylamine, respectively (Figure 6.1). The effect of the modification on the optical absorption on the COFs is studied for different ratios of coupling agent used in the reaction.

6.2 Results and Discussion

Azo coupling on primary amines is a two-step process. First, a diazotation is performed to establish diazonium ($-\text{N}\equiv\text{N}-$) moieties. These groups are unstable at higher temperatures and would decompose under cleavage of N_2 to leave the COF with hydroxyl groups, if water is present. Therefore, the coupling agents, *N,N*-dimethylaniline or diphenylamine were introduced *in situ* to the reaction. In order to limit the fraction of amine groups that undergo azo coupling, we limited the amount of the diazotation agent NaNO_2 while the coupling agent was always added in excess.

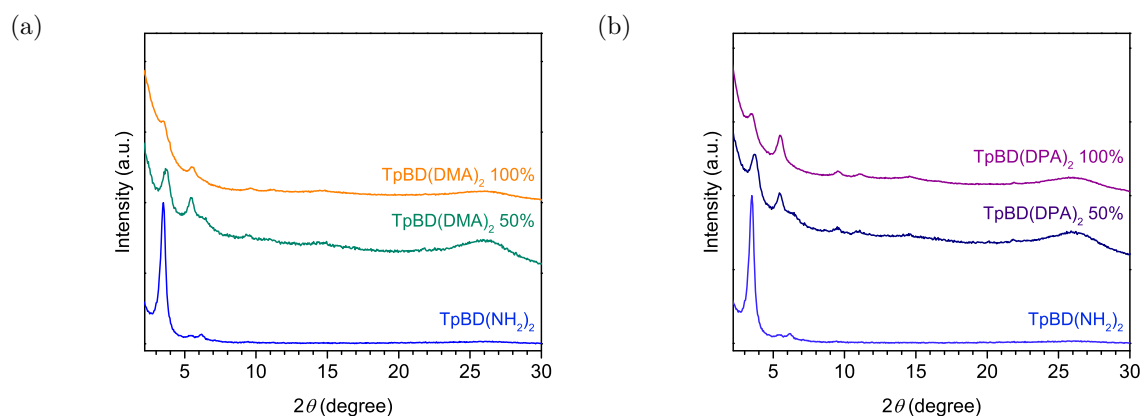


Figure 6.2: PXRD patterns of $\text{TpBD}(\text{NH}_2)_2$ (blue) and azo coupling products $\text{TpBD}(\text{DMA})_2$ (a) and $\text{TpBD}(\text{DPA})_2$ (b).

In a typical reaction, the diazotation agent NaNO_2 was applied in THF at -15°C to -5°C for 90 minutes. The coupling reagent was then added slowly and the coupling reaction was allowed to take place in the next 24 h. Subsequently, the COF was filtered off and washed with acetone. Powder X-ray diffraction was performed to evaluate the integrity of the frameworks. The PXRD patterns of $\text{TpBD}(\text{NH}_2)_2$ and the coupling prod-

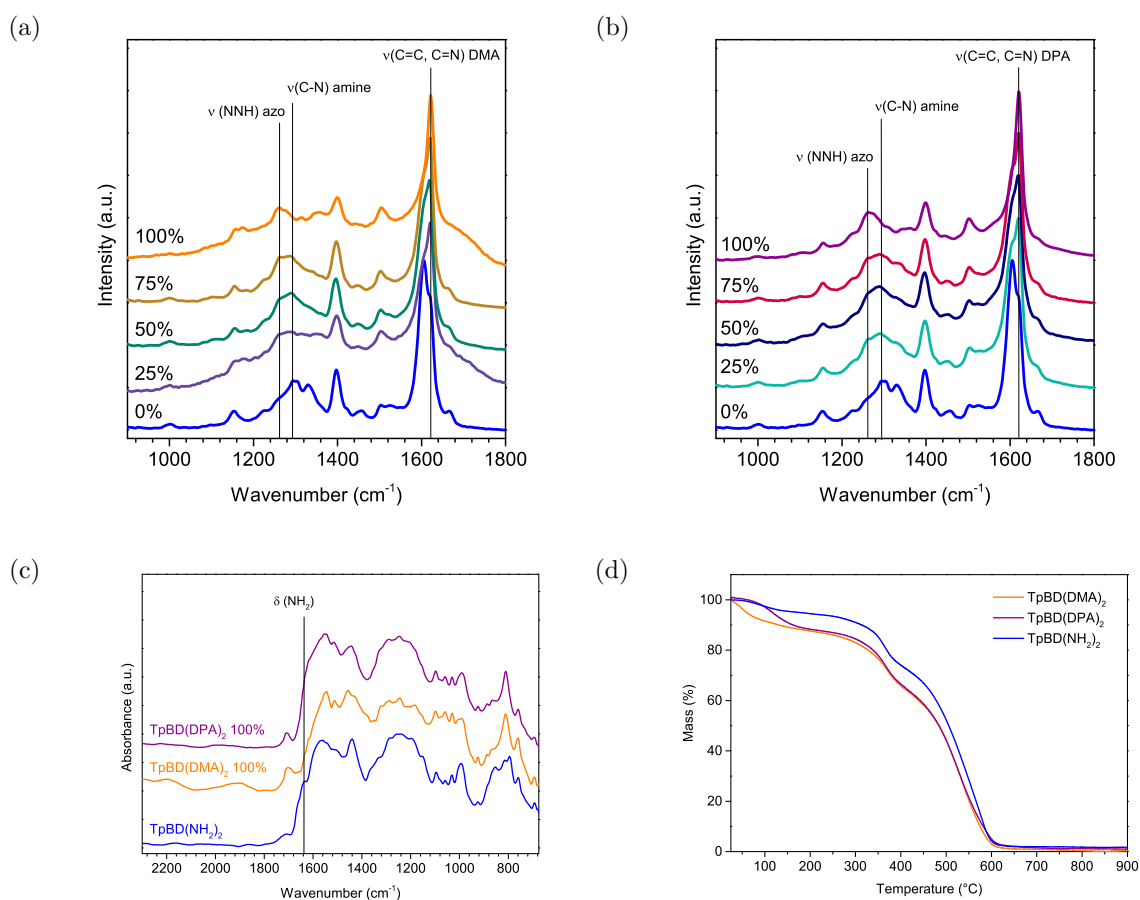


Figure 6.3: Spectroscopic characterization. Raman spectra of TpBD(NH₂)₂ (blue) and the coupling products (a) TpBD(DMA)₂ and (b) TpBD(DPA)₂ obtained with different reagent ratios, (c) IR spectra, and (d) TGA traces of the COFs.

ucts TpBD(DMA)₂ and TpBD(DPA)₂ are depicted in Figure 6.2. TpBD(NH₂)₂ features a strong reflection at 3.5° that is attributed to the (100) plane and smaller peaks at 6.0°, 9.4°, and ≈ 26° that correspond to the (110), (210), and (001) planes, respectively.

After the azo coupling, the above peaks are still visible in the PXRD patterns, although the intensity of the (100) reflection is significantly decreased for high coupling yields. This reduction of the reflections in the PXRD pattern is partially attributed to the filling of the pores with the organic substituents, an effect comparable to solvent filling that was previously reported to change the signal intensities of the reflections in COF-1,³⁰ thus decreasing the X-ray contrast. This change in XRD peak intensity has been reported previously for the postsynthetic modification of COFs.^{7,9} In addition, the crystalline order of the COFs is also reduced at high coupling levels (see below).

Raman and FTIR spectra show the established azo linkage upon the postsynthetic modification of TpBD(NH₂)₂ with the different coupling partners. In the infrared spectra,

a decrease of the NH_2 stretching vibration band at 1291 cm^{-1} is visible, showing the conversion of the primary amine, see Figure 6.3c. As the vibrations of azo groups are IR inactive, Raman spectroscopy was applied to investigate the nature of the established bonds in the coupling reaction products. The analysis of the Raman spectra was performed following the peak assignments of protonated and unprotonated azo dyes, reported by Bisset et al.³¹ and Otal et al.³² Upon azo coupling, the C–N stretch vibration band of the primary amine at 1293 cm^{-1} vanishes for both tested coupling agents, indicating a quantitative conversion of the amino group.

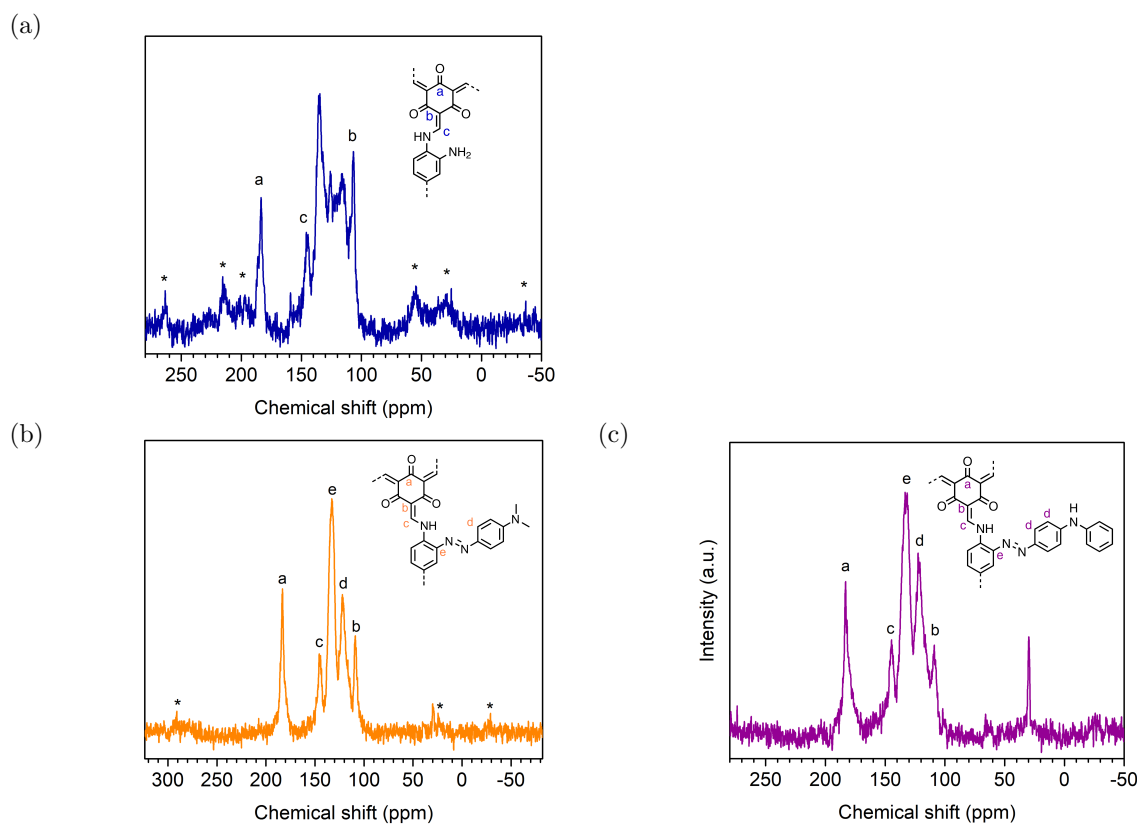


Figure 6.4: ^{13}C solid state NMR spectra of (a) $\text{TpBD}(\text{NH}_2)_2$, (b) $\text{TpBD}(\text{DMA})_2$, and (c) $\text{TpBD}(\text{DPA})_2$.

The azo coupling with *N,N*-dimethylaniline leads to the rise of a strong band at 1623 cm^{-1} in the Raman spectrum that corresponds to C=C and C=N vibrations in the quinoid ring system in the protonated form of the azo compound (see Figure 6.3a). Similarly, signals at 1261 cm^{-1} and 1173 cm^{-1} can be assigned to $\nu(\text{NNH})$ and $\nu(\text{N=N})$ of the protonated species (see Figure 6.9a), respectively.

Upon azo coupling of $\text{TpBD}(\text{NH}_2)_2$ with diphenylamine, the band of the the NH_2 stretching vibration is decreased in the infrared spectrum (Figure 6.3c), indicating a reac-

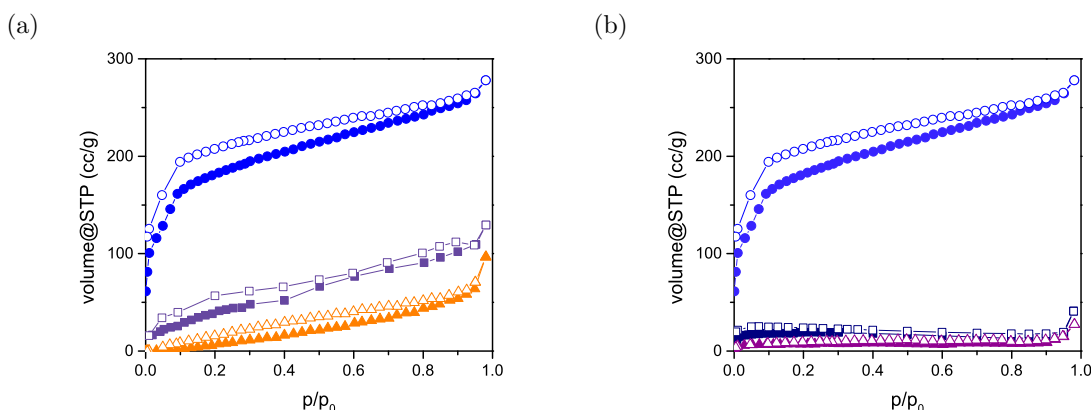


Figure 6.5: Nitrogen sorption isotherms with adsorption branch (closed symbols) and desorption branch (open symbols) of (a) TpBD(DMA)₂: precursor COF TpBD(NH₂)₂ (blue), TpBD(DMA)₂ 25% (purple), TpBD(DMA)₂ 100% (orange); (b) TpBD(DPA)₂: precursor COF TpBD(NH₂)₂ (blue), TpBD(DMA)₂ 25% (dark purple), TpBD(DMA)₂ 100% (bright purple).

tion of the amino group similar to the reaction with *N,N*-dimethylaniline. In the Raman spectrum (Figure 6.3b), C=C and C=N vibrations of the diphenylamine resonance structure (Figure 6.9b) lead to the rise of a strong signal at 1621 cm⁻¹. The signal at 1261 cm⁻¹ can be attributed to the *v* (NNH) vibration of the protonated azo group.

The formation of azo compounds was also verified with ¹³C solid state NMR measurements. In the ¹³C NMR spectra of TpBD(DMA)₂ and TpBD(DPA)₂, a strong signal of the azo coupling partners DMA and DPA is present at 122 ppm, which is absent in the starting material TpBD(NH₂)₂. Furthermore, the signal of the carbon atom at the amino functional group is shifted from 135 ppm to 132 ppm upon azo coupling in both reactions (Figure 6.4).

Thermogravimetric analysis (TGA) traces show a similar thermal stability for fully modified frameworks of TpBD(DMA)₂, TpBD(DPA)₂, and the starting material TpBD(NH₂)₂, indicating no decrease of the thermal stability of the COFs upon post-synthetic azo coupling (Figure 6.3d).

Nitrogen sorption measurements were performed to investigate the porosity of the azo coupling products. The amino functionalized COF TpBD(NH₂)₂ revealed an isotherm that represents a combination of Type I and Type IV, indicating a pore size between the mesoporous and the microporous range, in agreement with the calculated pore size distribution (Figure 6.11) and our previous report on this compound.²⁰ The azo coupling products showed strongly decreased BET surface areas already for the 25% converted products of only 113 m² g⁻¹ for TpBD(DMA)₂ 25% and 74 m² g⁻¹ for TpBD(DPA)₂ 25%.

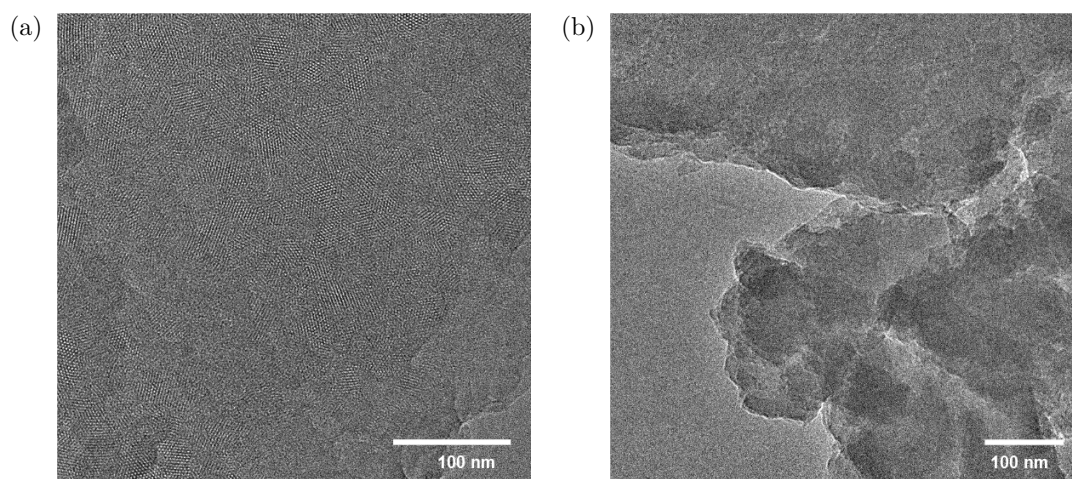


Figure 6.6: Transmission electron microscopy images of (a) TpBD(DPA)₂ 25%, (b) TpBD(DPA)₂ 100%.

In the samples obtained upon quantitative conversion, the surface areas decreased even more to 9 and 28 m² g⁻¹ for the 100% converted coupling products with DMA and DPA, respectively, leading to almost non-porous products (Figure 6.5).

Scanning electron microscopy (SEM) micrographs of TpBD(NH₂)₂ show spherical particles decorated with thin rods. After the postsynthetic azo couplings a partial deterioration of the structural integrity was observed that was most pronounced for fully modified products (Figure 6.10). These observations indicate a gradual degradation of the COF structure for higher degrees of modification.

Transmission electron microscopy (TEM) images were recorded for partially (25%) modified and 100% modified TpBD(DPA)₂. In TpBD(DPA)₂ 25% (Figure 6.6a), the hexagonal pores of the COF are visible, demonstrating the still highly ordered character of the partially modified structure. We furthermore measured a fully modified sample of TpBD(DPA)₂ 100% to investigate if the reduction of XRD signal intensity might originate from a delamination of the COF layers to single sheets that are aligned in a random fashion. In TpBD(DPA)₂ 100% (Figure 6.6b) no crystalline order could be observed, but the COF appears to consist of thick, agglomerated material. Apparently, the individual sheets of the COF are still assembled after postsynthetic modification, but they may be offset or rotated such that sheet-to-sheet correlation and long-range order is reduced.

UV-vis diffuse reflectance spectra of the modified COF powders were recorded to investigate the impact of the azo functionalization on the optical absorption of the COFs. Figure 6.7 shows the diffuse reflectance spectra of DMA-modified COF. For the modification with 25% to 75%, no distinct change in the optical adsorption can be detected while

for the 100% modified sample, the absorption onset is even shifted to lower wavelengths. This might indicate a less efficient electronic layer-to-layer coupling in the disordered state of the COF.

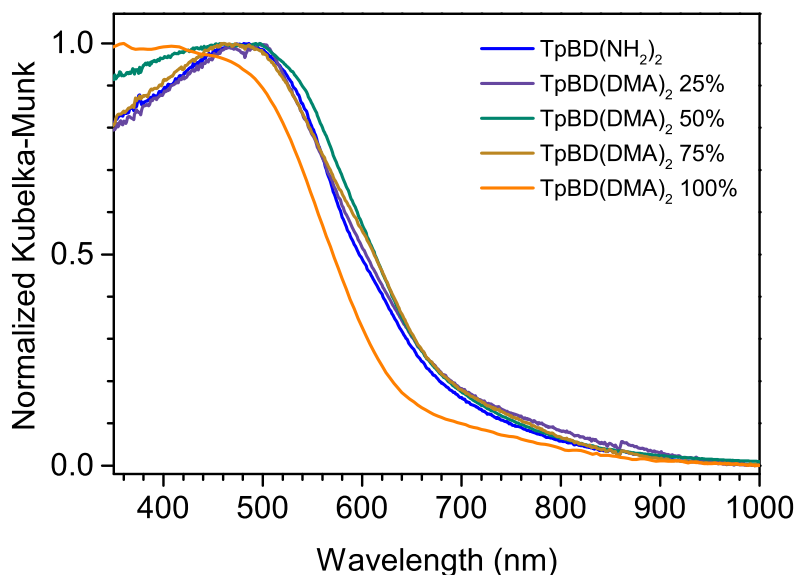


Figure 6.7: UV-Vis spectra of $\text{TpBD}(\text{NH}_2)_2$ (blue) and $\text{TpBD}(\text{DMA})_2$ 25% to $\text{TpBD}(\text{DMA})_2$ 100%, recorded from powders in diffuse reflectance.

In contrast, postsynthetic modification with DPA leads to a bathochromic shift of the absorption that is most pronounced for the sample with 50% modification (Figure 6.8). Similar to the modification with DMA, a hypsochromic shift is observed with DPA when the modification degree is further increased, leading to an absorption onset of the 100% samples that is lower than for the unmodified COF, an effect that we attribute to a partial structural disintegration of the COF structure at high modification yields, indicating less efficient electronic layer-to-layer coupling in the disordered state. The COF with 50% modification exhibits the largest red shift of the optical absorption, representing an optimum between the degree of modification and the structural integrity of the resulting COF.

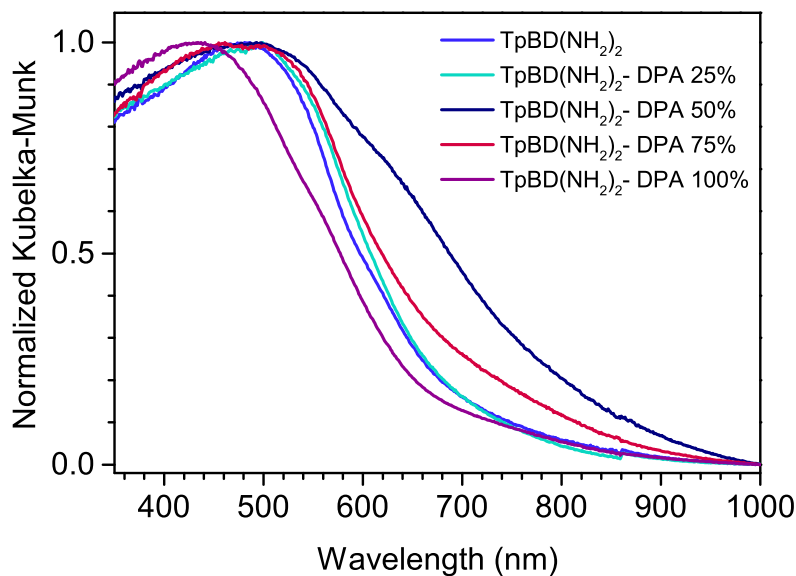


Figure 6.8: UV-Vis spectra of $\text{TpBD}(\text{NH}_2)_2$ (blue) and $\text{TpBD}(\text{DPA})_2$ 25% to $\text{TpBD}(\text{DPA})_2$ 100%, recorded from powders in diffuse reflectance.

6.3 Conclusion

Postsynthetic azo coupling with *N,N*-dimethylaniline and diphenylamine was performed on the NH_2 groups of the β -ketoenamine COF $\text{TpBD}(\text{NH}_2)_2$. We were able to achieve quantitative conversion with both coupling partners. To the best of our knowledge, this represents the first application of azo coupling reactions for the postsynthetic modification of COFs.

While the postsynthetic modification of $\text{TpBD}(\text{NH}_2)_2$ with *N,N*-dimethylaniline had only a small impact on the UV-vis adsorption of the COF, a significant bathochromic shift of the adsorption onset was observed for the COF modified with diphenylamine, with a maximum shift for a COF with 50% modification. With this reaction pathway, we could demonstrate the ability of postsynthetic modifications to tune the optical absorption range of a Covalent Organic Framework.

6.4 Experimental

All materials (if not otherwise noted) were purchased from Aldrich, Fluka, or Acros in the common purities purum and puriss and used as received without further purification. The

building block TPG was synthesized according to a method described by Yelamaggad et al.³³ Analytical data were found to match literature data.

6.4.1 Methods and Characterization

Fourier transform infrared (FT-IR) analysis was performed on a Thermo Scientific Nicolet iN10/iZ10 IR microscope reflection-absorption mode with a liquid-N₂ cooled MCT-A detector in the scan range 650-4000 cm⁻¹. FT-Raman spectra were recorded on a Bruker Equinox 55 equipped with an Nd:YAG laser of 1064 nm wavelength at a laser power of 10 mW. Nitrogen sorption was measured with a Quantachrome AUTOSORB-1 station at 77.3 K after degassing the sample for at least 12 h under vacuum at 120 °C. The Brunauer-Emmett-Teller (BET) surface areas were calculated from the adsorption branch. The range for the calculation was $p/p_0 = 0.05-0.2$ for TpBD(NH₂)₂ and $p/p_0 = 0.005-0.1$ for the azo coupling products. Pore sizes were calculated with a QSDFT adsorption model of N₂ on carbon (cylindrical pore model, adsorption branch). Pore size determination was conducted with a QSDFT adsorption model of N₂ on carbon (cylindrical/slit pore model, adsorption branch).

Powder X-ray diffraction (PXRD) measurements were carried out in reflection mode on a Bruker D8 Discover diffractometer with Ni-filtered K α radiation ($\lambda = 1.54060$ Å) and a position-sensitive detector (LynxEye). Scanning electron microscopy (SEM) was performed on a JEOL 6500F instrument at acceleration voltages of 2-5 kV. The samples were coated with a thin carbon layer by carbon fiber flash evaporation under high vacuum. Transmission electron microscopy (TEM) data were obtained with a FEI Titan Themis at an acceleration voltage of 300 kV.

UV-vis measurements were performed using a PerkinElmer Lambda 1050 spectrometer equipped with a 150 mm integrating sphere and InGaAs detector. Diffuse reflectance spectra were recorded applying a Praying Mantis (Harrick) accessory. Barium sulfate was used as a white standard. Cross-polarized ¹³C solid-state NMR (ssNMR) measurements were performed on a Bruker Avance III-500 spectrometer in a 2.5 mm ZrO₂ rotor with a spinning rate of 20 kHz. Thermogravimetric analyses (TGA) were recorded on a Netzsch STA 440 C TG/DSC. The measurements proceeded at a heating rate of 10 °C/min up to 900 °C, in a stream of synthetic air of about 25 mL/min.

6.4.2 Synthesis of TpBD(DMA)₂

TpBD(NH₂)₂ was prepared following a procedure reported earlier by us.²⁰ For the postsynthetic modification to TpBD(DMA)₂, 10 mg TpBD(NH₂)₂ (corresponding to 0.062 mmol NH₂ groups) was suspended in 0.8 mL dry THF in a culture tube and cooled down to $-15\text{ }^{\circ}\text{C}$ in an ice/NaCl bath under moderate stirring of 300 rpm. To this, 0.09 mL of 2 M HCl solution were added. For a 100% modification, a solution of 4.3 mg (0.062 mmol) NaNO₂ in 0.1 mL of a 1 : 1 (v/v) THF/H₂O mixture was added dropwise and the mixture was kept in the temperature range of $-15\text{ }^{\circ}\text{C}$ to $-5\text{ }^{\circ}\text{C}$ for 90 min.

Subsequently, 43 μL (0.37 mmol) of *N,N*-dimethylaniline was added and the reaction mixture was kept below $-5\text{ }^{\circ}\text{C}$ for 2 h. Afterwards, it was allowed to warm to room temperature under stirring (300 rpm) overnight. The red brown solid was filtered off, washed with acetic acid (10 mL) and acetone (20 mL) and dried under vacuum.

6.4.3 Synthesis of TpBD(DPA)₂

TpBD(NH₂)₂ was prepared following a procedure reported earlier by us.²⁰ 10 mg TpBD(NH₂)₂ (corresponding to 0.062 mmol NH₂ groups) was suspended in 0.8 mL dry THF in a culture tube and cooled down to $-15\text{ }^{\circ}\text{C}$ in an ice/NaCl bath under stirring with a speed of 300 rpm.

To this mixture, 0.09 mL of 2 M HCl solution were added dropwise, followed by a solution of 4.3 mg (0.062 mmol) NaNO₂ (for a 100% modified sample) in 0.1 mL of a 1 : 1 (v/v) THF/H₂O mixture. The reaction mixture was kept in the temperature range of $-15\text{ }^{\circ}\text{C}$ to $-5\text{ }^{\circ}\text{C}$ for 90 min. Afterwards, 62 mg (0.37 mmol) of diphenylamine in 1 mL acetic acid were added dropwise and the reaction mixture was allowed to warm up to room temperature overnight under moderate stirring of 300 rpm. Subsequently, the precipitate was filtered off and washed with acetic acid (10 mL) and acetone (20 mL) and dried under vacuum.

6.5 Appendix

6.5.1 Protonation Equilibria

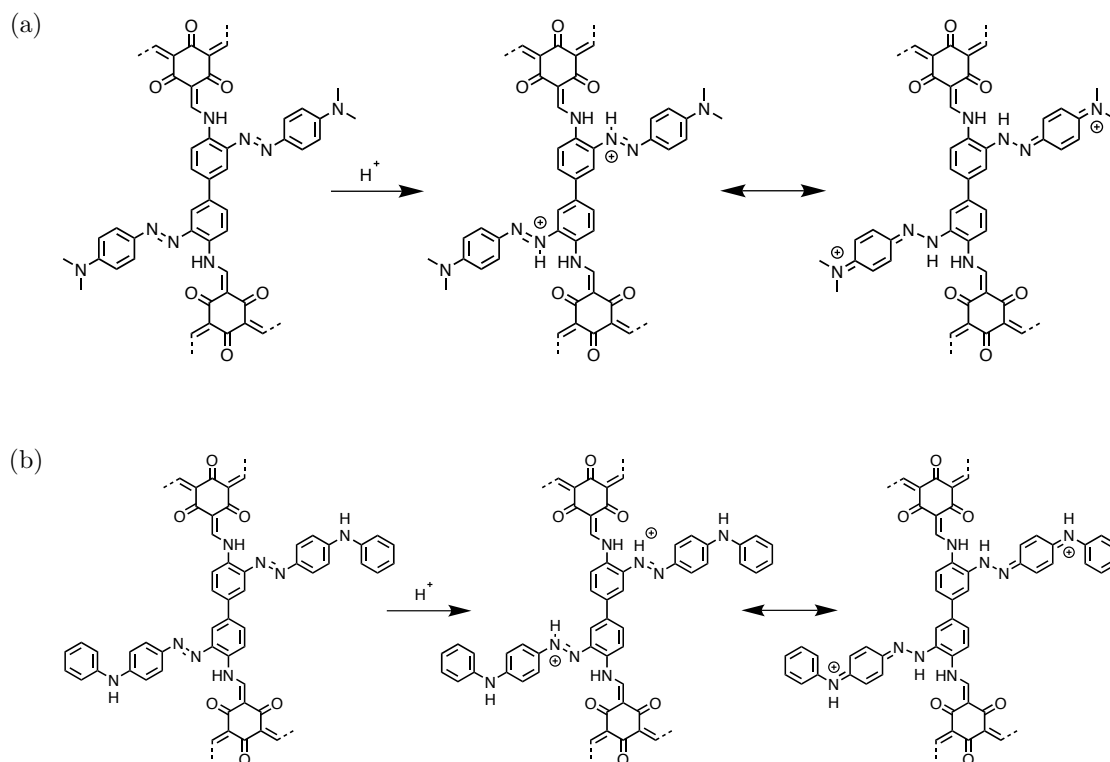


Figure 6.9: Protonation equilibria of (a) TpBD(DMA)₂ and (b) TpBD(DPA)₂.

6.5.2 Scanning Electron Microscopy Images

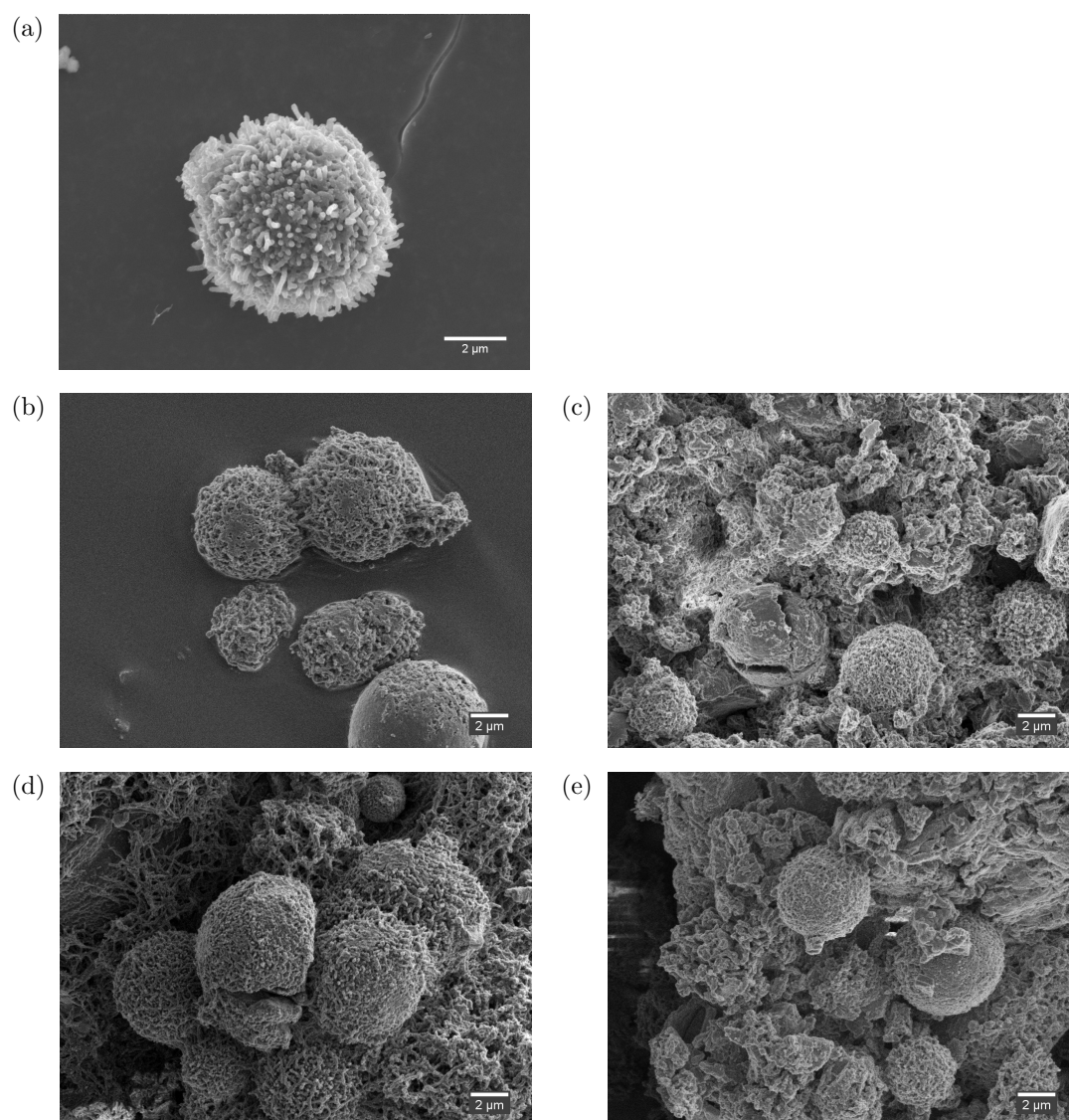
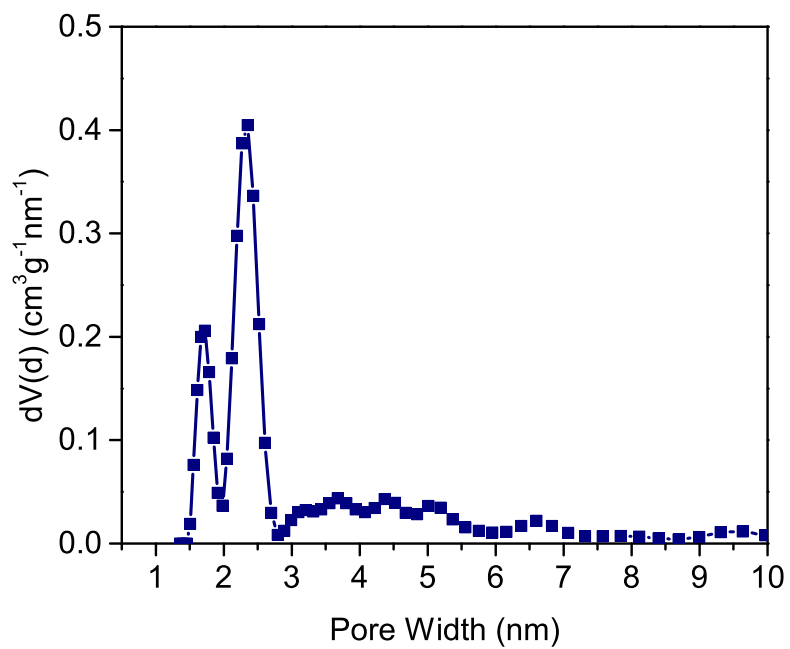


Figure 6.10: Scanning electron microscopy images of (a) TpBD(NH₂)₂, (b) TpBD(DMA)₂ 50%, (c) TpBD(DMA)₂ 100%, (d) TpBD(DPA)₂ 50%, (e) TpBD(DPA)₂ 100%.

6.5.3 Pore Size Distribution of TpBD(NH₂)₂

Bibliography

- [1] A. P. Côté, A. I. Benin, N. W. Ockwig, M. O’Keeffe, A. J. Matzger, and O. M. Yaghi. *Science*, **2005**, *310*, 1166–1170.
- [2] S.-Y. Ding and W. Wang. *Chem. Soc. Rev.*, **2013**, *42*, 548–568.
- [3] X. Feng, X. Ding, and D. Jiang. *Chem. Soc. Rev.*, **2012**, *41*, 6010–6022.
- [4] J. W. Colson and W. R. Dichtel. *Nat. Chem.*, **2013**, *5*, 453–65.
- [5] N. Huang, P. Wang, and D. Jiang. *Nat. Rev. Mater.*, **2016**, *1*, 16068.
- [6] P. J. Waller, F. Gándara, and O. M. Yaghi. *Acc. Chem. Res.*, **2015**, *48*, 3053–3063.
- [7] A. Nagai, Z. Guo, X. Feng, S. Jin, X. Chen, X. Ding, and D. Jiang. *Nat. Commun.*, **2011**, *2*, 1542/1–1542/8.
- [8] L. Chen, K. Furukawa, J. Gao, A. Nagai, T. Nakamura, Y. Dong, and D. Jiang. *J. Am. Chem. Soc.*, **2014**, *136*, 9806–9809.
- [9] H. Xu, X. Chen, J. Gao, J. Lin, M. Addicoat, S. Irle, and D. Jiang. *Chem. Commun.*, **2014**, *50*, 1292–1294.
- [10] N. Huang, R. Krishna, and D. Jiang. *J. Am. Chem. Soc.*, **2015**, *137*, 7079–7082.
- [11] F. Xu, H. Xu, X. Chen, D. Wu, Y. Wu, H. Liu, C. Gu, R. Fu, and D. Jiang. *Angew. Chem., Int. Ed.*, **2015**, *54*, 6814–6818.
- [12] H. Xu, J. Gao, and D. Jiang. *Nat. Chem.*, **2015**, *7*, 905–912.
- [13] B. K. Hughes, W. A. Braunecker, D. C. Bobela, S. U. Nanayakkara, O. G. Reid, and J. C. Johnson. *J. Phys. Chem. Lett.*, **2016**, *7*, 3660–3665.
- [14] D. N. Bunck and W. R. Dichtel. *Chem. Commun.*, **2013**, *49*, 2457–2459.
- [15] Q. Sun, B. Aguila, J. Perman, L. D. Earl, C. W. Abney, Y. Cheng, H. Wei, N. Nguyen, L. Wojtas, and S. Ma. *J. Am. Chem. Soc.*, **2017**, *139*, 2786–2793.
- [16] N. Huang, X. Chen, R. Krishna, and D. Jiang. *Angew. Chem., Int. Ed.*, **2015**, *54*, 2986–2990.
- [17] S. Zhao, B. Dong, R. Ge, C. Wang, X. Song, W. Ma, Y. Wang, C. Hao, X. Guo, and Y. Gao. *RSC Adv.*, **2016**, *6*, 38774–38781.

- [18] S. Mitra, H. S. Sasmal, T. Kundu, S. Kandambeth, K. Illath, D. Diaz Diaz, and R. Banerjee. *J. Am. Chem. Soc.*, **2017**, *139*, 4513–4520.
- [19] B. Dong, L. Wang, S. Zhao, R. Ge, X. Song, Y. Wang, and Y. Gao. *Chem. Commun.*, **2016**, *52*, 7082–5.
- [20] M. S. Lohse, T. Stassin, G. Naudin, S. Wuttke, R. Ameloot, D. De Vos, D. D. Medina, and T. Bein. *Chem. Mater.*, **2016**, *28*, 626–631.
- [21] S. B. Kalidindi and R. A. Fischer. *Phys. Status Solidi B*, **2013**, *250*, 1119–1127.
- [22] Y. Zeng, R. Zou, and Y. Zhao. *Adv. Mater.*, **2016**, *28*, 2855–2873.
- [23] Q. Fang, S. Gu, J. Zheng, Z. Zhuang, S. Qiu, and Y. Yan. *Angew. Chem., Int. Ed.*, **2014**, *53*, 2878–2882.
- [24] D. B. Shinde, S. Kandambeth, P. Pachfule, R. R. Kumar, and R. Banerjee. *Chem. Commun.*, **2015**, *51*, 310–313.
- [25] C. R. DeBlase, K. Hernandez-Burgos, K. E. Silberstein, G. G. Rodriguez-Calero, R. P. Bisbey, H. D. Abruna, and W. R. Dichtel. *ACS Nano*, **2015**, *9*, 3178–3183.
- [26] L. Bai, Q. Gao, and Y. Zhao. *J. Mater. Chem. A*, **2016**, *4*, 14106–14110.
- [27] X. Yang, B. Dong, H. Zhang, R. Ge, Y. Gao, and H. Zhang. *RSC Adv.*, **2015**, *5*, 86137–86143.
- [28] M. Dogru and T. Bein. *Chem. Commun.*, **2014**, *50*, 5531–5546.
- [29] D. D. Medina, T. Sick, and T. Bein. *Adv. Energy Mater.*, **2017**, *7*, 1700387.
- [30] J. Gao and D. Jiang. *Chem. Commun.*, **2016**, *52*, 1498–1500.
- [31] A. Bisset and T. J. Dines. *J. Chem. Soc., Faraday Trans.*, **8 1997**, *93*, 8, 1629–1636.
- [32] E. H. Otal, M. L. Kim, M. E. Calvo, L. Karvonen, I. O. Fabregas, C. A. Sierra, and J. P. Hinestroza. *Chem. Commun.*, **40 2016**, *52*, 40, 6665–6668.
- [33] C. V. Yelamaggad, A. S. Achalkumar, D. S. S. Rao, and S. K. Prasad. *J. Org. Chem.*, **2009**, *74*, 3168–3171.

Chapter 7

Conclusion and Outlook

In this work structural aspects regarding the formation of covalent organic frameworks (COFs) have been investigated, with a view on the formation of oriented films and the impact of side groups on the crystallinity of COFs in powder materials. Furthermore, the variety of structures and the scope of application of COFs have been broadened by the development of postsynthetic modifications of these frameworks.

Chapter 2 provided a comprehensive overview over the COF structures reported to date alongside with the development of synthesis techniques and the different fields of applications for COFs.

In a systematic study, the impact of the incorporation of ethoxy (OEt) side groups into the framework of BDT-COF has been investigated (Chapter 3). To this end, the ethoxy-functionalized benzodithiophene COF BDT-OEt was synthesized and a structural series with increasing fractions of OEt-functionalized linker has been prepared. It was found that for all compositions, a crystalline and porous structure is achieved, while the pore size is decreasing with increasing OEt content due to the OEt groups pointing into the pores. Furthermore, the crystallite domain size is decreasing with increasing OEt amount, indicating a disturbing influence of the OEt groups on the structural order in the framework. Moreover, the ratio of the building units in the framework could be determined prior to COF synthesis allowing for a fine tuning of the COF's properties. Molecular dynamics simulation and DFT calculations showed a preferential orientation of the oxygen in the ethoxy side chains towards the BDT sulfur and a facilitated lateral offset of the COF layers upon insertion of OEt-functionalized BDT.

Furthermore, the impact of different terminal functional groups of self-assembled monolayers on gold on the solvothermal growth of thin films of COF-5 was investigated (Chapter 4). While on all substrates oriented films were formed where the COF sheets were aligned parallel to the substrate surface, for COF films grown on SAMs terminated with -OH or -COOH groups, a particularly high degree of order was observed by GID measurements,

compared to functionalization with alkyl chains or on bare gold. This finding indicates that the SAM terminal OH- and COOH-groups might act as modulators in the growth of boronic ester COF thin films to produce an improved alignment of the COF crystallites. The enhanced orientation of the crystallites found for COF-5 grown on OH- and COOH-terminated SAMs may be applied for the formation of COF films with a higher degree of order and thus improve the quality and functionality of COF films.

In the second part of this thesis, the spectrum of COF structures was expanded by post-synthetic modification reactions, thereby further tuning the properties of the frameworks. In Chapter 5, the postsynthetic formation of aromatic NH₂-groups in a COF was demonstrated. First, the chemically highly stable β -ketoenamine-linked COF TpBD(NO₂)₂ was synthesized. Subsequently, the nitro groups were reduced to yield the framework TpBD(NH₂)₂ while retaining the crystallinity and porosity of the COF. The chemical accessibility of the established amino groups was demonstrated by a sequential modification step, the reaction with acetic anhydride to form the amide COF TpBD(NHCOCH₃)₂. This exemplary modification demonstrates the feasibility of two subsequent postsynthetic modification reactions in a COF network, which were demonstrated in this work for the first time. The high chemical stability of the frameworks was then utilized to study the task of lactic acid adsorption in the pore system in the liquid phase. A strong impact of the pore functionalization on the lactic acid uptake was found with a strong increase in capacity upon the reduction of the nitro groups to the primary amines. This demonstrates the benefit of primary amines as functional groups in COF pores for H-bonding interactions with guest molecules.

Based on the above findings, the newly synthesized NH₂-functionalized COF TpBD(NH₂)₂ was then post-synthetically modified to increase the light absorption range of the COF in the visible region (Chapter 6). For this purpose, a two-step azo coupling reaction was employed to connect amines *via* azo linkages to the COF. A quantitative conversion to the azo-functionalized COF was reached both with *N,N*-dimethylaniline and diphenylamine. With the partial introduction of diphenylamine, a bathochromic shift of the UV-vis adsorption onset of the COF was achieved, thus accomplishing the postsynthetic tuning of the optical absorption of a COF.

In summary, the structural impact of side chains in the linkers as well as substrate modifications on the growth of COFs have been investigated in this thesis. The reported postsynthetic formation of primary aromatic amines as functional groups at the pore walls of a chemically highly stable COF provides a versatile starting point for further postsyn-

thetic modifications. Together with the azo coupling reaction developed in this thesis, it expands the range of possible modification reactions in COFs and thus the postsynthetic tunability of the properties of COFs.

